THE UNIVERSITY *of* EDINBURGH

This thesis has been submitted in fulfilment of the requirements for a postgraduate degree (e.g. PhD, MPhil, DClinPsychol) at the University of Edinburgh. Please note the following terms and conditions of use:

This work is protected by copyright and other intellectual property rights, which are retained by the thesis author, unless otherwise stated.
A copy can be downloaded for personal non-commercial research or study, without prior permission or charge.
This thesis cannot be reproduced or quoted extensively from without first obtaining permission in writing from the author.
The content must not be changed in any way or sold commercially in any format or medium without the formal permission of the author.
When referring to this work, full bibliographic details including the author, title, awarding institution and date of the thesis must be given.

Heavier group 13 based frustrated Lewis pairs for catalytic C–H borylation

A Thesis Submitted for the Degree of Doctor of Philosophy

THE UNIVERSITY *of* EDINBURGH

Daniel M. De Rosa

School of Chemistry

Science and Engineering

December 2020

Author Declaration

I declare that this thesis is an original report of my research, has been written by me and has not been submitted for any previous degree. Except where otherwise stated, experimental and computational work is my own. Collaborative contributions are acknowledged. Due references have been provided to all supporting literature and resources.

Daniel Matthew De Rosa

Lay Abstract

A catalyst is a chemical added to a chemical reaction to speed up that reaction without being used up during the reaction and the process of using a catalyst in a chemical reaction is called catalysis. Catalysis is very important as lots of chemical reactions need a catalyst to work. Therefore chemists want to discover as many catalysts as possible to make new chemical reactions possible.

Many of the catalysts that are currently heavily used are made from rare precious metals such as gold and platinum. These catalysts are very good at speeding up the reactions they are used for, but because of their rarity, they are very expensive to make (think about the cost of jewellery made from these metals!). Because of this, chemists are now looking to make new catalysts from much more sustainable resources.

This thesis looks at making new catalysts from aluminium, which is the most common metal in the earth's crust and due its abundance is very cheap and widely used for many applications (cans, foil, pans etc.). Unfortunately, aluminium is not as good at acting as a catalyst as the precious metals and so special changes must be made to make a good catalyst from aluminium. In this work this is achieved by incorporating the aluminium into a molecule called a frustrated Lewis pair (FLP).

In this molecule there are both the aluminium and also nitrogen. Normally aluminium and nitrogen bond together and will not react with other molecules.

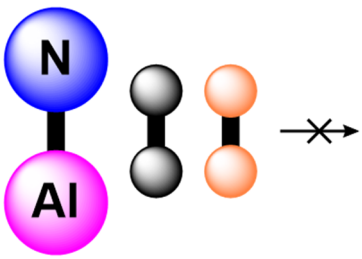

In the FLP, they are held apart so that they cannot bond. This means that the aluminium and nitrogen are not as stable they want to be since they are missing the bond that they would normally have. Because of this they will react with other molecules and split them

apart. The split molecule can then react with another molecule to make the products. This is what allows the FLP to be a catalyst.

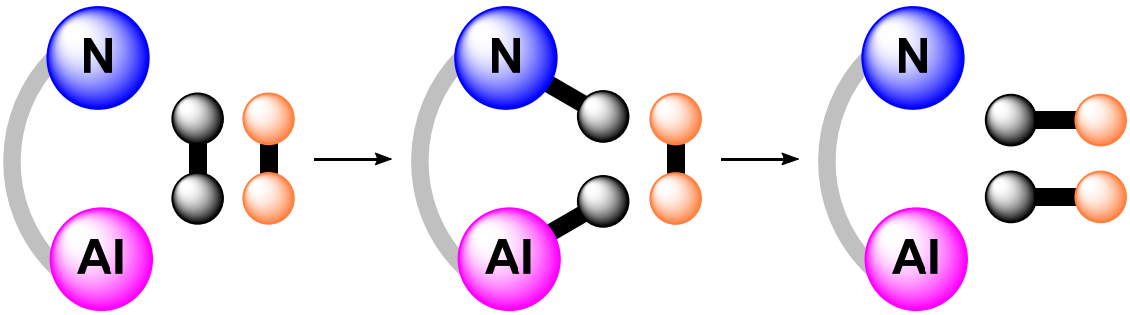

Abstract

Research into catalysis has always been of great interest to both academic researchers and in industry, due to the great utility that catalysts possess. In particular, research into catalysts that are based on more earth-abundant elements has gained increasing attention, due to the advantages these have, namely lower cost and generally lower toxicity, relative to the currently most commonly used platinum group based catalysts.

Frustrated Lewis pairs (FLPs) are one of the most researched class of molecules in this field of earth-abundant element catalysis. They are highly reactive molecules comprised of a Lewis acid and a Lewis base that are unable to form an adduct due to steric constraints. This leads to remarkable reactivity when these pairs react with small molecules, activating many E–H bonds. They can then subsequently deliver these activated molecules to unsaturated molecules such as imines in a catalytic manner.

Despite the already significant amount or research into the field of FLPs, there is a notable lack of diversity in the elements chosen for the Lewis acidic and basic centres of the molecules, with more focus on the surrounding architecture of the FLP. Most FLPs utilise phosphorus or nitrogen as the Lewis basic element and boron as the Lewis acidic element. As such, the aim of this work is to investigate less utilised elements for the Lewis acidic portion of the FLP, in particular, other members of group 13.

Chapter 1 is an introduction that gives an overview of main-group catalysis as a whole and also covers methods for C–H borylation of both aryl compounds and also terminal alkynes. This is to provide context to the work presented in the following chapters.

Chapter 2 introduces two target novel aluminium based FLP compounds and describes the synthetic steps on route towards them. This leads to the characterisation of several novel FLP compounds although the two target compounds were not synthesised due to issues with ligand exchange steps on the proposed synthetic routes. Computational analysis of these ligand exchange reactions is also presented, to explain the unexpected results of these reactions.

Chapter 3 focuses on the usage of the novel FLP species synthesised in chapter 2 as precatalysts for the C–H borylation of both aryl compounds and terminal alkynes, examining how to generate a catalytically active species, optimisation of conditions for the catalytic reactions, and the scope of reactivity with both classes of substrate.

Chapter 4 investigates in detail the mechanism of the catalytic terminal C–H borylation of alkynes presented in chapter 3. Also examined is the competing mechanism of hydroboration of the alkyne triple bond, which is the usual reactivity for aluminium hydride compounds. By looking at both of these mechanisms an explanation of the catalyst selectivity towards the terminal C–H borylation over the hydroboration is given. Additionally, examination of how the catalytically active species are generated under reaction conditions is carried out. Additionally, experimental work was carried out to attempt to isolate some of the on cycle species to provide additional evidence for the proposed mechanism. However, these structures could not be isolated, presumably due to their highly reactive nature and instead products from overreaction were isolated. Computational analysis is used to attempt to explain how these overreaction products form. From all of the above results an in depth model of the catalytic reaction is presented.

Chapter 5 presents a computational investigation into other potential new FLP species, with a focus on finding candidates to perform C–H borylation of the widest range of aryl compounds possible. Therefore the C–H activation step has been calculated for a wide range of potential FLP candidates, with changes in the steric bulk of the FLP, changes to the Lewis basicity of the FLP, and also changes to the Lewis acidity of the FLP examined to extract trends in how the reactivity changes and therefore propose a set of possible candidates for experimental synthesis and trialling.

Acknowledgements

Firstly, I would like to thank my two primary supervisors, Dr Michael Cowley and Dr Stephen Thomas, for providing me with a place in their groups to undertake my PhD and for their constant help and support throughout my studies, with both day to day planning and execution of research, and with bigger issues like switching to computational chemistry. I would also like to thank the CRITICAT CDT for providing the funding for my PhD studies. Having enough money to live in a flat and eat food has been greatly appreciated.

To Dr Carole Morrison, many thanks for teaching me the ins and outs of computational chemistry, virtually from scratch when I decided to move from experimental work in the lab to computational modelling in the middle of my PhD. You were very patient with me even when I asked what I know were many silly questions about all the theory behind it all and helping fix the calculations when they refused to cooperate.

Thanks to all the technical staff at the university, especially those in the NMR, Mass Spec, and IT departments, and also in the chemistry stores, for helping with any problems I had and making the department a cheery place.

Many thanks to all the members of both the Cowley group (Amy, Steph, Alex, Lena, Clément, Martin, Rosie, Abi, Jack, Arthur, Andryj, Ella, new Alex, and Peter) and Thomas group (Jim, James, Kevin, Amy, Pete, Jon, Peter, Jingying, Joanne, Liam, Andrew, Kieran, Dom, and Luke) throughout my time here in Edinburgh for providing a cheerful and fun working environment in both the lab and office spaces. Extra thanks in particular to Abi, Dom, Jack, and Arthur for their collaborative help in the research carried out in this thesis.

Thanks to Bec for being a great friend throughout the CRITICAT CDT training period in St Andrews and beyond into research at Edinburgh, with numerous good chats in the office and drinks down the pub over these past few years.

Thanks to Rebecca for providing a steady stream of the best baked goods in the department. My taste buds are better for having tasted all your food, even if I have consumed slightly more than the recommended dosage of sugar over the past few years.

Thanks to Cath and Gavin for bringing me and single cask Scotch whisky together by introducing me to the Scotch Malt Whisky Society. Many an excellent dram has been had without which my life would be a significantly duller (if slightly less inebriated) experience.

Thanks to Chris, Sinj, Elliot, John, Dan, and Mishi for being my ever present online squad of friends, always up for a few games and idiotic conversations to blow off steam after particularly infuriating or strenuous days of research or thesis writing.

The biggest and warmest of thanks to Helen, for being here for me through everything and for being more patient with me than any person should reasonably be expected to be, enduring my complaints, bad moods and general idiocy throughout my research and writing up period.

And finally, a huge thanks to my family, and especially to Mum and Dad, who have always believed in me, throughout everything, even when I have been unable to believe in myself.

Thanks again to all of these people, because of whom I have managed to get all this way and finally submit this thesis. I couldn't have done it without them, and for that I am eternally grateful.

Thesis Contents

Author Declaration i

Lay Abstract ii

Abstract iv

Acknowledgements vi

List of Abbreviations xii

1 Introduction 1

1.1 Overview 1

1.2 Main-group element small-molecule activation and catalysis 4

1.2.1 Carbenes 4

1.2.2 Heavier group 14 carbene analogues 8

1.2.3 Group 13 carbene analogues 12

1.2.4 Group 14 alkyne analogues 14

1.2.5 Constrained-geometry compounds 16

1.2.6 Main-group element heterocycles 20

1.2.7 Frustrated Lewis pairs 21

1.3 C–H Borylation 27

1.3.1 Aromatic and saturated aliphatic compounds 28

1.3.2 Alkynes 30

1.4 Aims of this work 36

1.5 References 37

2 Synthesis and characterisation of novel aluminium based FLPs 41

2.1 Introduction and aims 41

2.2 Synthesis of dialkyl aluminium FLPs 44

2.3 Substituent-exchange reactions of dimethyl aluminium FLPs with $B(C_6F_5)_3$ 52

2.4 Computational analysis of substituent-exchange reactions 57

2.4.1 Exchange between $AlMe_3$ and $B(C_6F_5)_3$ 58

2.4.2 Exchange reaction between 6 and $B(C_6F_5)_3$ 63

2.5 Conclusions 68

2.6 References 68

3 Catalysis using in-situ generated aluminium hydride FLPs 70

3.1 Introduction and aims 70
3.2 Generation of aluminium hydride FLPs 71
3.3 Catalytic conditions and substrate scope for aromatic compounds 75
3.4 Catalytic conditions and substrate scope for terminal alkynes 79
3.5 Conclusions 85
3.6 References 86
4 Computational investigation of aluminium FLP alkyne borylation mechanisms 87
4.1 Introduction and aims 87
4.2 Terminal borylation mechanism 92
4.3 Hydroboration mechanism 98
4.4 Explanation of catalyst selectivity 102
4.5 Catalyst activation 105
4.6 Experimentally isolated structure analysis 109
4.7 Final catalytic cycle model 118
4.8 Conclusions 119
4.9 References 120
5 Computational investigation of other group 13 based FLP compounds 121
5.1 Introduction and aims 121
5.2 Steric bulk 123
5.2.1 Boron 125
5.2.2 Aluminium 128
5.2.3 Gallium 132
5.2.4 Intramolecular N–H interactions in IM2 133
5.2.5 Effect of steric bulk on the reaction profile 136
5.3 Lewis basicity 138
5.3.1 Boron 140
5.3.2 Aluminium 144
5.3.3 Gallium 146
5.3.4 Effect of Lewis basicity on the reaction profile 147
5.4 Effect of changing Lewis acidity on C–H activation 148
5.4.1 Boron 150
5.4.2 Aluminium 154

5.4.3 Gallium 156
5.4.4 Effect of Lewis acidity on the reaction profile 157
5.5 Conclusions and future aims 158
5.6 References 160
6 Experimental and computational methods 161
6.1 Chapter 2 experimental procedures 161
6.1.1 General considerations 161
6.1.2 Preparation of 2-lithio-*N*,*N*-dimethylaniline (4) 162
6.1.3 Preparation of 2-dimethylaluminium-*N*,*N*-dimethylaniline (6) 163
6.1.4 Reaction of 2-Lithio-*N*,*N*-dimethylaniline with dimethyl aluminium chloride to form 2-dimethyl aluminium-*N*,*N*-dimethylaniline dimethyl aluminium chloride adduct (8) 164
6.1.5 Reaction of 2-dimethylaluminium-*N*,*N*-dimethylaniline with trispentafluorophenyl borane to form 2-bispentafluorophenylaluminium-*N*,*N*-dimethylaniline (10) 165
6.1.6 Preparation of *N*-(2-iodophenyl)-2,2,6,6-tetramethylpiperidine (3) ... 166
6.1.7 Preparation of *N*-(2-lithiophenyl)-2,2,6,6-tetramethylpiperidine (5) .. 167
6.1.8 Preparation of *N*-(2-dimethyl aluminium phenyl)-2,2,6,6-tetramethylpiperidine (7) 168
6.1.9 Reaction of *N*-(2-Lithiobenzyl)-2,2,6,6-tetramethylpiperidine with dimethyl aluminium chloride to form *N*-(2-methyl chloro aluminium phenyl)-2,2,6,6-tetramethylpiperidine (9) 170
6.1.10 Reaction of *N*-(2-dimethyl aluminium phenyl)-2,2,6,6-tetramethylpiperidine with trispentafluorophenyl borane to form *N*-(2-bispentafluorophenyl aluminium phenyl)-2,2,6,6-tetramethylpiperidine (11) . 171
6.2 Chapter 3 experimental procedures 172
6.2.1 General considerations 172
6.2.2 Reaction of 2-dimethylaluminium-*N*,*N*-dimethylaniline (3) with HBpin to form 2-dihydroaluminium-*N*,*N*-dimethylaniline (5) 173
6.2.3 C–H borylation of heteroaromatics scope 174
6.2.7 C–H borylation of alkynes scope 177
6.3 Chapter 4 experimental procedures 183
6.3.1 General considerations 183
6.3.2 Preparation of 2-dihydroaluminium-*N*,*N*-dimethylaniline (3) by $AlCl_3$ then $LiAlH_4$ 184

6.3.3 Preparation of 2-dihydroaluminium-*N*,*N*-dimethylaniline (3) by $AlH_3.NEtMe_2$ 185
6.3.4 Preparation of AlH_2Cl 186
6.3.5 Preparation of 2-dihydroaluminium-*N*,*N*-dimethylaniline (3) by AlH_2Cl 186
6.3.6 Preparation of tris(phenylethynyl)aluminium *N*,*N*-dimethylaniline adduct (47)..... 187
6.4 Computational chemistry..... 188
6.4.1 Computational modelling..... 188
6.4.2 Quantum Mechanical Theory..... 188
6.4.3 Quantum Mechanical Calculations..... 195
6.4.4 Method choice..... 199
6.4.5 Computational details for chapter 2..... 200
6.4.6 Computational details for chapter 4 and chapter 5. 201
6.5 References..... 202
7 Appendix ..... a

List of Abbreviations

Cp*H	1,2,3,4,5-pentamethylcyclopentadiene
Cp*	1,2,3,4,5-pentamethylcyclopentadienyl anion
DABCO	1,4-diazabicyclo[2.2.2]octane
HB(dan)	1,8-Naphthalenediaminatoborane
HBpin	4,4,5,5-Tetramethyl-1,3,2-dioxaborolane
aAAC	acyclic alkyl amino carbene
AAC	alkyl amino carbene
Å	Ångstrom
Ar	aryl
atm.	atmosphere
CSD	Cambridge structural database
J	coupling constant
cAAC	cyclic alkyl amino carbene
°C	degrees Celsius
DFT	density functional theory
dipp	di-isopropylphenyl
d	doublet
d br	doublet broad
dd	doublet of doublets

dt	doublet of triplets
dq	doublet of quartets
EI-MS	electron impact mass spectroscopy
FLP	frustrated Lewis pair
Hz	hertz
MHz	megahertz
µmol	micromole
mbar	millibar
mL	millilitre
mg	milligram
mmol	millimole
Me	methyl
m	multiplet
m br	multiplet broad
Mes	mesityl
n-BuLi	*n*-butyllithium
NMR	nuclear magnetic resonance
NHC	nucleophilic heterocyclic carbene
ppm	parts per million
Ph	phenyl

Bpin	pinacolato boron
pip	piperidyl
Pn	pnictogen
PCM	Polarisable Continuum Model
PES	potential energy surface
qu	quintet
s	singlet
s br	singlet broad
SMD	Solvation Model based on Density
s.d.	standard deviation
^{t}Bu	tertiary butyl
TMP	tetramethylpiperidyl
TS	transition state
TST	transition state theory
OTf	trifluoromethanesulfonate
tt	triplet of triplets
WBI	Wiberg bond index

1 Introduction

1.1 Overview

Over the past few decades, there has been a steadily increasing view from both the scientific community and the general public that an increase in the sustainability of chemical processes must be achieved, in order to more efficiently manage the earth's resources.

Catalysis is of great importance in almost all industrial chemical processes, with an estimated 90% of all chemical products requiring a catalyst for at least one of the steps in their manufacture.[1] As such, finding more efficient catalytic processes is attractive for increasing the sustainability of chemical processes.

In order to assess the sustainability of catalytic processes, a number of different factors must be considered. Atom economy of the process is of foremost importance. Ideally all processes will be 100% atom economic, utilising all reactant atoms in the products. However, the sustainability of the reagents themselves is also a factor. Using a combination of reactants and catalyst that come from the most sustainable sources is attractive. For instance, if reactants from a biomass feedstock can be used in a process instead of fossil fuel derived reactants, this greatly increases the sustainability of the process. Equally, using a catalyst derived from more sustainable elements will again greatly increase the sustainability of the process. When assessing the sustainability of an element, a number of factors contribute.

While crustal abundance of the elements is one of the more obvious contributing factors, the annual global production of the element, combined with how easy the element is to recycle are also important. The geographical concentration of the ore sources is also a concern, as sources located in politically unstable regions may lead to a sudden cut-off of supply due to shifts in the political climate. These factors are combined to give each element a rating that reflects its long term supply risk over the next 100 years.[2]

Currently, many catalytic processes rely on late transition metals, especially in the field of homogeneous catalysis. Late transition metals are very powerful catalysts as they can easily perform processes such as oxidative addition and reductive elimination, which are key steps in almost all transition metal catalysed processes. This is due to due to a unique combination of properties, namely the finely balanced energetics and spatial arrangement of frontier d-orbitals that these elements possess.[3] However, late transition metals are not without their problems. Firstly, late transition metals tend to be relatively toxic, and this is reflected in their low permitted daily exposure limits, which are around the 100 µg per day level.[4] In addition, many of the late transition metals are classified using the previously discussed risk factors as having increased risk to supply in the next 100 years. While the usage of these elements will never be completely excluded due to how powerful they are as catalysts, finding alternative catalysts based on more long term sustainable elements to in some cases replace and in others compliment these systems to reduce their usage is an attractive goal.

In this search for new more sustainable catalysts, there are a number of emerging areas. The most logical of these is to look to the first row transition metals, which still possess the d-orbitals that are of such importance in this catalysis and can in theory exhibit analogous reaction mechanism steps to their lower group counterparts, although in practice this is challenging. Late transition metals are relatively air and moisture stable even upon changing oxidation state, while the first row metals are highly air and moisture sensitive in low oxidation states making them much harder to handle and use. Despite this, the area of first-row transition-metal catalysis is expanding rapidly and the range of transformations that are achievable with first row transition metals is constantly growing. Iron, cobalt, and nickel are by far the most thoroughly investigated first row elements, but examples of manganese, chromium and copper are also increasingly prevalent. Recent examples of work in the field can be found in review articles by Bauer and Knölker, Webster, and also Taylor and Kays along with extensive references.[5–7]

Organocatalysis is another area that has received significant attention. The ability to replace metals entirely in catalysis has significant environmental benefits, but this is also

extremely attractive in pharmaceutical applications, where the removal of trace transition metal elements from drug products to meet regulation levels is an extremely costly process. Replacing transition-metal catalysis processes with purely organic processes can remove the need for these metal scavenging steps, although it is worth noting that some organocatalysts can themselves be toxic and require removal. Organocatalysts work through vastly different mechanisms to that of transition metal catalysts. The organic catalyst usually activates one of the reagents, increasing its reactivity and allowing the reaction to proceed. This can occur either *via* a covalent transition complex or *via* a noncovalent activation complex. There are also examples of phase transfer catalysis and reactivity mimicking that of enzymes by using a chiral cavity to control reactivity in the area of organocatalysis. As for the first row transition-metal catalysis, a more detailed overview can be found in review articles by MacMillan and also Dalko and Moisan.[8,9]

A further area where research has been concentrated is on the p-block, due to the generally lower toxicity of these elements, and also much greater crustal abundance and therefore lower cost. The challenge with these elements lies in the fact that they are much less able to easily shuttle between oxidation states than the d-block elements, as usually one oxidation state is much more stable than the others. Therefore, specialist main group species must be developed in order to access the desired reactivity needed for catalytic transformations. While not as heavily developed or widely applied as transition-metal catalysis, a number of main-group systems have recently emerged that are able to perform catalytic reactions capable of replacing or complimenting transition metal catalysts. These include heavier Group 14 carbene analogues,[10] constrained geometry compounds,[11] and frustrated Lewis pairs (FLPs).[12] These systems are capable of activating small molecules and delivering them to unsaturated substrates. P-block catalysis is the subject of this thesis and as such, an overview of catalytically relevant main group chemistry will be given to provide context. Additionally, current methods for the C–H borylation of aromatic compounds and alkynes will be discussed as these particularly relevant to the novel results discussed herein.

Focus is on the seminal examples of small molecule activation reactions and catalysis, so as to keep the introduction as concise as possible.

1.2 Main-group element small-molecule activation and catalysis

Many catalytic transformations focus on adding functionality to a substrate by the addition of a small molecule. As such, activation of the small molecule by the catalyst is a key step in these cycles. Therefore, research into small molecule activation is important for the development of new catalytic systems.

Extensive research has been carried out in the field of main group chemistry in the area of small molecule activation in order to develop main group catalytic systems. The most relevant examples will be discussed here, focussing on the activation of important E–H bonds (E = H, C, N) and subsequent catalytic transformations that have come from this research.

1.2.1 Carbenes

Carbenes as a class of molecule were first discovered 164 years ago,[13] and have been extensively studied since that initial discovery. Carbenes are a neutral divalent carbon-based species with six valence electrons. Due to their electron deficiency, carbenes display high levels of reactivity.

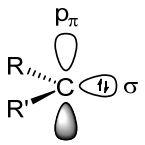

Figure 1 – Frontier orbital arrangement in singlet carbenes.

Carbenes exist in one of two ground state forms, either the singlet or triplet form. While carbenes can be linear, they are more commonly found in a bent form with non-degenerate σ and p_π orbitals (Figure 1).[14] The substituents around the carbon atom determine whether the carbene exists in the singlet or triplet configuration, as the substituents effect the energy of predominantly the p_π orbital. π-electron donors favour the singlet state of the carbene as they can be stabilised by delocalisation into the

unoccupied p_π orbital of the carbene, which cannot occur for the triplet state where the p_π orbital is occupied. Conversely π-acceptors will favour the triplet state where delocalisation of the electron in the p_π orbital into the accepting orbital can occur.

Due to their high reactivity, isolation of a stable carbene is tricky. It was not until 1991 that Arduengo *et al.* isolated a stable singlet carbene with the synthesis of the first nucleophilic heterocyclic carbene (NHC).[15] By incorporating two nitrogen substituents next to the carbon centre, the carbene was greatly stabilised through a combination of σ-withdrawing and π-donating effects, significantly lowering the energy of the singlet state. NHCs have since seen widespread usage as strongly σ-donating ligands, due to the significant nucleophilic character these carbenes possess.[16] However, NHCs are largely unreactive towards small molecules due to how great the stabilisation of the carbene by the two nitrogen centres is.

Subsequently, acyclic alkyl amino carbenes (aAACs) and cyclic alkyl amino carbenes (cAACs) were developed, by Alder and co-workers,[17] and Bertrand and co-workers respectively.[18] These carbenes have only one nitrogen substituent attached to the carbene centre. This reduces the σ-withdrawing and π-donating effects relative to an NHC. Therefore, aAACs and cAACs have a reduced singlet-triplet gap and so show both increased nucleophilicity and electrophilicity relative to that of NHCs. This increased reactivity allows AACs to activate small molecule substrates.

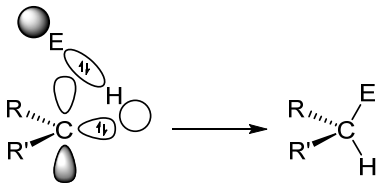

Figure 2 – Orbital arrangement in carbene mediated E–H bond activation.

The singlet state of these carbenes is of great importance in the ability of these carbenes to react with small molecules. The singlet state gives them the spatial orbital arrangement to promote activation of small molecule substrates *via* formal oxidative addition. In the singlet state the carbene can simultaneously attack the E–H σ* orbital while accepting electron density from the E–H σ orbital into its unoccupied p_π orbital

(Figure 2). This orbital arrangement is similar to that of a d-block transition metal, for which E–H bond activation occurs in an analogous manner. This type of mechanism would not be possible for a triplet carbene, although triplet carbenes are capable of activating small molecules such as dihydrogen and some small hydrocarbons through a radical mechanism.[19]

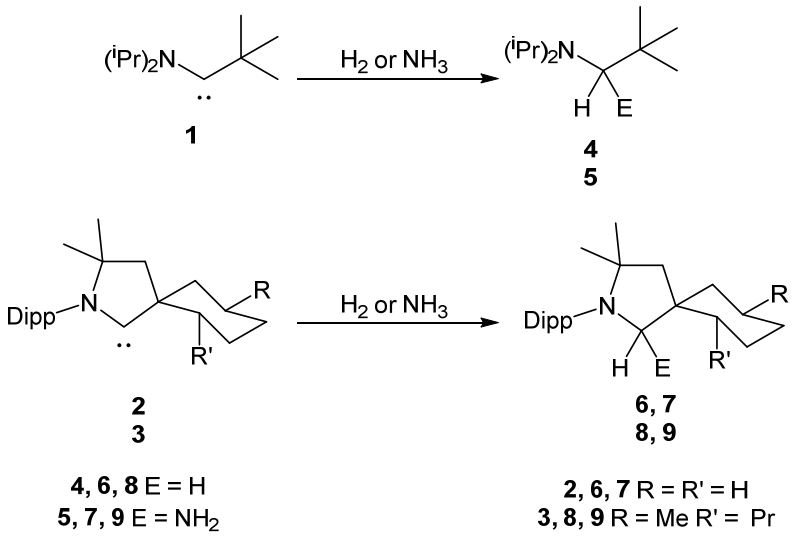

Scheme 1 – Activation of H_2 and NH_3 by aAACs and cAACs, adapted from Frey *et al.*[20]

The aAAC **1** and cAAC systems **2** and **3** reported by Bertrand and co-workers have been shown to activate dihydrogen and ammonia, giving the range of E–H activation compounds **4**-**9** (Scheme 1). H_2 and NH_3 are challenging substrates to activate due to their high bond-dissociation energies. Activation of ammonia is of particular interest, as for transition metals, activation of ammonia is difficult to achieve due to it being more likely to ligate the metal centre in preference to reacting with it.

Carbenes have also shown the ability to activate a range of C–H bonds. Acidic C–H bonds were the first to be activated, with Arduengo and co-workers showing the ability of NHC **10** To activate the C–H bonds of acetylene, methyl phenyl sulfone, acetonitrile, and chloroform to give the activation compounds **11**-**14** (Scheme 2a).[21]

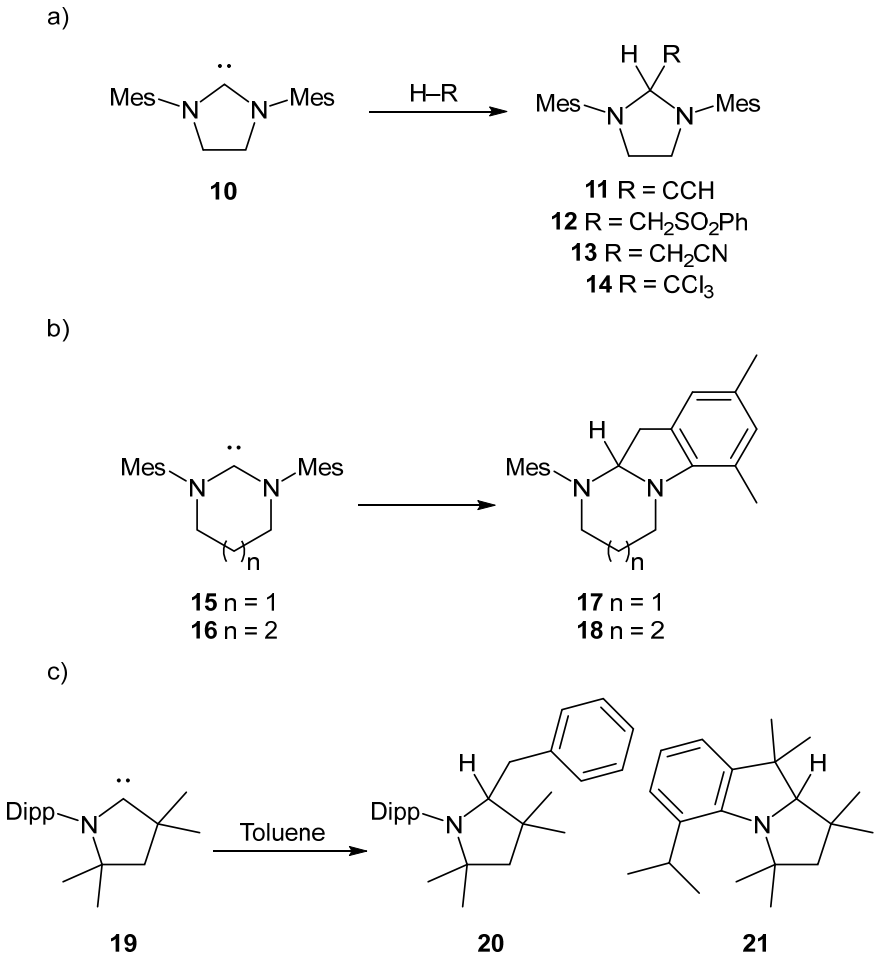

Scheme 2 – Activation of C–H bonds by carbenes, adapted from a) Iii *et al*,[21] b) Holdroyd *et al*,[22] and c) Turner.[23]

The activation of non-acidic C–H bonds was subsequently shown by Holdroyd *et al.* using ring expanded NHCs **15** and **16** which both intramolecularly activate the CH_3 group of their mesityl substituent to give the tricyclic compounds **17** and **18** (Scheme 2b).[22,24] Intermolecular activation of non-acidic C–H bonds was first reported by Turner, with cAAC **19** activating the C–H bond on the methyl group of toluene to give **20**, although this process is in competition with the intramolecular activation of the di-isopropylphenyl (dipp) group to give the tricyclic compound **21** (Scheme 2c).[23] Activation of toluene was favoured over intramolecular activation at lower reaction temperatures with a large excess of toluene.

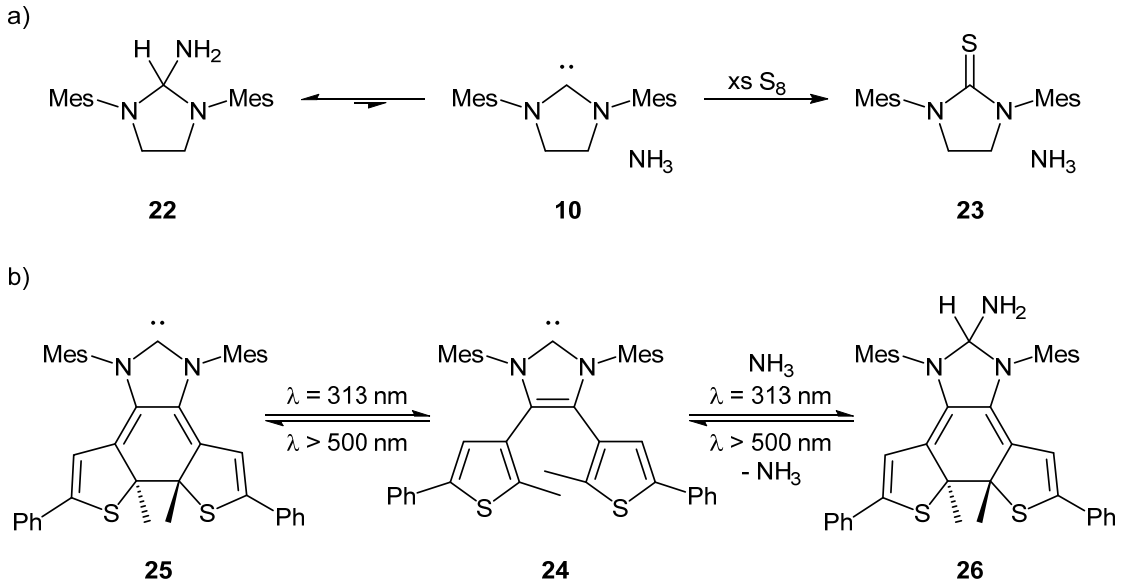

Scheme 3 – Reversible activation of ammonia by NHCs, adapted from a) Moerdyk *et al.* and b) Teator *et al.*[25,26]

More recently, two examples of NHCs have emerged that have shown the ability to reversibly activate ammonia. In 2013 Moerdyk *et al.* showed the ability of the simple NHC **10** to reversibly activate ammonia giving the amine **22**.[25] Proof of the reversibility was shown by addition of elemental sulphur to the activated product **22**. Reaction of the sulphur with the small amounts of **10** in solution eventually forces the equilibrium back towards **10** and therefore eventually gives full conversion to the thiourea **23** and ammonia, which was observed by NMR spectroscopy. In 2015 Teator *et al.* reported the photoswitchable NHC **24** which under irradiation by λ = 313 nm light rearranges to the isomer **25** and rearranged back to **24** under irradiation by λ > 500 nm light (Scheme 3). If the same reaction is carried out in the presence of ammonia, the amine **26** is generated reversibly instead of the isomeric form **25** (Scheme 3).

While all of the above examples are of fundamental interest, none of the shown activation products show reactivity with secondary substrates such as alkenes and so are unsuitable for catalytic applications.

1.2.2 Heavier group 14 carbene analogues

The preparation and isolation of stable carbene equivalents of the heavier group 14 elements is also challenging, as they have a tendency to dimerise or form polymeric

species, making their monomeric forms difficult to isolate. In order to isolate these monomeric forms, the design of ligands with large amounts of steric bulk is required to protect the reactive centre of the molecule. The first example of this class of molecule was isolated by Lappert and co-workers in 1973, where the stannylene :SnR_2 (R = $CH(SiMe_3)_2$) was prepared.[27] Since this initial discovery, examples of the germylene,[28] silylene,[29] and plumbylene have also been isolated.[30]

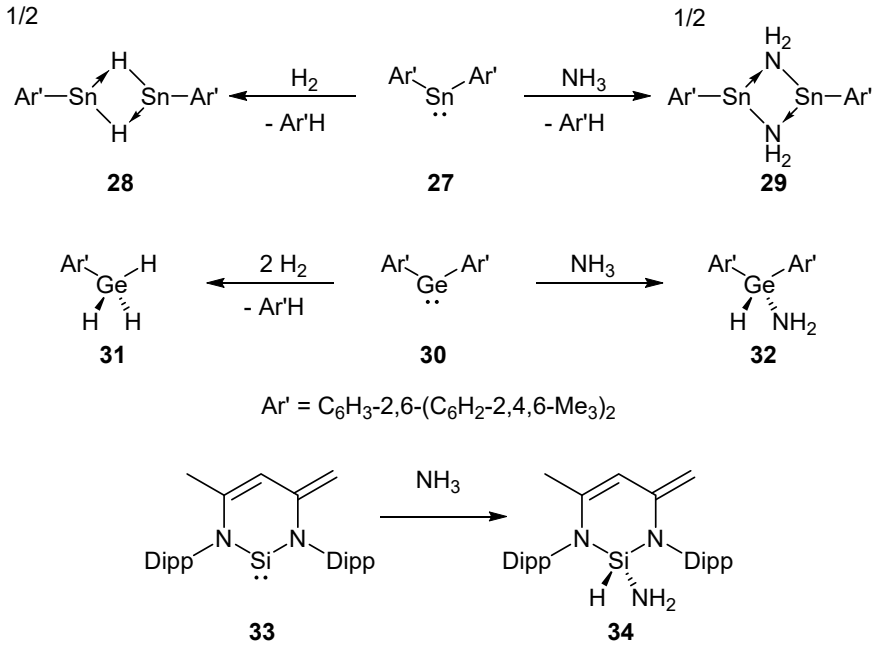

Scheme 4 – Reactions of stannylenes, germylenes and silylenes with H_2 and NH_3, adapted from Peng *et al*,[31] Peng *et al*,[32] and Jana *et al.*[33]

Early reports of the reactivity of these molecules showed their ability to activate small molecules. The stannylene **27** has been shown by Power and co-workers to activate H_2 and NH_3 to form the dimeric products **28** and **29** (Scheme 4).[31] It is assumed that the mechanism proceeds by initial oxidative addition, analogous to the carbene case, followed by reductive elimination of the arene group and H atom, to generate Ar'H and a new stannylene, which then dimerises forming the bridged species. Following this initial report, the analogous germylene **30** was also shown to react with H_2 and NH_3, although only the H_2 activation showed the reductive elimination as evidenced by generation of Ar'H and the germanium trihydride **31**, and the products are not

dimers.[32] The silylene **33** has also shown the ability to activate NH_3 giving the silyl amine **34** (Scheme 4).[33]

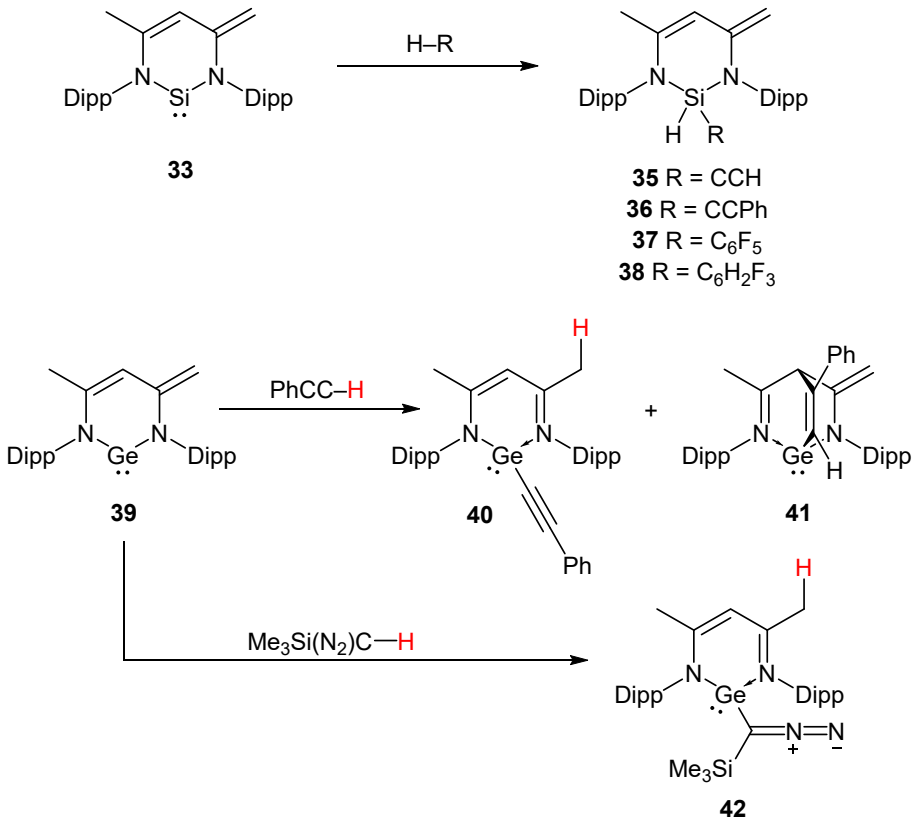

Scheme 5 – Formal C–H activation by silylenes and germylenes, adapted from Yao *et al*,[34] and Yao *et al.*[35]

Silylene **33** also shows the ability to activate C–H bonds, reacting with acetylene and phenylacetylene to give the products **35** and **36** (Scheme 5).[34] Computational investigation of the mechanism of these reactions showed that the direct C–H insertion using the lone pair and empty p_π-orbital at the silicon centre was unfeasible with a barrier of 41.3 kcal mol^{-1} and that the mechanism instead proceeded *via* deprotonation of the alkyne by the basic exocylic methylene group of the silylene **33** followed by hydrogen migration to the silicon atom. Silylene **33** has also been shown to activate the C–H bonds of pentafluorobenzene and 1,3,5-trifluorobenzene to give **37** and **38** (Scheme 5).[36] The analogous germylene **39** has also shown activation of the C–H bonds of phenylacetylene and trimethylsilyl diazomethane, giving the activation products **40** and **42** (Scheme 5).[35,37] It is notable in these cases that the C–H bond is split across the germanium centre and the exocylic methylene group which is in contrast to the silylene

where both the carbon and hydrogen are bound to the silicon. Additionally, in the case of reaction with phenylacetylene, the reaction competes with a 2+4 cycloaddition to give **41** (Scheme 5).

While these initial reports were promising they were shown to be irreversible processes and so unable to be used for catalytic purposes.

More recently germylenes and stannylenes have been shown by Jones and co-workers to be catalytically active for the hydroboration of carbonyls using 4,4,5,5-tetramethyl 1,3,2-dioxaborolane (HBpin) (Scheme 6).[38] They utilise germanium and tin species **42** and **43** with hydride ligands to effect the initial hydrometallation of the carbonyl in the catalytic cycle (Scheme 6).

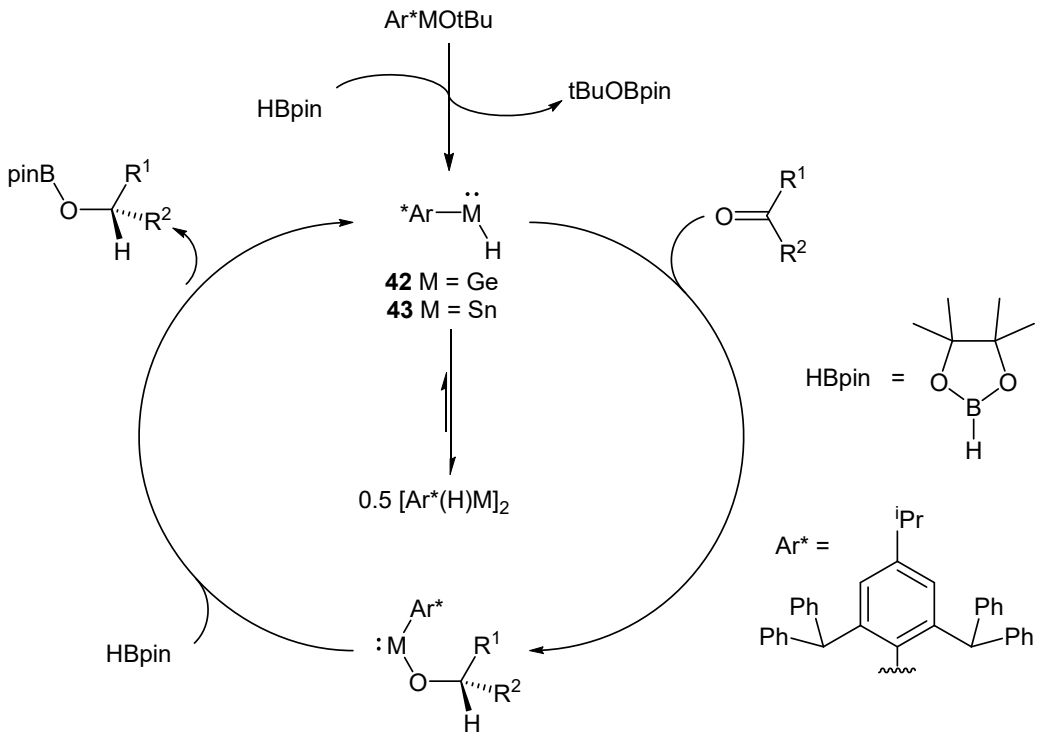

Scheme 6 – Catalytic hydroboration of carbonyls, adapted from Hadlington *et al*.[38]

While it may be expected that these species would not be stable, as the hydride does not sterically shield the reactive centre, they are in fact stable in solution due to existing mostly as stable dimers that release small amounts of the catalytically active monomers *in situ*.

Later work by the same group has used a related system for the hydroboration of CO_2 to form methanol equivalents,[39] and Wu *et al*. have used a nucleophilic heterocyclic germylene for the hydroboration of carbonyls.[40]

1.2.3 Group 13 carbene analogues

Group 13 carbene analogues are also highly reactive species, again due to their electron deficiency. Nevertheless, examples of the boron,[41] aluminium,[42] gallium,[43] and indium analogues have all been reported.[44] These examples utilise a similar design of ligand framework as for examples of the heavier group 14 carbene analogues, that being 1,3-diketimine derived ligands. For group 14, it is a formally dianionic ligand with two bonds to the group 14 centre and eight valence electrons (Figure 3). However, for group 13 the ligand acts in a different manner, as a formally monoanionic ligand with one bond and one donor interaction with the group 13 centre, which has six valence electrons. This donor arm is key in stabilising these highly electron deficient species.

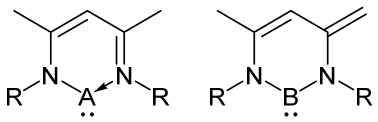

Figure 3 – Differing coordination of 1,3-diketimine derived ligands to group 13 (A) and 14 (B) elements.

Of the available examples of the group 13 carbene analogues, the aluminium and gallium analogues have shown reactivity in the activation of E–H bonds. Specifically, the dipp-substituted β-diketiminate gallium and aluminium complexes **44** and **47** are especially active towards a wide range of substrates of which the most relevant are displayed herein (Scheme 7).

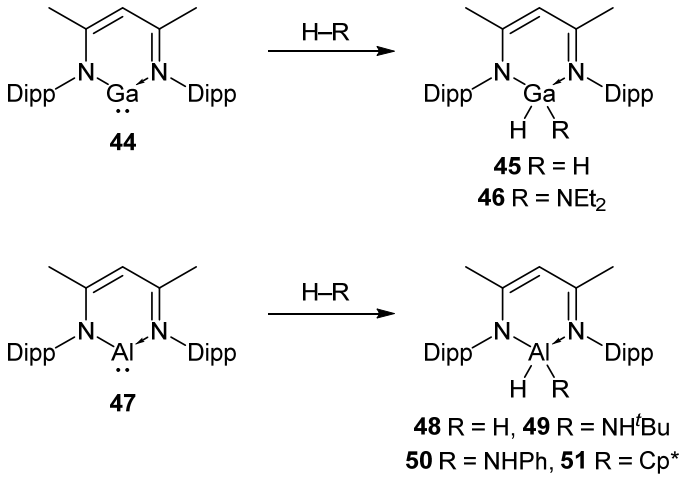

Scheme 7 – E–H bond activations with aluminium and gallium β-diketiminate complexes adapted from Seifert *et al*,[45] and Chu *et al.*[46]

The gallium β-diketiminate complex **44** has shown the ability to activate dihydrogen and diethylamine to give **45** and **46**.[45] The aluminium β-diketiminate complex **47** has shown the ability to activate dihydrogen, tertbutylamine, phenylamine, and 1,2,3,4,5-pentamethylcyclopentadiene (Cp*H) to give **48**-**51**.[46]

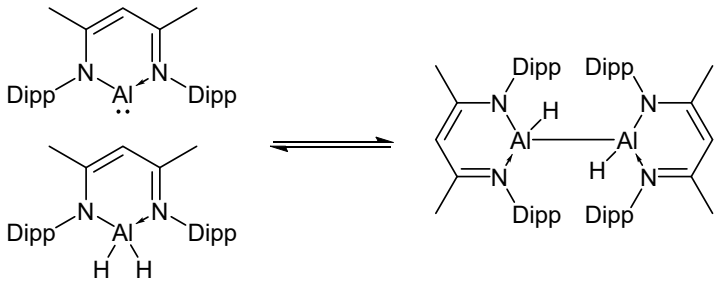

Scheme 8 – Reversible Al-H activation using 47 and 48, adapted from Chu *et al.*[46]

Most of these products have not shown further reactivity. However, the H_2 activation product **48** has been shown to react reversibly with the aluminium β-diketiminate complex **47**, giving a symmetrical Al(II) species (Scheme 8). This is one of only two examples of reversible oxidative addition utilising an Al(I) species, the other of which is the addition of Cp*H to Cp*Al to form Cp^*_2AlH.[47] These examples are a good proof of concept for the ability of aluminium to engage in reversible redox cycling similar to transition metals. However, these examples are very specific to only the precise substrates **48** and Cp*H. Further work is required to expand the range of substrates that aluminium is capable of reversibly activating, and eventually engaging in catalysis.

1.2.4 Group 14 alkyne analogues

Until relatively recently, there were very few examples of stable alkyne analogues of heavier group 14, on account of their highly reactive nature. However, by utilising a variety of bulky substituents to protect the highly reactive centres, examples of alkyne analogues featuring each of the group 14 elements have now been isolated.[48–51]

This series of compounds exhibit an interesting trend in molecular geometry when descending group 14, with a gradual change from a linear geometry at alkynes to progressively more bent structures.[52] This reflects the change in the nature of the bonding in the heavier elements. There is a progression from a formal triple bond in the alkyne to a single bond with two lone pairs in the diplumbyne (Figure 4).

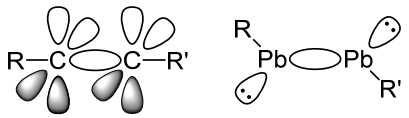

Figure 4 – Representations of the orbital interactions in an alkyne and diplumbyne.

This structural trend results in an increase in reactivity of the molecules when descending the group by increasing both the nucleophilicity and electrophilicity of the molecules.[52] The greater lone pair character increases the nucleophilicity, while the lower energy LUMO increases the electrophilicity.

Of this family of compounds, the digermyne **52** was the first to exhibit reactivity towards small molecules after it was shown to cleave dihydrogen (Scheme 9).[53]

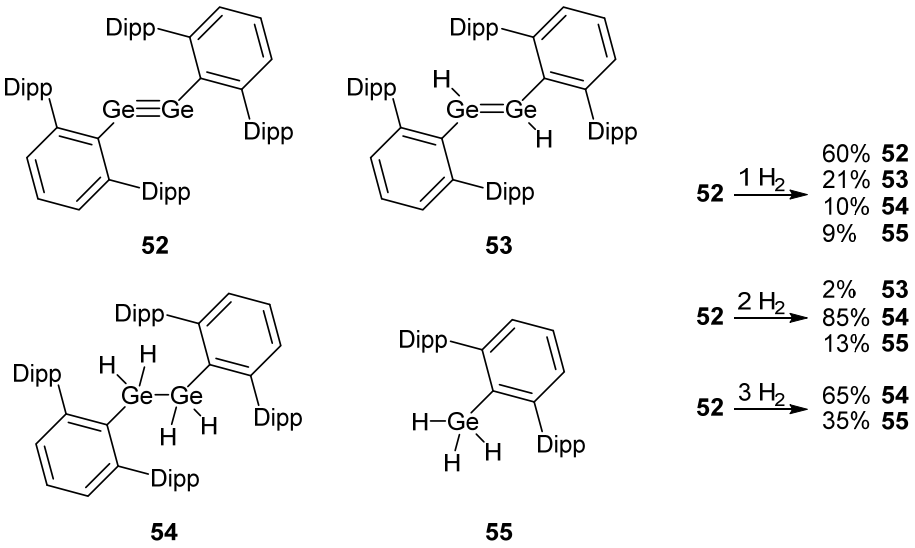

Scheme 9 – Reaction of a digermyne with H_2, adapted from Spikes *et al.*[53]

The digermyne **52** is able to activate up to three equivalents of dihydrogen per molecule producing a mixture of germanium hydride products **53**-**55**. One equivalent of H_2 gave mainly the starting material **52** with small amounts of the three hydrogen addition products **53**-**55**. Increasing the equivalents of H_2 increased the proportions of the more saturated germanium species.

Two possible explanations have been given for the activation of H_2 by digermyne **52**. The first is that a combination of the low-lying LUMO, and a high-lying HOMO allow for activation of H_2 in a manner analogous to that of transition metals to give digermene **53**.[54] Alternatively, due to substantial singlet diradical character in the digermyne,[55] it is possible that the reaction proceeds *via* abstraction of a single hydrogen atom from H_2 leaving a H· radical and Ar'Ge·GeHAr' (Ar' = C_6H_3-2,6(C_6H_3-2,6-iPr_2)$_2$). These two radicals can then recombine to give digermene **53**.

Following production of digermene **53**, direct reaction with another equivalent of H_2 gives digermane **54**. The route to produce the monomeric germane **55** is thought to involve a low concentration of the bridged species Ar'Ge(μ–H)$_2$GeAr', as an isomer of the digermene **53**. The possibility of this intermediate has been supported by

computations, and also experimentally by the isolation of the related Ar*Sn(μ–H)$_2$SnAr* (Ar* = C_6H_3-2,6(C_6H_3-2,4,6-$^iPr_3$)$_2$) species.[56] The proposed Ar′Ge(μ–H)$_2$GeAr′ intermediate has no Ge–Ge bond and so provides a route into the formation of Ar′GeH_3 through reaction with further equivalents of H_2.

This chemistry differs from that of the carbenes and carbene analogues mechanistically, with the most striking difference being the proposed radical-mediated activation in the first step. Unfortunately this activation is irreversible, as H_2 cannot be abstracted from the products to regenerate the starting materials. More recently, the same group has shown the ability of digermynes and distannynes to activate the C–H bonds of some cyclic alkenes,[57] but similarly to the digermyne above, no further reactivity was reported.

1.2.5 Constrained-geometry compounds

As mentioned previously, the main challenge in effecting reversible oxidative addition and reductive elimination in main group systems is the large gap in energy between their oxidation states. One strategy that has been used to attempt to overcome this obstacle is the use of a ligand to constrain the geometry of a species, changing the energy of the two oxidation states to bring the gap between them closer together.

Arduengo was the first to report constrained geometry p-block compounds in 1987, where a range of T-shaped three coordinate complexes of the pnictogens (group 15) were reported.[58] These compounds are remarkable due to the unusual geometric arrangement that they possess which then produces unusual electronic properties. Typically three co-ordinate pnictogen compounds would be expected to be pyramidal species due to their lone pair and therefore possess eight valence electrons. These are referred to as 8-Pn-3 compounds (Figure 5). However, when constrained to the T-shaped geometry, donation of electrons from the ligand to the Pn centre can occur giving a hypervalent 10-Pn-3 electron configuration (Figure 5). This stabilises the +3 oxidation state and therefore brings the gap between the +3 and +5 states closer together. Another intentional effect of constraining the geometry to the T-shape is that it changes the atomic orbital configuration at the Pn centre in the 8-Pn-3 configuration,

generating an empty p-orbital that is not present in the pyramidalised Pn centre. The combination of lone pair and empty p-orbital is ideal for bond activations as it can behave similarly to transition metals with their combination of s- and d-orbitals, with both donating and accepting properties.

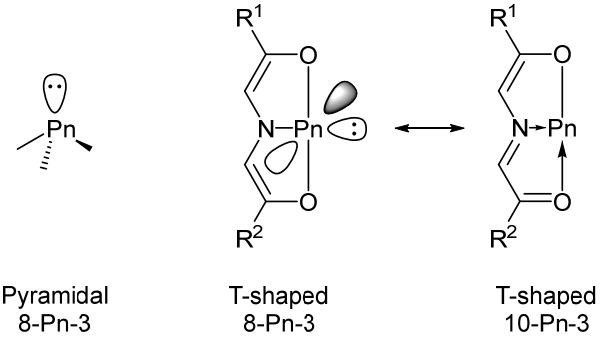

Figure 5 – Geometries of three co-ordinate pnictogen compounds.

No activation of dihydrogen or C–H bonds has been reported for this class of molecule, but examples of successful N–H bond activation are present in the literature. The first example was reported by Radosevich and co-workers, utilising the 3 co-ordinate constrained geometry phosphorus compound **56** initially reported by Arduengo, which activated ammonia gas and a range of amines to give the 5 co-ordinate phosphorus compounds **57**-**63** (Scheme 10).[59] Shortly after, Kinjo and co-workers reported **64**, also capable of activating ammonia gas to give **65** (Scheme 10).[60] Radosevich and co-workers then reported **66**, again capable of activating ammonia and a range of amines giving **67**-**73** (Scheme 10).[61] In this case the activation of *tert*-butyl amine in particular to give **70** was found to be a reversible process.

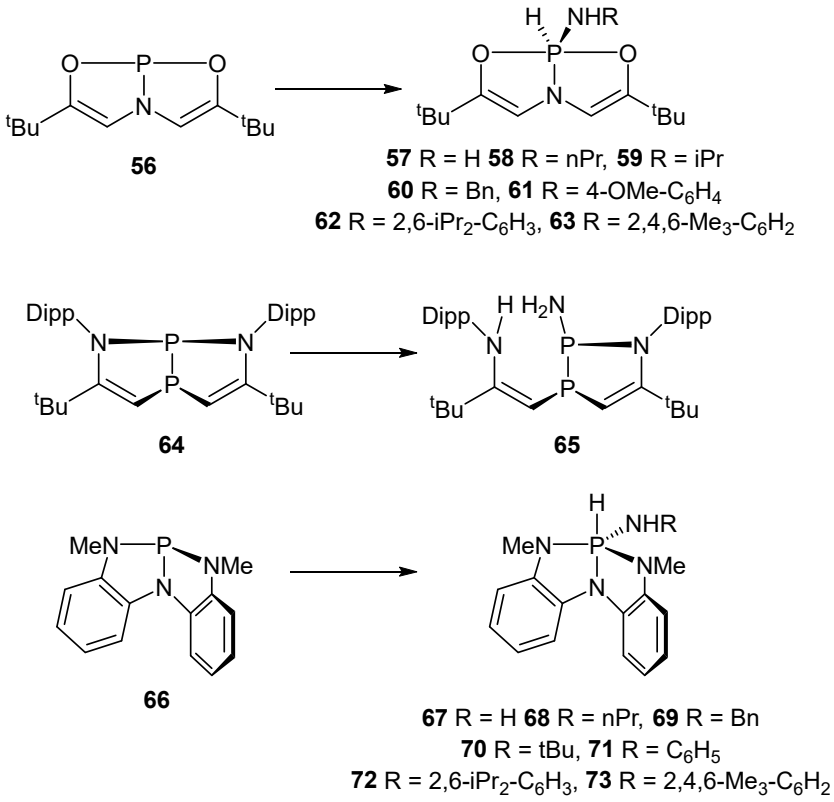

Scheme 10 – Activation of ammonia and amines by constrained geometry compounds, adapted from McCarthy *et al*,[59] Cui *et al*,[60] and Zhao *et al*.[61]

These three examples differ quite drastically in the manner of activation, despite all utilising phosphorus and the close similarity of the T-shaped geometries of the ligands. **56** activates the amine substrates in the equatorial coordination sites of the phosphorus, while for **66**, the hydrogen and amine occupy axial and equatorial spots respectively, causing the ligand to bend upon oxidative addition. **64** meanwhile, has an entirely different mode of activation, splitting the ammonia across both the phosphorus centre and the amide ligand, meaning that the phosphorus does not change oxidation state from +3 to +5. These three examples demonstrate just how finely balanced the energetics of these systems are, changing drastically with slight changes in the ligand scaffold.

The first example of use of these constrained geometry compounds to enable catalytic activity was reported by Radosevich *et al*. using one of Arduengo's original T-shaped P(III) compounds **56**. Using ammonia borane as a hydrogen source, they showed the catalytic hydrogenation of *E*-1,2-diphenylazene, achieving 80% conversion to the

hydrogenated product, using a 10% loading of the catalyst at 40 °C in 24 hours (Scheme 11).[62]

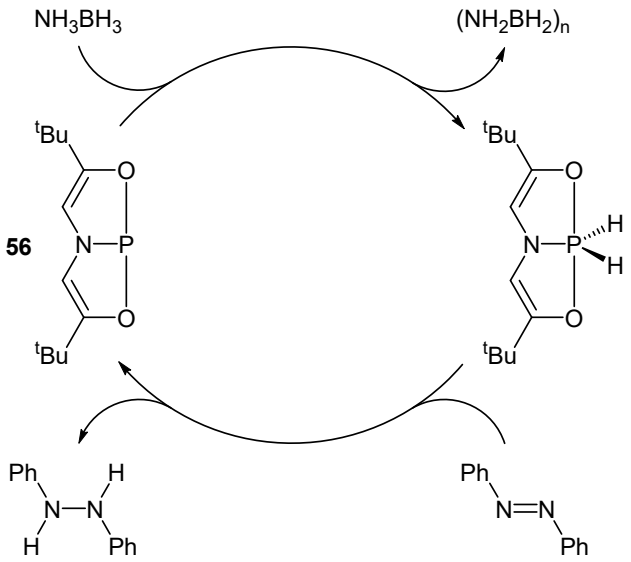

Scheme 11 - Catalytic hydrogenation of *E*-1,2-diphenyldiazene, adapted from Dunn *et al.*[62]

Whilst this was an exciting discovery, the usage of ammonia borane as a source of hydrogen is problematic as it is highly inefficient, forming borazine and polymeric $(NH_2BH_2)_n$ as waste by-products.

1.2.6 Main-group element heterocycles

Main-group element heterocycles are widespread in organic chemistry, with many examples containing nitrogen, oxygen, and more occasionally sulphur atoms in the aromatic systems. Inorganic chemists have put significant effort in generating analogues of these aromatic compounds using other elements from the p-block in order to study differences in their reactivity.

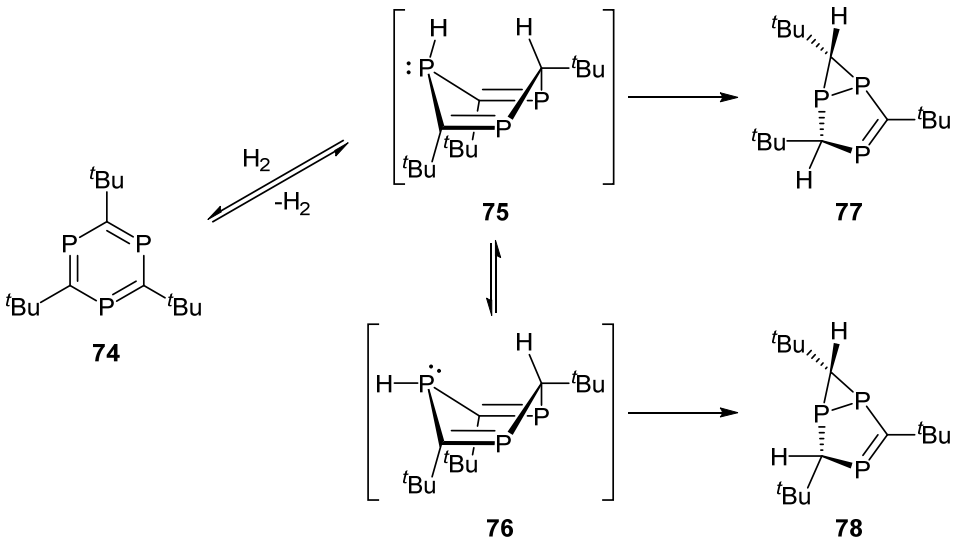

Scheme 12 – H_2 activation by triphosphabenzene 74, adapted from Longobardi *et al.*[63]

Two recent examples of these main group heterocycles have shown the ability to reversibly activate dihydrogen. Firstly, 1,3,5-triphosphabenzene **74** has been shown to reversibly activate dihydrogen across the 1 and 4 positions of the aromatic ring, giving the boat shaped compound **75** (Scheme 12).[63] This can then rearrange by inversion of the phosphorus centre to give the isomeric boat shaped compound **76**. Both of these molecules then irreversibly rearrange to form diastereomers **77** and **78**.

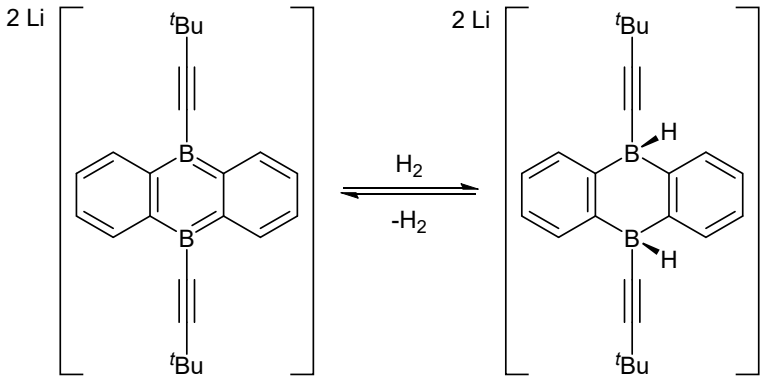

79 **80**

Scheme 13 – Reversible H_2 activation by diboraanthracene 79, adapted from von Grotthuss *et al.*[64]

Secondly, diboraanthracene anion **79** has been shown to reversibly activate dihydrogen in a similar manner to the 1,3,5-triphosphabenzene **74**. Diboraanthracene anion **79** was heated at 100 °C under an atmosphere of H_2 gas and showed formation of the hydrogen activation product **80** (Scheme 13).[64] After 34 hours the system reached equilibrium mixture with a 1:1 ratio of **79** and **80**. On lowering the temperature to 50 °C, greater amounts of **80** were formed. This proves the reversibility of the reaction. Activation was confirmed by calculation to occur directly across the 9 and 10 positions of the anthracene. Initial proof of concept reactivity in using stoichiometric diboraanthracene **79** to reduce chlorosilanes to hydrosilanes was shown, but with some degradation of the anthracene backbone.

1.2.7 Frustrated Lewis pairs

Frustrated Lewis pairs (FLPs) are a class of reactive species comprised of a Lewis acid and a Lewis base that are unable to form an adduct due to steric constraints. This leads to remarkable reactivity when these pairs react with small molecules. This is as a result of the cooperative nature of the lone pair on the Lewis base and empty p-orbital on the Lewis acid.

The first report of frustrated Lewis pair behaviour was in 1942, where it was observed that 2,6-lutidine and BMe_3 did not form a Lewis adduct, while for 2,6-lutidine and BF_3 the expected adduct was observed.[65] This behaviour was attributed to the steric clash between the methyl groups of the 2,6-lutidine and the BMe_3. However, at the time

further activity of this pair was not explored. The first example of the reactivity of FLPs was observed by Wittig and Benz in 1959. Addition of PPh_3 and BPh_3 to benzyne did not result in the Lewis acid/base adduct, instead forming a zwitterionic salt of the benzyne (Scheme 14).[66]

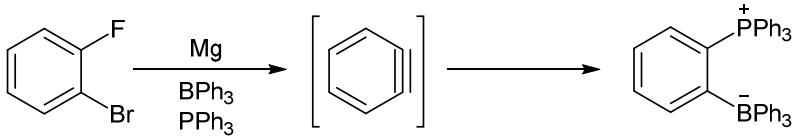

Scheme 14 – Reaction of PPh_3/BPh_3 FLP with benzyne, adapted from Wittig and Benz.[66]

The most important and significant advance in the chemistry of frustrated Lewis pairs came with the discovery that they could reversibly cleave dihydrogen in a heterolytic manner (Scheme 15).[67]

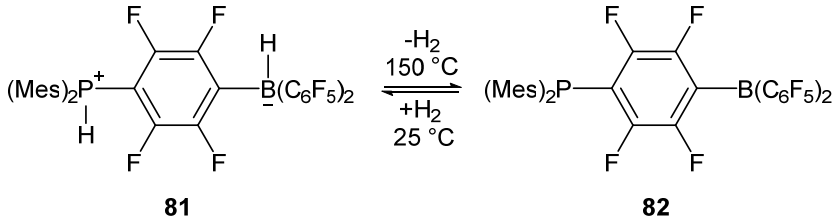

Scheme 15 - Reversible activation of H_2 by an FLP, adapted from G. Welch *et al.*[67]

This reactivity was discovered by Stephan and co-workers when looking into the reactivity of tethered FLP systems. Upon preparation of zwitterionic phosphonium borate **81** on the path to a targeted FLP it was expected that dihydrogen would be lost spontaneously under ambient conditions. However, it was observed that this species was remarkably air and moisture stable under standard conditions. It was found that heating to 150 °C was required to cause the loss of H_2 from the zwitterionic species and form the free target FLP **82**. It was subsequently found that exposure of the free FLP to H_2 gas at room temperature regenerated the zwitterionic phosphonium borate species **81**. At the time this reversible activation of H_2 gas was reactivity that had only been observed for transition-metal systems.

Further study on this system showed that it could be utilised for catalytic hydrogenation of imines.[68] Full conversion of a range of imines to their corresponding amines was

achieved using moderate conditions (80–120 °C, 1–5 atm. H_2 gas) using 5 mol% of the FLP pre-catalyst **81**. The mechanism for this catalysis is shown below (Scheme 16).

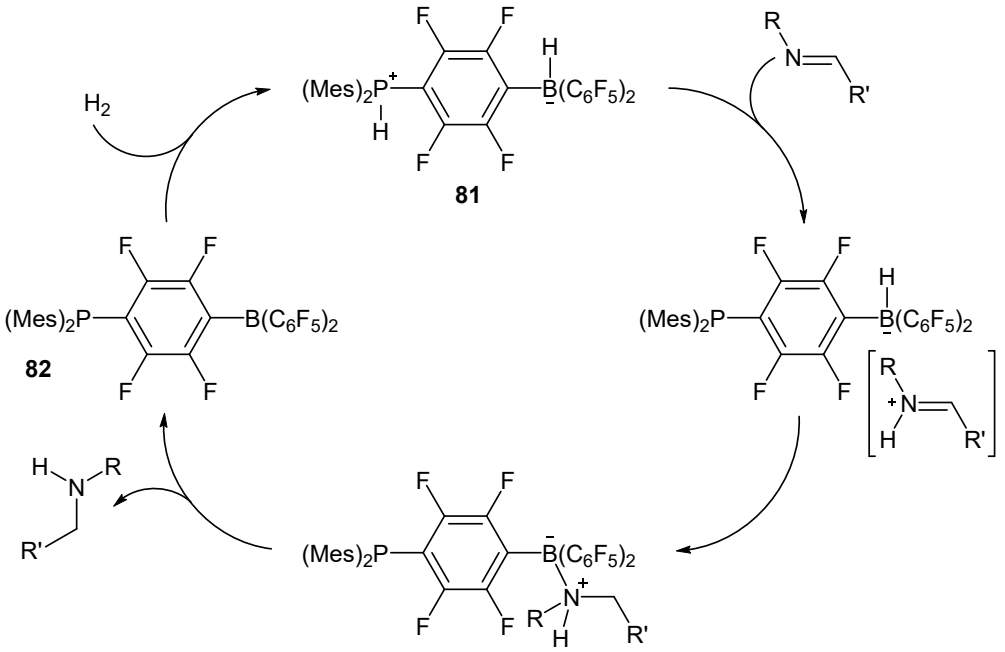

Scheme 16 – Catalytic hydrogenation of an imine to an amine, adapted from Chase *et al.*[68]

However, there are limitations on the substrate scope of this reaction. The imines chosen must be sufficiently bulky, otherwise the amine produced in the reaction causes poisoning of the catalyst by coordination to the boron centre. Later work has expanded on this reactivity by using a chiral FLP to perform enantioselective reductions of imines to the corresponding chiral amines.[69]

Since this initial hydrogenation discovery many other examples have been reported. The hydrogenations of enamines,[70] silylenol-ethers,[70,71] enones,[72] oximes,[73] olefins,[74] and polyaromatics.[75]

Of greatest importance to the subject of this thesis is the recent report by Fontaine and co-workers of the catalytic usage of FLP **83** to C–H borylate heteroaromatics, with *N*-methylpyrrole shown as an example substrate (Scheme 17).[76]

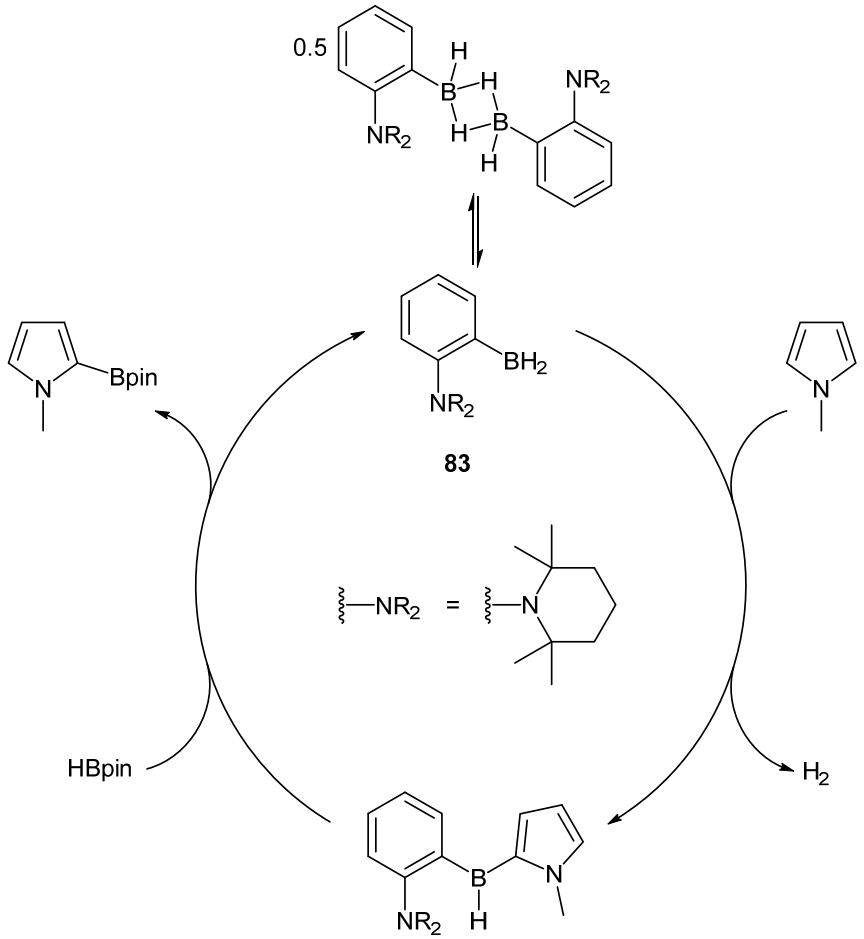

Scheme 17 – Borylation of heteroaromatic compounds with an FLP adapted from Légaré *et al.*[76]

This reactivity uses an extremely simple FLP system and effects a highly important transformation. Borylated aromatics are highly important starting materials in a wide variety of organic transformations, most notably in cross couplings. The substrate scope of the reaction is good, with borylation of *N*-substituted pyrroles and indoles, furans, and thiophenes shown. Borylation occurs in both the 2 and 3 positions in some cases, while is selective for only the 2 or 3 position in others, due to a combination of electronic effects and also steric reasons based on the substitution pattern of the substrate. It is notable for this system that only heteroaromatic compounds can be borylated. It is suggested by DFT calculation that the nucleophilicity of the carbon centre is the limiting factor in the substrate scope, with the Lewis acidity of the catalyst not allowing activation of more challenging C–H bonds.

Following this initial report, Fontaine and co-workers reported a range of FLPs based on this initial design, changing the bulk of the NR_2 group to assess its effect on the catalytic activity of the system.[77] Comparing the rates of four different FLPs, where NR_2 = NMe_2, NEt_2, piperidyl (N(pip)), and tetramethylpiperidyl (N(TMP)), it was found that in general, the smaller the steric bulk around the nitrogen, the faster the reaction proceeded. However, N(pip) was found the be the fastest catalyst, not NMe_2. In the case of NMe_2 the reaction is actually slower, as the dimeric form of the catalyst is much more stable, meaning that much less of the active monomeric form is available in solution to react. This is a good example of the fine balance required in FLP design, as too much bulk hinders reactivity, while not enough means that not enough FLP character exists.

Following this report by Fontaine and co-workers, an analogous aluminium FLP **84** was synthesised by Roesky and co-workers.[78] This FLP was utilised for the C–H activation of both *N*-methyl pyrrole and *N*-methyl indole leading to the generation of aryl aluminium species **85** and **86** (Scheme 18).

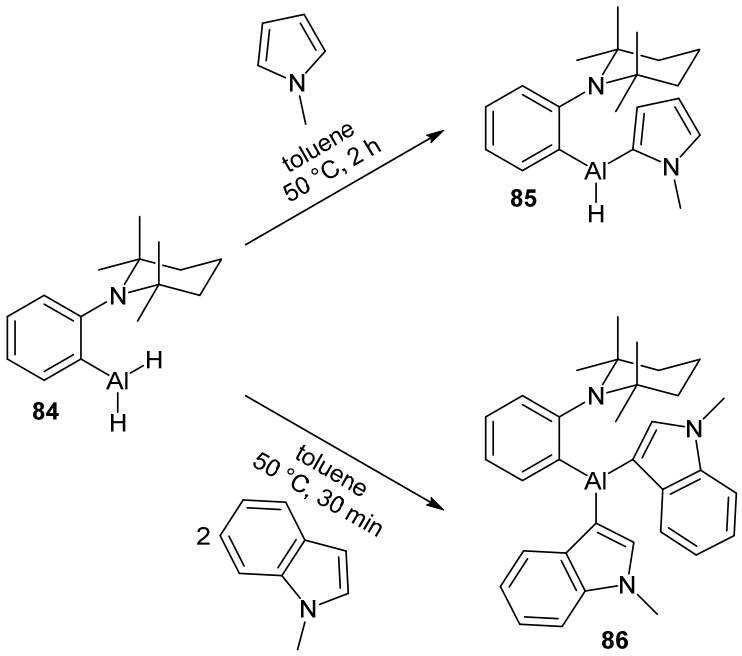

Scheme 18 – Reaction of 84 with *N*-methyl pyrrole and *N*-methyl indole to form 85 and 86.

For reaction with *N*-methyl pyrrole a single C–H deprotonation was observed giving the diaryl aluminium hydride **85** and for *N*-methyl indole two deprotonations occurred

giving the triaryl aluminium **86**. However, no turnover was reported for these products at the time of publication.

Several other examples of FLP mediated C–H functionalisation reactions have also been reported. Erker and co-workers have demonstrated C–C bond formation using *N*,*N*-dimethylmesitylamine and dimethyl acetylenedicarboxylate in the presence of $B(C_6F_5)_3$ (Scheme 19 a).[79] Wasa and co-workers have used FLPs to perform Mannich-type reactions through the use of $B(C_6F_5)_3$ and 1,2,2,6,6-pentamethylpiperidine to generate a range of α- and β-amino esters (Scheme 19 b).[80] Using a chiral amine instead of 1,2,2,6,6-pentamethylpiperidine, these reactions proceed diastereoselectively. Using 1,2,2,6,6-pentamethylpiperidine and a chiral diborane, enantiomerically pure aminocarbonyl products were obtained from carbonyl compounds and imines.[81]

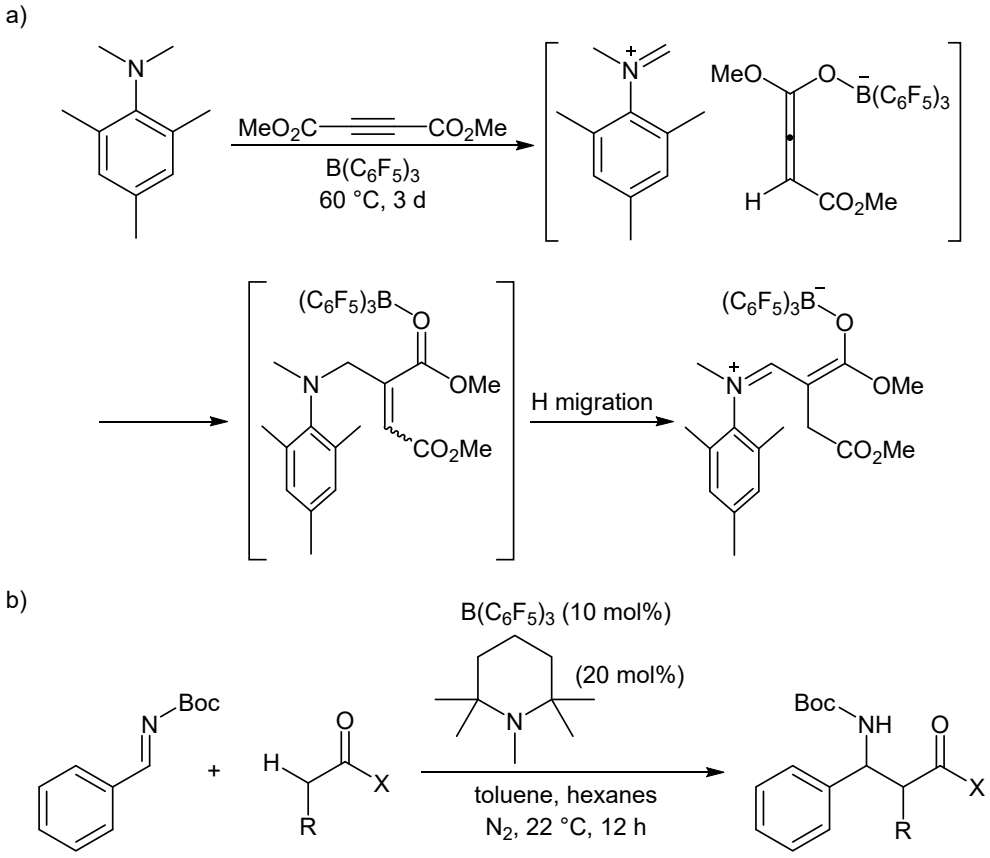

Scheme 19 – FLP C–H functionalization reactions, adapted from a) Chen *et al.* and b) Chan *et al.*

In addition, $B(C_6F_5)_3$ and a chiral magnesium complex have been used to effect the functionalization of α-amino C–H bonds to give enantio-enriched α-substituted amines using *N*-alkylamines and α,β-unsaturated compounds.[82]

As demonstrated by the examples above, the field of FLP chemistry is extremely productive, with many examples of highly useful catalytic transformations performed by this class of systems. This field is still relatively new and it is certain that many more reactions of great importance and utility will be discovered in this field.

1.3 C–H Borylation

Borylated compounds have great synthetic utility as the C–B bond can be transformed into a great range of different functionalities. Oxidation or protonolysis of organoboranes can generate a variety of useful organic products, including alcohols, carbonyl compounds, alkenes, and halides.[83] However, one of the most common and relevant usages of C–B bonds is in cross coupling reactions such as the Suzuki-Miyaura reaction, which are used commonly in both research chemistry and also on industrial scale for the production of pharmaceuticals.

For example, the synthesis of CI-1034, a potent endothelin receptor antagonist, includes in its synthesis a Suzuki-Miyaura reaction between a boronic acid and an aromatic sulfonate ester as the key synthetic step (Scheme 20).[84]

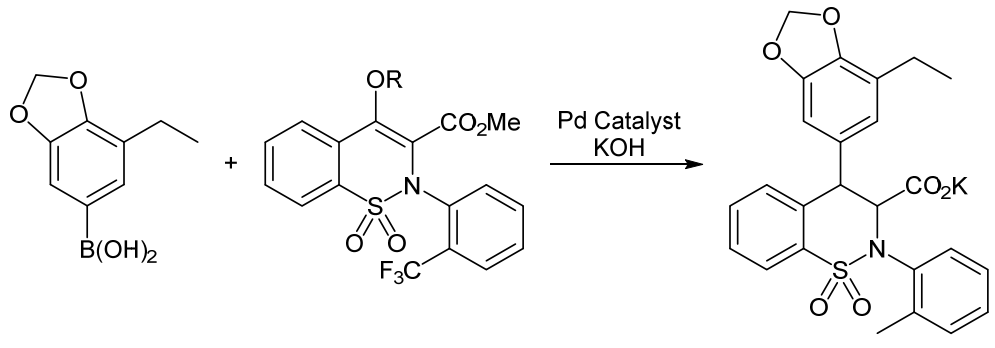

Scheme 20 – Suzuki-Miyaura reaction in the synthesis of CI-1034, adapted from Jacks *et al.*[84]

Due to the synthetic utility of these C–B bond containing molecules, methods for the generation of these borylated building blocks are of great interest.

A brief overview of the state of the art methods for borylating aromatic compounds and alkynes will be given as these are particularly relevant to the novel results discussed herein.

1.3.1 Aromatic and saturated aliphatic compounds

Current state-of-the-art catalytic borylation techniques use transition metal catalysts derived from elements such as rhodium and iridium. Rhodium is the main metal used for the borylation of saturated aliphatic compounds,[85,86] while iridium is the main metal for the borylation of aromatic compounds (Scheme 21).[87–90]

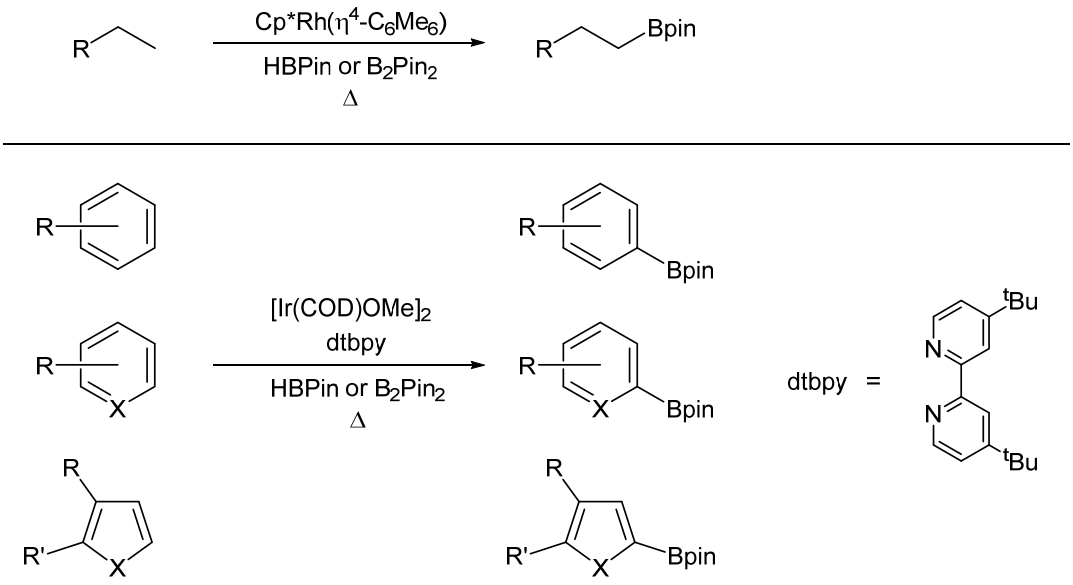

Scheme 21 – Borylation of aliphatic and aromatic compounds using rhodium and iridium.

The mechanisms for these reactions follow standard transition-metal catalysis steps such as ligand loss (to create vacant co-ordination sites), oxidative addition, and reductive elimination. Examples of the mechanism of both the rhodium catalysed alkane functionalisation and the iridium catalysed arene functionalisation are shown below (Scheme 22).

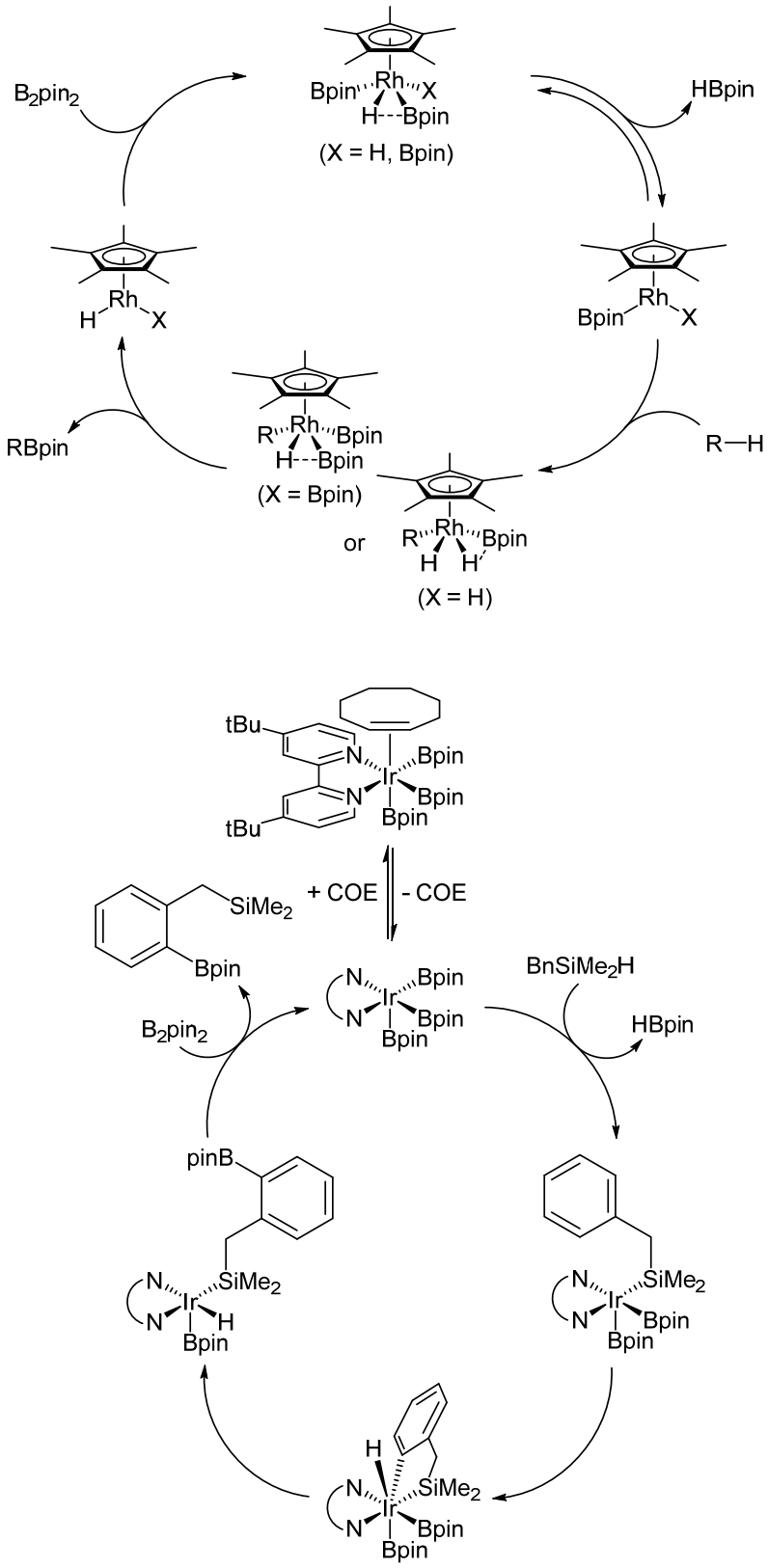

Scheme 22 – Example mechanisms of rhodium catalysed alkane C–H borylation and iridium catalysed alkane C–H borylation, adapted from Hartwig.[89]

This chemistry is well established and the scope of possible substrates is excellent, but as mentioned earlier, despite these advantages there is a focus on moving away from the usage of these metals, towards more sustainable alternative catalysts.

1.3.2 Alkynes

The catalytic C–H borylation of terminal alkynes is a relatively new field with the first example being reported in 2013 by Ozerov and co-workers using an iridium catalyst **87** and HBpin as the boron source (Scheme 23).[91]

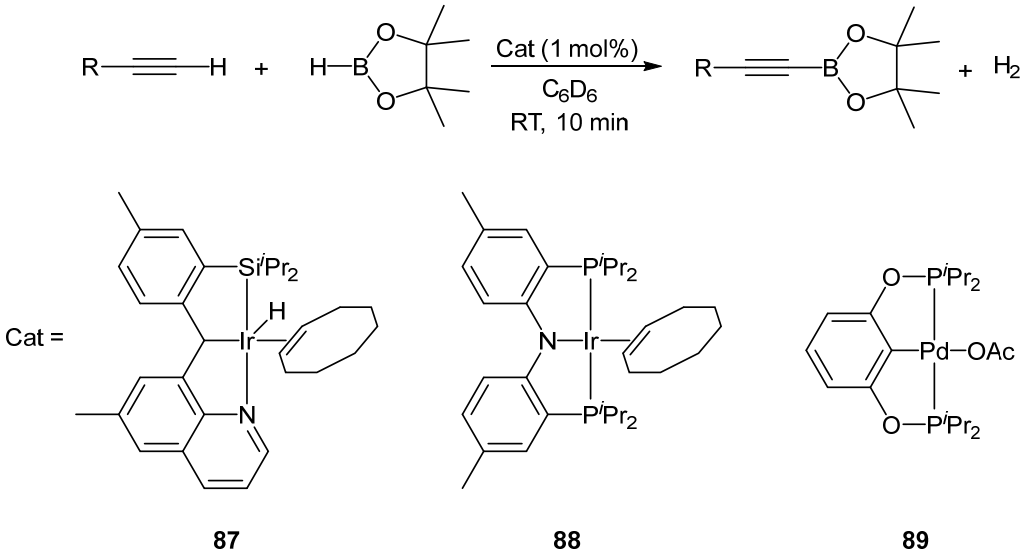

Scheme 23 – C–H borylation of terminal alkynes using Pt group transition metal complexes, adapted from Lee *et al.*[91]

Since this initial report, an extensive ligand screen was carried out by the group, leading to another example of a highly active iridium catalyst **88** (Scheme 23).[92] The group then later reported a small series of highly related palladium pincer complexes also capable of catalysing the dehydrogenative borylation of alkynes, of which the most active **89** is shown (Scheme 23).[93] These reactions proceed in an analogous manner to the previously shown complexes for aromatic and saturated aliphatic C–H borylation.

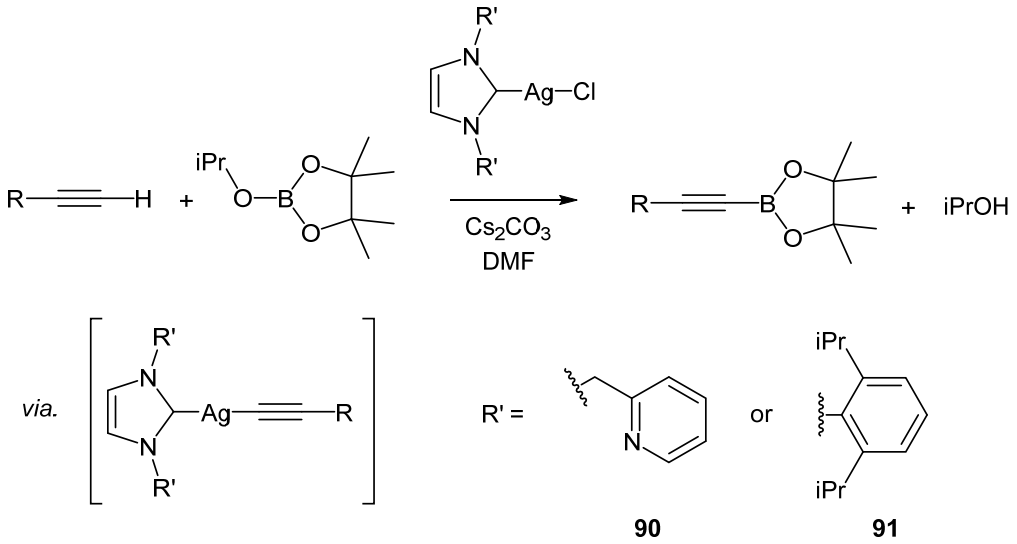

Scheme 24 – C–H borylation of terminal alkynes using a silver NHC complex, adapted from Hu *et al.*[94]

In addition to these examples of classic transition metal catalysts, examples of other metals performing this reaction have emerged. Firstly, Hu *et al.* reported the usage of silver(I) catalysts **90** and **91** with NHC ligands and base to affect the transformation with good scope and yields (Scheme 24).[94] The mechanism is not discussed in detail in this paper, but presumably proceeds *via* a silver acetylide species, as shown in previous silver alkynylation reactions.[95] This silver acetylide would then turnover by sigma bond metathesis with the iPrO–Bpin bond.

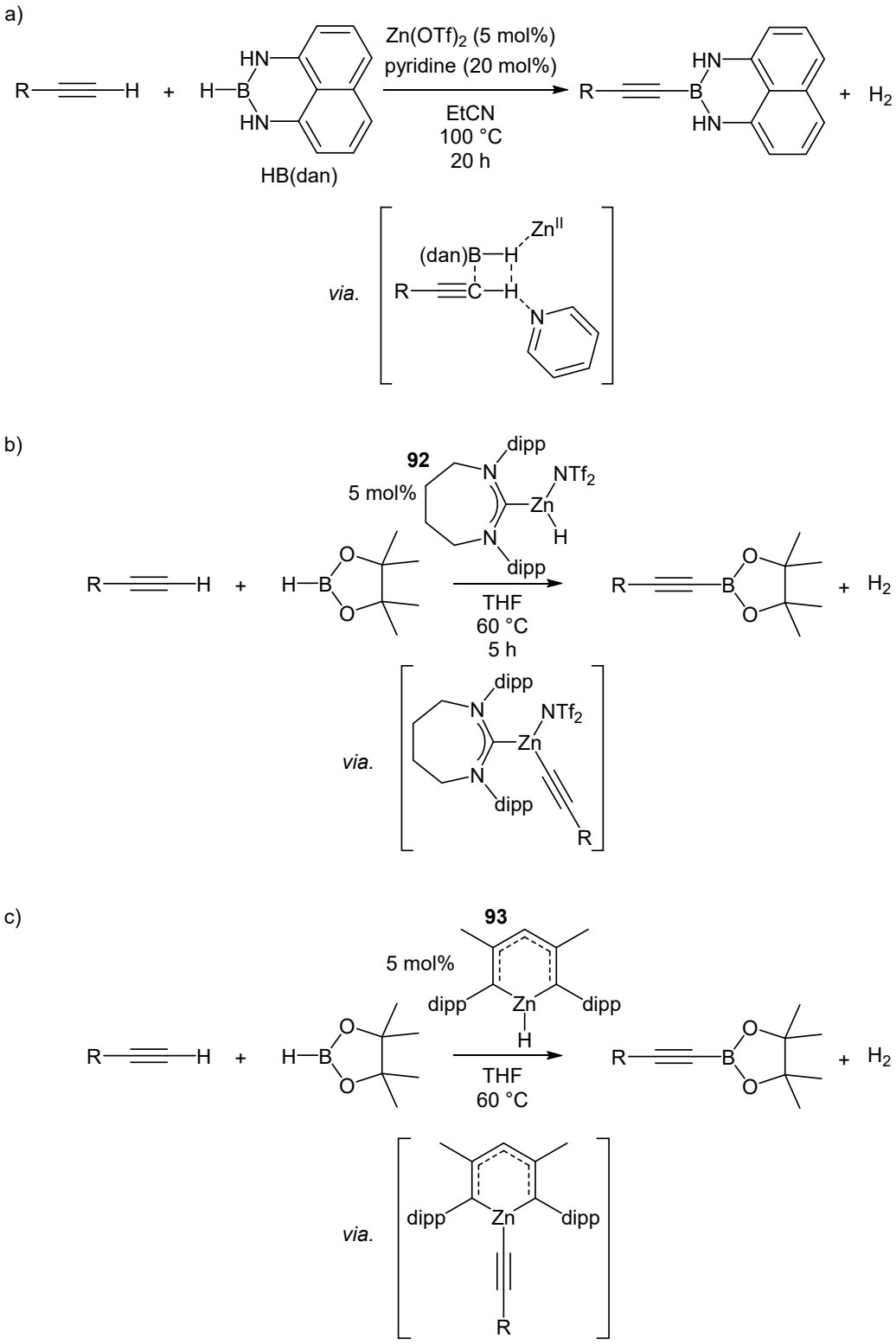

Scheme 25 – C–H borylation of terminal alkynes using zinc catalysts, adapted from a) Tsuchimoto *et al*,[96] b) Procter *et al*,[97] and c) Uzelac *et al.*[98]

In another example, a zinc-catalysed reaction was reported by Tsuchimoto *et al.* utilising the simple $Zn(OTf)_2$ reagent in combination with pyridine (Scheme 25a).[96] This reaction

proceeds *via* a direct σ-bond metathesis of the borane B–H and alkyne C–H bonds, with the zinc activating the B–H bond and the pyridine activating the C–H bond. In this reaction however, HBpin could not be used and only 1,8-Naphthalenediaminatoborane (HB(dan)) was found to be operative in the reaction. It was shown that the product alkynyl boronates were unstable under the reaction conditions when using HBpin, but were stable when HB(dan) was used.

More recently two other examples of zinc-catalysed terminal C–H borylation of alkynes has been reported by the Ingleson group, this time utilising an NHC-zinc hydride complex **92** and zinc β-diketiminate complex **93** (Scheme 25b).[97,98] In contrast to the previous zinc catalysed example, these reactions proceed *via* initial deprotonation of the alkyne to form a zinc acetylide and H_2 gas, followed by σ-bond metathesis with the borane to form the product and regenerate the catalyst. In this case the reaction does proceed with HBpin to form the terminally borylated products and when using excess equivalents of HBpin, can also provide the 1,1-diborylated or 1,1,1-triborylated products, having formally undergone the C–H borylation followed by one or two hydroboration reactions. This system shows great utility in selectively preparing a range of useful borylated intermediates.

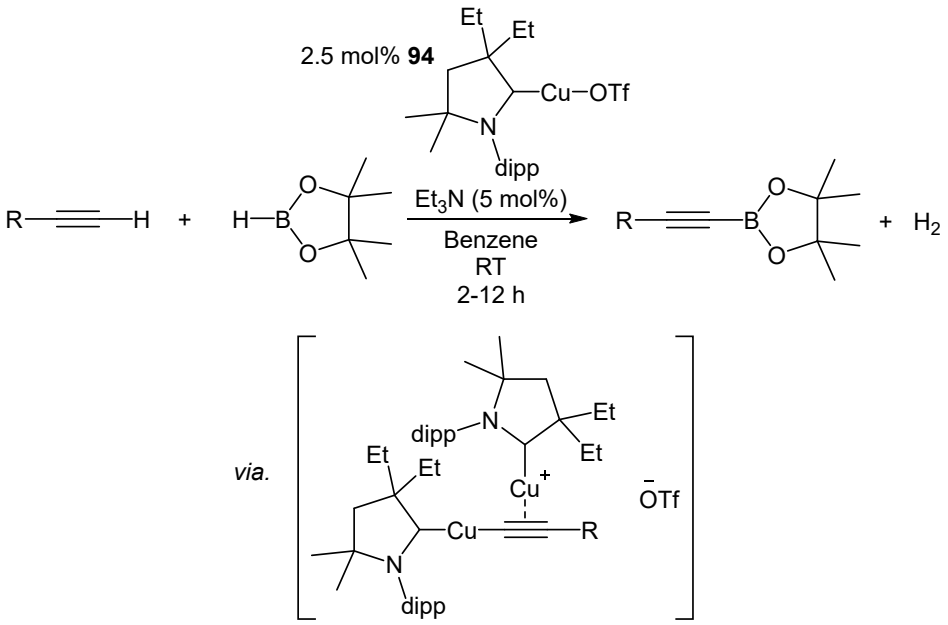

Scheme 26 – C–H borylation of terminal alkynes using a copper cAAC complex, adapted from Romero et al.[99]

A copper-catalysed example has been reported by the Bertrand group, using cAAC ligand stabilised CuOTf species **94** (Scheme 26).[99] In this case there is cooperativity between two copper centres, with one deprotonating the alkyne and another coordinated to the triple bond. It is proposed that this coordinated copper protects the triple bond from hydroboration, giving selectivity to the terminally borylated product.

Finally, from the Darcel group, there is an example of catalytic C–H borylation of terminal alkynes using an iron catalyst.[100] This utilises very similar conditions to the original zinc catalysed case (Scheme 25 a). Here $Fe(OTf)_2$ is used and initial reactivity was discovered using pyridine as the base, although 1,4-diazabicyclo[2.2.2]octane (DABCO) was subsequently shown to give better reactivity. Additionally, HBpin can be used in this reaction in contrast to the zinc-catalysed case where only HB(dan) was tolerated.

Additionally to the catalytic work in this area, there is a very recent example of stoichiometric activation of the terminal alkyne C–H bond that is particularly relevant, which involves a N/Al based FLP. This utilises the tetramethylpiperidyl substituted FLP **84** originally reported for the C–H activation of *N*-methyl pyrrole and *N*-methyl indole.[78] In this case the FLP **84** undergoes reaction with a range of terminal alkynes with substitution including Ph, 1-C_4H_3S, and PPh_2.[101] For the former two substituted alkynes, reaction proceeded to afford a bis-alkynyl aluminium species analogous to **95** and no further reaction was seen. However, with the PPh_2 substituted alkyne, further reaction was seen giving a zwitterionic species **96**. This is attributed to an electronic influence by the alkyne substituent. No turnover with secondary substrates is reported for any of these compounds.

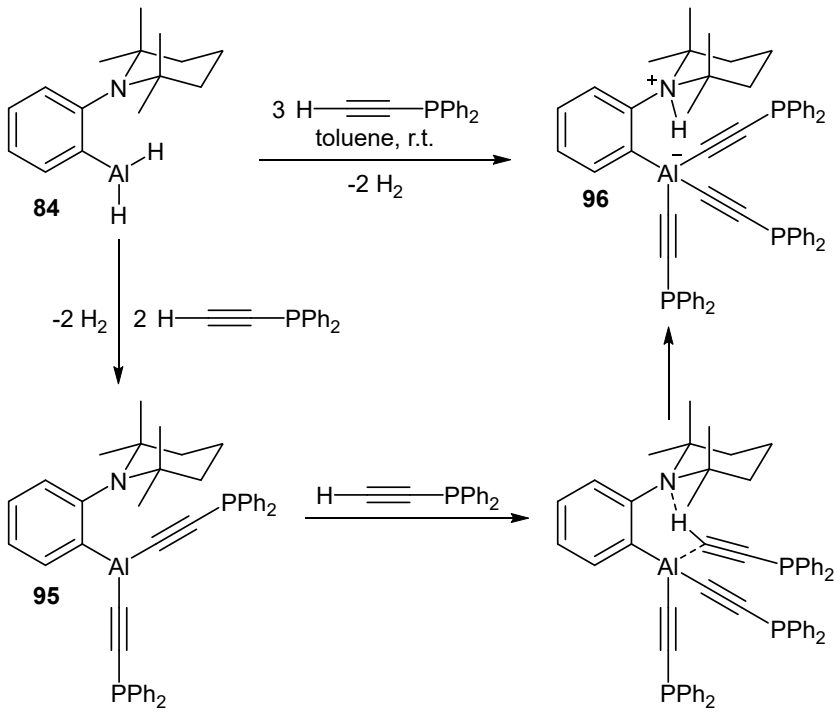

Scheme 27 – C–H activation of terminal alkynes by FLP 84, adapted from Chen *et al.*[101]

The initial work in the area of C–H borylation of terminal alkynes is very promising, but as a relatively unexplored field, there is significant scope for the discovery of new and exciting systems in both the transition metals and other areas.

1.4 Aims of this work

As has been shown in the above examples of main group catalysis, this field shows immense promise, with the number of useful catalytic transformations possible using main group systems steadily increasing over time. In particular, FLPs have a wide range of transformations that they are capable of achieving. However, of note in the field of FLPs is the widespread usage of boron as the Lewis acidic partner in the FLP, with examples of other group 13 elements being relatively neglected. There are a limited number of FLPs utilising aluminium, and even fewer using gallium,[102–104] and indium.[103,104] As such, creating more examples of these and importantly attempting to understand and quantify the effects that changing the Lewis acidic atom has on the FLP, is important in helping to drive the field forward.

For this work, we took the catalytic C–H borylation by Fontaine and co-workers as a starting point.[76] The main drawback of this work was the inability of the catalyst to activate purely carbon-based aromatic C–H bonds and so the main aim of this work was to design a new FLP catalyst based on a similar ligand framework that would be able to activate these more challenging bonds. We postulated that modifying the Lewis acidic character of the group 13 FLP atom could allow this. A search of the literature revealed a report of the ability of trispentafluorophenyl alane to activate the C–H bonds of toluene in combination with 2,6-ditertbutylpyridine in an FLP-like manner,[105] while analogous reactivity is not seen for trispentafluorophenyl borane. Based on this observation, we decided to design a new FLP system based on aluminium and test its reactivity in the C–H borylation of aryl substrates. Computational assessment of the developed FLP was also carried out to gain insight into the system. The results of this research are communicated in the following chapters.

1.5 References

[1] *Res. Dev. World Mag.* **2005**, 20.
[2] "The Periodic Table of Endangered Elements," can be found under https://www.acs.org/content/acs/en/greenchemistry/research-innovation/endangered-elements.html, **n.d.**
[3] S. Niu, M. B. Hall, *Chem. Rev.* **2000**, *100*, 353–406.
[4] "ICH Q3D Elemental impurities," can be found under https://www.ema.europa.eu/en/ich-q3d-elemental-impurities, **2018**.
[5] I. Bauer, H.-J. Knölker, *Chem. Rev.* **2015**, *115*, 3170–3387.
[6] R. L. Webster, *Dalton Trans.* **2017**, *46*, 4483–4498.
[7] L. J. Taylor, D. L. Kays, *Dalton Trans.* **2019**, *48*, 12365–12381.
[8] D. W. C. MacMillan, *Nature* **2008**, *455*, 304–308.
[9] P. I. Dalko, L. Moisan, *Angew. Chem. Int. Ed.* **2004**, *43*, 5138–5175.
[10] T. J. Hadlington, M. Hermann, G. Frenking, C. Jones, *J. Am. Chem. Soc.* **2014**, *136*, 3028–3031.
[11] N. L. Dunn, M. Ha, A. T. Radosevich, *J. Am. Chem. Soc.* **2012**, *134*, 11330–11333.
[12] D. W. Stephan, G. Erker, *Angew. Chem. Int. Ed.* **2010**, *49*, 46–76.
[13] M. Hermann, *Justus Liebigs Ann. Chem.* **1855**, *95*, 211–225.
[14] D. Bourissou, O. Guerret, F. P. Gabbaï, G. Bertrand, *Chem. Rev.* **2000**, *100*, 39–92.
[15] A. J. Arduengo, R. L. Harlow, M. Kline, *J. Am. Chem. Soc.* **1991**, *113*, 361–363.
[16] C. Boehme, G. Frenking, *J. Am. Chem. Soc.* **1996**, *118*, 2039–2046.
[17] R. W. Alder, P. R. Allen, M. Murray, A. G. Orpen, *Angew. Chem. Int. Ed. Engl.* **1996**, *35*, 1121–1123.
[18] V. Lavallo, Y. Canac, C. Präsang, B. Donnadieu, G. Bertrand, *Angew. Chem. Int. Ed.* **2005**, *44*, 5705–5709.
[19] W. Sander, R. Hübert, E. Kraka, J. Gräfenstein, D. Cremer, *Chem. Eur. J.* **2000**, *6*, 4567–4579.
[20] G. D. Frey, V. Lavallo, B. Donnadieu, W. W. Schoeller, G. Bertrand, *Science* **2007**, *316*, 439–441.
[21] A. J. A. Iii, J. C. Calabrese, F. Davidson, H. V. Rasika Dias, J. R. Goerlich, R. Krafczyk, W. J. Marshall, M. Tamm, R. Schmutzler, *Helv. Chim. Acta* **1999**, *82*, 2348–2364.
[22] R. S. Holdroyd, M. J. Page, M. R. Warren, M. K. Whittlesey, *Tetrahedron Lett.* **2010**, *51*, 557–559.
[23] Z. R. Turner, *Chem. Eur. J.* **2016**, *22*, 11461–11468.
[24] M. Iglesias, D. J. Beetstra, J. C. Knight, L.-L. Ooi, A. Stasch, S. Coles, L. Male, M. B. Hursthouse, K. J. Cavell, A. Dervisi, et al., *Organometallics* **2008**, *27*, 3279–3289.
[25] J. P. Moerdyk, G. A. Blake, D. T. Chase, C. W. Bielawski, *J. Am. Chem. Soc.* **2013**, *135*, 18798–18801.
[26] A. J. Teator, Y. Tian, M. Chen, J. K. Lee, C. W. Bielawski, *Angew. Chem. Int. Ed.* **2015**, *54*, 11559–11563.
[27] P. J. Davidson, M. F. Lappert, *J. Chem. Soc. Chem. Commun.* **1973**, 317a–317a.
[28] D. E. Goldberg, D. H. Harris, M. F. Lappert, K. M. Thomas, *J. Chem. Soc. Chem. Commun.* **1976**, 261–262.

[29] M. Denk, R. Lennon, R. Hayashi, R. West, A. V. Belyakov, H. P. Verne, A. Haaland, M. Wagner, N. Metzler, *J. Am. Chem. Soc.* **1994**, *116*, 2691–2692.
[30] M. Stürmann, M. Weidenbruch, K. W. Klinkhammer, F. Lissner, H. Marsmann, *Organometallics* **1998**, *17*, 4425–4428.
[31] Y. Peng, B. D. Ellis, X. Wang, P. P. Power, *J. Am. Chem. Soc.* **2008**, *130*, 12268–12269.
[32] Y. Peng, J.-D. Guo, B. D. Ellis, Z. Zhu, J. C. Fettinger, S. Nagase, P. P. Power, *J. Am. Chem. Soc.* **2009**, *131*, 16272–16282.
[33] A. Jana, C. Schulzke, H. W. Roesky, *J. Am. Chem. Soc.* **2009**, *131*, 4600–4601.
[34] S. Yao, C. van Wüllen, X.-Y. Sun, M. Driess, *Angew. Chem. Int. Ed.* **2008**, *47*, 3250–3253.
[35] S. Yao, C. van Wüllen, M. Driess, *Chem. Commun.* **2008**, 5393–5395.
[36] A. Jana, P. P. Samuel, G. Tavčar, H. W. Roesky, C. Schulzke, *J. Am. Chem. Soc.* **2010**, *132*, 10164–10170.
[37] A. Jana, I. Objartel, H. W. Roesky, D. Stalke, *Inorg. Chem.* **2009**, *48*, 7645–7649.
[38] T. J. Hadlington, M. Hermann, G. Frenking, C. Jones, *J. Am. Chem. Soc.* **2014**, *136*, 3028–3031.
[39] T. J. Hadlington, C. E. Kefalidis, L. Maron, C. Jones, *ACS Catal.* **2017**, *7*, 1853–1859.
[40] Y. Wu, C. Shan, Y. Sun, P. Chen, J. Ying, J. Zhu, L. (Leo) Liu, Y. Zhao, *Chem. Commun.* **2016**, *52*, 13799–13802.
[41] Y. Segawa, M. Yamashita, K. Nozaki, *Science* **2006**, *314*, 113–115.
[42] C. Cui, H. W. Roesky, H.-G. Schmidt, M. Noltemeyer, H. Hao, F. Cimpoesu, *Angew. Chem. Int. Ed.* **2000**, *39*, 4274–4276.
[43] E. S. Schmidt, A. Jockisch, H. Schmidbaur, *J. Am. Chem. Soc.* **1999**, *121*, 9758–9759.
[44] M. S. Hill, P. B. Hitchcock, *Chem. Commun.* **2004**, 1818–1819.
[45] A. Seifert, D. Scheid, G. Linti, T. Zessin, *Chem. Eur. J.* **2009**, *15*, 12114–12120.
[46] T. Chu, I. Korobkov, G. I. Nikonov, *J. Am. Chem. Soc.* **2014**, *136*, 9195–9202.
[47] C. Ganesamoorthy, S. Loerke, C. Gemel, P. Jerabek, M. Winter, G. Frenking, R. A. Fischer, *Chem. Commun.* **2013**, *49*, 2858–2860.
[48] A. Sekiguchi, R. Kinjo, M. Ichinohe, *Science* **2004**, *305*, 1755–1757.
[49] M. Stender, A. D. Phillips, R. J. Wright, P. P. Power, *Angew. Chem. Int. Ed.* **2002**, *41*, 1785–1787.
[50] A. D. Phillips, R. J. Wright, M. M. Olmstead, P. P. Power, *J. Am. Chem. Soc.* **2002**, *124*, 5930–5931.
[51] L. Pu, B. Twamley, P. P. Power, *J. Am. Chem. Soc.* **2000**, *122*, 3524–3525.
[52] P. P. Power, *Nature* **2010**, *463*, 171–177.
[53] G. H. Spikes, J. C. Fettinger, P. P. Power, *J. Am. Chem. Soc.* **2005**, *127*, 12232–12233.
[54] T. L. Allen, W. H. Fink, P. P. Power, *J. Chem. Soc. Dalton Trans.* **2000**, 407–412.
[55] Y. Jung, M. Brynda, P. P. Power, M. Head-Gordon, *J. Am. Chem. Soc.* **2006**, *128*, 7185–7192.
[56] B. E. Eichler, P. P. Power, *J. Am. Chem. Soc.* **2000**, *122*, 8785–8786.
[57] O. T. Summerscales, J. C. Fettinger, P. P. Power, *J. Am. Chem. Soc.* **2011**, *133*, 11960–11963.
[58] A. J. Arduengo, C. A. Stewart, F. Davidson, D. A. Dixon, J. Y. Becker, S. A. Culley, M. B. Mizen, *J. Am. Chem. Soc.* **1987**, *109*, 627–647.

[59] S. M. McCarthy, Y.-C. Lin, D. Devarajan, J. W. Chang, H. P. Yennawar, R. M. Rioux, D. H. Ess, A. T. Radosevich, *J. Am. Chem. Soc.* **2014**, *136*, 4640–4650.
[60] J. Cui, Y. Li, R. Ganguly, A. Inthirarajah, H. Hirao, R. Kinjo, *J. Am. Chem. Soc.* **2014**, *136*, 16764–16767.
[61] W. Zhao, S. M. McCarthy, T. Y. Lai, H. P. Yennawar, A. T. Radosevich, *J. Am. Chem. Soc.* **2014**, *136*, 17634–17644.
[62] N. L. Dunn, M. Ha, A. T. Radosevich, *J. Am. Chem. Soc.* **2012**, *134*, 11330–11333.
[63] L. E. Longobardi, C. A. Russell, M. Green, N. S. Townsend, K. Wang, A. J. Holmes, S. B. Duckett, J. E. McGrady, D. W. Stephan, *J. Am. Chem. Soc.* **2014**, *136*, 13453–13457.
[64] E. von Grotthuss, M. Diefenbach, M. Bolte, H.-W. Lerner, M. C. Holthausen, M. Wagner, *Angew. Chem. Int. Ed.* **2016**, *55*, 14067–14071.
[65] H. C. Brown, H. I. Schlesinger, S. Z. Cardon, *J. Am. Chem. Soc.* **1942**, *64*, 325–329.
[66] G. Wittig, E. Benz, *Chem. Ber.* **1959**, *92*, 1999–2013.
[67] G. C. Welch, R. R. S. Juan, J. D. Masuda, D. W. Stephan, *Science* **2006**, *314*, 1124–1126.
[68] P. A. Chase, G. C. Welch, T. Jurca, D. W. Stephan, *Angew. Chem. Int. Ed.* **2007**, *46*, 8050–8053.
[69] D. Chen, Y. Wang, J. Klankermayer, *Angew. Chem. Int. Ed.* **2010**, *49*, 9475–9478.
[70] D. W. Stephan, G. Erker, *Angew. Chem. Int. Ed.* **2015**, *54*, 6400–6441.
[71] D. W. Stephan, G. Erker, *Angew. Chem. Int. Ed.* **2010**, *49*, 46–76.
[72] G. Erős, K. Nagy, H. Mehdi, I. Pápai, P. Nagy, P. Király, G. Tárkányi, T. Soós, *Chem. Eur. J.* **2012**, *18*, 574–585.
[73] J. Mohr, M. Oestreich, *Angew. Chem. Int. Ed.* **2014**, *53*, 13278–13281.
[74] J. Paradies, *Angew. Chem. Int. Ed.* **2014**, *53*, 3552–3557.
[75] Y. Segawa, D. W. Stephan, *Chem. Commun.* **2012**, *48*, 11963–11965.
[76] M.-A. Légaré, M.-A. Courtemanche, É. Rochette, F.-G. Fontaine, *Science* **2015**, *349*, 513–516.
[77] J. Légaré Lavergne, A. Jayaraman, L. C. Misal Castro, É. Rochette, F.-G. Fontaine, *J. Am. Chem. Soc.* **2017**, *139*, 14714–14723.
[78] S. Chen, B. Li, X. Wang, Y. Huang, J. Li, H. Zhu, L. Zhao, G. Frenking, H. W. Roesky, *Chem. Eur. J.* **2017**, *23*, 13633–13637.
[79] G.-Q. Chen, G. Kehr, C. G. Daniliuc, M. Bursch, S. Grimme, G. Erker, *Chem. Eur. J.* **2017**, *23*, 4723–4729.
[80] J. Z. Chan, W. Yao, B. T. Hastings, C. K. Lok, M. Wasa, *Angew. Chem. Int. Ed.* **2016**, *55*, 13877–13881.
[81] M. Shang, M. Cao, Q. Wang, M. Wasa, *Angew. Chem. Int. Ed.* **2017**, *56*, 13338–13341.
[82] M. Shang, J. Z. Chan, M. Cao, Y. Chang, Q. Wang, B. Cook, S. Torker, M. Wasa, *J. Am. Chem. Soc.* **2018**, *140*, 10593–10601.
[83] E.-I. Negishi, M. J. Idacavage, in *Org. React.*, American Cancer Society, **2004**, pp. 1–246.
[84] T. E. Jacks, D. T. Belmont, C. A. Briggs, N. M. Horne, G. D. Kanter, G. L. Karrick, J. J. Krikke, R. J. McCabe, J. G. Mustakis, T. N. Nanninga, et al., *Org. Process Res. Dev.* **2004**, *8*, 201–212.
[85] H. Chen, S. Schlecht, T. C. Semple, J. F. Hartwig, *Science* **2000**, *287*, 1995–1997.

[86] J. D. Lawrence, M. Takahashi, C. Bae, J. F. Hartwig, *J. Am. Chem. Soc.* **2004**, *126*, 15334–15335.
[87] T. Ishiyama, J. Takagi, K. Ishida, N. Miyaura, N. R. Anastasi, J. F. Hartwig, *J. Am. Chem. Soc.* **2002**, *124*, 390–391.
[88] T. A. Boebel, John. F. Hartwig, *J. Am. Chem. Soc.* **2008**, *130*, 7534–7535.
[89] J. F. Hartwig, *Chem. Soc. Rev.* **2011**, *40*, 1992–2002.
[90] J. F. Hartwig, *Acc. Chem. Res.* **2012**, *45*, 864–873.
[91] C.-I. Lee, J. Zhou, O. V. Ozerov, *J. Am. Chem. Soc.* **2013**, *135*, 3560–3566.
[92] C.-I. Lee, J. C. DeMott, C. J. Pell, A. Christopher, J. Zhou, N. Bhuvanesh, O. V. Ozerov, *Chem. Sci.* **2015**, *6*, 6572–6582.
[93] C. J. Pell, O. V. Ozerov, *Inorg. Chem. Front.* **2015**, *2*, 720–724.
[94] J.-R. Hu, L.-H. Liu, X. Hu, H.-D. Ye, *Tetrahedron* **2014**, *70*, 5815–5819.
[95] X. Zhang, W.-Z. Zhang, X. Ren, L.-L. Zhang, X.-B. Lu, *Org. Lett.* **2011**, *13*, 2402–2405.
[96] T. Tsuchimoto, H. Utsugi, T. Sugiura, S. Horio, *Adv. Synth. Catal.* **2015**, *357*, 77–82.
[97] R. J. Procter, M. Uzelac, J. Cid, P. J. Rushworth, M. J. Ingleson, *ACS Catal.* **2019**, *9*, 5760–5771.
[98] M. Uzelac, K. Yuan, M. J. Ingleson, *Organometallics* **2020**, *39*, 1332–1338.
[99] E. A. Romero, R. Jazzar, G. Bertrand, *Chem. Sci.* **2016**, *8*, 165–168.
[100] D. Wei, B. Carboni, J.-B. Sortais, C. Darcel, *Adv. Synth. Catal.* **2018**, *360*, 3649–3654.
[101] Y. Chen, W. Jiang, B. Li, G. Fu, S. Chen, H. Zhu, *Dalton Trans.* **2019**, *48*, 9152–9160.
[102] W. Uhl, J. Possart, A. Hepp, M. Layh, *Z. Für Anorg. Allg. Chem.* **2017**, *643*, 1016–1029.
[103] M. Xu, J. Possart, A. E. Waked, J. Roy, W. Uhl, D. W. Stephan, *Philos. Trans. R. Soc. Math. Phys. Eng. Sci.* **2017**, *375*, 20170014.
[104] J. Possart, W. Uhl, *Organometallics* **2018**, *37*, 1314–1323.
[105] D. Chakraborty, E. Y.-X. Chen, *Macromolecules* **2002**, *35*, 13–15.

2 Synthesis and characterisation of novel aluminium based FLPs

The work described in section 2.4 was carried out by a BSc student, Huaizhong Zhang, under my supervision.

2.1 Introduction and aims

Frustrated Lewis pairs are a highly promising area of chemical research that has rapidly expanded in recent years. Despite this, there is still scope for significant innovation in the field of FLPs. Many of the prominent examples of FLPs performing catalytic activity utilise FLPs with boron as the Lewis acidic element and either nitrogen,[1–8] or phosphorus,[1,9,10] as the Lewis basic element, with the main differences being in the surrounding ligand architecture. This leaves a significant gap in knowledge surrounding the modification of especially the Lewis acidic side of the FLP, where little research has been focused. There are a small number of examples of other group 13 elements being used in FLP synthesis,[11–17] but with no significant examples of catalytic reactions reported. Research in this area has the potential to both increase the scope of the reactions they currently perform and to discover new modes of reactivity due to the differing electronics these other group 13 elements possess.

A recent paper from the group of Fontaine and co-workers showed highly promising catalytic borylation chemistry using a boron and nitrogen FLP (Scheme 28).[3] C–H borylation of a range of heteroaromatic substrates including pyrroles, indoles, furans, and thiophenes was demonstrated. This is a rare example of metal-free C–H borylation, as this field is traditionally restricted to transition metal catalysts using elements such as rhodium and iridium.

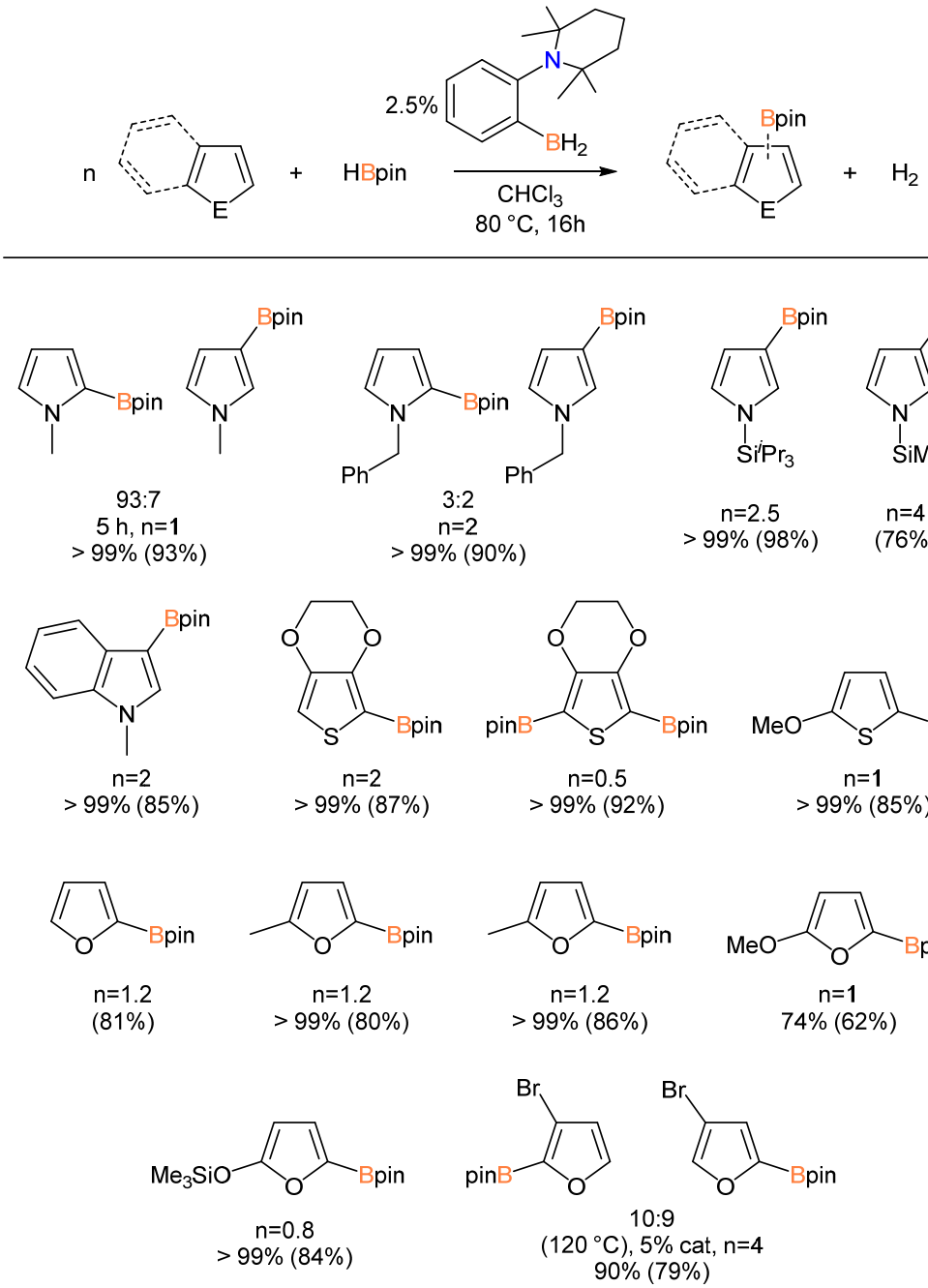

Scheme 28 – C–H borylation of heterocycles by Fontaine and co-workers.[3] Numbers in brackets denote isolated yields.

However, while this is an excellent advance in the field, there are areas for improvement. Although the scope of the reaction contains a range of substituted heteroaromatic substrates, Fontaine and co-workers were unable to activate more challenging aromatic substrates. Notably, purely carbon containing arenes such as benzene or indene based substrates are absent from the scope. Therefore, the initial

aim of our research was to attempt to expand the scope of this reactivity by designing and synthesising an FLP capable of performing C–H borylation on these more challenging aromatic substrates. We postulated that one method of achieving this would be to modify the Lewis acidity of the FLP. A search of the literature revealed a report of the ability of $Al(C_6F_5)_3$ (in combination with 2,6-ditertbutylpyridine in an FLP manner) to activate the C–H bonds of toluene (Scheme 29),[18] while analogous reactivity is not seen for $B(C_6F_5)_3$.

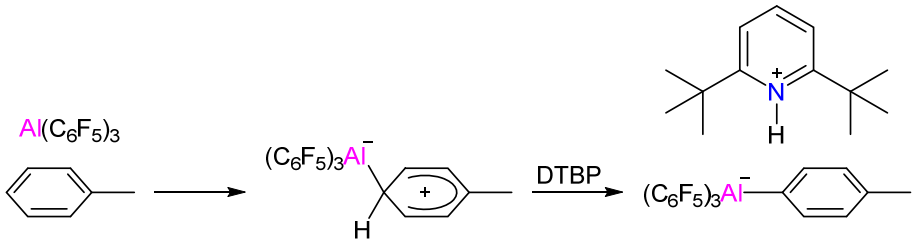

Scheme 29 – C–H activation of toluene by $Al(C_6F_5)_3$ and 2,6-ditertbutylpyridine.

This suggests that that changing the Lewis acidic atom to aluminium may allow the desired C–H activation steps to occur. As such, we chose the following initial target FLPs **1** and **2** for synthesis (Figure 6).

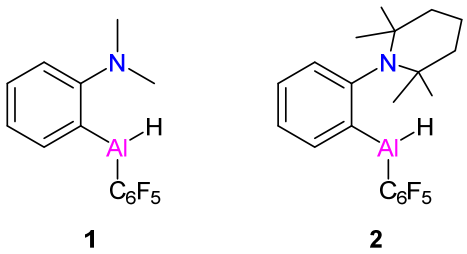

Figure 6 – Target FLPs.

In **1** and **2** the Lewis acidic atom has been changed to aluminium. In addition, an electron withdrawing substituent has been added onto the Lewis acid centre in the form of a C_6F_5 group to keep the electronics closer to the system shown to activate toluene. Two different nitrogen donor substituents were chosen to assess the effect of sterics on the reactivity of the FLPs. A synthetic pathway to reach these two targets was devised (Scheme 30). This would proceed by initial lithiation of ortho-halo anilines to give the ortho-lithiated anilines. These would then be reacted with dimethylaluminium chloride

to give the basic FLP framework based on analogous reactions to make boron FLPs.[19] Reaction of these ortho-dimethylalumino anilines with $B(C_6F_5)_3$ in a known ligand exchange reaction,[20] would then give the bis-pentafluoro substituted FLP. Finally reaction with hydrogen would result in elimination of an equivalent of pentafluorobenzene, based on analogous reactivity with the boron analogue of this FLP structure.[21]

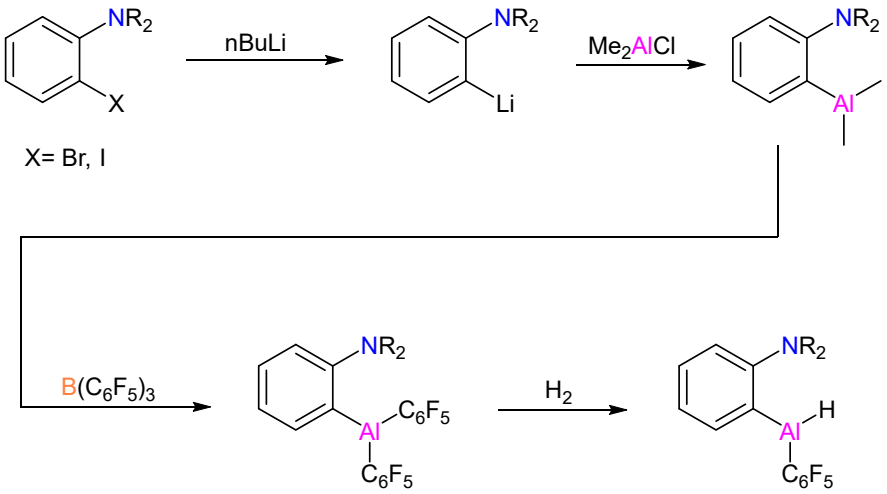

Scheme 30 – Proposed synthetic pathway to FLPs 1 and 2.

2.2 Synthesis of dialkyl aluminium FLPs

Synthesis of the dimethylaniline-substituted FLP **1** could proceed directly from 2-bromo-*N*,*N*-dimethylaniline as a commercially available starting material. However, the analogous compound **3** with a tetramethylpiperidine substituent is not a commercially available chemical and so had to be synthesised (Scheme 31).

Compound **3** was prepared according to a literature procedure,[19] by initial reaction of 2,2,6,6-tetramethylpiperidine with *n*-butyl lithium, followed by addition of iodobenzene to form the desired product in low yield, along with a number of side products (Scheme 31). Vacuum distillation of this mixture gave the desired product in 87% purity with a yield of 30%. This was confirmed using ^{1}H NMR spectroscopy by comparison to the reported literature values.

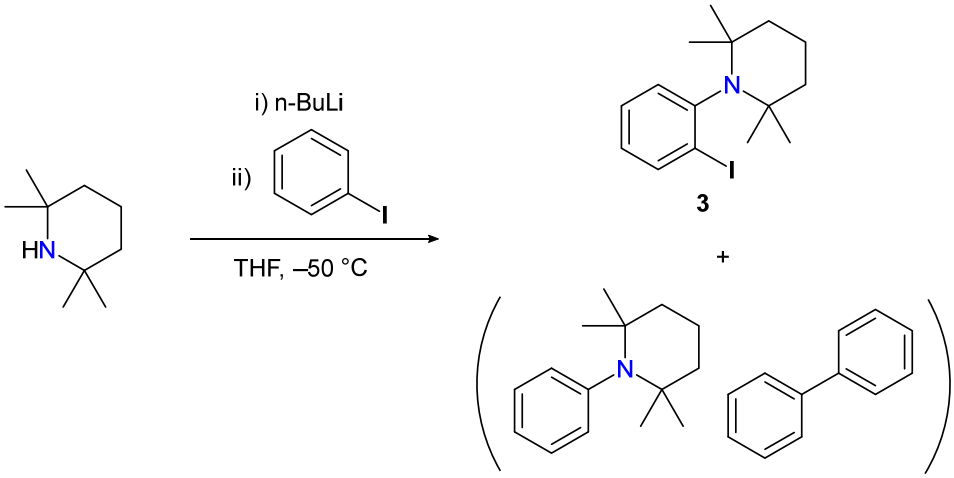

Scheme 31 – Synthesis of *N*-(2-iodophenyl)-2,2,6,6-tetramethylpiperidine 3.

From ortho-bromo dimethylaniline and **3** the first step in synthesis of the target FLP compounds is their lithiation *via* a lithium-halogen exchange reaction (Scheme 32). These reactions both proceed easily using the conditions reported by Chernichenko *et al*. to give the lithiated compounds in good yields of 89% [**4**] and 70% [**5**].[19] **4** and **5** were isolated by washing with hexanes and then drying *in vacuo* to give off-white amorphous powders. The identity of the products was again confirmed using ^{1}H NMR spectroscopy by comparison to the reported literature values.

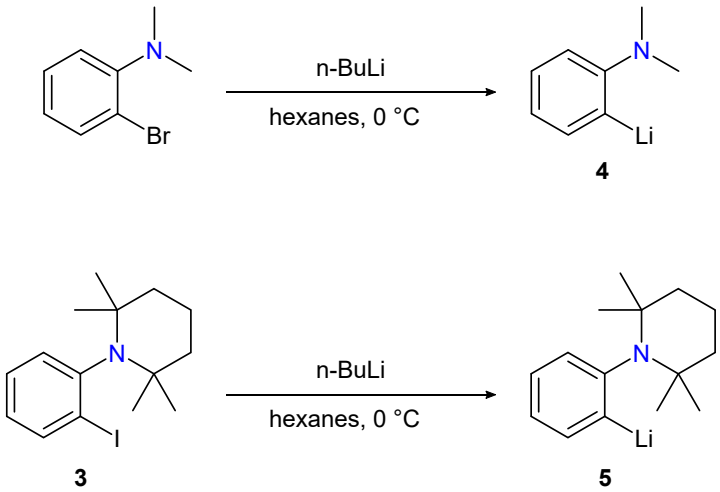

Scheme 32 – Lithiation of 2-bromo-*N*,*N*-dimethyl aniline and 3, to give 4 and 5 respectively.

The next step in the synthesis was the transmetallation reaction of the lithiated species **4** and **5** with dimethylaluminium chloride (Scheme 33). The conditions chosen were

based upon those used for the similar reactions of these lithiated species with $ClB(C_6F_5)_2$ to make related boron-based FLPs.[19]

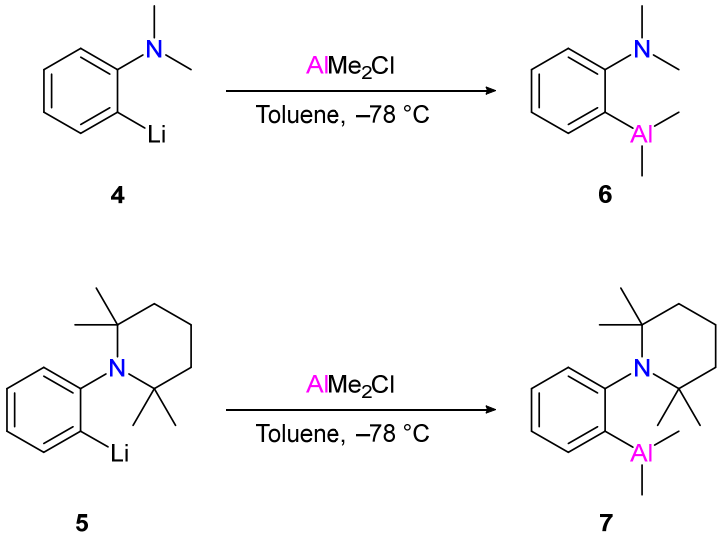

Scheme 33 – Transmetallation of 4 and 5, to form 6 and 7 respectively.

Reaction of the lithiated species **4** with dimethyl aluminium chloride followed by separation of the lithium chloride by-product gave a viscous oil containing the desired product as the major component. This was determined by ^{1}H NMR, which showed full consumption of the dimethyl aluminium chloride methyl resonances at –0.34 ppm and a new set of aluminium methyl resonances at –0.30 ppm. In addition, all other expected resonances were seen for the ligand aryl group between 6.61-7.71 ppm and the methyl environments at 2.10 ppm. The aluminium NMR spectrum showed a broad peak at 182 ppm. The product was purified by sublimation to give the product **6** as pure colourless plate-shaped crystals with a moderate yield of 44% from which a crystal structure was obtained (Figure 7).

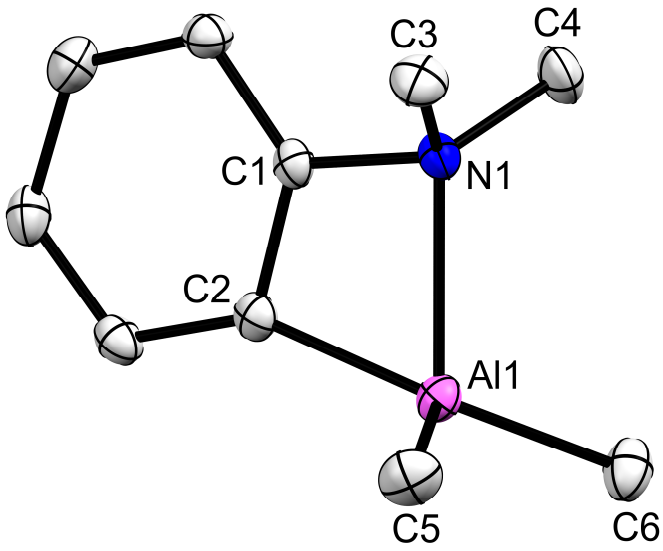

Figure 7 – Molecular structure of 6. Thermal ellipsoids shown at the 50% probability level and all protons omitted for clarity. Selected bond distances [Å] and angles for 6: N1–Al1 2.0998(11), C2-C1-N1 110.12(10)°, C1-C2-Al1 93.12(8)°.

6 exhibits a N1–Al1 bond (2.100(1) Å), which shows that the molecule does not have enough steric bulk to be a true FLP. Searching the CSD for N–Al bonds with 3 carbon substituents at both nitrogen and aluminium revealed the average bond length to be 2.044 Å (s.d. 0.039 Å).[22] From this it can be seen that the N1–Al1 bond length in **6** of (2.100(1) Å) lies on the higher end of the distribution, suggesting that some strain may exist in the bond. Additionally, the sum of angles around the Al1 centre with C2, C5 and C6 is 356.88(19)°, showing very little distortion form the ideal trigonal planar geometry has occurred. It is worth noting that this almost planar geometry could also be caused by five-coordinate aluminium. To check that this was not the cause the extended crystal structure was examined and no atoms were found coordinated in the site opposite the nitrogen. A combination of the bond length and angle sum factors indicate that the adduct bond formed is potentially weaker than a normal N–Al adduct bond. This indicates that **6** may still be able to access FLP-like reactivity.

An analogous method was followed for lithiated species **5** to give species **7** with a yield of 50%. In the same manner as **6**, ^{1}H NMR spectrum showed full consumption of the dimethyl aluminium chloride methyl resonances at –0.34 ppm and a new set of aluminium methyl resonances at 0.03 ppm. The ligand aryl resonances were seen between 7.02-7.71 ppm, the methyl resonances at 0.91 and 1.38 ppm, and the CH_2

resonances between 0.95-1.63 ppm. The aluminium NMR spectrum showed a broad peak at 185 ppm. The crystal structure for **7** is shown below (Figure 8).

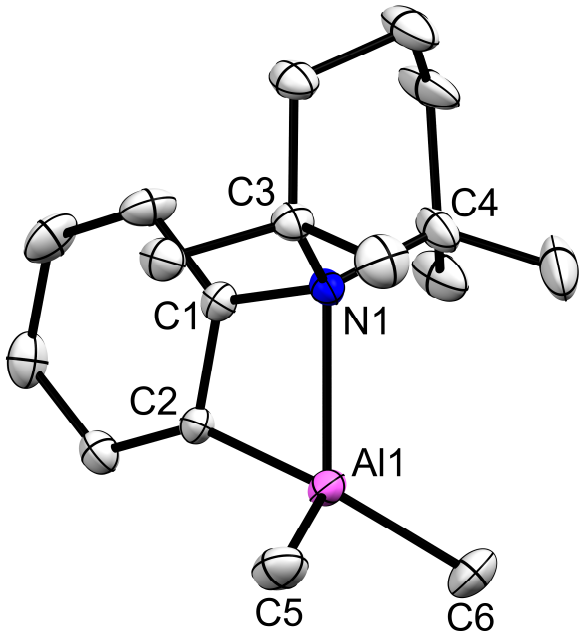

Figure 8 – Molecular structure of 7. Thermal ellipsoids shown at the 50% probability level and all protons omitted for clarity. Selected bond distances [Å] and angles for 7: N1–Al1 2.1753(13) C2-C1-N1 110.85(13)°, C1-C2-Al 95.09(10)°.

The structure of **7** is very similar to that of **6**. However, the N1–Al1 bond length in **7** (2.175(1) Å) is longer than that of **6** (2.100(1) Å). This seems to indicate that the adduct in **7** is weaker than that of **6**. However, despite this longer N1–Al1 bond length, **7** shows a smaller sum of angles around the Al1 centre with C2, C5 and C6 of 348.17(23)°. This is most likely due to crystal-packing effects. Again no atoms were found in the potential 5th coordination site at aluminium.

Optimisation of these reactions to give higher yields of **6** and **7** was attempted by adding two equivalents of dimethyl aluminium chloride, in an attempt to reduce the amount of side products formed. However, in both cases this led to the formation of different products (Scheme 34).

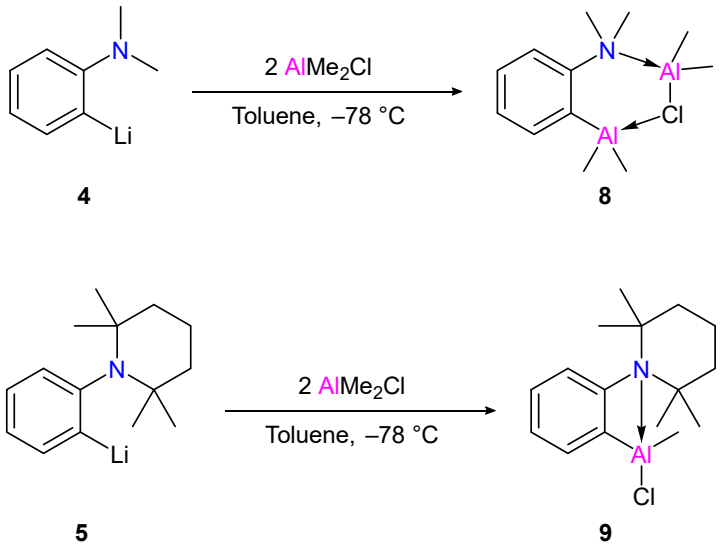

Scheme 34 - Reactions of 4 and 5 with two equivalents of dimethyl aluminium chloride, to form 8 and 9 respectively.

In the reaction of **4** with two equivalents of dimethyl aluminium chloride, product **8** was obtained by spontaneous crystallisation from the crude viscous oil. From these crystals the molecular structure was obtained (Figure 9).

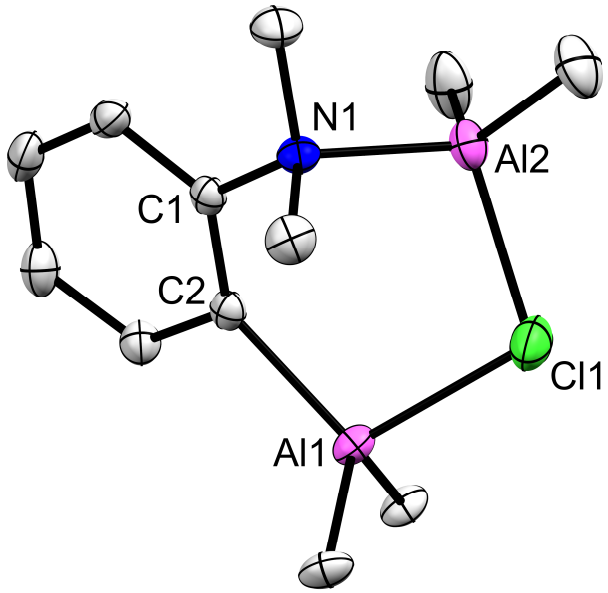

Figure 9 – Molecular structure of 8. Thermal ellipsoids shown at the 50% probability level and all protons omitted for clarity. Selected bond distances [Å] for 8: 2.2458(9), Al1–Cl1 2.3391(8).

The formation of **8** is easily explained by formation of **6** followed by adduct formation with the remaining equivalent of dimethyl aluminium chloride. An interesting and initially unexpected feature of this structure is the push pull adduct nature, with

donation from the nitrogen to the aluminium centre of the dimethyl aluminium chloride, and donation from the chloride to the aluminium centre of **8**. The six membered ring formed by this adduct formation adopts a heavily distorted half chair conformation (Figure 10). The structure of **8** was additionally confirmed by ^{1}H NMR, showing two new sets of aluminium methyl resonances at –0.68 ppm and –0.04 ppm, as well as the ligand aryl resonances between 6.43-7.80 ppm. The fact that the aluminium methyl resonances for **8** are different from **6** (–0.30 ppm) indicates that the adduct **8** exists in solution as well as in the solid state structure.

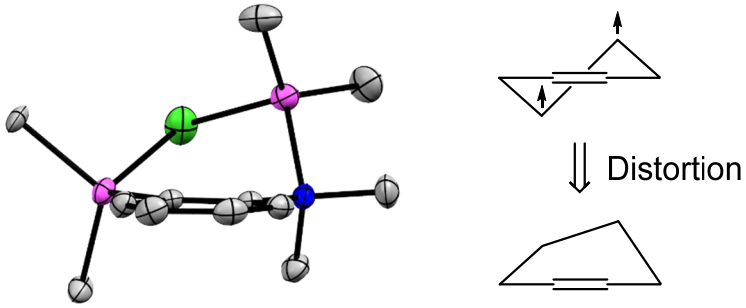

Figure 10 – View of distorted half chair conformation of 8, and representation of normal and distorted half chair conformations.

In contrast, the reaction of **5** with two equivalents of dimethyl aluminium chloride did not give the analogous adduct. Instead species **9** was obtained by spontaneous crystallisation from the crude viscous oil. From these crystals the molecular structure was obtained (Figure 12).

9 is assumed to be formed by initial formation of **7** followed a ligand scrambling reaction with the remaining dimethyl aluminium chloride to form **9** and trimethyl aluminium. This type of aluminium alkyl group and chloride group exchange is known in the literature with rapid exchange at room temperature, and so this result is unsurprising.[23]

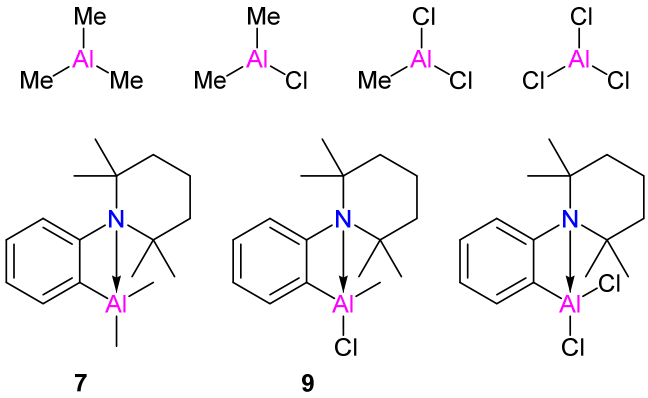

Figure 11 – Potential ligand-scrambled species present in solution.

The ^{1}H NMR spectrum of the crude oil showed a mixture of species that were not identifiable from the spectrum. It is assumed that multiple species with varying degrees of ligand scrambling exist in the crude oil (Figure 11), and that species **9** crystallised preferentially.

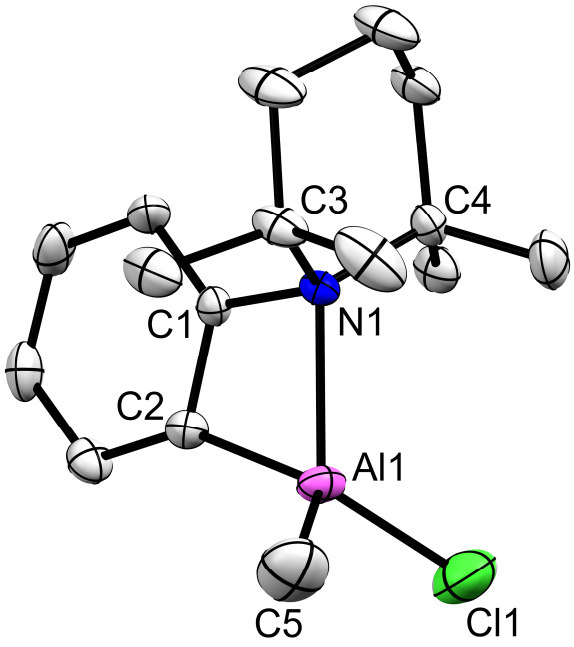

Figure 12 - Molecular structure of 9. Thermal ellipsoids shown at the 50% probability level. Disorder of C5 and Cl1 over their respective positions not shown. A second molecule in the asymmetric unit and all protons omitted for clarity. Selected bond distance [Å] for 9: N1–Al1 2.1448(18)

The structure of **9** is similar in geometry to that of **7.** In this case the N1–Al1 bond length is 2.145(2) Å, slightly shorter than for **7** (2.175(1) Å), which is expected due to the chloride substituent increasing the Lewis acidity of the aluminium centre.[24] The sum of

angles around the Al1 centre with C2, C5 and C6 in this structure is 345.62(24)° which also indicates a stronger N–Al interaction than for **7**.

The differing results for the two FLP precursors is already indicative of how much greater the steric bulk is for the tetramethylpiperidine substituent. This is evident from the fact that **6** is able to form the adduct species **8**, while **7** is unable to do this and instead undergoes ligand scrambling to form **9**, and presumably other scrambled species. This suggests that the target FLP **2** derived from **7** may be a more reactive species, due to a larger degree of frustration.

2.3 Substituent-exchange reactions of dimethyl aluminium FLPs with $B(C_6F_5)_3$

The penultimate step in the synthesis of the target FLP compounds is the exchange of the aluminium methyl groups of **6** and **7** for pentafluorophenyl groups (Scheme 35).

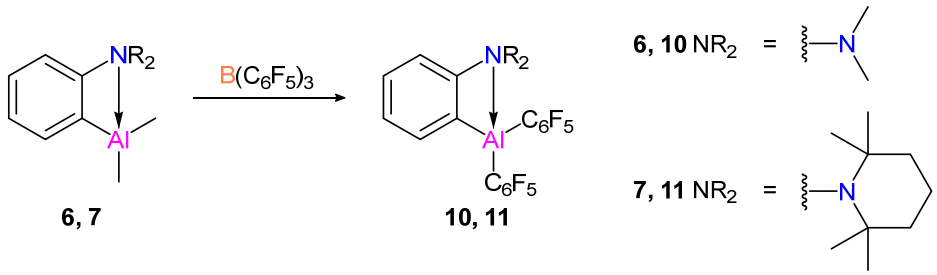

Scheme 35 – Proposed synthesis of target FLPs 10 and 11 from precursors 6 and 7 and $B(C_6F_5)_3$.

This reaction is based on the reported exchange of ligands in the reaction between $AlMe_3$ and $B(C_6F_5)_3$.[20] This reaction proceeds stoichiometrically with full ligand exchange to form BMe_3 and $Al(C_6F_5)_3$ (Scheme 36).

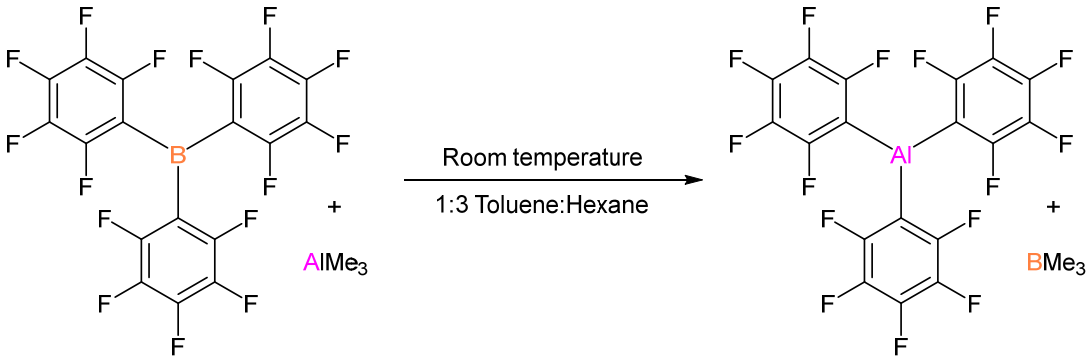

Scheme 36 – Ligand exchange reaction of $AlMe_3$ and $B(C_6F_5)_3$.

The initial conditions trialled for the exchange of the aluminium methyl groups of **6** and **7** to pentafluorophenyl groups were 1 equivalent of **6** or **7** to $^2/_3$ equivalents of $B(C_6F_5)_3$ to preserve the 1:1 methyl group to C_6F_5 group ratio. However, upon trialling these conditions a complex mixture of products was observed, showing that the reaction had not proceeded cleanly to the expected products. It was postulated that the presence of the nitrogen donor in the FLP precursor molecules was preventing the exchange by coordination to the borane. This prompted a change in the stoichiometry to use $1^2/_3$ equivalents of $B(C_6F_5)_3$ such that if coordination of the nitrogen to the borane was occurring, there would still be $^2/_3$ equivalents of borane free to exchange. These conditions did lead to a cleaner reaction. However, the main boron species observed by NMR spectroscopy was $MeB(C_6F_5)_2$ with only trace amounts of $Me_2B(C_6F_5)$. This indicates that further exchange of pentafluorophenyl groups from $MeB(C_6F_5)_2$ is slow, and so this led to using a final set of optimised conditions for this exchange reaction, using 2 equivalents of borane relative to the FLP precursors **6** and **7** (Scheme 37).

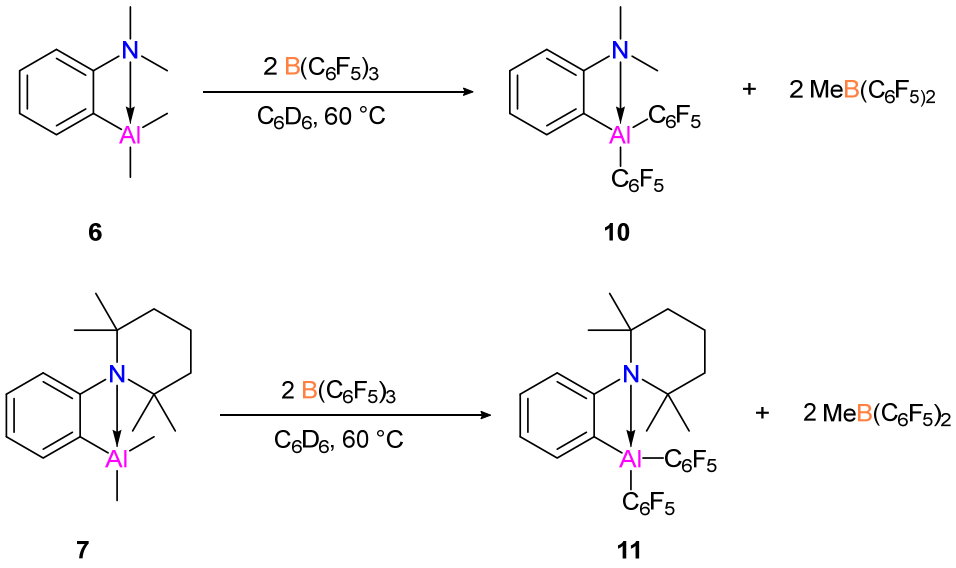

Scheme 37 – Optimised exchange reactions of 6 and 7 with $B(C_6F_5)_3$.

NMR spectroscopy gave insight into the mechanism of the exchange. Upon initial mixing of the **6** and two equivalents of $B(C_6F_5)_3$ there are four observable species in the ^{11}B NMR spectrum (Figure 13). The main component as expected is $B(C_6F_5)_3$ at 60.0 ppm. Also seen is a small amount of $MeB(C_6F_5)_2$ at 71.9 ppm, but of greater interest are the two species at –14.2 ppm and –15.9 ppm, which are in the range for four co-ordinate boron anions. They are also significantly sharper signals, indicating a tetrahedral environment.

Upon leaving the NMR sample to stand at room temperature for 16 hours, a biphasic system is formed, with a 2 mm tall yellow phase at the bottom of the NMR tube and a 3.8 cm tall colourless phase on top. The small yellow phase at the bottom is presumed to be a clathrate ionic phase. ^{11}B NMR spectroscopy of this sample shows a decrease in concentration of $B(C_6F_5)_3$ and an increase in $MeB(C_6F_5)_2$ as expected, as well as formation of a small amount of $Me_2B(C_6F_5)$ at 80.8 ppm. It also still exhibits the resonance at –15.9 ppm but the resonance at –14.2 ppm is no longer present.

Heating of this sample for a further 20 hours at 60 °C caused the sample to once again become homogeneous with a pale yellow colour, and the NMR spectrum showed further conversion of $B(C_6F_5)_3$ to $MeB(C_6F_5)_2$ and a slightly greater amount of $Me_2B(C_6F_5)$.

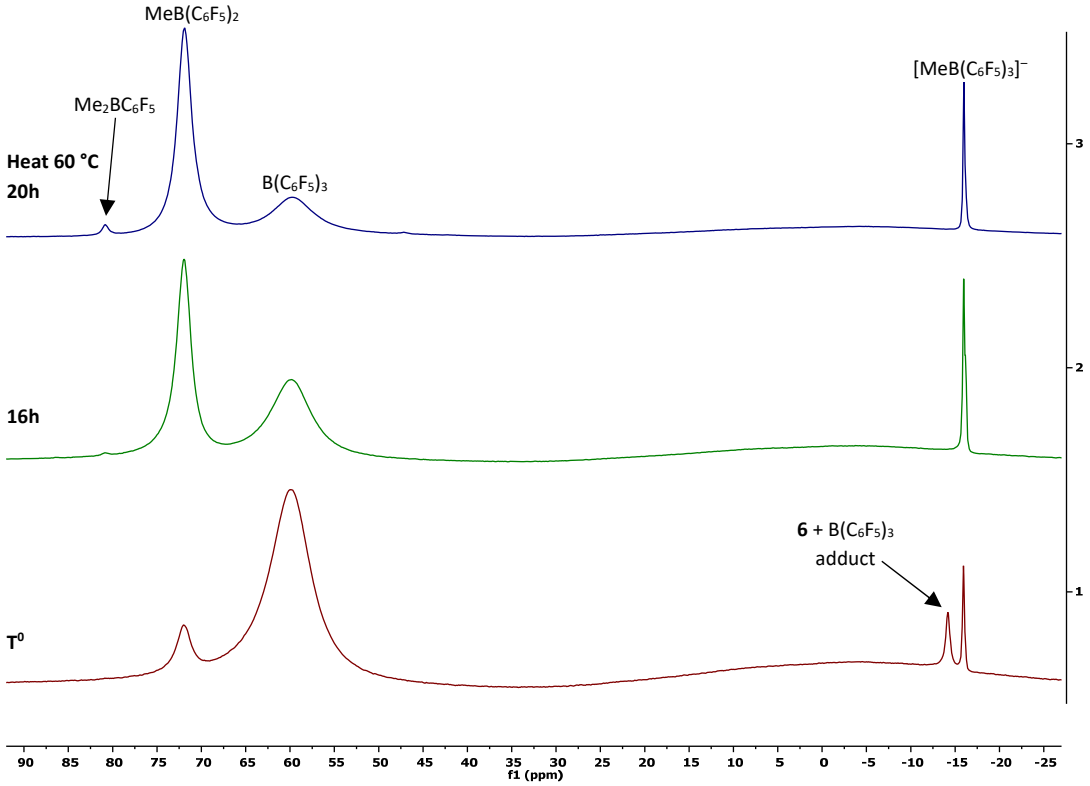

Figure 13 – ^{11}B NMR spectra of exchange reaction of 6 with $B(C_6F_5)_3$.

From these observations the following mechanism was proposed (Scheme 38), and therefore the peak at –14.2 ppm is assigned as the adduct between **6** and $B(C_6F_5)_3$ and the peak at –15.9 ppm as the $[MeB(C_6F_5)_3]^-$ anion. Assignment of the peak at –14.2 ppm is further supported by the observation that the analogous peak is not observed in the exchange reaction of **7** and $B(C_6F_5)_3$, presumably as the bulk of the tetramethylpiperidine group prevents this adduct formation.

Additionally it can be inferred that the reason that $^2/_3$ equivalents of $B(C_6F_5)_3$ is not sufficient for the exchange is that the produced $MeB(C_6F_5)_2$ is not Lewis acidic enough to abstract aluminium methyl groups at any considerable rate, as only trace amounts of $Me_2B(C_6F_5)$ are observed.

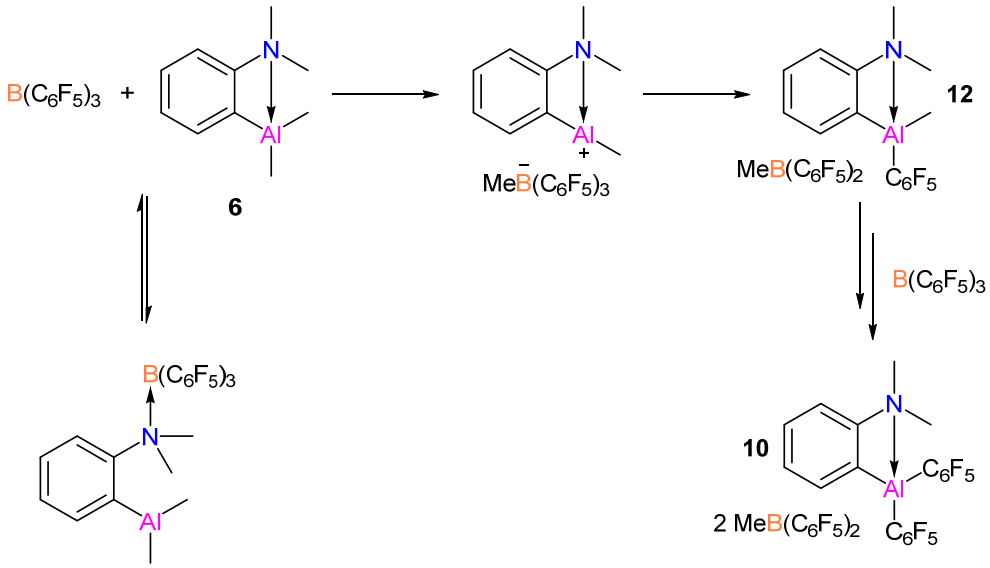

Scheme 38 – Proposed mechanism of exchange reaction of 6 with $B(C_6F_5)_3$.

Having found conditions to give full conversion to the desired bispentafluorophenyl FLPs **10** and **11**, scaled up reactions were performed in order to attempt to isolate the FLPs by separation from the undesired borane by-products.

The reaction of **6** with $B(C_6F_5)_3$ was the first to be scaled up. ^1H NMR spectroscopy of the crude mixture after reaction showed full conversion to the desired product with complete loss of the aluminium methyl resonances at –0.30 ppm and generation of the $MeB(C_6F_5)_2$ resonance at 1.33 ppm. Crystallisation of the product from this crude mixture was the first attempted method of purification. However, due to the fact that the desired product is the minor component of the mixture, with the undesired $MeB(C_6F_5)_2$ being the major component, only crystals of the by-product were obtained, regardless of solvent choice or crystallisation conditions. As crystallisation proved unsuccessful, sublimation was then attempted. Unfortunately this also proved unsuccessful due to the very similar molecular weights and properties of the desired product and borane by-products. Only mixtures of various amounts of **10** and $MeB(C_6F_5)_2$ were obtained, with the ratio varying slightly depending on the sublimation temperature and decomposition occurring when heating to over 120 °C.

As isolation of **10** was proving challenging, the exchange to form **11** was scaled up with the hope that the increased molecular weight of the TMP group would aid the

separation by sublimation. Unfortunately, little difference in the ratios of product and by-product borane was observed relative to **10** when attempting the sublimation.

It was concluded that while the exchange reaction had worked as planned, the separation of the product from the by-products was too challenging and another route into the FLPs **10** and **11** would be required to obtain them as pure materials for further study. This was not attempted in this work. However, these exchange reactions are still interesting from a fundamental viewpoint, due to their differing reactivity from the parent exchange reaction involving $AlMe_3$ and $B(C_6F_5)_3$ where full exchange of all substituent groups is observed.

2.4 Computational analysis of substituent-exchange reactions

Details of functionals and basis sets used can be found in chapter 6.4.5 (vide infra).

In order to better understand the differences in the mechanisms of the parent exchange reaction of $AlMe_3$ and $B(C_6F_5)_3$ and the exchange reactions with **6** and **7** and $B(C_6F_5)_3$, computational analysis was carried out. Two potential mechanisms can be envisaged for these exchange reactions. A mechanism that proceeds *via* ionic intermediates (Scheme 39 a), or a mechanism that proceeds *via* covalent 3-centre 2-electron bonded intermediates (Scheme 39 b).

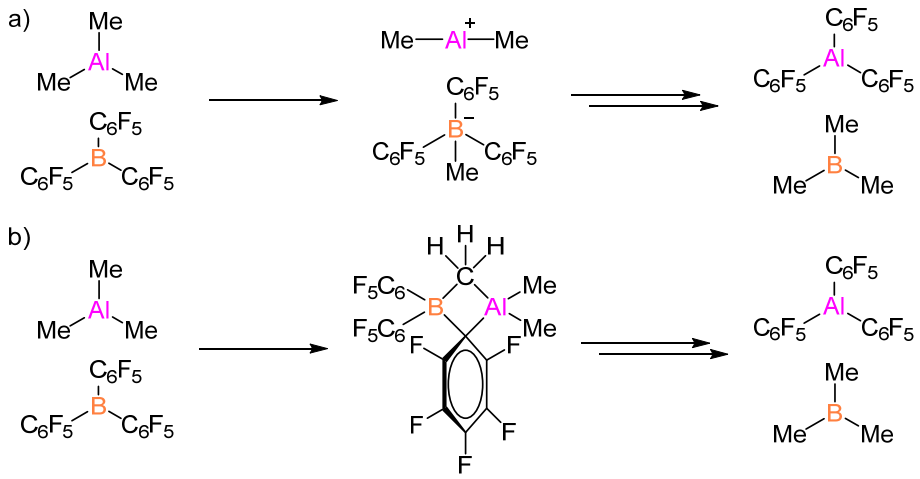

Scheme 39 – Mechanisms for substituent exchange at B and Al centres, using $AlMe_3$ and $B(C_6F_5)_3$ as example reagents, by a) ionic intermediates and b) 3-centre 2-electron bonded intermediates.

2.4.1 Exchange between $AlMe_3$ and $B(C_6F_5)_3$

Analysis was first carried out on the less complicated exchange reaction between $AlMe_3$ and $B(C_6F_5)_3$ as this is computationally simpler.

Based on the NMR spectra of the exchange reactions performed between **6** and $B(C_6F_5)_3$ (Figure 13), it appears that ionic intermediates are involved in the mechanism of these exchange reactions due to the presence of the resonance for $[MeB(C_6F_5)_3]^-$ anion in the ^{11}B NMR spectrum. Therefore, optimisation of structures for an ionic-type mechanism for the exchange between $AlMe_3$ and $B(C_6F_5)_3$ was the initial focus. The intermediate ion pairs were optimised as two separate ion structures. Initially, only the easier to locate reactant, intermediate, and product stationary points of the reaction were optimised. This gave the energy profile as seen below (Figure 14).

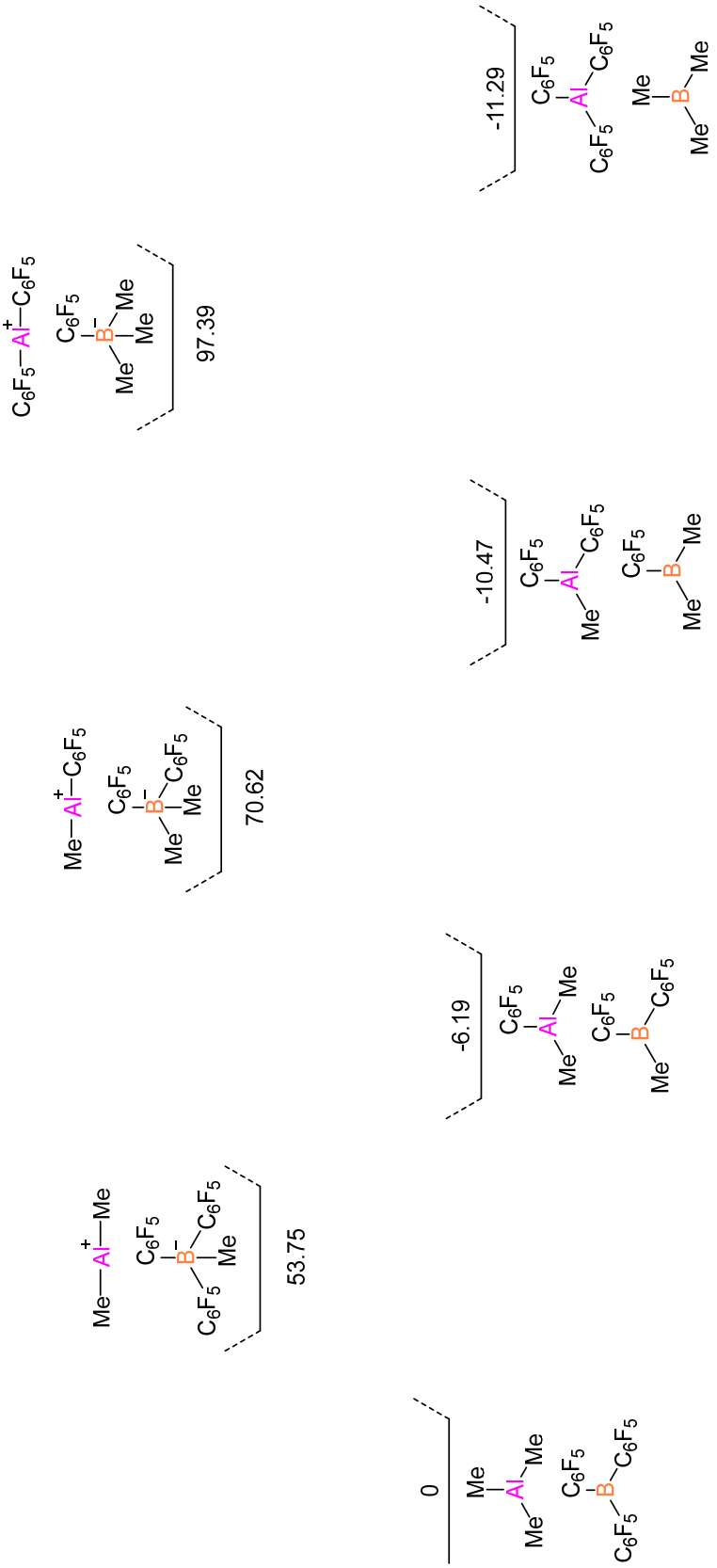

Figure 1 – Ionic reaction mechanism intermediates for the exchange reaction between $AlMe_3$ and $B(C_6F_5)_3$. Transition states not located and so structures not linked. All energies are Gibbs free energies given in kcal mol^{-1} relative to the starting materials. Calculations carried out at the wb97xd/6-31+g(d,p) level of theory with SMD solvation (toluene).

From this profile it can be seen that each sequential exchange of methyl and pentafluorophenyl group is thermodynamically favourable, as expected. However, the high lying ionic intermediates have energies that are far too high to be accessible at room temperature which are the reported conditions for this reaction.

Since the ionic mechanism is unlikely based on the energy of the ion pair intermediates, optimisation of a mechanism involving 3-centre 2-electron bonded intermediates was carried out. This gave us the new energy profile as seen below (Figure 15).

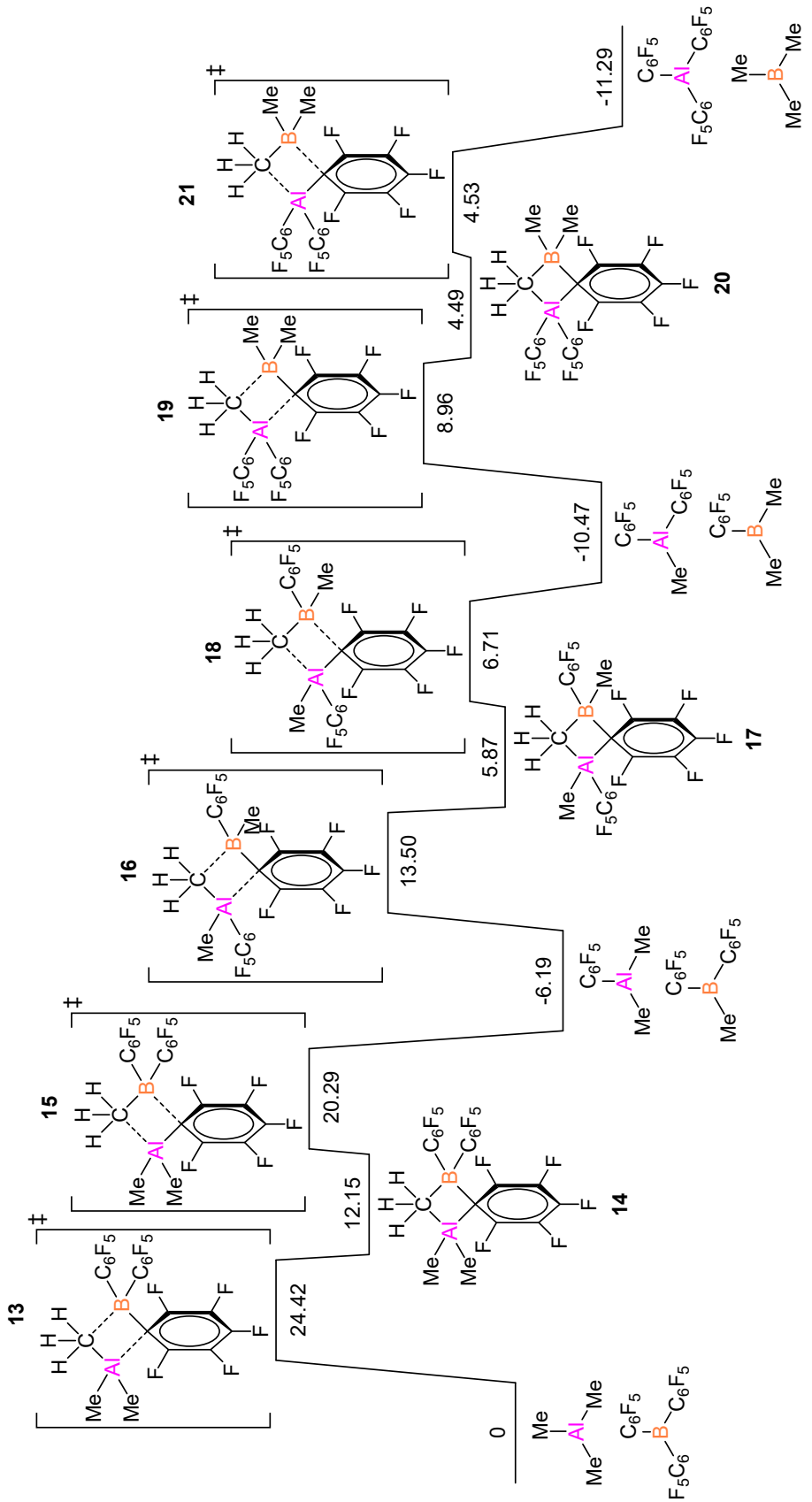

Figure 2 – 3-centre 2-electron bonded reaction mechanism intermediates for the exchange reaction between $AlMe_3$ and $B(C_6F_5)_3$. All energies are Gibbs free energies given in kcal mol^{-1} relative to the starting materials. Calculations carried out at the wb97xd/6-31+g(d,p) level of theory with SMD solvation (toluene).

This energy profile shows lower and much more reasonable energies for the high-lying intermediates (Figure 15 - **14**, **17**, **20**), compared to the ionic pathway.[25] This leads us to believe that the reaction between $AlMe_3$ and $B(C_6F_5)_3$ occurs *via* this 3-centre 2-electron bonded type mechanism, where the energies are much lower.

Examination of the three steps of this reaction reveal some interesting details, especially when looking at the energy differences in the transition states. The barriers to exchange of the methyl and pentafluorophenyl groups grow successively smaller as the exchange progresses. The first exchange to form $AlMe_2(C_6F_5)$ and $BMe(C_6F_5)_2$ has a barrier of 24.42 kcal mol^{-1}. The second exchange to form $AlMe(C_6F_5)_2$ and $BMe_2(C_6F_5)$ has a barrier of 13.50 kcal mol^{-1}, a 10.92 kcal mol^{-1} lower energy barrier that the first exchange. The third exchange to form the final products $Al(C_6F_5)_3$ and BMe_3 is the then more similar to that of the second exchange with a barrier of 8.96 kcal mol^{-1}, 4.54 kcal mol^{-1} lower in energy than the second exchange. This is likely due to the changing Lewis acidity of the aluminium centre throughout the reaction. As the aluminium gains more C_6F_5 groups, its Lewis acidity increases and it is more able to abstract further C_6F_5 groups from the boron centre as the increased Lewis acidity makes the formed intermediates more stable.

The result of decreasing energy cost in successive exchange steps for $AlMe_3$ and $B(C_6F_5)_3$ already suggests that the exchange mechanism between **6**/**7** and $B(C_6F_5)_3$ will have a different mechanism, as the experimental results suggest that the second exchange in the reactions between **6**/**7** and $B(C_6F_5)_3$ is disfavoured relative to the first exchange.

2.4.2 Exchange reaction between 6 and $B(C_6F_5)_3$

When investigating the exchange reactions between **6**/**7** and $B(C_6F_5)_3$ only the exchange with **6** was modelled and not with **7**, for computational simplicity.

For the exchange between **6** and $B(C_6F_5)_3$, two competing mechanisms must be considered (Scheme 40). In both cases the first step is identical. Reaction of **6** with $B(C_6F_5)_3$ to give intermediate **12**. Following this there are two possibilities. **12** may either react with the generated $MeB(C_6F_5)_2$ (Pathway A), or with another equivalent of $B(C_6F_5)_3$ (Pathway B), both to generate **10**, but differing borane by-products.

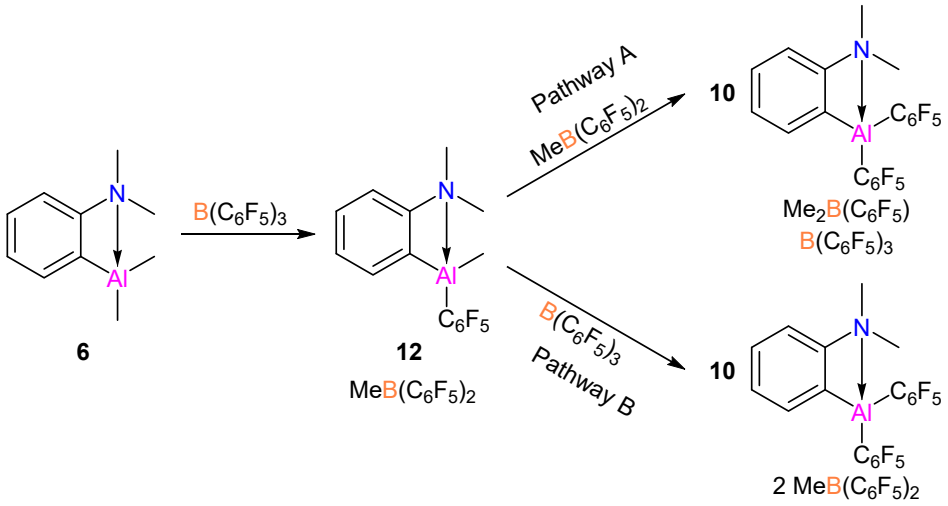

Scheme 40 – Two possible reaction mechanisms for exchange of 6 with $B(C_6F_5)_3$.

Both pathways A and B were optimised to attempt to explain the experimentally observed preference to react with a second equivalent of $B(C_6F_5)_3$ over the $MeB(C_6F_5)_2$. Key intermediate structures were calculated, and an energy profile was compiled and examined to attempt to explain the selectivity (Figure 16). Due to time constraints in Huazhong's project, optimisation of the transition states of this exchange were not possible, but suggestions about the mechanism can still be made from the intermediates of the reaction.

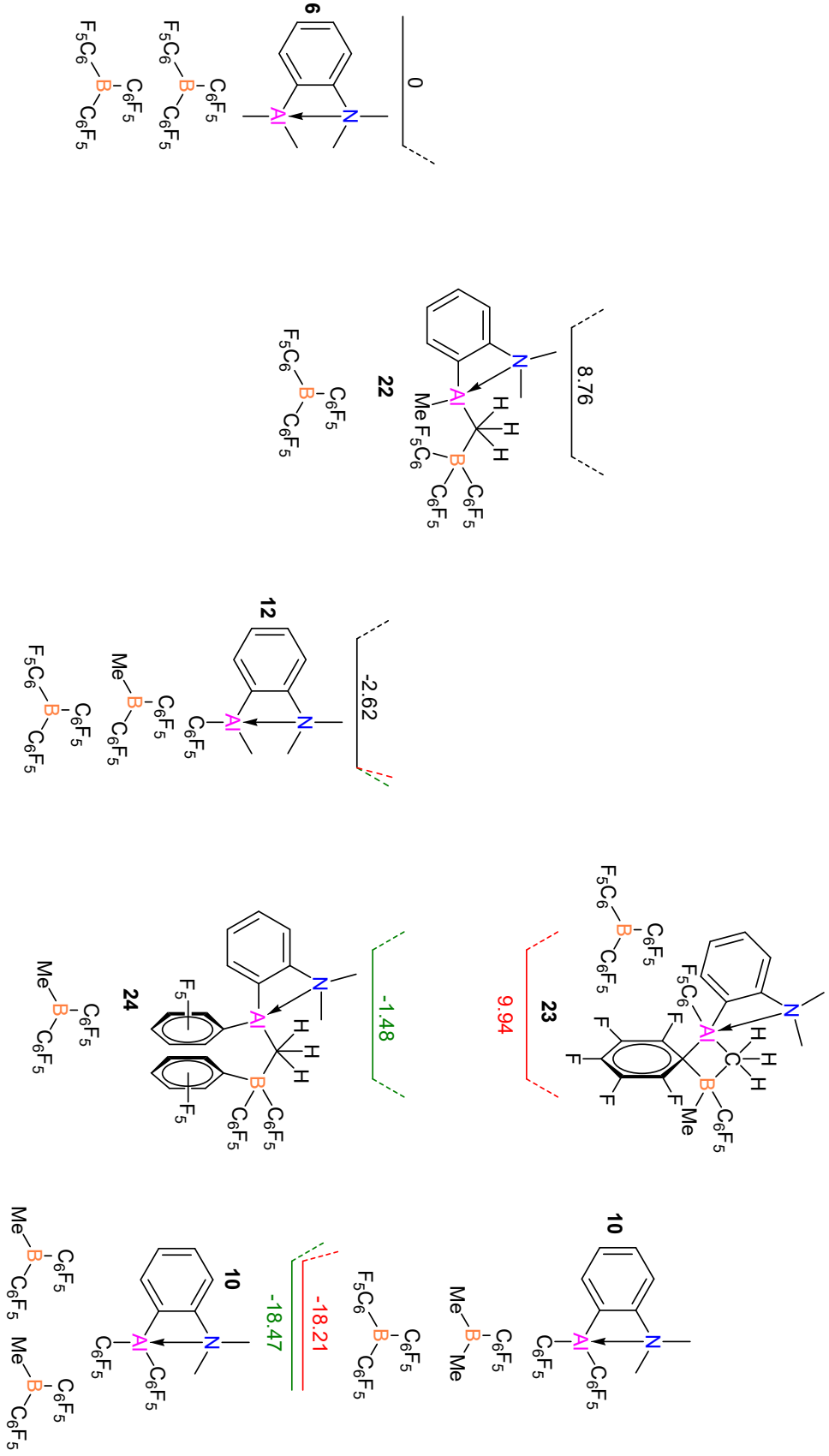

Figure 3 – Reaction intermediates for exchange of 6 and $B(C_6F_5)_3$. All energies are Gibbs free energies given in kcal mol^{-1} relative to the starting materials. Transition states not located and so structures not linked. Calculations carried out at the wb97xd/6-31+g(d,p) level of theory with SMD solvation (benzene).

Upon optimising the structure of the intermediate of the first exchange step for the exchange between **6** and $B(C_6F_5)_3$ and comparing it visually to the first step of the exchange between $AlMe_3$ and $B(C_6F_5)_3$, it was immediately apparent that the mechanism differed in character significantly.

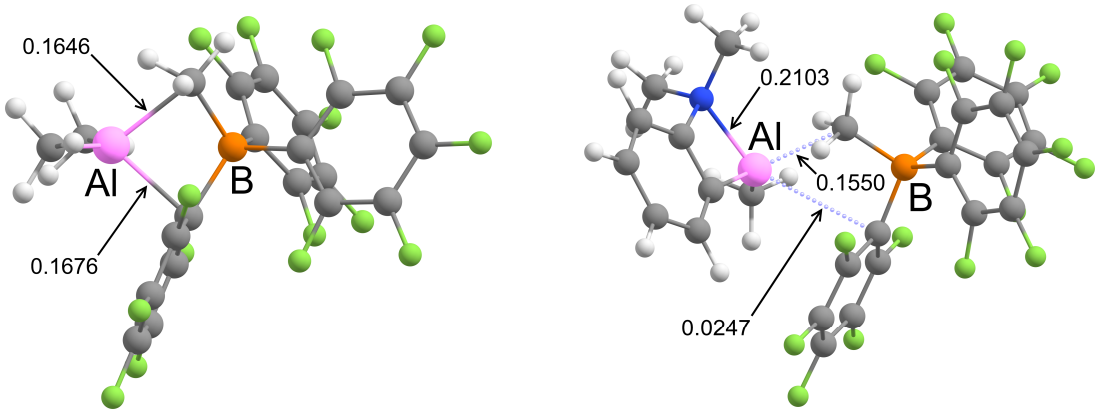

14 **22**

Intermediate	Al-C(Me $_{bridging}$)	Al-C(C_6F_5 $_{bridging}$)	B-C(Me $_{bridging}$)	B-C(C_6F_5 $_{bridging}$)
14	2.21 Å	2.20 Å	1.71 Å	1.72 Å
22	2.33 Å	3.17 Å	1.66 Å	1.66 Å

Figure 17 – First intermediates from the exchange reactions between $AlMe_3$ and $B(C_6F_5)_3$ (14) and 6 and $B(C_6F_5)_3$ (22) and select bond lengths in table and Wiberg bond indices on figure.

For **14**, the structure resembles a classical double bridged structure like that of B_2H_6,[26] with equal bond lengths and Wiberg bond indices to both bridging groups from both aluminium and boron. For **22**, the structure appears to be ionic in nature with an aluminium-based cation and boron-based anion, which is consistent with the experimental observation of the $[MeB(C_6F_5)_3]^-$ anion in the ^{11}B NMR spectrum. In **22** there is effectively no bond between the aluminium and pentafluorophenyl group, and a weaker interaction between the aluminium and the methyl group. It is likely that this is possible due to significant stabilisation of the aluminium cation by the pendant nitrogen donor built into the ligand.

In order to further examine this, NBO analysis of the bonding in the structures of the first intermediates **14** and **22** from the exchange reactions between $AlMe_3$ and $B(C_6F_5)_3$

and **6** and $B(C_6F_5)_3$ was carried out, in order to see how the Wiberg bond indices differed in the two reaction steps. In **14** there is a bond to both the bridging CH_3 (WBI 0.1646) and C_6F_5 (WBI 0.1678) groups, while in **22** the bond to the bridging CH_3 (0.1550) is still present but slightly weaker, but there is now effectively no bond to the C_6F_5 group (WBI 0.0247). It has instead been replaced by a bond to the amine donor group (WBI 0.2103). As such, the structure of **22** can be seen as that of an ion pair, which in solution can dissociate to give the free ions. This is due to the amine donor built into the ligand stabilising the aluminium centre, allowing it to dissociate as a free cation.

Having gained valuable insight into the bonding in the first step of the exchange, examination of the structures of the intermediates of the two divergent pathways which determine the reaction selectivity was carried out.

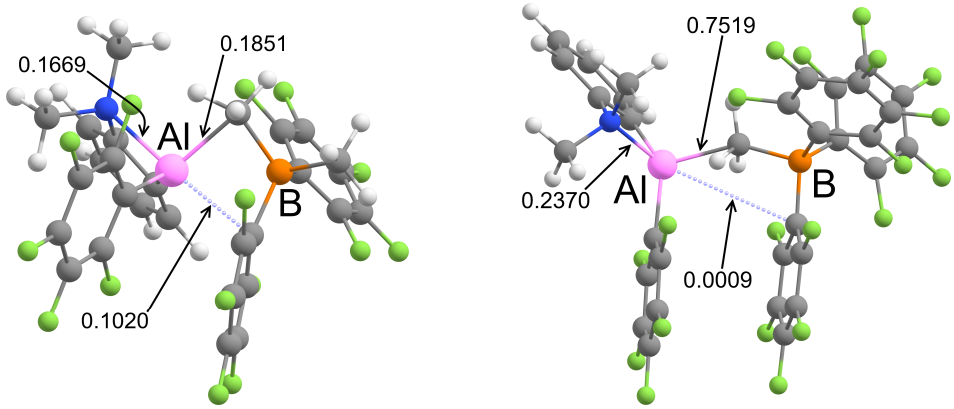

23 (Pathway A) **24 (Pathway B)**

Intermediate	Al-C(Me $_{bridging}$)	Al-C(C_6F_5 $_{bridging}$)	B-C(Me $_{bridging}$)	B-C(C_6F_5 $_{bridging}$)
23	2.16 Å	2.49 Å	1.74 Å	1.70 Å
24	2.14 Å	3.99 Å	1.70 Å	1.66 Å

Figure 18 – The two possible intermediates 23 and 24 from pathways A and B in the exchange between 6 and $B(C_6F_5)_3$ and select bond lengths in table and Wiberg bond indices on figure.

When **12** reacts with $MeB(C_6F_5)_2$ (Pathway A) to generate **23**, the structure clearly shows evidence of two 3-centre 2-electron bonds through bridging of both the methyl (WBI 0.1851) and pentafluorophenyl (WBI 0.1020) groups, in a similar manner to **14**. However, unlike for **14**, the structure is not symmetrical and the Al–C(C_6F_5 $_{bridging}$) is weaker (WBI 0.1020) than in **14** (WBI 0.1676). This is due to the amine donor and

bridging pentafluorophenyl group both trying to donate into the aluminium p-orbital. This destabilises this 3-centre 2-electron bonded intermediate raising the energy of the reaction step.

In contrast, when **12** reacts with $B(C_6F_5)_3$ (Pathway B) to generate **24**, the structure is much more similar to **22**, showing only bridging of the methyl (WBI 0.7519) group with no bridging pentafluorophenyl (WBI 0.009) group. However, in this case an additional π-π stacking interaction is also seen between the pentafluorophenyl groups on the aluminium and boron centres. Intermediate **24** seems to be earlier on in the reaction step than **22**, as in **24** the Al-C($Me_{bridging}$) bond has a much higher WBI of 0.7519 than for **22** (WBI 0.1550). This is likely due to this π-π stacking interaction between the pentafluorophenyl groups changing the location of the energy minimum.

Having examined all of the possible intermediates in the exchange between **6** and $B(C_6F_5)_3$, the following explanation is offered for the preference of **12** to react with $B(C_6F_5)_3$ over $MeB(C_6F_5)_2$, with the major caveat that no transition states have been optimised. Since the 3-centre 2-electron bonded intermediates are greatly destabilised by the amine donor on **6**/**12**, the reaction must proceed by an ionic mechanism where the boron abstracts a methyl group from the aluminium centre to form an ion pair. $B(C_6F_5)_3$ is highly Lewis acidic and so is able to abstract the methyl group forming the $[MeB(C_6F_5)_3]^-$ anion as seem in intermediates **22** and **24**, while $MeB(C_6F_5)_2$ has lower Lewis acidity and so is unable to abstract the methyl group from the aluminium centre, instead forming a much more unstable 3-centre 2-electron bonded type intermediate **23**. Therefore reaction with $B(C_6F_5)_3$ is highly preferred over $MeB(C_6F_5)_2$ and this is indeed the experimentally observed result.

These calculations have therefore been able to give some insight into the selectivity difference between the exchange reactions between $AlMe_3$ and $B(C_6F_5)_3$ and **6** and $B(C_6F_5)_3$. Additionally, it can be suggested that the exchange reaction between $AlMe_3$ and $B(C_6F_5)_3$ proceeds *via* a series of 3-centre 2-electron bonded intermediates while the exchange reaction between **6** and $B(C_6F_5)_3$ has intermediates that are more ionic in nature, due to the stabilisation that the pendant nitrogen donor provides to the

aluminium cation centre. This is consistent with the experimental observation of the biphasic system formed during the reaction and observation of anionic boron species in the ^{11}B NMR spectrum.

2.5 Conclusions

The novel aluminium FLP species **6** and **7** have been synthesised and fully characterised. Further species **8**-**11** have been synthesised and partially characterised. Due to complications with the isolation of the exchange reaction products **10** and **11**, the proposed synthesis could not be continued and the initial target FLPs **1** and **2** have not been isolated as pure species.

Through computational analysis, preliminary proposals relating to the mechanism of the substituent exchange of methyl and pentafluorophenyl groups between aluminium and boron have been suggested, with two differing mechanisms when using $AlMe_3$ or **6**/**7** as the aluminium exchange reagent. However, these suggestions come with the caveat that some of the transition states of the reactions were not optimised, and so important information is missing from the potential energy surface.

2.6 References

[1] G. Erős, K. Nagy, H. Mehdi, I. Pápai, P. Nagy, P. Király, G. Tárkányi, T. Soós, *Chem. Eur. J.* **2012**, *18*, 574–585.
[2] J. Mohr, M. Oestreich, *Angew. Chem. Int. Ed.* **2014**, *53*, 13278–13281.
[3] M.-A. Légaré, M.-A. Courtemanche, É. Rochette, F.-G. Fontaine, *Science* **2015**, *349*, 513–516.
[4] J. Légaré Lavergne, A. Jayaraman, L. C. Misal Castro, É. Rochette, F.-G. Fontaine, *J. Am. Chem. Soc.* **2017**, *139*, 14714–14723.
[5] G.-Q. Chen, G. Kehr, C. G. Daniliuc, M. Bursch, S. Grimme, G. Erker, *Chem. Eur. J.* **2017**, *23*, 4723–4729.
[6] J. Z. Chan, W. Yao, B. T. Hastings, C. K. Lok, M. Wasa, *Angew. Chem. Int. Ed.* **2016**, *55*, 13877–13881.
[7] M. Shang, M. Cao, Q. Wang, M. Wasa, *Angew. Chem. Int. Ed.* **2017**, *56*, 13338–13341.
[8] M. Shang, J. Z. Chan, M. Cao, Y. Chang, Q. Wang, B. Cook, S. Torker, M. Wasa, *J. Am. Chem. Soc.* **2018**, *140*, 10593–10601.
[9] D. Chen, Y. Wang, J. Klankermayer, *Angew. Chem. Int. Ed.* **2010**, *49*, 9475–9478.
[10] Y. Segawa, D. W. Stephan, *Chem. Commun.* **2012**, *48*, 11963–11965.
[11] M. A. Dureen, D. W. Stephan, *J. Am. Chem. Soc.* **2009**, *131*, 8396–8397.

[12] Y. Zhang, G. M. Miyake, E. Y.-X. Chen, *Angew. Chem. Int. Ed.* **2010**, *49*, 10158–10162.
[13] C. Appelt, J. C. Slootweg, K. Lammertsma, W. Uhl, *Angew. Chem. Int. Ed.* **2013**, *52*, 4256–4259.
[14] T. E. Stennett, J. Pahl, H. S. Zijlstra, F. W. Seidel, S. Harder, *Organometallics* **2016**, *35*, 207–217.
[15] S. Styra, M. Radius, E. Moos, A. Bihlmeier, F. Breher, *Chem. Eur. J.* **2016**, *22*, 9508–9512.
[16] W. Uhl, J. Possart, A. Hepp, M. Layh, *Z. Für Anorg. Allg. Chem.* **2017**, *643*, 1016–1029.
[17] M. Xu, J. Possart, A. E. Waked, J. Roy, W. Uhl, D. W. Stephan, *Philos. Trans. R. Soc. Math. Phys. Eng. Sci.* **2017**, *375*, 20170014.
[18] D. Chakraborty, E. Y.-X. Chen, *Macromolecules* **2002**, *35*, 13–15.
[19] K. Chernichenko, M. Nieger, M. Leskelä, T. Repo, *Dalton Trans.* **2012**, *41*, 9029–9032.
[20] S. Feng, G. R. Roof, E. Y.-X. Chen, *Organometallics* **2002**, *21*, 832–839.
[21] K. Chernichenko, Á. Madarász, I. Pápai, M. Nieger, M. Leskelä, T. Repo, *Nat. Chem.* **2013**, *5*, 718–723.
[22] *Cambridge Structural Database, Ver. 5.38, June 2017. A Search of the CSD Revealed 58 N–Al Single Bond Containing Species with Three Carbon Based Substituents on Each Centre. Mean N–Al Bond Length: 2.044 Å (s.d. 0.039 Å).*, **n.d.**
[23] M. Boleslawski, S. Pasynkiewicz, K. Jaworski, *J. Organomet. Chem.* **1971**, *30*, 199–209.
[24] P. Laszlo, M. Teston, *J. Am. Chem. Soc.* **1990**, *112*, 8750–8754.
[25] P. Atkins, J. de Paula, *Atkins' Physical Chemistry*, OUP Oxford, **2010**.
[26] H. Meislich, *J. Chem. Educ.* **1967**, *44*, 118.

3 Catalysis using in-situ generated aluminium hydride FLPs

3.1 Introduction and aims

In chapter 2 the target FLPs **1** and **2** could not be synthesised *via* the chosen synthetic pathway. However, novel FLPs **3** and **4** were synthesised, isolated and fully characterised (Figure 19).

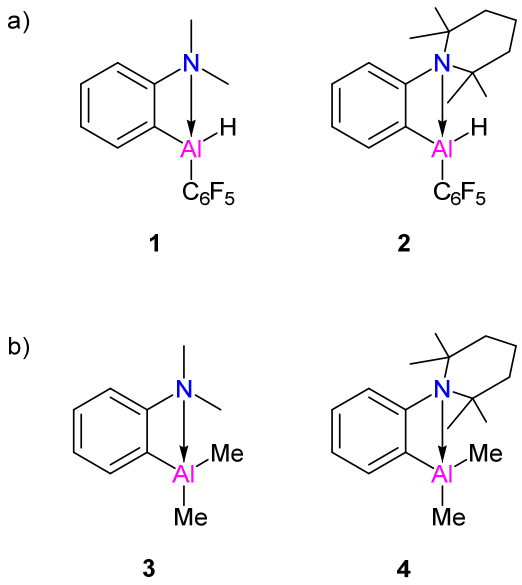

Figure 19 – a) Targeted and b) synthesised FLPs from chapter 2.

Even though FLPs **1** and **2** could not be synthesised, the generation of related FLPs that have an $–AlH_2$ moiety instead of the $–Al(C_6F_5)H$ moiety is still an attractive target, as related boron-based FLPs of this form have been successfully used for the C–H borylation of heteroaromatic compounds.[1]

From the FLPs **3** and **4**, we postulated that generation of the dihydride FLPs **5** and **6** would be possible, *via* a sigma bond metathesis reaction with HBpin, generating MeBpin as a byproduct (Scheme 41).

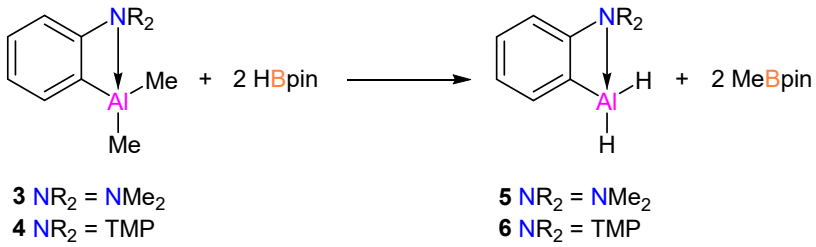

Scheme 41 – Proposed reaction for generation of dihydride FLPs 5 and 6 from 3 and 4.

The dihydride FLPs **5** and **6** could then be used for the catalytic C–H borylation reactions that were initially targeted with FLPs **1** and **2**.

3.2 Generation of aluminium hydride FLPs

In order to produce catalytically active FLPs, exchange of the methyl groups on FLPs **3** and **4** for hydrides was necessary. It was proposed that this could be easily achieved by reaction of the FLPs with HBpin. This is based on previous work in the group where an aluminium hydride was generated by reaction of $AlMe_3$ with HBpin.[2] The reaction between **3**/**4** and HBpin should therefore result in the corresponding dihydrides **5** and **6** along with MeBpin as a byproduct. This method has the additional advantage that **3** and **4** could be used directly in catalytic borylation reactions as a precatalyst, as the FLP hydride species would be generated *in situ* from the HBpin present as the borylation reagent.

Upon addition of two equivalents of HBpin to a colourless solution of **3** in C_6D_6, the solution remained colourless. ^1H and ^{11}B NMR spectroscopy showed that exchange between the aluminium methyl groups and boron hydride had not occurred. However, it was apparent that an adduct had formed between the boron and the nitrogen of the FLP as two doublet signals were seen in the ^{11}B NMR spectrum (Figure 20 c). One signal was seen for free HBpin at 28.5 ppm and one at 6.0 ppm which was attributed as the HBpin adduct due to the upfield shift, indicating a more shielded environment.[3] This was accompanied by two sets of signals for all the CH_3 protons in the FLP species and four sets of signals for the HBpin CH_3 protons in the ^1H NMR spectrum (Figure 20 b).

a) ^{1}H NMR spectrum of **3**

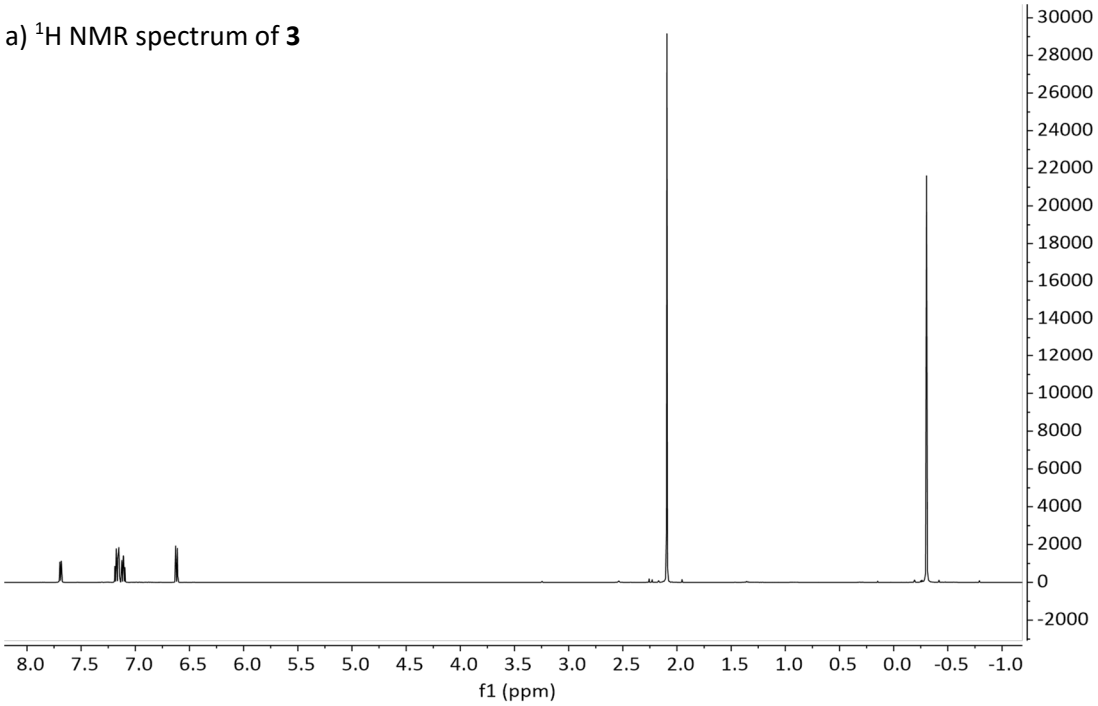

b) ^{1}H NMR spectrum of **3** and HBpin

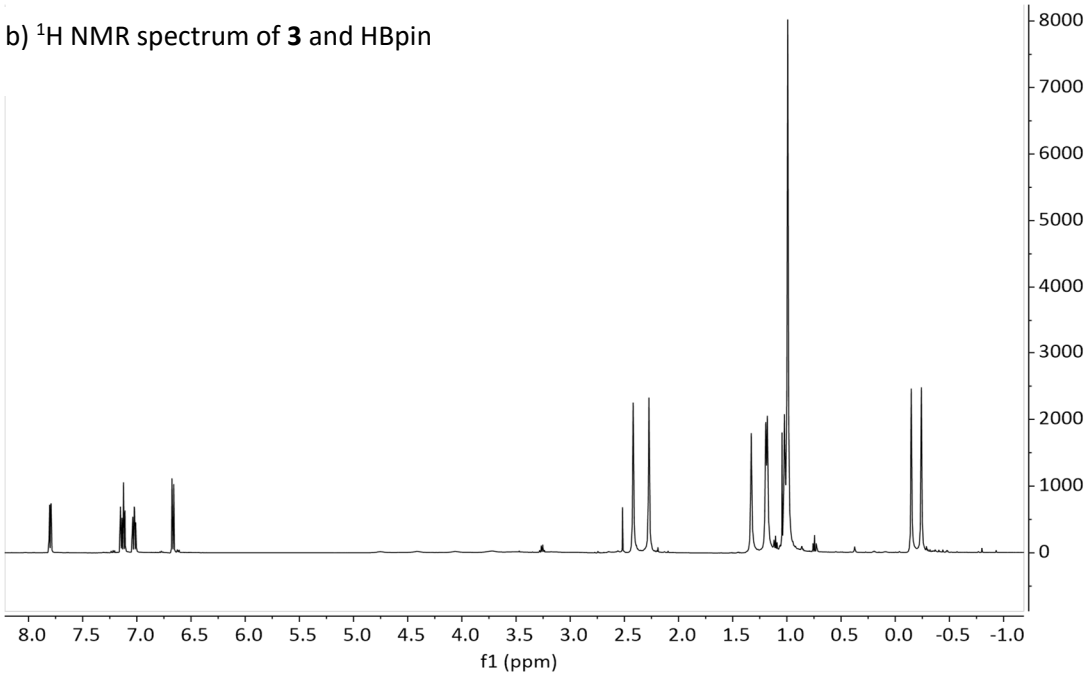

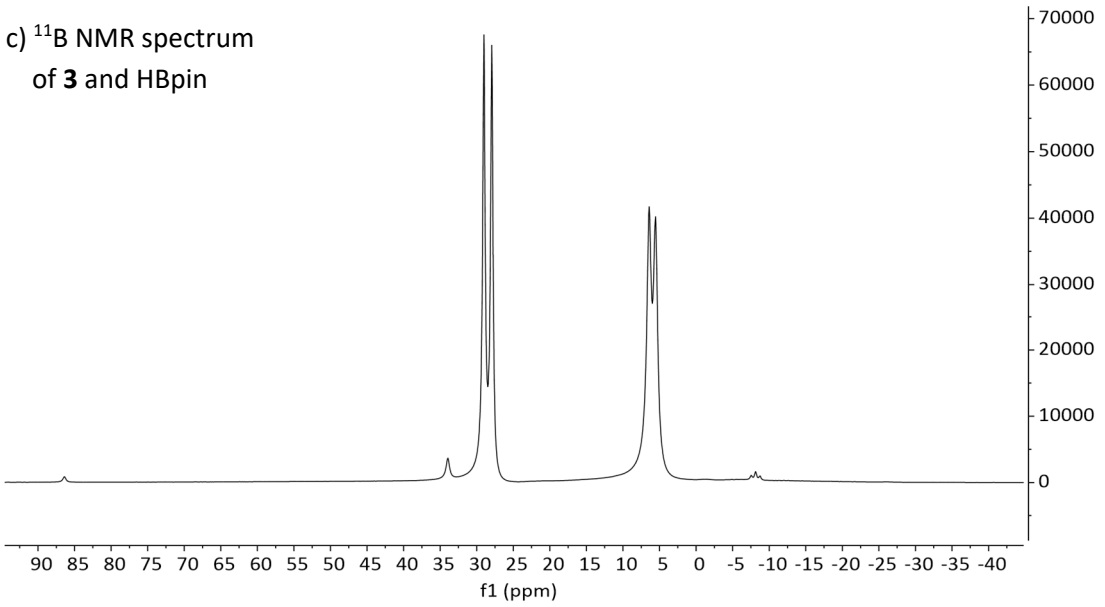

Figure 20 – a) ^{1}H NMR spectrum of 3 and b) ^{1}H and c) ^{11}B NMR spectra 3 + HBpin at room temperature.

The fact that multiple environments are observed for the adduct means that the adduct has desymmetrised both the FLP and the HBpin. This indicates there is no rotation about the N–B bond. In order for this to be the case another interaction must be holding the bond in place. This means that the adduct likely has a form like that of B, rather than that of A which would initially be expected (Figure 21).

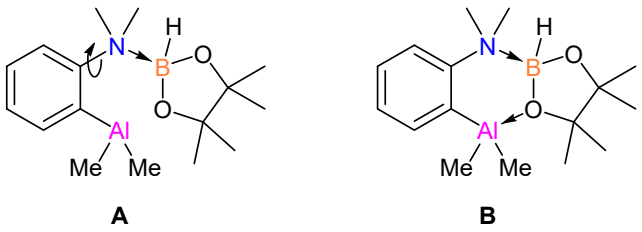

Figure 21 – Possible adduct forms A and B for the adduct between 3 and HBpin.

Upon heating the sample to 70 °C for 16 hours, the solution again remained colourless. However, ^{11}B NMR spectroscopy revealed that MeBpin was generated as expected at 34.0 ppm along with other boron-containing minor products, including what are likely to be borohydrides in the –28 to –38 ppm range, and boron-nitrogen adduct species in the 12 to –18 ppm range with varying substitution on the boron and nitrogen species (Figure 22 c).[3,4] ^{1}H NMR spectroscopy showed a large number of signals which were

difficult to assign, but complete consumption of the Al–Me peaks of **3** was observed (Figure 22 a+b). While these NMR spectra do not clearly inform the identity of the formed aluminium species, this was not unanticipated, as previous work in the group has shown similarly unselective reactivity for this type of exchange for both $AlMe_3$ and $AlEt_3$ reacting with HBpin.[2]

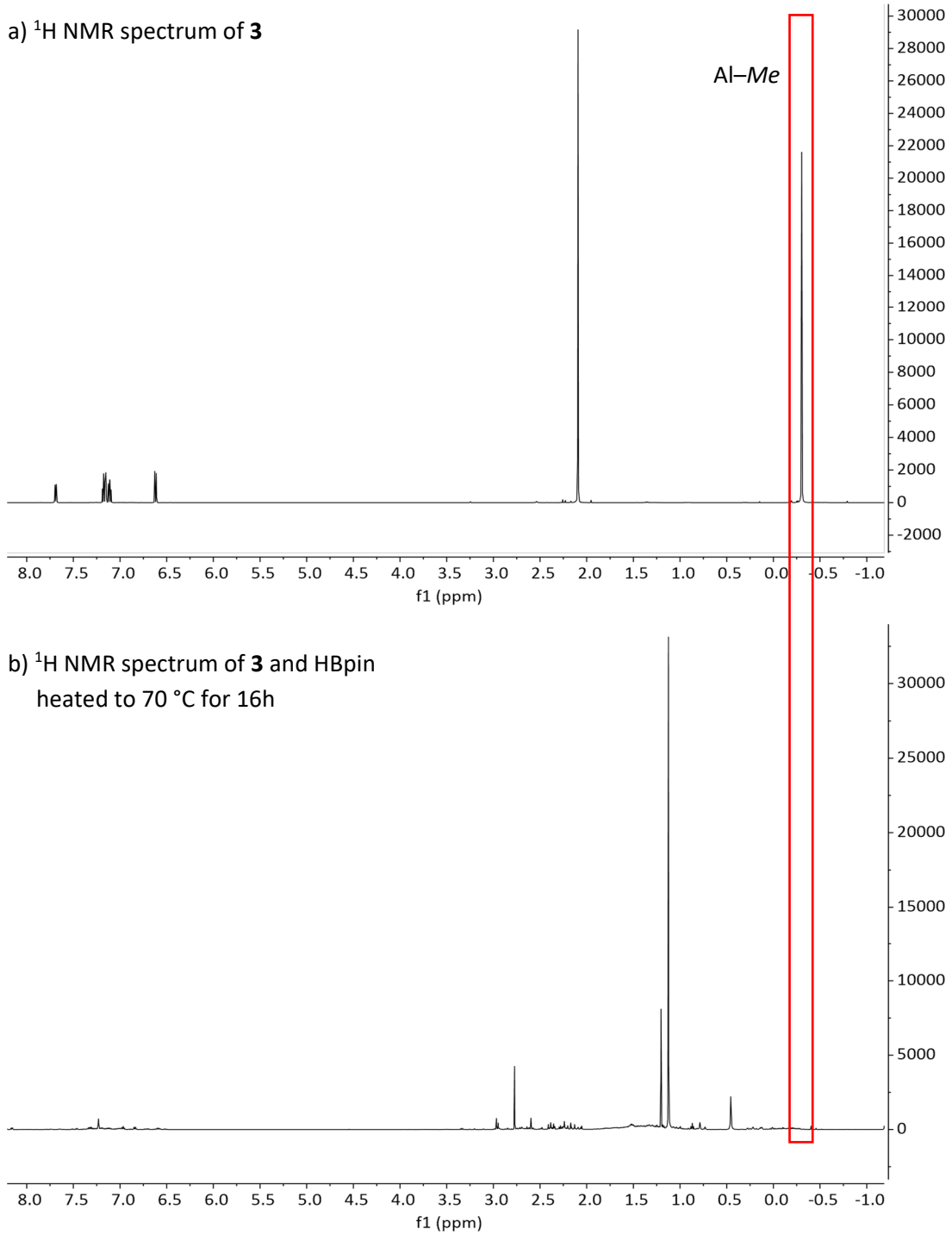

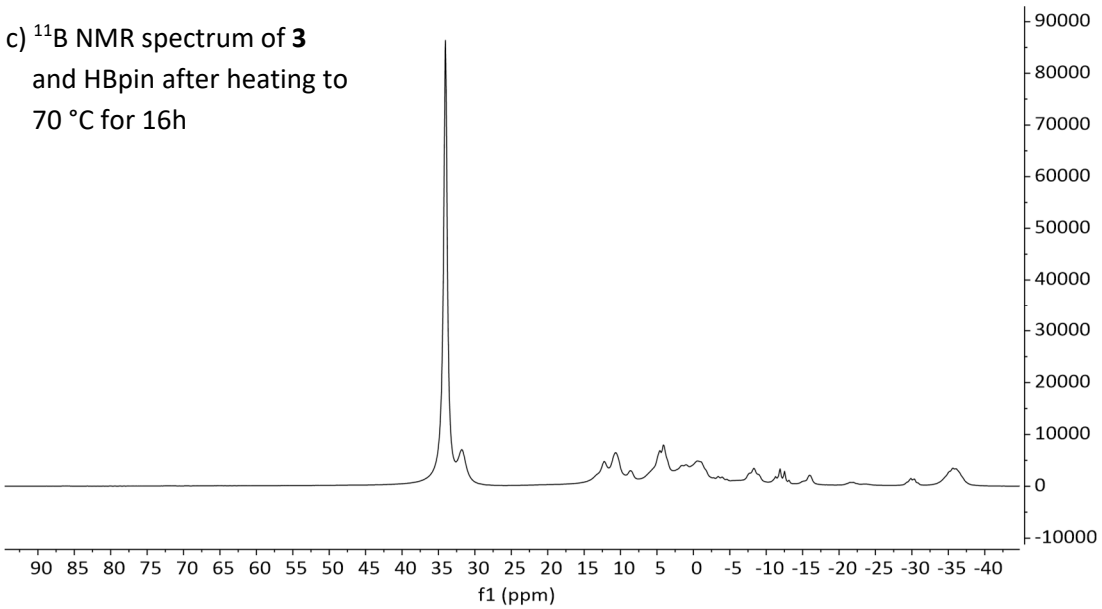

Figure 22 – a) ^{1}H NMR spectrum of 3 and b) ^{1}H and c) ^{11}B NMR spectra 3 + HBpin after heating to 70 °C for 16h.

From this evidence we concluded that a mixture of aluminium hydride species had formed. While not as clean a reaction as initially anticipated, we decided to attempt C–H borylation catalysis reactions using **3** and **4** as precatalysts.

3.3 Catalytic conditions and substrate scope for aromatic compounds

In order to get a sense of the relative reactivity of the FLP precatalysts **3** and **4**, *N*-methylpyrrole was chosen as a trial substrate, based on the scope from Fontaine's work with the analogous boron based FLP.[1] *N*-methylpyrrole was shown to have a fast reaction time with Fontaine's catalyst and additionally had a mixture of borylation at the 2 and 3 positions. Therefore *N*-methylpyrrole would give good information on both the relative speed and selectivity of **3** and **4**.

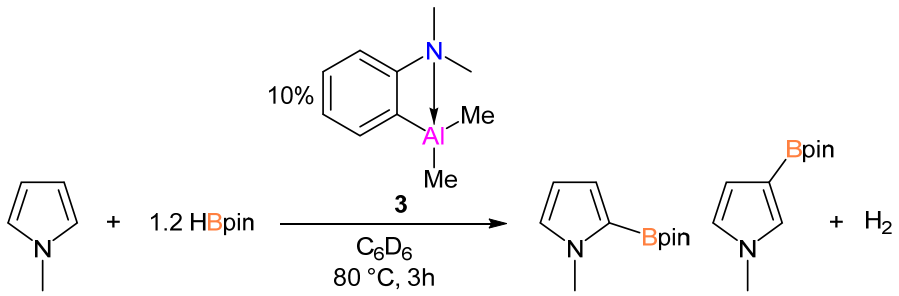

Scheme 42 – Trial catalytic reaction conditions.

The initial trial catalytic reaction was done on NMR scale (Scheme 42). A 10% loading of precatalyst **3** was added to the NMR tube and dissolved in C_6D_6. 1.2 equivalents of HBpin relative to the substrate were added to allow for the catalyst generation step consuming 0.2 equivalents of HBpin. *N*-methylpyrrole was then added resulting in a colour change from colourless to pale yellow but no observable reaction had occurred by NMR spectroscopy. Upon heating to 80 °C for 3 hours the yellow colour intensified. ^{1}H NMR spectroscopy showed 66% conversion of the *N*-methylpyrrole to the borylated products with a ratio of 86:14 for the 2 and 3 positions.

Following this the analogous reaction was attempted with **4**. In this the case the reaction was extremely slow and even after heating for 5 days at 80 °C, only 43% conversion was observed. In this case the ratio of borylation at the 2 and 3 positions was 88:12. This result showed that the reactivity of the FLP is highly sensitive to the sterics of the nitrogen centre, as expected. In this case the increased steric bulk of the TMP has improved the selectivity of the reaction, but also hinders the speed of reactivity to a prohibitive extent, making **4** a much less effective pre-catalyst than **3**.

This is an interesting result, as Fontaine and co-workers have also compared rates of reaction of related boron-based FLPs with varying nitrogen substitution, including both dimethylamino- and TMP-substituted boron FLPs.[5] They found that in general increased steric bulk increased the size of the barrier to C–H borylation. However, decreased steric bulk also has the effect of stabilising an inactive dimeric form of the FLP. This leads to a sweet spot in the size of the nitrogen group, where the dimeric form is the most destabilised while not raising the barrier height of the C–H borylation prohibitively.

As such the rate of reaction increases when moving from dimethylamino-substituted FLP **A** through to piperidyl-substituted FLP **C**, but then decreases again for the TMP-substituted FLP **D** (Figure 23). In this case the TMP-substituted FLP **D** has a faster rate of reaction than the dimethylamino-substituted FLP **A**, which is the opposite of the result for **3** and **4**, where the TMP-substituted FLP **4** has a much slower rate of reaction than the dimethylamino-substituted FLP **3**. This indicates that the active catalysts

generated from **3** and **4** may have forms different to the dimeric forms of the boron based FLP catalysts **A**-**D**. This is investigated in detail in chapter 4 (*vide infra*).

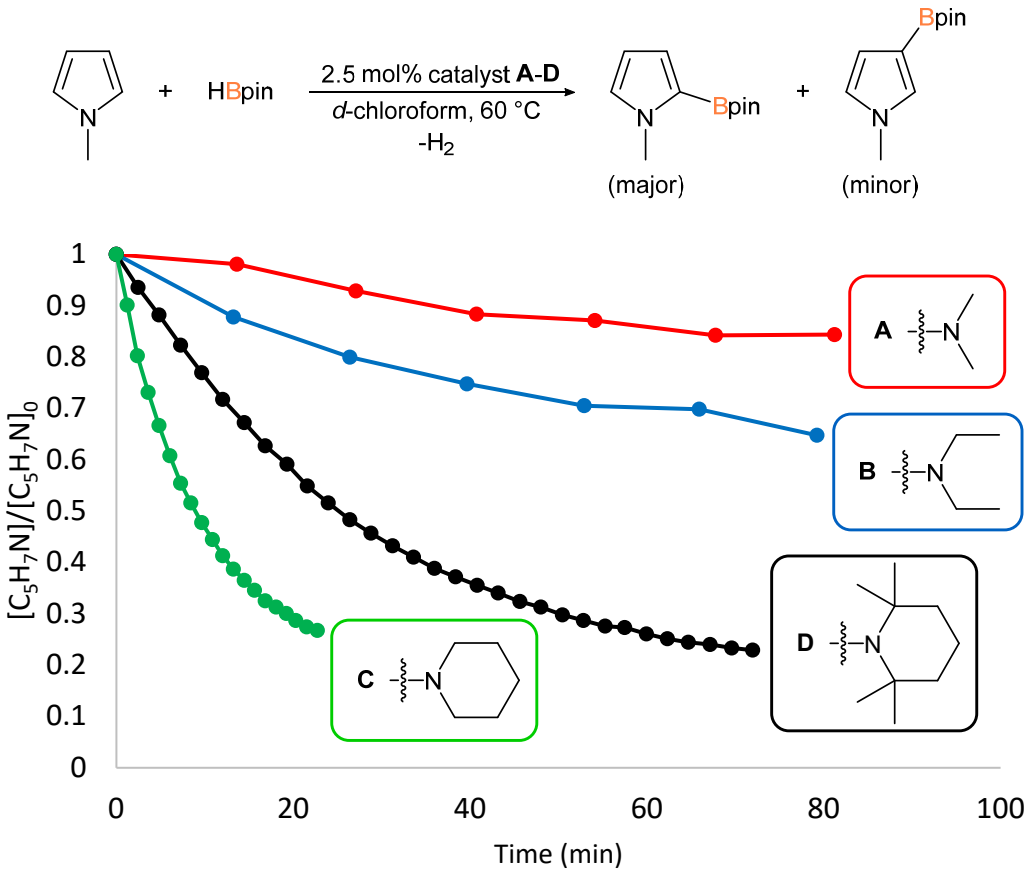

Figure 23 – Rates of C–H borylation of N-methyl pyrrole by FLPs A-D adapted from Lavergne *et al.*[5]

While our initial reactivity had been carried out in C_6D_6, we decided to also attempt the reactivity in d-chloroform, as this was the solvent used by Fontaine.[1] Repeating the reactivity of **3** in d-chloroform and after heating for 1 hour at 80 °C gave a conversion of 40% with a 2 and 3 position selectivity of 88:12. Heating for a further 15 hours gave a final conversion of 82% with 90:10 selectivity for 2 and 3 position borylation.

With this information in hand, we decided to focus our efforts on **3** as a precatalyst and attempt to assess the scope of reactivity with various substrates in $CDCl_3$. Firstly, a small scope of other common heteroaromatic molecules was carried out (Scheme 43).

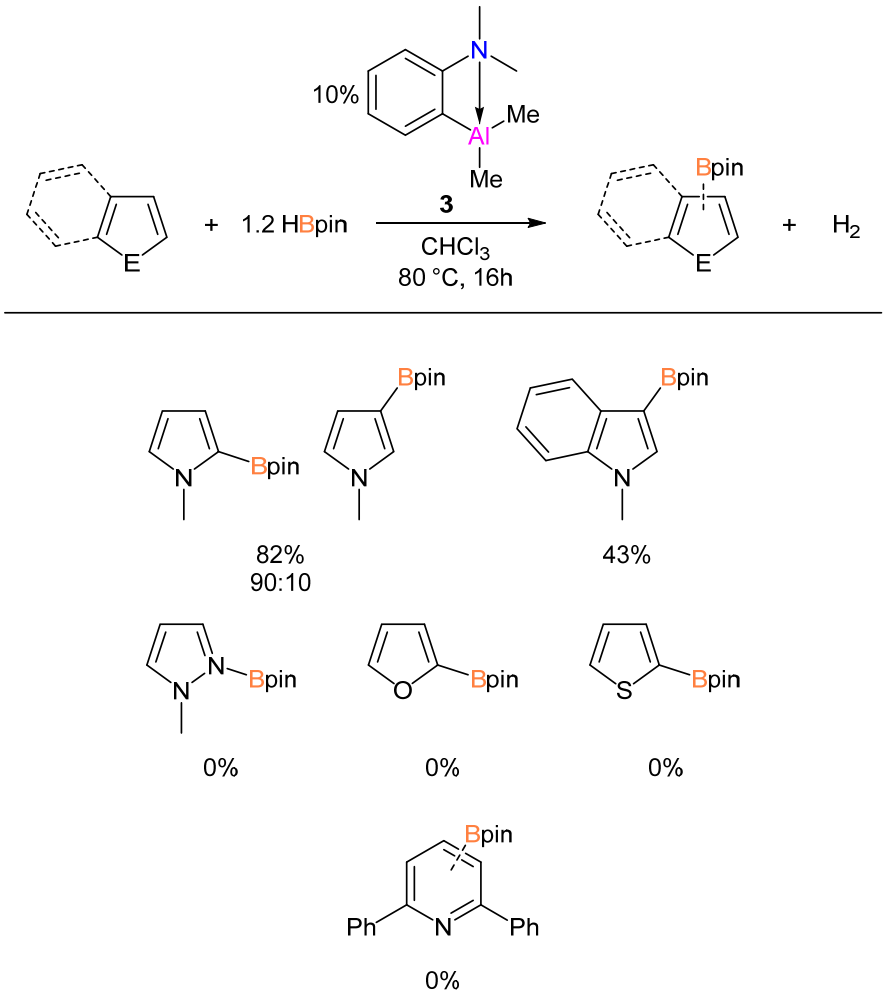

Scheme 43 – Investigation of scope of reactivity with heteroaromatic compounds. Conversion determined by NMR spectroscopy by integration of the pinacol backbone methyl groups of the product versus the remaining HBpin backbone methyl peaks.

Unfortunately, the scope proved extremely limited, with only *N*-methylpyrrole and *N*-methylindole reacting to give the borylated products. *N*-methylpyrrole gave a mixture of 2 and 3 borylated products while *N*-methylindole only gave the 3 borylated product. For the other common heteroaromatic frameworks (pyrazole, furan, thiophene, pyridine), no reactivity was observed.

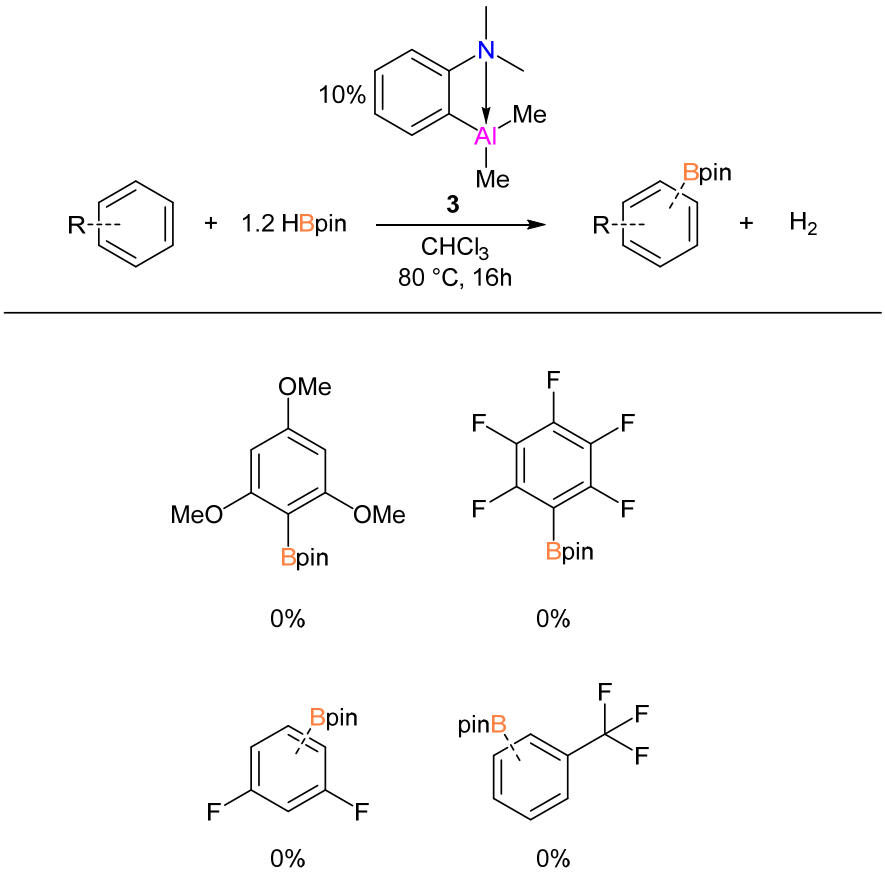

Scheme 44 – Investigation of scope of reactivity with arenes.

As the initial goal of this research was to increase the substrate scope relative to Fontiane's originally reporsted FLP,[1] a range of activated arenes were also trialled as shown (Scheme 44). Unfortunately, no reaction was seen with any of these substrates, even with highly activated arenes such as 1,3,5-trimethoxybenzene.

This is unsurprising, as the reactivity with the heteroaromatic substrates was limited and these carbon-based arene substrates are less nucleophilic than the heteroaromatic substrates, even when using these highly activated substrates with multiple electron withdrawing groups.

3.4 Catalytic conditions and substrate scope for terminal alkynes

While the C–H borylation of heteroaromatics and arenes with **3** and **4** was not as successful as we had hoped, we were keen to test the reactivity of **3** and **4** with other classes of substrate.

Previous work in the group had shown the ability of aluminium hydrides to be used for the hydroboration of alkynes and alkenes,[2] so we decided to investigate how **3** would react with alkynes, with hope that the relatively high acidity of the alkyne C–H bond would lead to some interesting reactivity.

We again started with trials conducted in C_6D_6 as our standard NMR solvent. Phenylacetylene was chosen for the first test reaction as an easy to handle readily available alkyne substrate.

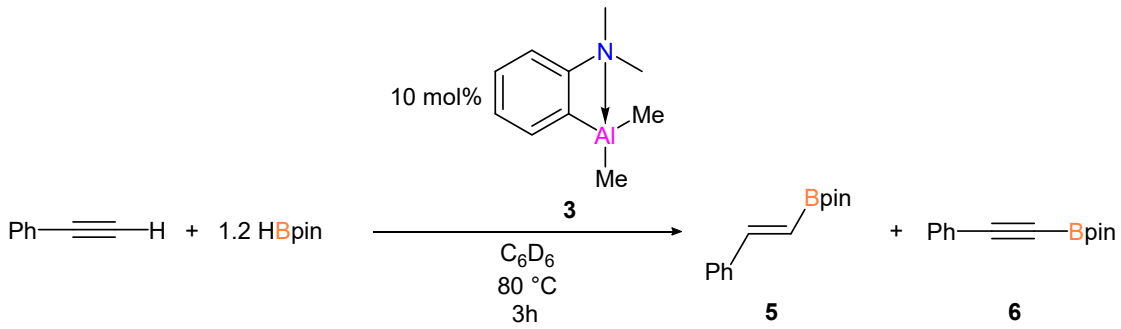

Scheme 45 – Trial conditions for the borylation of alkynes.

A 10% loading of precatalyst **3** was added to the NMR tube and dissolved in C_6D_6. 1.2 equivalents of HBpin relative to the substrate were added to allow for the catalyst generation step consuming 0.2 equivalents of HBpin. Phenylacetylene was then added resulting in a colour change from colourless to pale yellow. In a similar manner to the heteroaromatic reactions, no visible reaction with the substrate was seen at this point by NMR spectroscopy. Upon heating to 80 °C for 16 hours the yellow colour intensified. The ^{11}B NMR spectrum at this point clearly showed the generation of two different new boron-containing species with significantly different shifts, one at 30.5 ppm and one at 24.8 ppm. A search of the literature revealed that these corresponded to the expected hydroboration product **5** and also the terminal C–H borylation product **6** respectively.[6] After further heating the reaction reached an endpoint after 4 days, with a conversion by NMR spectroscopy of 76% by integration of the pinacol backbone methyl groups of the product versus the remaining HBpin backbone methyl peaks. The ratio of products **5** (hydroboration) and **6** (terminal) was 57:43. To our knowledge this represents the first example of an aluminium catalysed C–H borylation of an alkyne. The catalytic C–H

borylation of alkynes is relatively unknown, with only a few examples available in literature, with the first reported in 2013.[6]

This reactivity was very promising and we wanted to investigate it in further detail with a particular focus on promoting full selectivity towards the terminal borylation product. Firstly, we carried out the reaction at 3 different temperatures to see how this would affect the conversion and selectivity (Table 1).

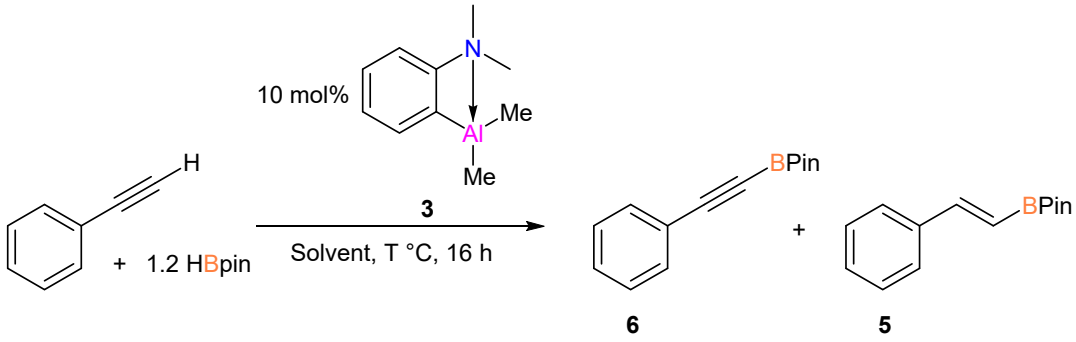

Entry	Solvent	T / °C	Time / h	**6** / %	**5** / %	**6**+**5** / %
1	C_6D_6	25	16	trace	trace	trace
2	C_6D_6	60	16	14	4	18
3	C_6D_6	80	16	23	16	39

Table 1 – Temperature screen. Conversion determined by NMR spectroscopy by integration of the pinacol backbone methyl groups of the product versus the remaining HBpin backbone methyl peaks.

At room temperature the reaction proceeded extremely slowly and only a trace amount of product was observed. When comparing the results at 60 °C and 80 °C it is clear that increased temperature greatly increases the conversion, but also lowers the selectivity, with a greater proportion of the unwanted hydroboration product formed at higher temperature.

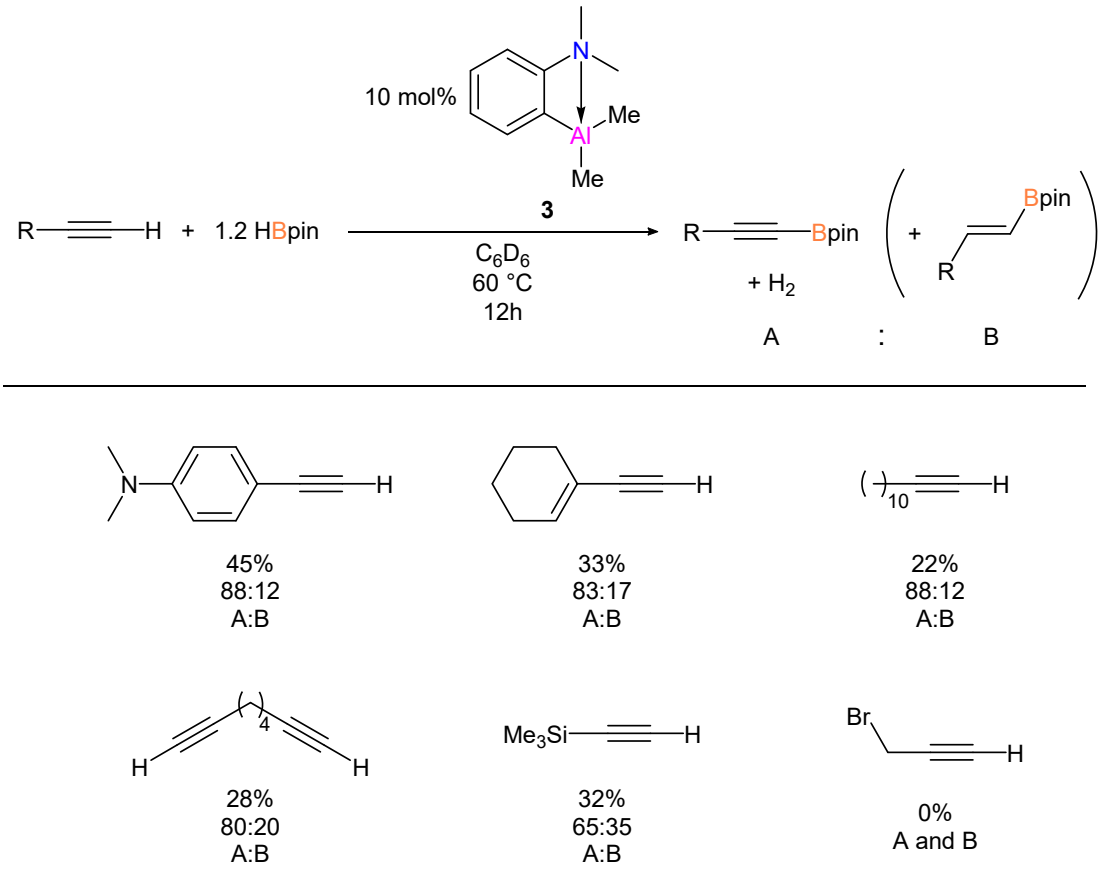

Scheme 46 – Preliminary scope of C–H borylation of alkynes with 3.

A small scoping study was then carried out (Scheme 46), to show that the reactivity was not isolated to a single or small number of examples as in the case of the heteroaromatic substrates (*vide supra*). 60 °C was chosen as the reaction temperature for the improved selectivity. This revealed that the reaction proceeded on alkyl and aryl alkynes, and tolerated other functionality such as amines, internal alkenes, and siloxy groups. In all cases selectivity was towards the terminal borylation product. However, conversions in all reactions remained low under these conditions.

Having proved the generality of the reaction, a collaborating PhD student Dominic Willcox performed further optimisation of the conditions and subsequently performed a substrate scope of the reaction. The full details of the optimisation and screening will not be discussed in this thesis. However, the relevant results from the final optimised conditions will be presented to give context to the following chapters.

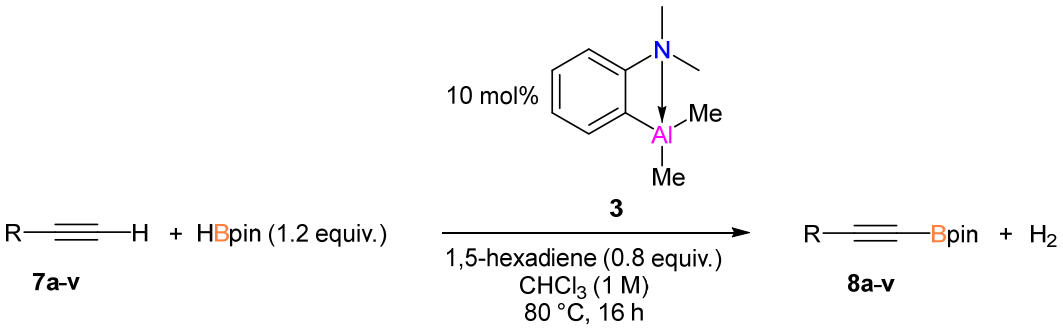

Scheme 47 – Optimised conditions for the terminal C–H borylation of alkynes using 3 as a precatalyst.

The optimised conditions are presented above with the scope including a range of alkyl and aryl substituted terminal alkynes (Scheme 47). The most notable difference in the conditions is the inclusion of an additive to the reaction, in the form of 1,5-hexadiene. It was found that this addition eliminated the formation of the unwanted hydroboration product in the reaction. This was interesting as the initial hypothesis for the source of the hydroboration product was two competing mechanisms for the catalyst (Scheme 48). These two postulated mechanisms are examined computationally in chapter 4 (*vide infra*).

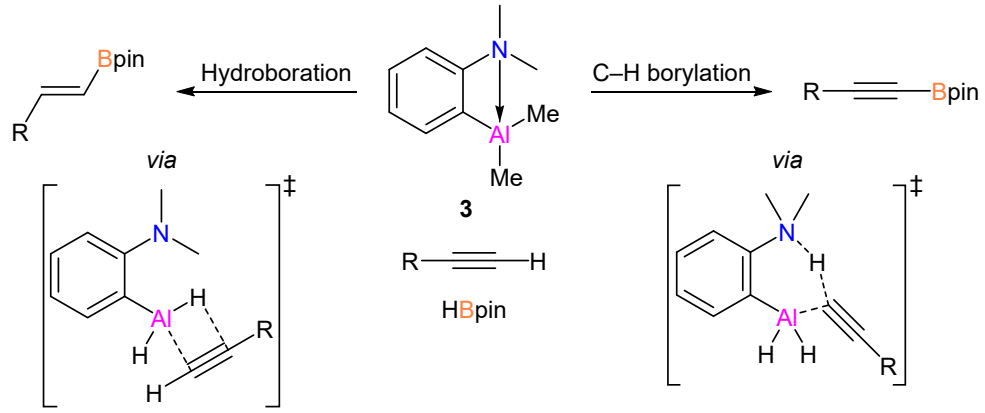

Scheme 48 – Competing reaction pathways for reaction of 3 with alkynes and HBpin.

However, previous work in the group has shown that HBpin can be degraded to BH_3 under these types of reaction conditions,[7] and that BH_3 is capable of catalysing the hydroboration of alkynes.[8] This is another possible source of the unwanted hydroboration product. The general mechanism for this degradation is by reaction of several equivalents of HBpin with a nucleophile (Scheme 49).

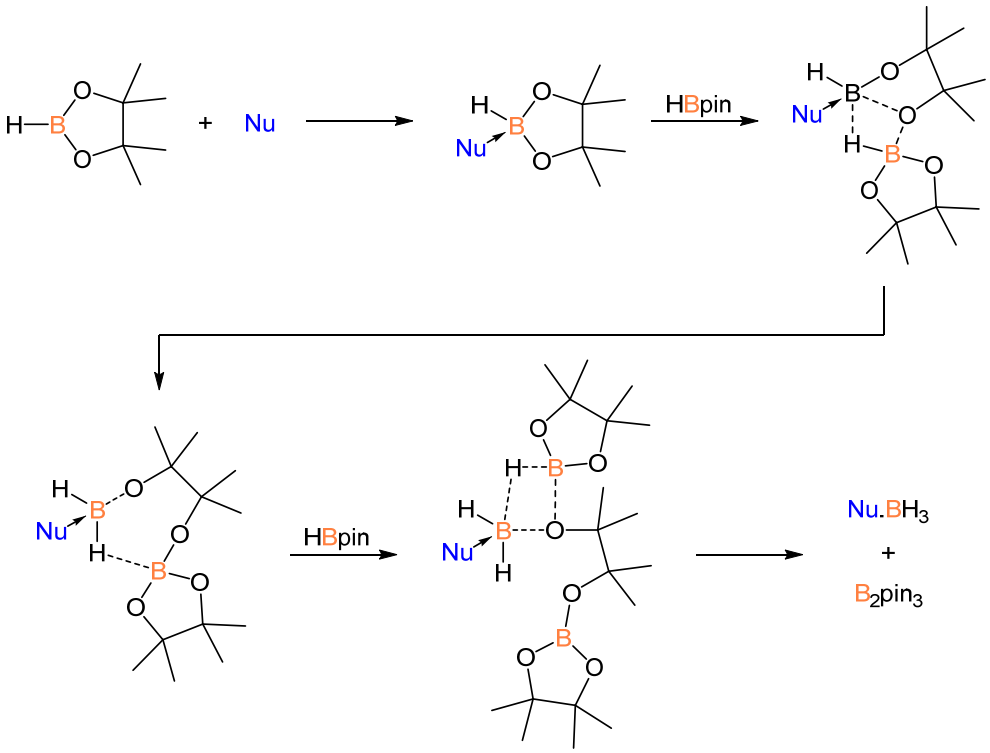

Scheme 49 – General mechanism for the degradation of HBpin to BH_3 and B_2pin_3 by a nucleophile, adapted from Calabrese *et al.*[9]

In the reactivity displayed in the reaction with **3** as the precatalyst, the degradation is likely a result of coordination of the nitrogen donor of the ligand on the catalyst to the HBpin facilitating this degradation process.

Addition of the 1,5-hexadiene does not stop this degradation occurring. However, it is postulated that reaction of the BH_3 with the 1,5-hexadiene occurs in preference to the alkyne, taking it out of solution and therfore preventing formation of the hydroboration product. This is supported by the fact that for 1,5-hexadiene it has been shown by Brown and co-workers that reaction with BH_3 lead to formation of an insoluble oligomeric species.[10]

When comparing the reactivity of this system with the FLP **3** as the precatalyst to the previously reported catalytic systems for the synthesis of alkynyl–Bpin compounds there are both benefits and drawbacks to the system. The earth abundance of the aluminium basis of **3** is a significant advantage over other systems, especially those based on iridium,[6,11] and silver,[12] which are of very low crustal abundance.

Additionally, catalysis with **3** has a wide substrate scope, capable of borylating most classes of substrate that the other examples can. The only classes of substrate notably missing from the scope of catalysis with **3** are substrates with alcohol or nitrile functionality, which can be achieved with the silver NHC catalyst reported by Hu *et al.*,[12] and the copper triflate catalyst reported by Romero *et al.* respectively.[13] However, the reaction conditions for catalysis with **3** are not the most ideal, with conditions of 80 °C and a long reaction time of 16 hours required to achieve the moderate yields of around 40-80%. In contrast, the best performing is the iridium catalyst which achieves almost complete conversion to the target borylated alkynes in 10 mins at room temperature,[6] and so is likely a much more attractive catalyst despite the rarity and cost of the iridium metal used.

3.5 Conclusions

In conclusion, it has been shown that **3** is a precatalyst for the C–H borylation of both heteroaromatic molecules and terminal alkynes. In the first case, the scope is poor, with only a select few examples reacting to give the borylated products. In contrast, the C–H borylation of terminal alkynes proceeds with good scope on both aryl and alkyl substituted terminal alkynes and is the first example of aluminium performing this kind of chemistry. It has also been shown that **4** is remarkably slower in catalysis than **3**. This is presumably a result of the steric effect that the TMP group imposes upon the system, which likely raises the energy of the transition states in the mechanism as was shown for related boron-based FLPs by Fontaine and co-workers.[5]

3.6 References

[1] M.-A. Légaré, M.-A. Courtemanche, É. Rochette, F.-G. Fontaine, *Science* **2015**, *349*, 513–516.
[2] A. Bismuto, S. P. Thomas, M. J. Cowley, *Angew. Chem. Int. Ed.* **2016**, *55*, 15356–15359.
[3] S. Hermanek, *Chem. Rev.* **1992**, *92*, 325–362.
[4] G. R. Eaton, *J. Chem. Educ.* **1969**, *46*, 547.
[5] J. Légaré Lavergne, A. Jayaraman, L. C. Misal Castro, É. Rochette, F.-G. Fontaine, *J. Am. Chem. Soc.* **2017**, *139*, 14714–14723.
[6] C.-I. Lee, J. Zhou, O. V. Ozerov, *J. Am. Chem. Soc.* **2013**, *135*, 3560–3566.
[7] A. D. Bage, T. A. Hunt, S. P. Thomas, *Org. Lett.* **2020**, *22*, 4107–4112.
[8] N. W. J. Ang, C. S. Buettner, S. Docherty, A. Bismuto, J. R. Carney, J. H. Docherty, M. J. Cowley, S. P. Thomas, *Synthesis* **2018**, *50*, 803–808.
[9] S. A. Westcott, H. P. Blom, T. B. Marder, R. T. Baker, J. C. Calabrese, *Inorg. Chem.* **1993**, *32*, 2175–2182.
[10] P. L. Burke, Eiichi. Negishi, H. C. Brown, *J. Am. Chem. Soc.* **1973**, *95*, 3654–3662.
[11] C. J. Pell, O. V. Ozerov, *Inorg. Chem. Front.* **2015**, *2*, 720–724.
[12] J.-R. Hu, L.-H. Liu, X. Hu, H.-D. Ye, *Tetrahedron* **2014**, *70*, 5815–5819.
[13] E. A. Romero, R. Jazzar, G. Bertrand, *Chem. Sci.* **2016**, *8*, 165–168.

4 Computational investigation of aluminium FLP alkyne borylation mechanisms

Details of functionals and basis sets used can be found in chapter 6.4.6 (vide infra).

The experimental work in section 4.6 was carried out by PhD student Abigail Levy and Mchem student Jack Howley. I then carried out computational analysis based on these experimental results.

4.1 Introduction and aims

In chapter 3, **1** was shown to be an effective precatalyst for the terminal C–H borylation of alkynes (Scheme 50).

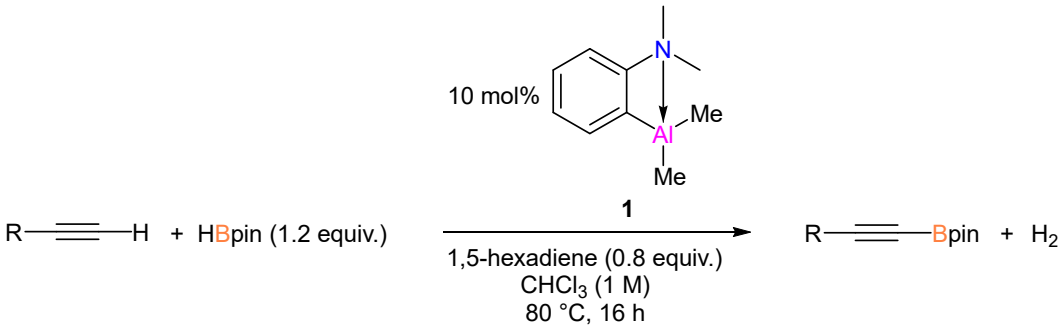

Scheme 50 – Optimised conditions for the catalytic terminal C–H borylation of alkynes using 1 as a precatalyst.

C–H borylation is previously unknown reactivity for alanes and is in contrast to the usual reactivity observed for aluminium hydrides with alkynes and HBpin, which is to effect hydroboration of the triple bond.[1–4] As such, investigation of the mechanism of the reaction is important to understand what causes this different selectivity.

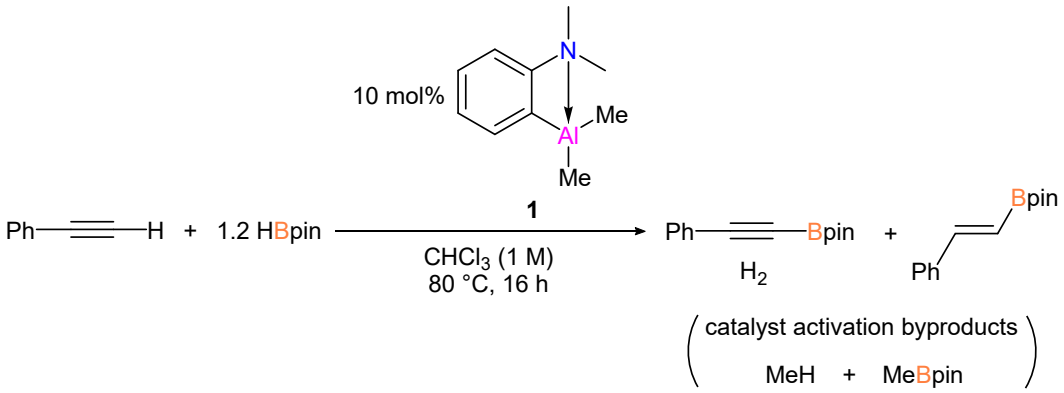

Scheme 51 – Catalytic terminal C–H borylation of alkynes using 1 as a precatalyst in the absence of 1,5-hexadiene.

When looking at the catalytic reactions in the absence of the 1,5-hexadiene additive (Scheme 51), there are several features to the reactivity that require investigation. Firstly, the origin of the reaction selectivity. Under the optimised conditions (Scheme 50), only the terminal C–H borylation product is observed, while during the initial discovery of the reactivity in the absence of 1,5-hexadiene, both terminal C–H borylation and hydroboration products were observed.

It was proposed that the catalyst was not responsible for the hydroboration product, but rather BH_3 that was formed *in situ* under the reaction conditions was performing the hydroboration,[5] and that addition of the 1,5-hexadiene stopped formation of the hydroboration product by reacting preferentially with the BH_3, preventing it from hydroborating the alkyne. In order to confirm the hypothesis that none of the observed hydroboration product comes from the catalyst, investigation of the mechanisms of both C–H borylation and hydroboration of the alkyne by the catalyst were carried out to see whether or not the catalyst is capable of performing the hydroboration.

Computational mapping of reaction pathways is a powerful tool and great insight into mechanisms can be gained from this technique. This was the method chosen to investigate the terminal C–H borylation of the alkyne and the hydroboration of the alkyne.

In the work by Fontaine and co-workers which was the inspiration for this work,[6] the authors carried out computational analysis of the mechanism of the C–H borylation of

their heteroaromatic substrates using *N*-methylpyrrole as an example substrate and arrived at the following cycle (Scheme 52).

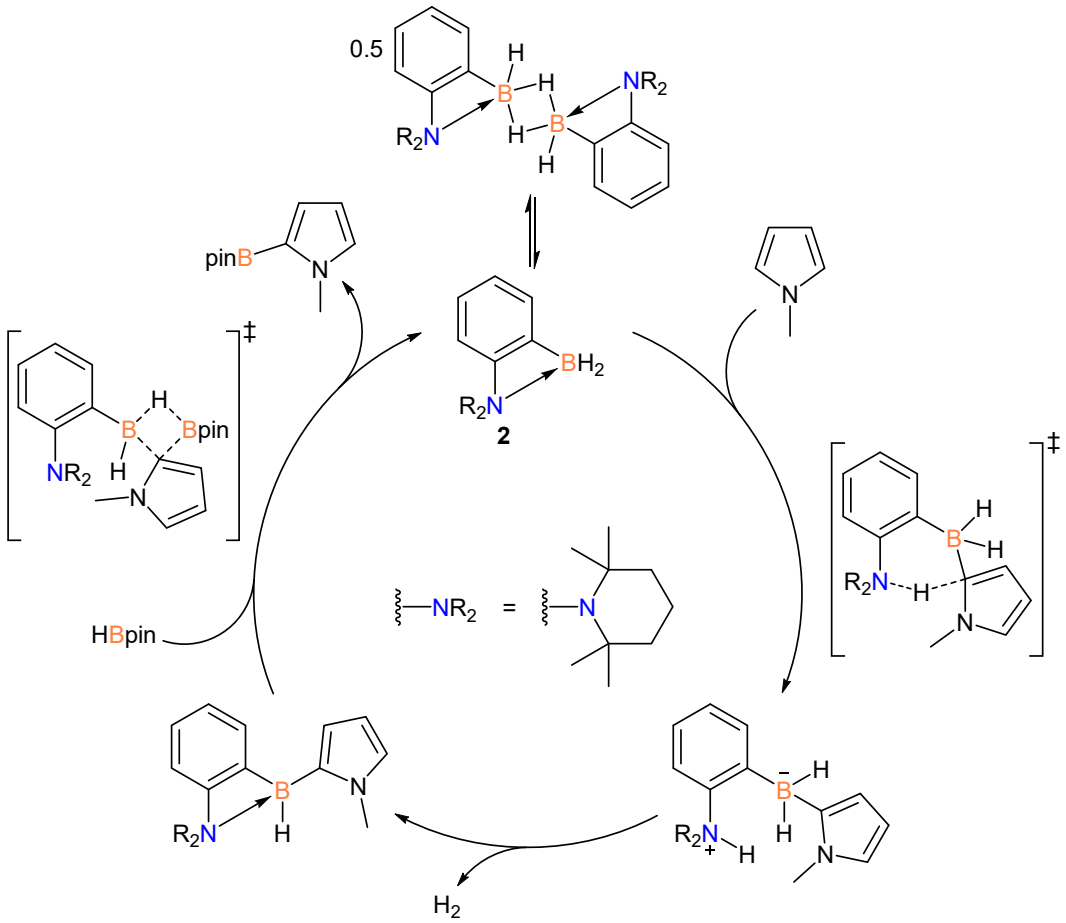

Scheme 52 – C–H borylation of *N*-methylpyrrole using 2 (shown for borylation in the 2 position), adapted from Légaré *et al.*[6]

The cycle starts with dissociation of a dimer of the catalyst into the monomeric species **2**. C–H activation of the *N*-methylpyrrole then occurs to give a zwitterionic FLP activation product. Loss of hydrogen gas then occurs to generate the *N*-methylpyrrole substituted FLP and finally transborylation occurs, regenerating the catalyst **2** and forming the borylated pyrrole. We took this cycle as a starting point for analysis of the steps in the terminal borylation mechanism of alkynes by replicating the steps shown. For the competing hydroboration mechanism we devised the following set of reaction steps as a starting point for calculation. This is based on previous hydroalumination work in the group,[4] and other examples of hydroalumination in the literature.[1–3] This gave the two cycles below as starting points for computational analysis (Scheme 53).

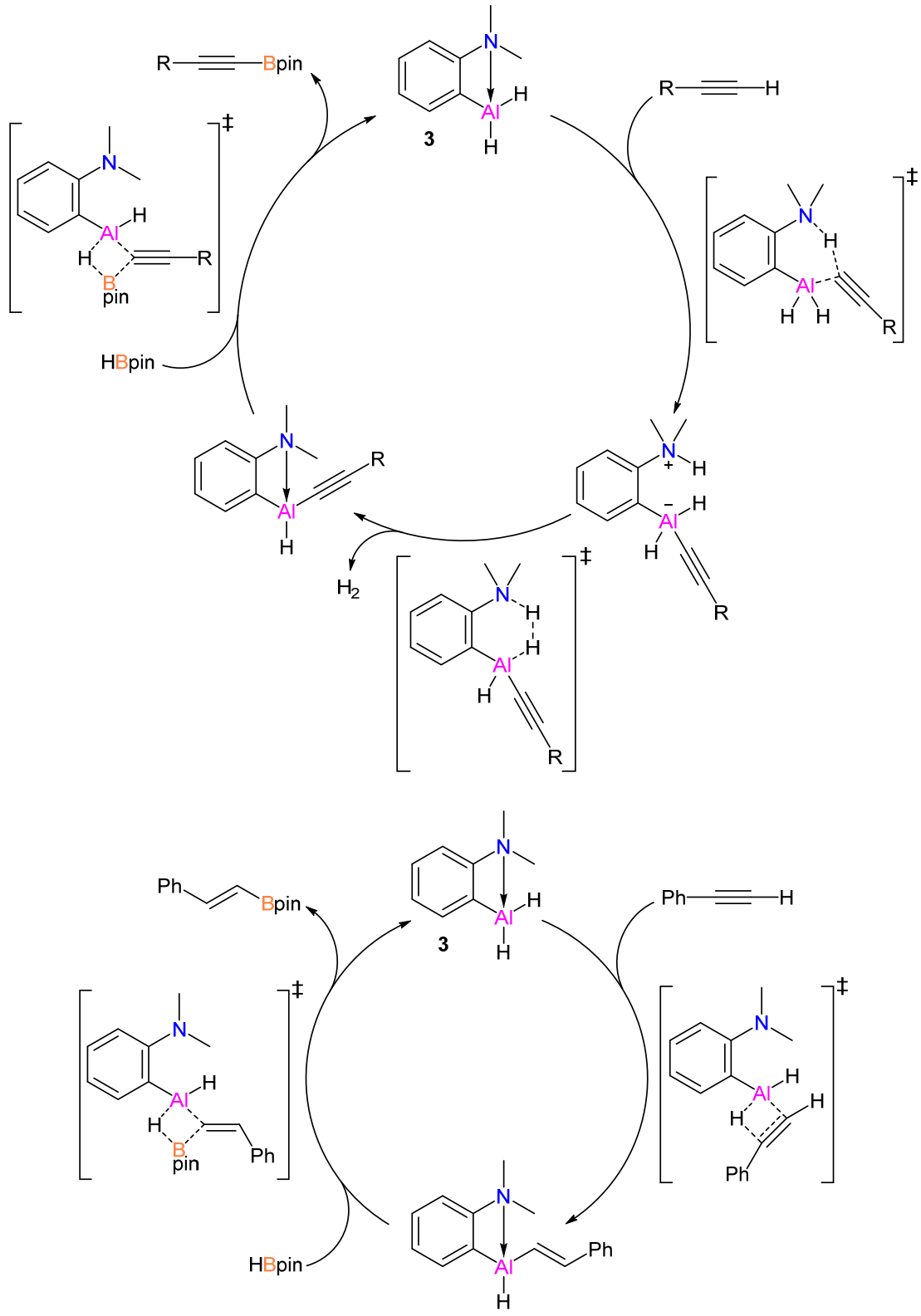

Scheme 53 – Initially proposed mechanisms for the C–H borylation and hydroboration of alkynes by 3.

The cycle for the C–H terminal borylation of alkynes follows the same steps as Fontaine's C–H borylation of heterocycles. The hydroboration starts with hydroalumination of the alkyne triple bond by **3** which is then followed by transmetallation of the HBpin with the vinyl aluminium species to generate the product and regenerate **3**.

The other feature of the reaction that requires investigation is the observation of both methane and MeBpin in the reaction mixture (Scheme 51). The initial proposal for catalyst activation involved the reaction of **1** with HBpin to form MeBpin and the catalytically active aluminium dihydride species **3** (Scheme 54).

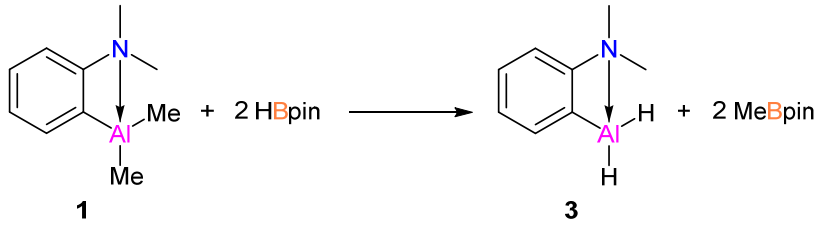

1 **3**

Scheme 54 – Proposed generation of 3 from 1 and HBpin.

The formation of methane as well as MeBpin indicates that more than one mechanism of catalyst activation may be occurring. We investigated these mechanisms through stoichiometric experimental reactions and computational modelling based on the results of these stoichiometric experiments.

4.2 Terminal borylation mechanism

The first pathway optimised was the one of greatest interest, the terminal C–H borylation of alkynes. Based on the mechanism of C–H borylation of heteroarenes reported by Fontaine and co-workers (Scheme 52),[6] a mechanism utilising analogous reaction steps was proposed (Scheme 55). This proposed mechanism was additionally supported by the experimental observation of hydrogen in the ^{1}H NMR spectra of the reaction mixtures.

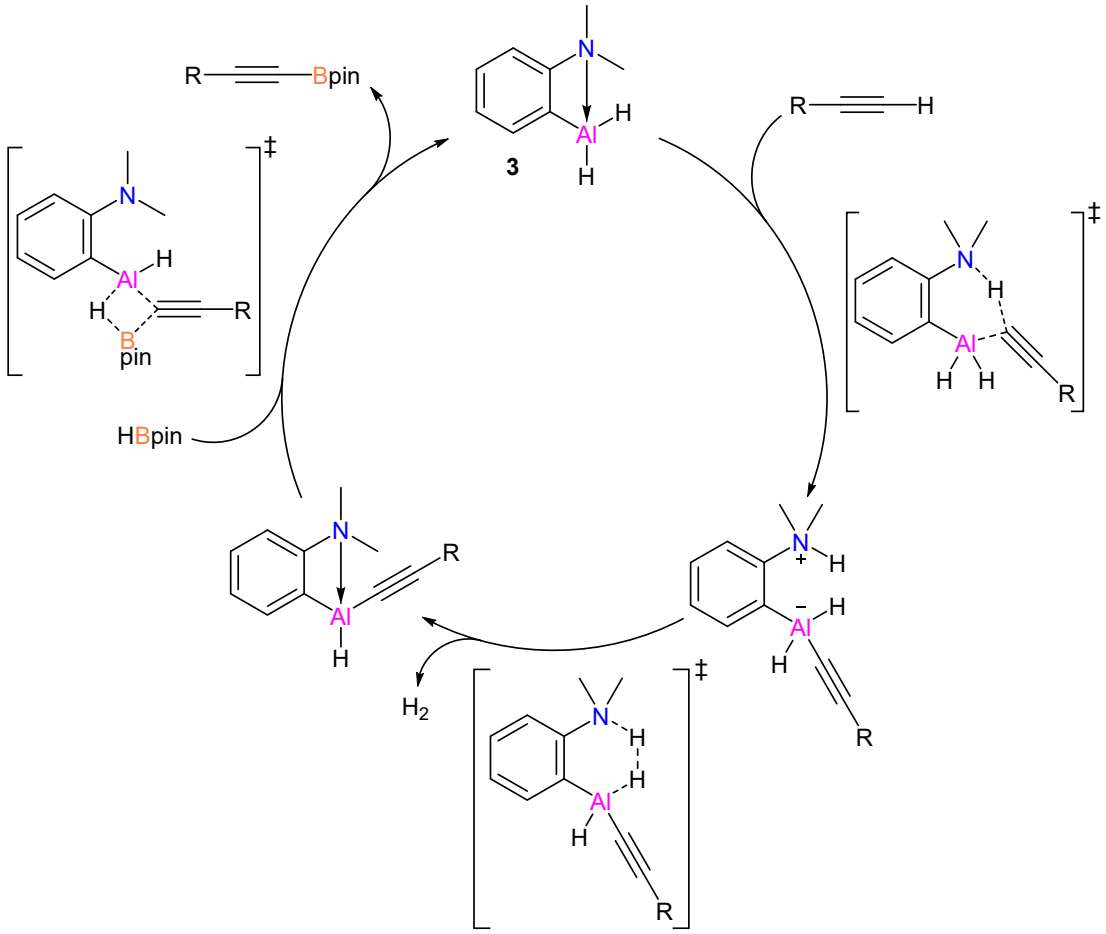

Scheme 55 – Initially proposed mechanism for the terminal C–H borylation of alkynes by 3.

All the structures along this proposed pathway were optimised in order to verify the energetic viability of this route to the product borylated alkynes. For the purposes of the calculations phenyl acetylene was used as the alkyne as a model substrate as aromatic alkynes are the most common substrate in the scope of reactivity. This produced the energy profile seen below (Figure 24).

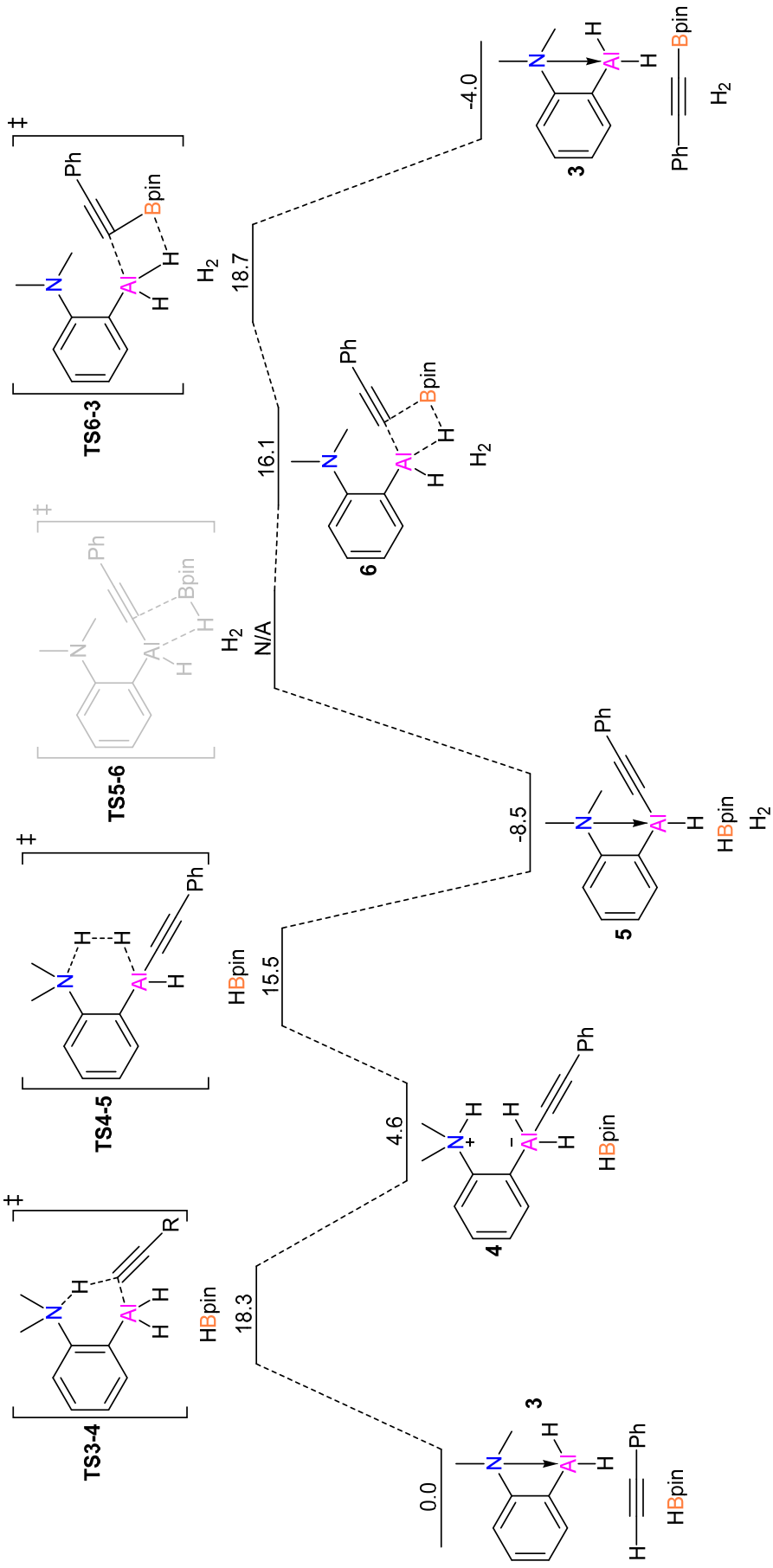

Figure 4 – Computed reaction profile for terminal C–H borylation of phenyl acetylene by 3 with HBpin. All energies given in kcal mol^{-1} relative to the starting materials. TS5-6 could not be optimised. Calculations carried out at the wb97xd/6-311++g(d,p) level of theory with SMD solvation (chloroform).

The profile starts with deprotonation of the alkyne by **3** *via* **TS3-4** to form zwitterion **4**. **4** then loses H_2 gas by **TS4-5** to form **5**. Transmetallation of **5** with HBpin then occurs through high-lying intermediate **6** and **TS6-3** to form the terminally borylated alkyne and regenerate **3**.

The profile is almost as initially expected. However, during the optimisation of the **TS6-3** for the σ-bond metathesis step, the additional high lying intermediate **6** was found. It appears to simply be a midpoint in the σ-bond metathesis step, with both the Al–C bond lengthened in **6** (2.14 Å) relative to **5** (1.94 Å), and the B–H bond lengthened in **6** (1.30 Å) relative the starting HBpin (1.19 Å), and bonds forming between the aluminium and the hydride of HBpin (1.84 Å) and between the boron and alkyne (1.65 Å). The existence of intermediate **6** implied the existence of an additional transition state **TS5-6** linking this high lying intermediate and the preceding intermediate **5**. However, all attempts to locate this transition state proved unsuccessful. Upon performing a scan of the potential energy surface by increasing the B–C bond distance in 0.1 Å increments starting from **6** the following profile was seen (Figure 25).

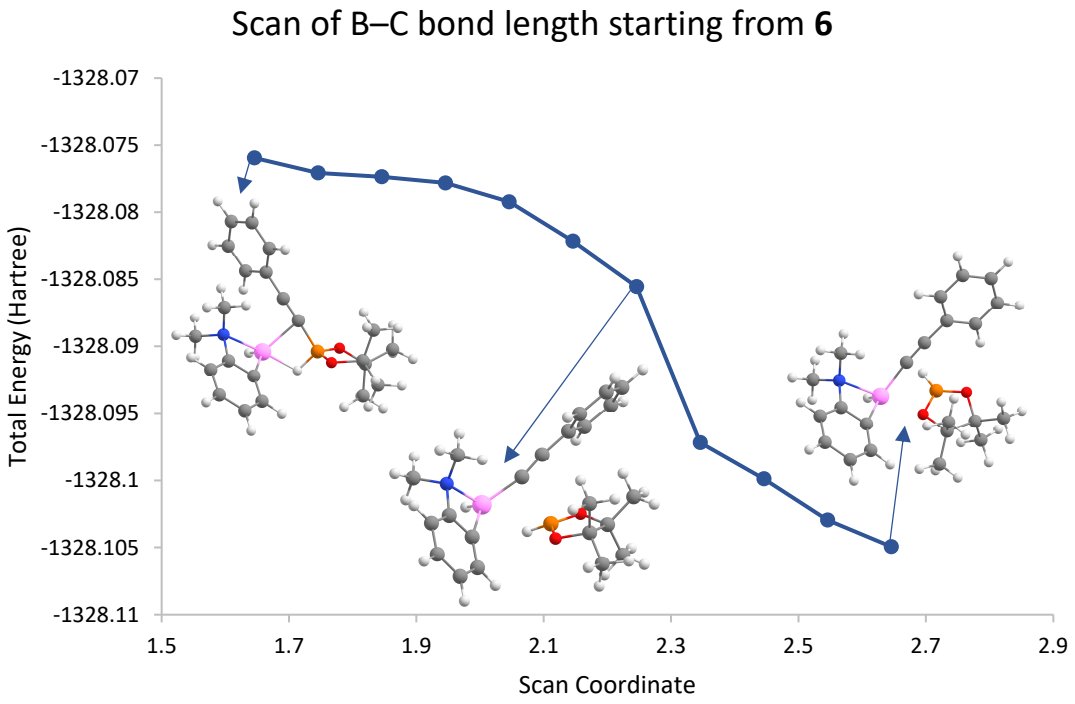

Figure 25 – Scan of the potential energy surface between 6 and 5 increasing the B–C bond length in 0.1 Å increments.

This shows that the transition between **6** and **5** is barrierless with a very flat PES near **6** and so it is unsurprising that postulated transition state **TS5-6** was unable to be located.

In addition to this extra structure **6** present in the reaction profile, the main information gained from the profile was that the reaction is energetically viable at the reaction temperature of 80 °C with the largest reaction barrier being 27.3 kcal mol^{-1} which is high but not unreasonable.[7] The fact that this largest barrier is between **5** and **TS6-3** indicates that the σ-bond metathesis is the rate determining step of the reaction.

While the exact analogous mechanism of catalytic C–H borylation of terminal alkynes has not been studied computationally, comparisons can still be drawn between the mechanism above and the C–H borylation of heteroarenes previously reported.[6] Firstly, it can be seen that the steps of the reactions with both aluminium and boron remain the same. Comparison of the C–H activation step energies is unlikely to give any useful information due to the different nature of the C–H bond being broken. However, it is notable that the σ-bond metathesis step to generate the products and regenerate the catalyst is significantly lower energy for the boron catalyst (7.1 kcal mol^{-1}) compared to the aluminium catalyst (27.3 kcal mol^{-1}). This is a significant advantage of the boron system over the aluminium system.

In addition to the above findings about the C–H borylation mechanism starting from **3**, it is notable that **5** still has an Al–H bond and so is also capable of performing the same catalytic cycle as **3**. Therefore, optimisation of the analogous reaction profile using **5** as the starting point was carried out to see how this would affect the reaction energies. This gave the reaction profile below (Figure 26). The transition state **TS8-9** could not be located for the same reason as for **TS5-6** as discussed above.

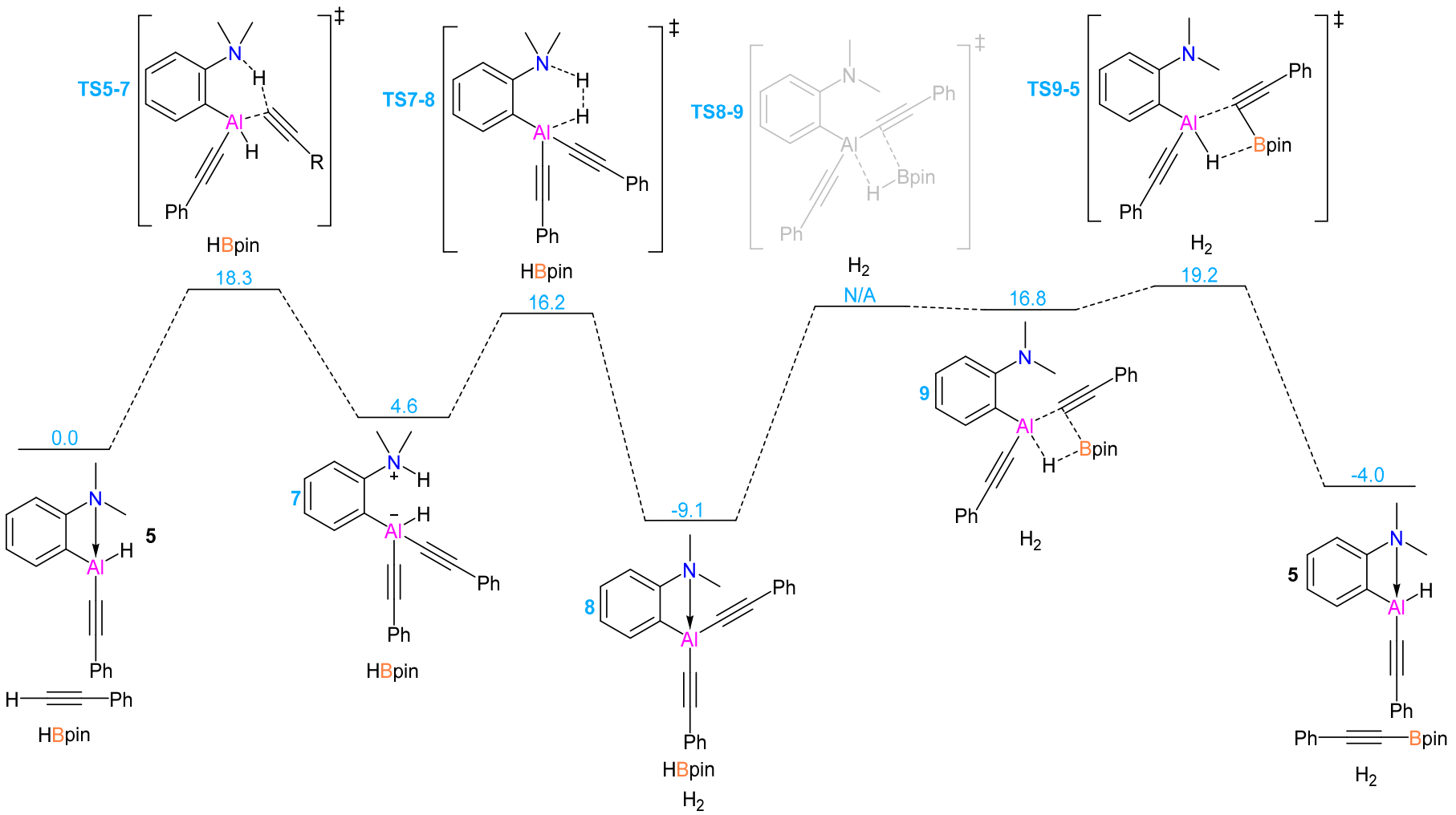

Figure 5 – Computed reaction profile for terminal C–H borylation of phenyl acetylene by 5 with HBpin. All energies given in kcal mol^{-1} relative to the starting materials. TS8-9 could not be optimised. Calculations carried out at the wb97xd/6-311++g(d,p) level of theory with SMD solvation (chloroform).

The energies of the profile with **5** as the starting point are very similar to the profile for **3** as the starting point. Only minor differences in energies were seen with the largest difference being 0.7 kcal mol^{-1}. This indicates that the identity of the "spectator" group (H or C≡CPh) on the aluminium centre is not of major importance in the reaction. When comparing the two energy profiles it can be seen that the barrier for **5** to undergo σ-bond metathesis to form the product borylated alkyne is actually much higher than for **5** to C–H activate a second equivalent of phenyl acetylene (Figure 27). Therefore from these two energy profiles it can be postulated that the resting state of the catalytic system is the diacetylide **8**.

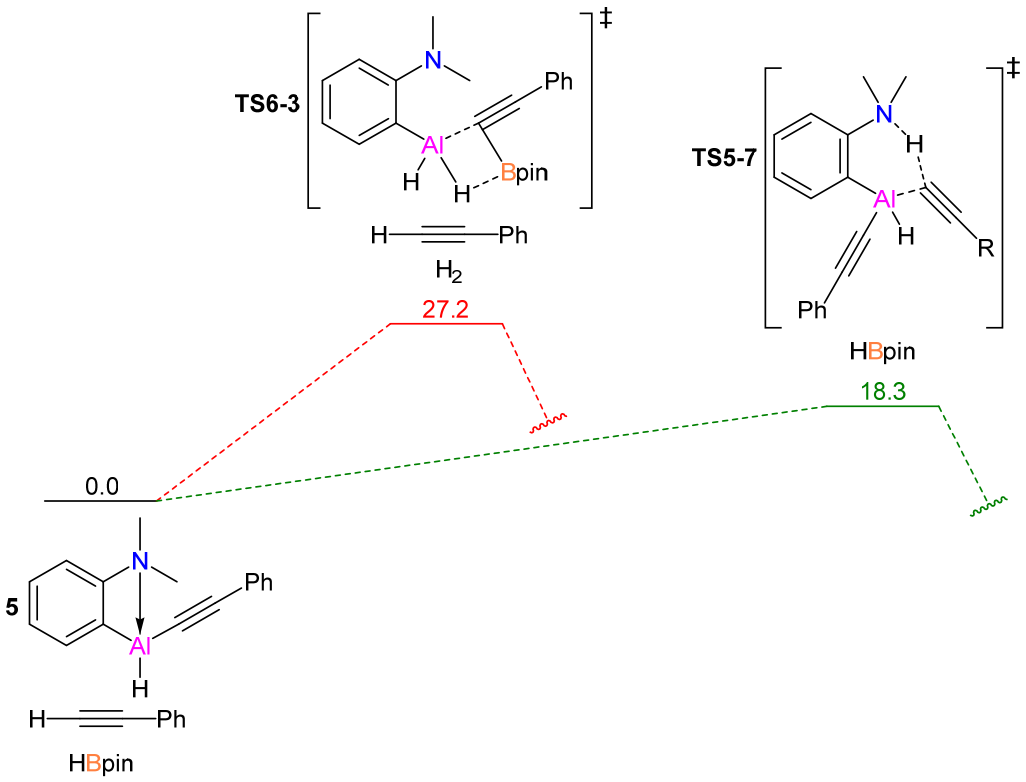

Figure 27 – σ-bond metathesis with HBpin vs C–H activation of phenyl acetylene for 5.

4.3 Hydroboration mechanism

The other profile of interest in this catalytic system was for the hydroalumination of the alkyne by the Al–H bond followed by σ-bond metathesis with HBpin to form a borylated alkene species (Scheme 56), which was the experimentally observed unwanted by-product of our catalytic system before optimisation by addition of 1,5-hexadiene. This type of hydroalumination has been seen for this type of aluminium FLP system, but only for internal alkynes.[8]

Investigating this mechanism would show whether the catalyst is capable of performing this hydroboration on the terminal alkyne, or whether the hydroboration product is produced exclusively by a side reaction, which was previously postulated to be by reaction of BH_3 formed *in situ* with the alkyne.

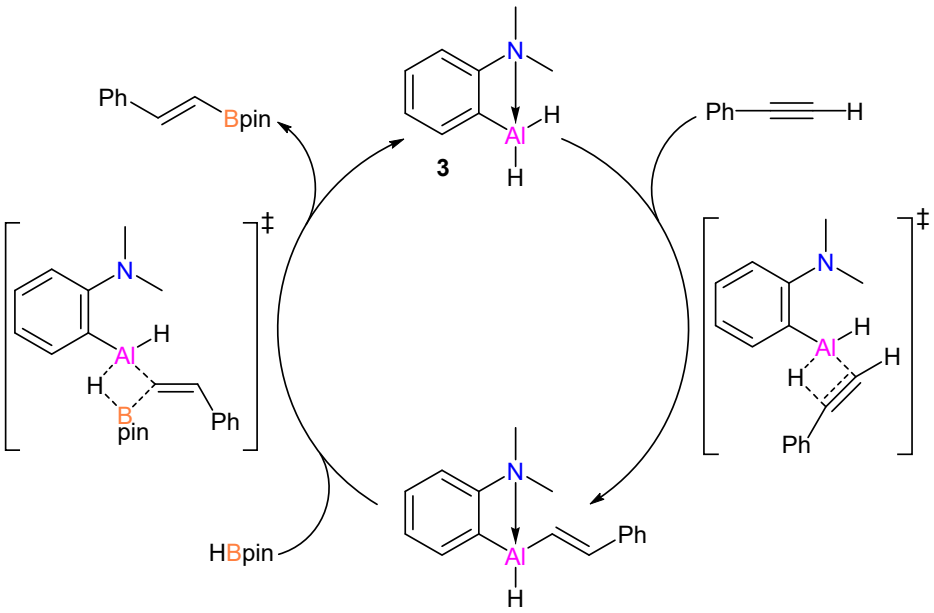

Scheme 56 – Initially proposed mechanism for the hydroboration of alkynes by 3/5.

Calculation of this reaction profile was carried out, using both **3** and **5** as starting points for the reaction, informed from our findings from the C–H borylation mechanism. This gave the following profiles below which have been condensed into one figure for ease of viewing (Figure 28).

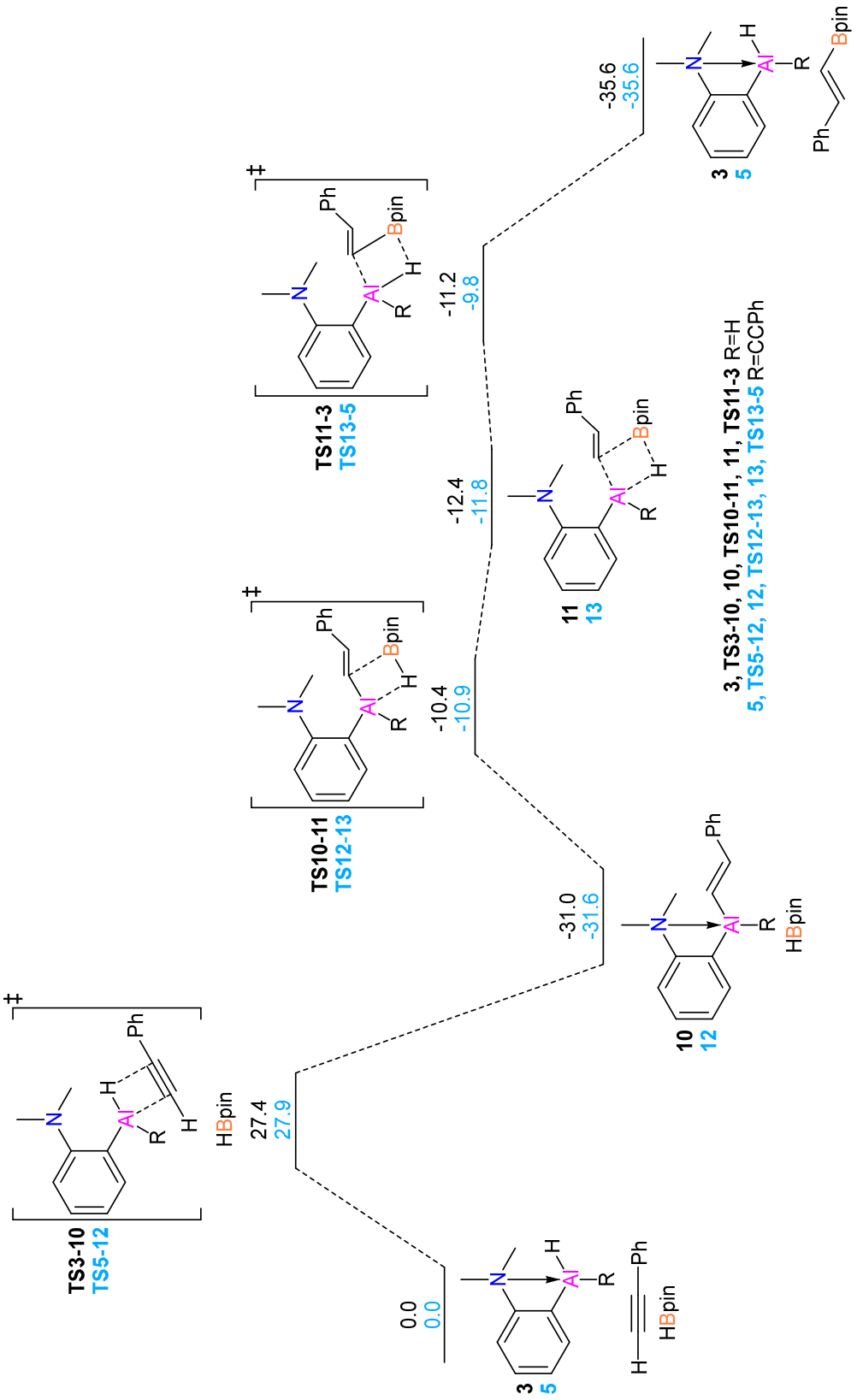

Figure 6 – Computed reaction profile for hydroboration of phenyl acetylene by 3 and 5 with HBpin. All energies given in kcal mol^{-1} relative to the starting materials. Calculations carried out at the wb97xd/6-311++g(d,p) level of theory with SMD solvation (chloroform).

This cycle begins with the Al–H bond of **3**/**5** hydroaluminating the alkyne triple bond via transition state **TS3-10**/**TS5-12** to give **10**/**12**. Transmetallation then occurs through transition state **TS10-11**/**TS12-13**, high lying intermediate **11**/**13**, and transition state **TS11-3**/**TS13-5**, to regenerate **3**/**5** and form the hydroborated product. In this case there were no issues optimising the transition states **TS10-11** and **TS12-13** which are analogous to **TS5-6** and **TS8-9**, which could not be found for the C–H borylation mechanisms.

In the same manner as for the C–H borylation reaction profiles, the two hydroboration profiles have very similar energies for all of the structures with a maximum difference of 1.4 kcal mol^{-1} again showing that the identity of the "spectator" group on the aluminium centre does not have a significant bearing on the reactivity of the FLP.

In order to draw together all of the data from the above analysis of the PES including both C–H borylation and hydroboration mechanisms, a full linked PES is shown here (Figure 29).

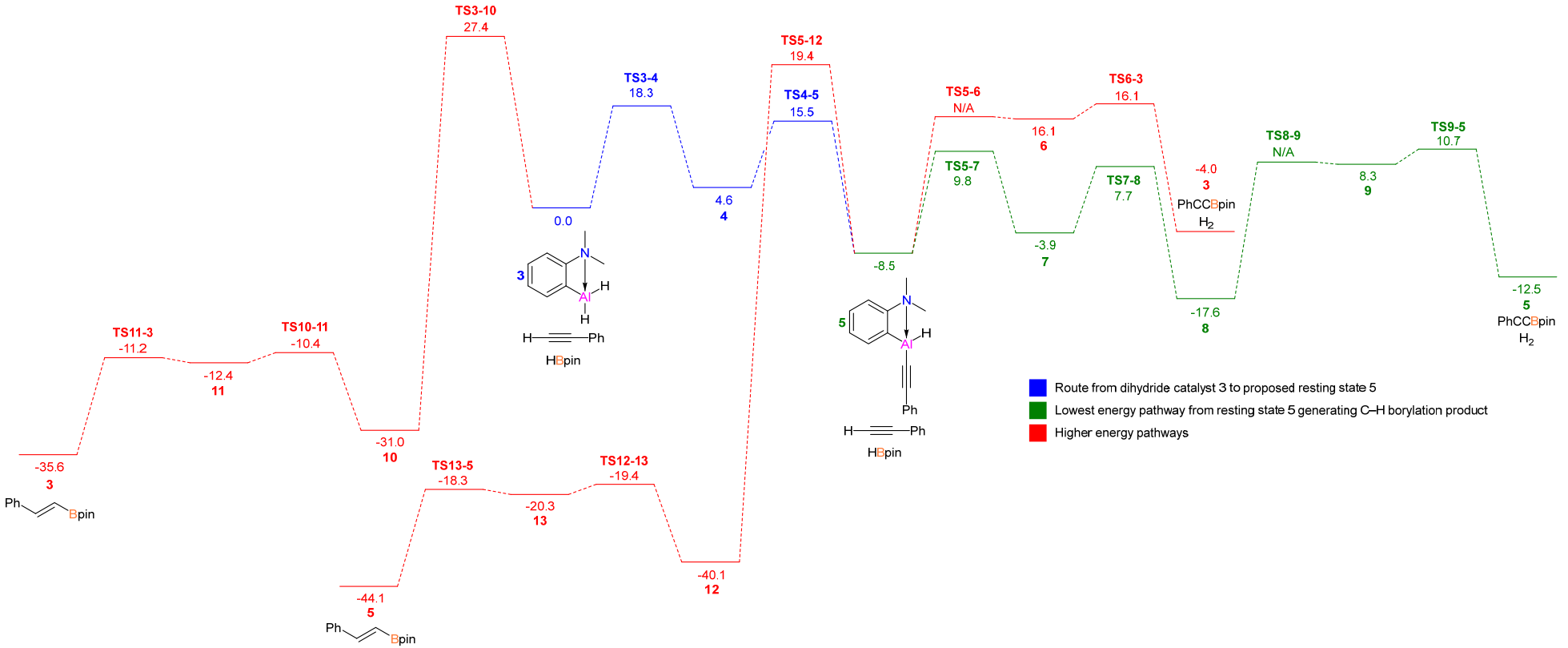

Figure 29 – Full PES showing all computed C–H borylation and hydroboration mechanisms joined together. All energies given in kcal mol^{-1} relative to the starting materials. Calculations carried out at the wb97xd/6-311++g(d,p) level of theory with SMD solvation (chloroform).

4.4 Explanation of catalyst selectivity

When comparing the profiles for hydroboration to those of the terminal C–H borylation it is observed that the product of hydroboration is significantly more thermodynamically favoured at –35.6 kcal mol^{-1} vs –4.0 kcal mol^{-1} for the C–H borylation product. This means the reaction must be kinetically controlled, or proceed through an irreversible step as the C–H borylation product is the only one observed under the optimised reaction conditions.

By looking at the two competing reaction profiles the reason that the catalytic system is selective towards the thermodynamically disfavoured C–H borylation product can be ascertained. Comparison of the first steps of the reaction profiles shows that the transition state **TS3-4**/**TS5-7** for deprotonation of the alkyne is a significantly lower barrier at 18.3(18.3) kcal mol^{-1} in comparison to the transition state **TS3-10**/**TS5-12** for hydroalumination of the alkyne triple bond which has a barrier of 27.4(27.9) kcal mol^{-1}. This gap of nearly 10 kcal mol^{-1} shows that the catalyst will preferentially perform the C–H deprotonation in this first step.

However, when comparing the largest barriers in both mechanisms it can be seen that the largest barrier in the C–H borylation mechanism is actually comparable to this first step for hydroboration. This barrier is for the transborylation from **5**/**8** to generate the product terminally borylated alkyne and has a barrier of 27.2(28.3) kcal mol^{-1}. If all of the steps in the reaction profiles are reversible, this would mean that hydroboration would be able to occur and we would see both products. Despite this, only the C–H borylation product is seen under the optimised reaction conditions. We postulate that once the initial deprotonation step has occurred to form **5**/**8**, the loss of hydrogen makes this step irreversible, as it is lost as a gas into the headspace above the reaction mixture. Therefore, once the catalyst has undergone the thermodynamically more favourable deprotonation step it can only proceed to make the observed product, the terminally borylated alkyne. This means that the hydroboration product observed in the reaction must come from another source, which is likely the BH_3 formed in situ under the reaction conditions.

In order to better understand the origin of the large barrier difference for the first steps of the two mechanisms, NBO analysis on the starting structures **3** and the two sets of transition states **TS3-4** and **TS3-10** was performed to see how the bonding changed. This gave the following data (Figure 30).

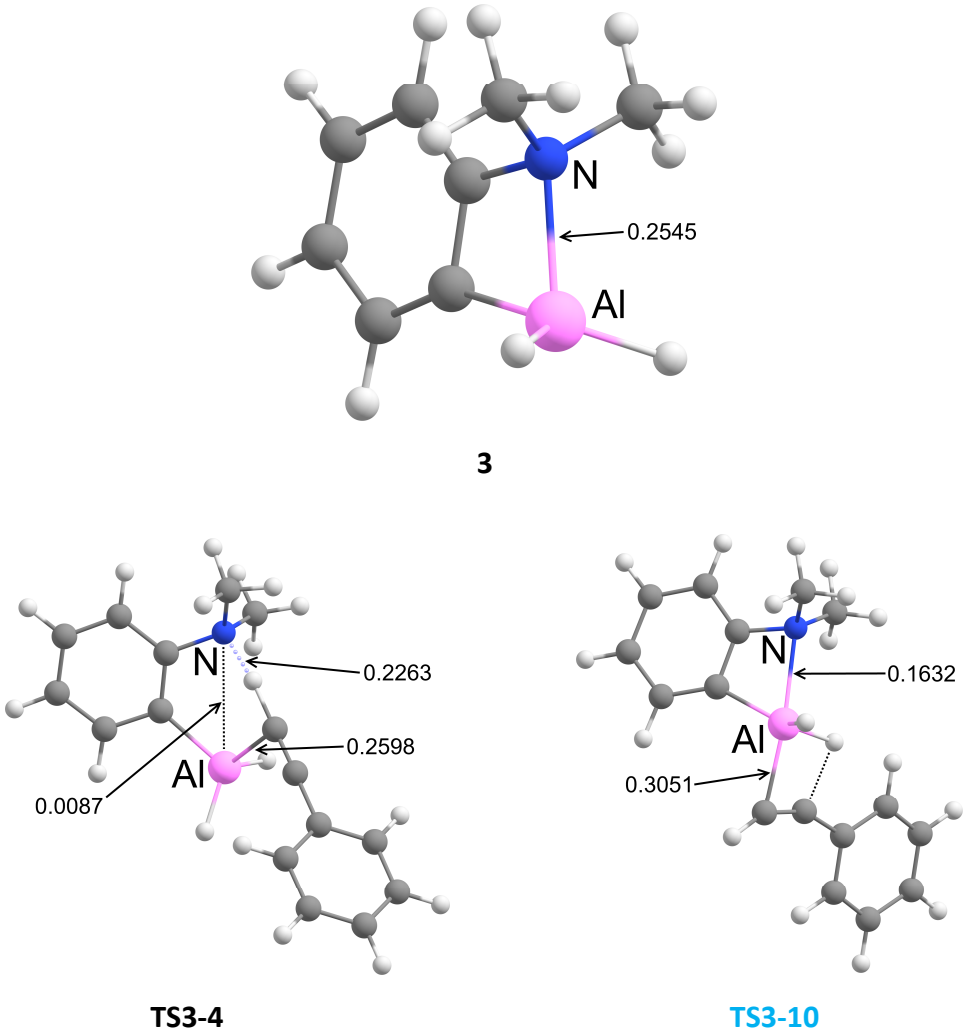

Figure 30 – Computed structures of 3, TS3-4, and TS3-10, and selected Wiberg bond indices.

The structure of **3** shows an Al–N dative bond (WBI 0.2545). For transition state **TS3-10** the Al–N bonding interaction that is present in the starting structure **3** has almost completely broken (WBI 0.0087). This is replaced by an N–H bonding interaction for the nitrogen (WBI 0.2263), and an Al–C carbon bonding interaction for the aluminium (WBI 0.2598).

In contrast, when looking at transition state **TS3-10**, the Al–N interaction has again weakened but not completely disappeared (WBI 0.1632). In this case however, while the aluminium is now involved in an Al–C bonding interaction (WBI 0.3051), the nitrogen centre has no compensating stabilisation to make up for its reduced bonding to aluminium.

To attempt to quantify the magnitude of effect this interaction has on the energy of the transition state, optimisation of the structure of **3** without the internal adduct was performed. The two structures are displayed below (Figure 31). This gave an estimate of the internal adduct bond energy of 16.65 kcal mol^{-1}.

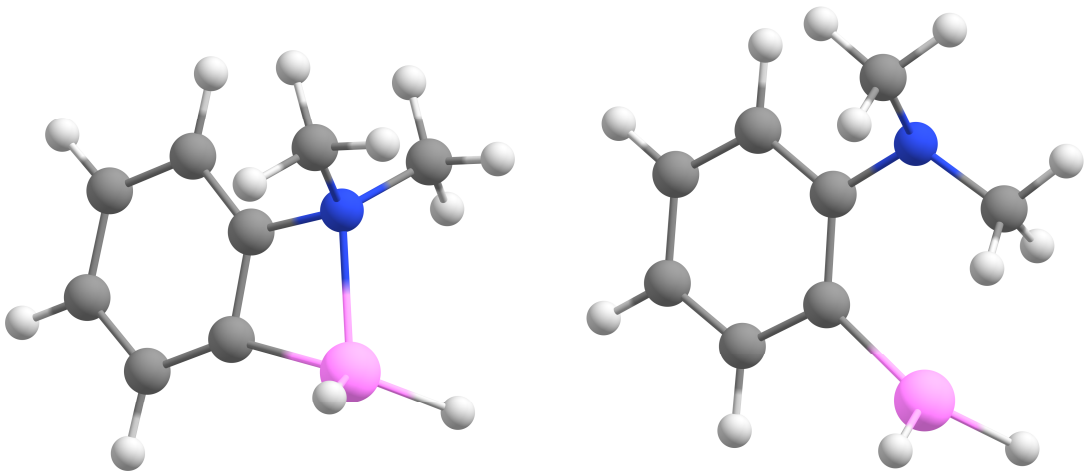

a) 0.0 kcal mol^{-1} b) 16.65 kcal mol^{-1}

Figure 31 – Structures and energies of 3 with a) the internal adduct present and b) no internal adduct present.

In order to be able to relate this to the energy of the transition state a scan of the bond length between the nitrogen and aluminium centres was performed to see how the energy changed with distance. This gave the plot below (Figure 32).

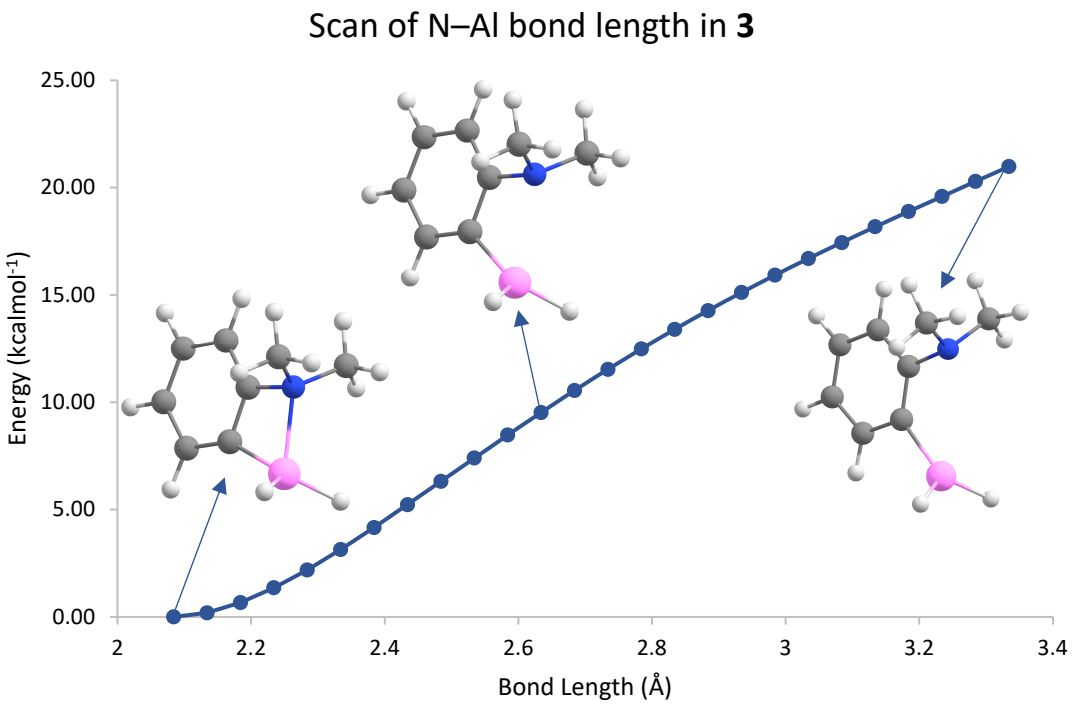

Figure 32 – Scan of N–Al bond length in 3.

Wiberg bond indices were then extracted from these scan structures and by comparing these values to the Wiberg bond index in **TS3-10** a rough estimate of the destabilising effect can be made. At a bond distance of 2.63 the Wiberg bond index of 0.1639 most closely matched that of the transition state at 0.1632. Here the energy was 9.52 kcal mol^{-1} higher than for **3** in its ground state. Therefore it can be estimated that the energetic cost of weakening this Al–N interaction in **TS3-10** raises the energy of this transition state by 9-10 kcal mol^{-1}, disfavouring hydroalumination significantly. This clearly shows the importance of the amine donor group on the ligand in determining the selectivity of the catalyst, both enabling the C–H borylation pathway and significantly destabilising the hydroalumination pathway.

4.5 Catalyst activation

Having proposed a potential origin of the selectivity for the catalyst system, examination of how the catalytically active species was generated from the dimethyl FLP precatalyst **1** to enter into the catalytic cycle was the next goal to be carried out. From our experiments of reaction of **1** with HBpin in chapter 3 (*vide supra*), we proposed that the

active dihydride **3** was generated, along with MeBpin as a byproduct. However, during catalytic runs where **1** was in contact with the substrate alkynes as well as HBpin, small quantities of methane were observed in the ^{1}H NMR spectra of the reactions as well as the expected MeBpin. Contamination of the reaction with small amounts of water was out first possible explanation of the presence of methane. However, after rigorous drying of reaction glassware and multiple reaction runs, methane was still present. Therefore to attempt to explain the presence of methane, computational investigation of the reactions of **1** with both HBpin and phenylacetylene was carried out. We started by considering the following possible reaction pathways (Scheme 57).

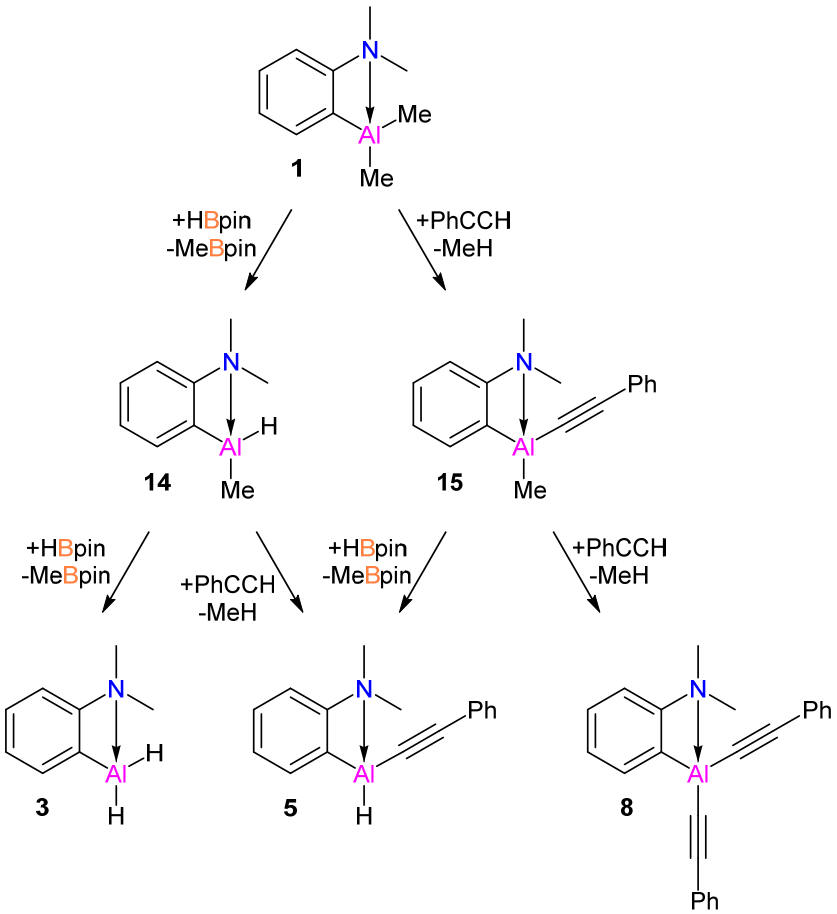

Scheme 57 – Reaction pathways for reaction of 1 with a) HBpin and b) PhCCH.

As previous calculations had shown that the identity of spectator ligands in the reactions did not affect the energies of the transition states and intermediates to any significant degree, only the structures in the steps to form **14** and **15** from **1** were calculated. From these energies suggestions about the whole scheme can be drawn as the four following

branching steps are analogous to the first two steps. Optimisation of the structures in these two steps gave the two following reaction profiles (Figure 33).

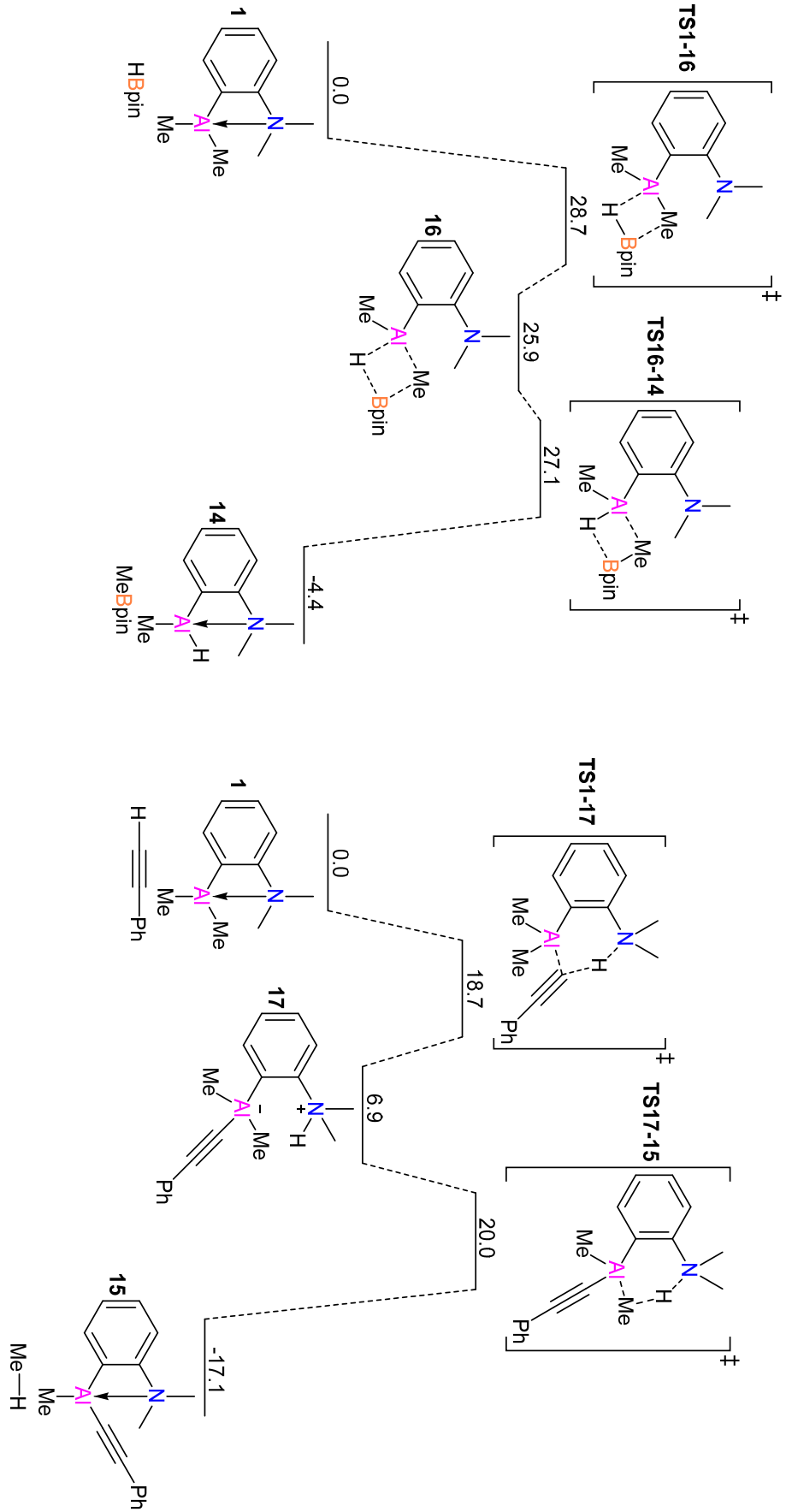

Figure 7 – Computed reaction profiles for reaction of 1 with a) HBpin and b) PhCCH to form 14 and 15 respectively. All energies given in kcal mol^{-1} relative to the starting materials. Calculations carried out at the wb97xd/6-311++g(d,p) level of theory with SMD solvation (chloroform).

These profiles reveal that both pathways are energetically viable, but reaction with phenylacetylene appears to be considerably more favourable with much lower barriers to reaction than for reaction with HBpin. When these results are applied while looking at the pathways in Scheme 57, then it is likely that the vast majority of generated species will be **8**. Small amounts of **3** and **5** must also be generated as some MeBpin is still observed under experimental conditions.

As such we have proposed an explanation for the experimental observation of methane generated in the reaction. Additionally, it is important to note that regardless of the activation pathway, all three of the potentially formed species **3**, **5**, and **8** are on cycle species and can participate in the catalytic reaction.

4.6 Experimentally isolated structure analysis

Alongside the computational investigation of the mechanism of the catalysis, isolation of some of the proposed on cycle intermediate species had been attempted to provide additional evidence for the mechanism and to provide support for our catalyst activation pathways. An independent synthesis of **3** was attempted by reaction of **18** with $AlCl_3$ to form **19**, followed by ligand exchange with $LiAlH_4$ (Scheme 58 a).

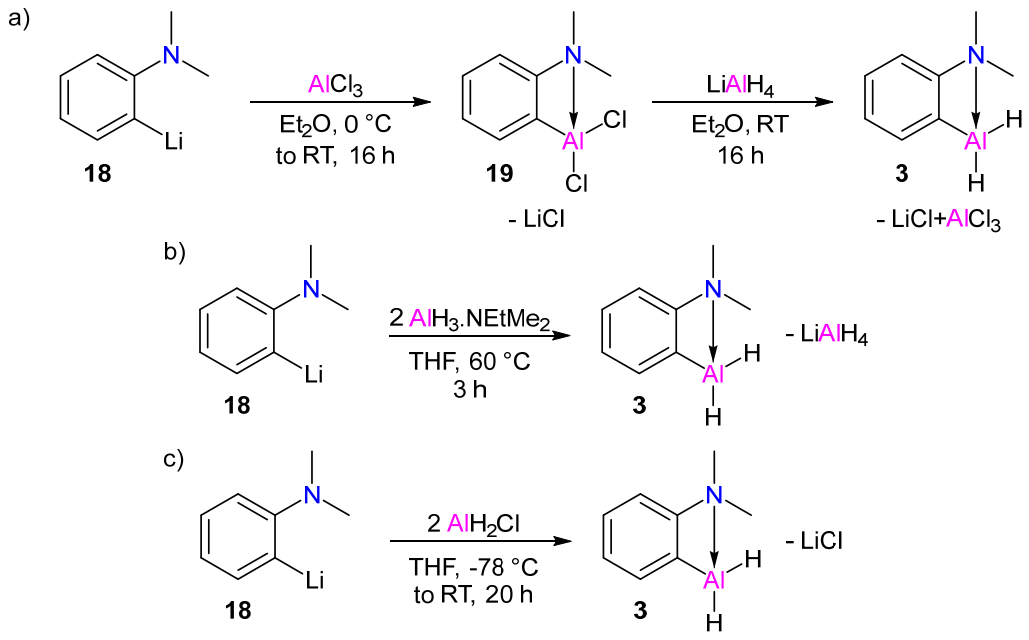

Scheme 58 – Independent synthesis routes to 3.

Instead of the expected product **3**, crystals of **20** were isolated from the reaction mixture (Figure 34). It was postulated that overreaction of **18** with the $AlCl_3$ could have occurred to form a doubly substituted aluminium chloride species before the ligand exchange with the $LiAlH_4$ and so two further synthetic routes were attempted, with a focus on avoiding this problem. Reaction of **18** directly with $AlH_3.NEtMe_2$ adduct to form **3** was attempted (Scheme 58 b), based on previous usage of this route to synthesise dihydrides in the group.[9] In addition, reaction of **18** with AlH_2Cl which had been pre-formed *in situ* from a 1:2 mixture of $AlCl_3$ and $LiAlH_4$ was also attempted (Scheme 58 c), based on literature precedent.[10] Both of these reactions again formed crystals of **20**.

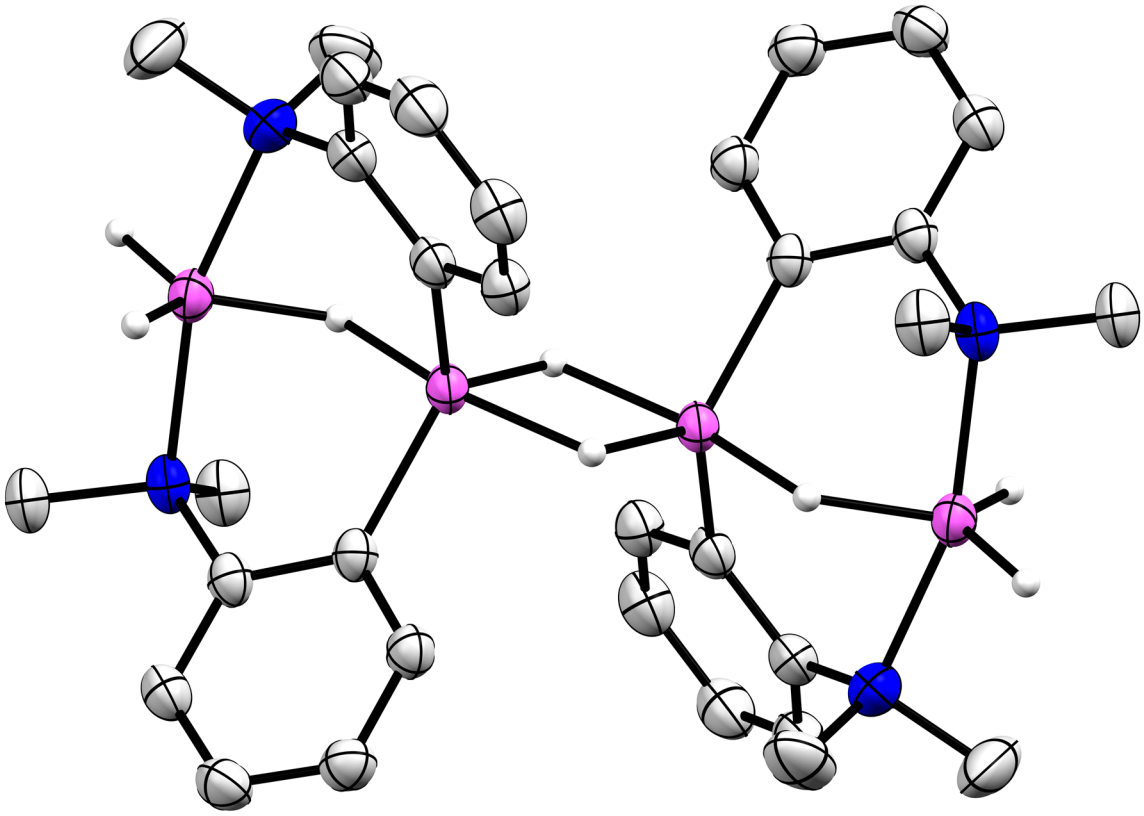

Figure 34 – Molecular structure of 20. Thermal ellipsoids shown at the 50% probability level. All non-essential protons as well as LiCl and Et_2O present in the unit cell omitted for clarity.

20 is a structural isomer of four equivalents of **3**. **20** is an oligomer of two equivalents of bis-ligated aluminium hydride and two equivalents of AlH_3, bound together through 3-centre 2-electron bonds between the hydride and aluminium centres. Since **20** was

isolated from all three routes instead of **3**, we believe that **20** is a more stable form of **3** and that in the reactions **3** is initially formed, but then ligand scrambling occurs to form the more stable **20**. While this is an undesired outcome, these types of ligand redistribution reactions are well known for aluminium compounds in the literature,[11,12] making this result unsurprising. In order to investigate this redistribution and the most stable form of **3**, the structures of several different conformers and oligomers of **3** were computed (Figure 35).

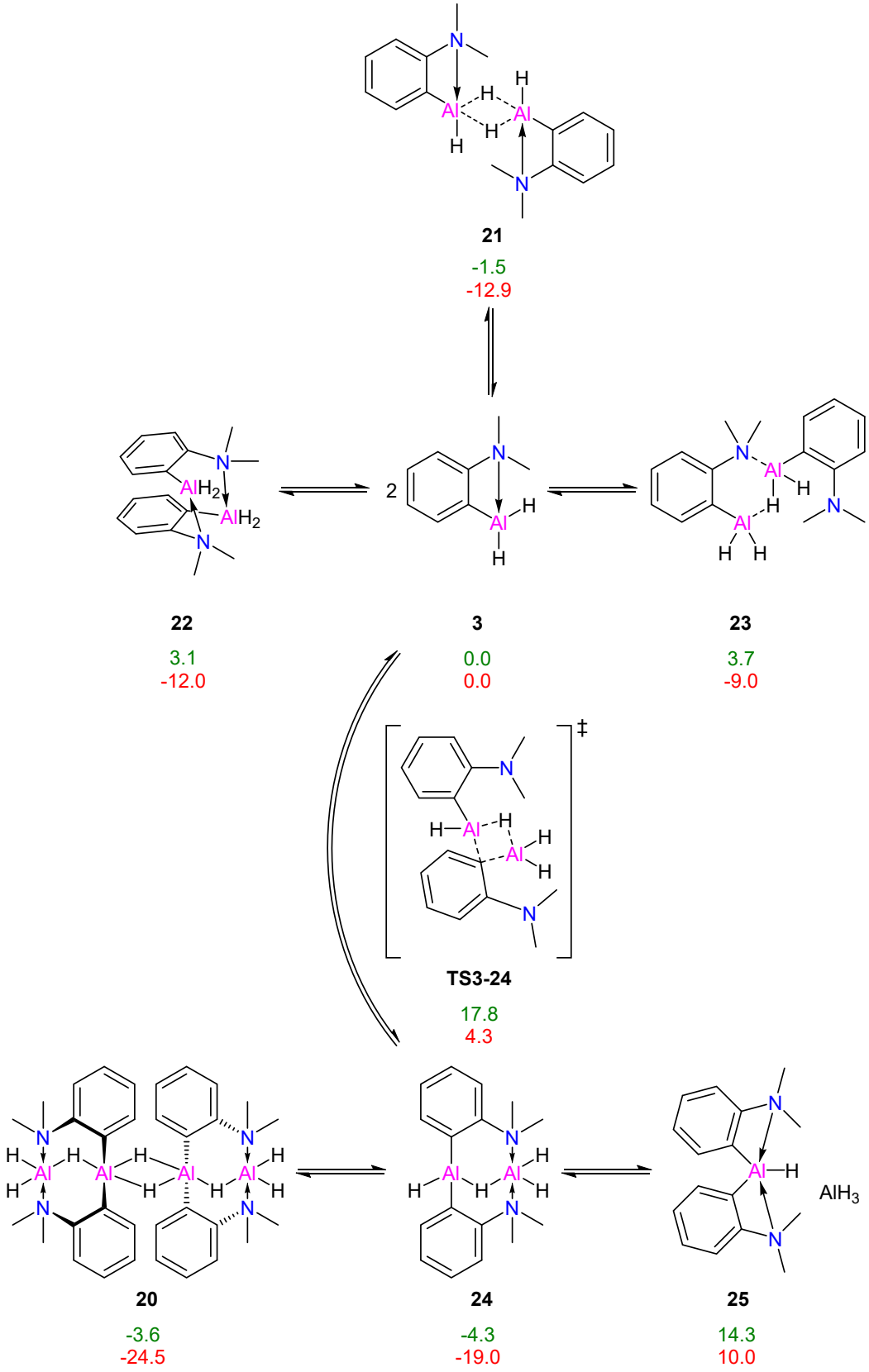

Figure 35 – Computed structural isomers and oligomers of 3. The energies presented are Gibbs free energies and enthalpies given in kcal mol^{-1} relative to the starting materials. Calculations carried out at the wb97xd/6-311++g(d,p) level of theory with SMD solvation (chloroform).

When computationally examining dimerisation of species in solution, it is important to be aware that the entropic contribution to the energy is affected heavily by solvation of both the monomer and dimer and so the entropic cost of dimerisation can be overestimated when using a simple implicit solvation model. As such, both the Gibbs free energies and enthalpies are presented to give an idea of the size of the entropic contribution and therefore uncertainty in the calculations.

When looking at the monomeric form and coordination dimers of **3**, it can be seen that for both free energies and enthalpies **21** is the most stable form. In the case of free energies **22** and **23** are both less stable than **3**. However, when looking at enthalpies **22** and **23** are more stable than **3**. The true free energy will be somewhere between these two extremes and so it is hard to draw any other conclusions from this than **21** being the most stable form.

Now looking at the ligand redistributed forms of **3**, it can be seen for both free energies and enthalpies that the experimentally isolated tetramer **20** is more stable than any of the coordination dimers. When comparing **20** to **24**, the ligand exchanged dimer of **3**, it is difficult to say which is the more stable form, as by free energies **24** (-4.5 kcal mol^{-1}) is more stable than **20** (-3.6 kcal mol^{-1}). However, by enthalpies **20** (-24.5 kcal mol^{-1}) is more stable than **24** (-19.0 kcal mol^{-1}). Again without being able to accurately assess the entropic contribution it is not possible to say which of these species is more stable in solution.

The other important findings from these calculations are that the transition state **TS3-24** to form the ligand exchanged dimer **24** from **3** has a reasonable energy barrier and that de-coordination of AlH_3 from **24** to form **25** is also energetically accessible, giving the bis-ligated aluminium hydride **25** as a potential catalytically active species.

When comparing the most stable form of the dihydride **3** to the systems reported by Fontaine *et al* for related boron based FLPs,[13] it can be seen that this system differs significantly. In Fontaine's systems, the most stable forms are the coordination dimers that do not involve ligand redistribution, simply bridging *via* the B–H bonds in a manner analogous to **21** or **23**. This shows another interesting difference in the reactivity of

these FLP species when changing the Lewis acidic element from boron to aluminium, where these dimers are disfavoured relative to the ligand redistribution.

The results of these calculations on the structure of the dihydride **3** show that the models of C–H borylation and hydroboration previously calculated (*vide supra*) are likely incomplete, as **25** is another possible starting structure. However, as previously shown, the identity of the spectator ligand in the catalysis seems to have very little effect on the energies of the reaction steps and so it is likely that a profile calculated using **25** as the starting point would have very similar energies to those already determined.

In addition to attempting to synthesise the dihydride **3**, synthesis of the diacetylide **8** was also attempted as this was the proposed resting state of the catalyst (Scheme 59).

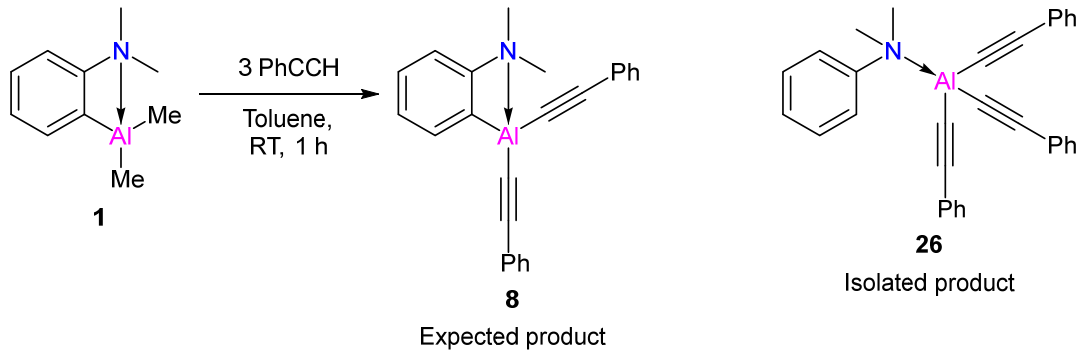

Scheme 59 – Attempted synthetic route to expected product 8 and experimentally isolated product 26.

The dimethyl species **1** was reacted with an excess of phenyl acetylene at room temperature with the goal of achieving full conversion to **8** with easy removal of the remaining phenyl acetylene under vacuum. However, instead of forming the expected diacetylide **8**, crystals of the adduct **26** were isolated from the reaction mixture (Scheme 59 and Figure 36). **26** was found to not be catalytically active.

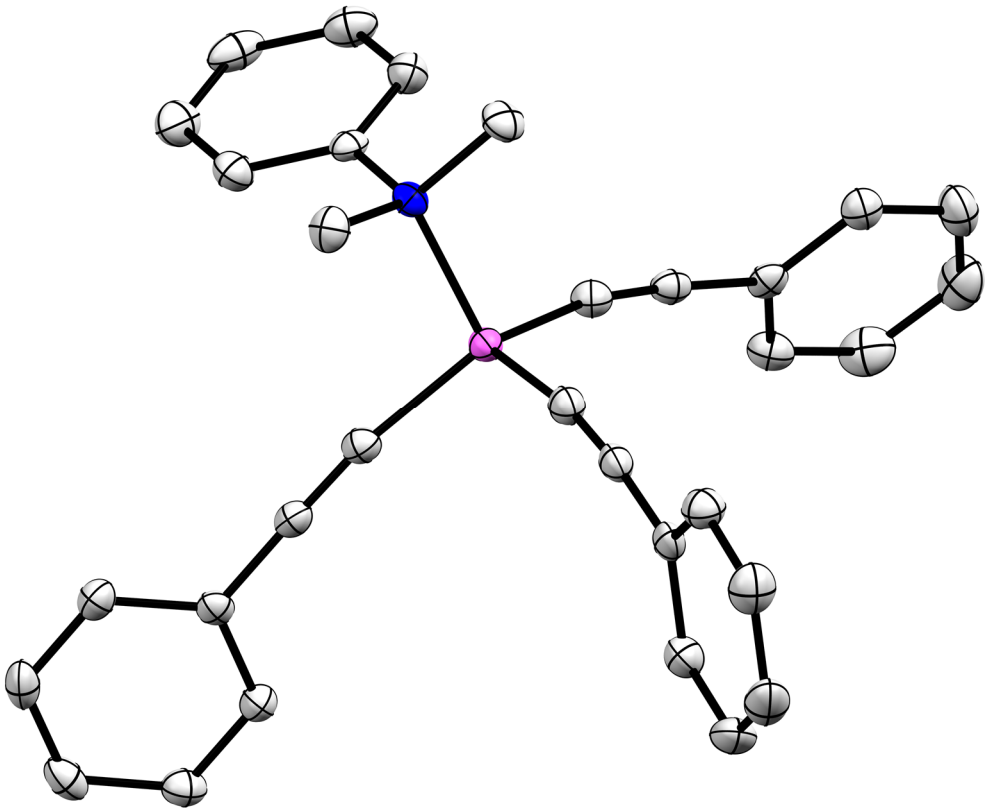

Figure 36 – Molecular structure of 26. Thermal ellipsoids shown at the 50% probability level. All protons omitted for clarity.

26 is presumably formed by **1** first reacting with two equivalents of PhCCH to form **8** with the release of two equivalents of methane and then reacting with a further equivalent of PhCCH. This type of adduct structure between nitrogen and an aluminium tris-acetylide species is known in the literature with a similar synthetic route,[14] but the precise mechanism with which this happens was not investigated.

Two possible single molecule mechanisms to the formation of **26** can be envisaged. Direct σ-bond metathesis of the Al–C(aryl) bond with the C–H bond of the PhCCH (Figure 37 a), or initial C–H activation of the PhCCH followed by protonolysis of the Al–C(aryl) bond by the generated N–H (Figure 37 b). These two routes were both investigated computationally, using acetylene instead of phenylacetylene for computational simplicity. However, no energetically reasonable pathway was found to explain the formation of **26** with this model system. In both cases the barrier to formation of the product is far too large to allow these reaction pathways to occur at room temperature, which is how the product was formed experimentally. This means that the phenyl

substituents on the acetylenes are important in lowering the energy of the transition states, or that the product **26** must be formed in some other manner. This would most likely by a more complex multi-molecule mechanism. Investigating either of these possibilities would be difficult due to the requirement to survey a large range of multi-molecular mechanisms and so this was not undertaken.

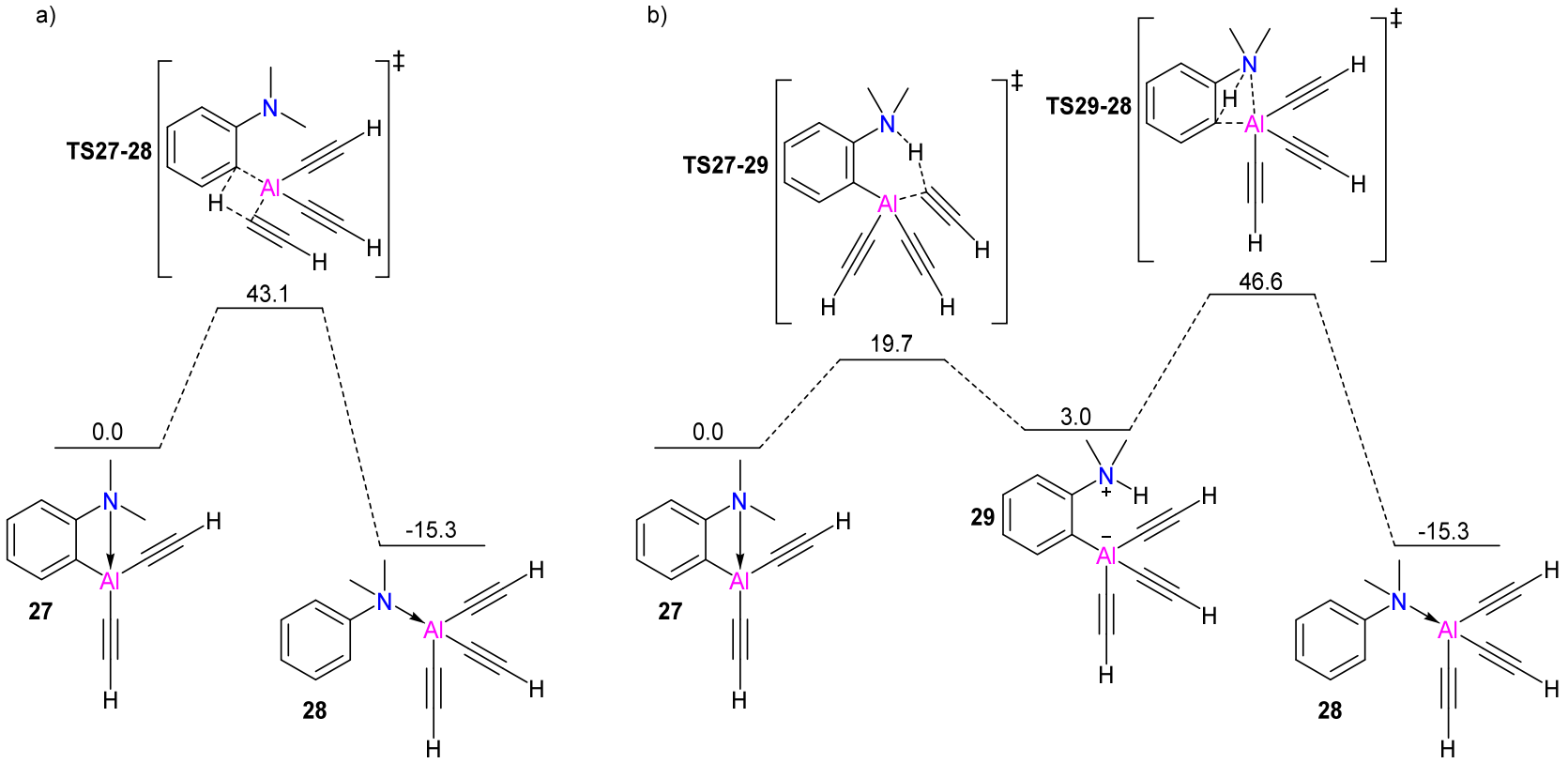

Figure 8 – Computed reaction profiles for reaction of 27 with HCCH by a) direct σ-bond metathesis and b) initial C–H activation followed by protonolysis. All energies given in kcal mol^{-1} relative to the starting materials. Calculations carried out at the wb97xd/6-311++g(d,p) level of theory with SMD solvation (chloroform).

4.7 Final catalytic cycle model

Drawing together the computational finding from the previous sections allowed us to build an improved model of the catalytic cycle for the C–H borylation of alkynes using **1** as a precatalyst (Scheme 60).

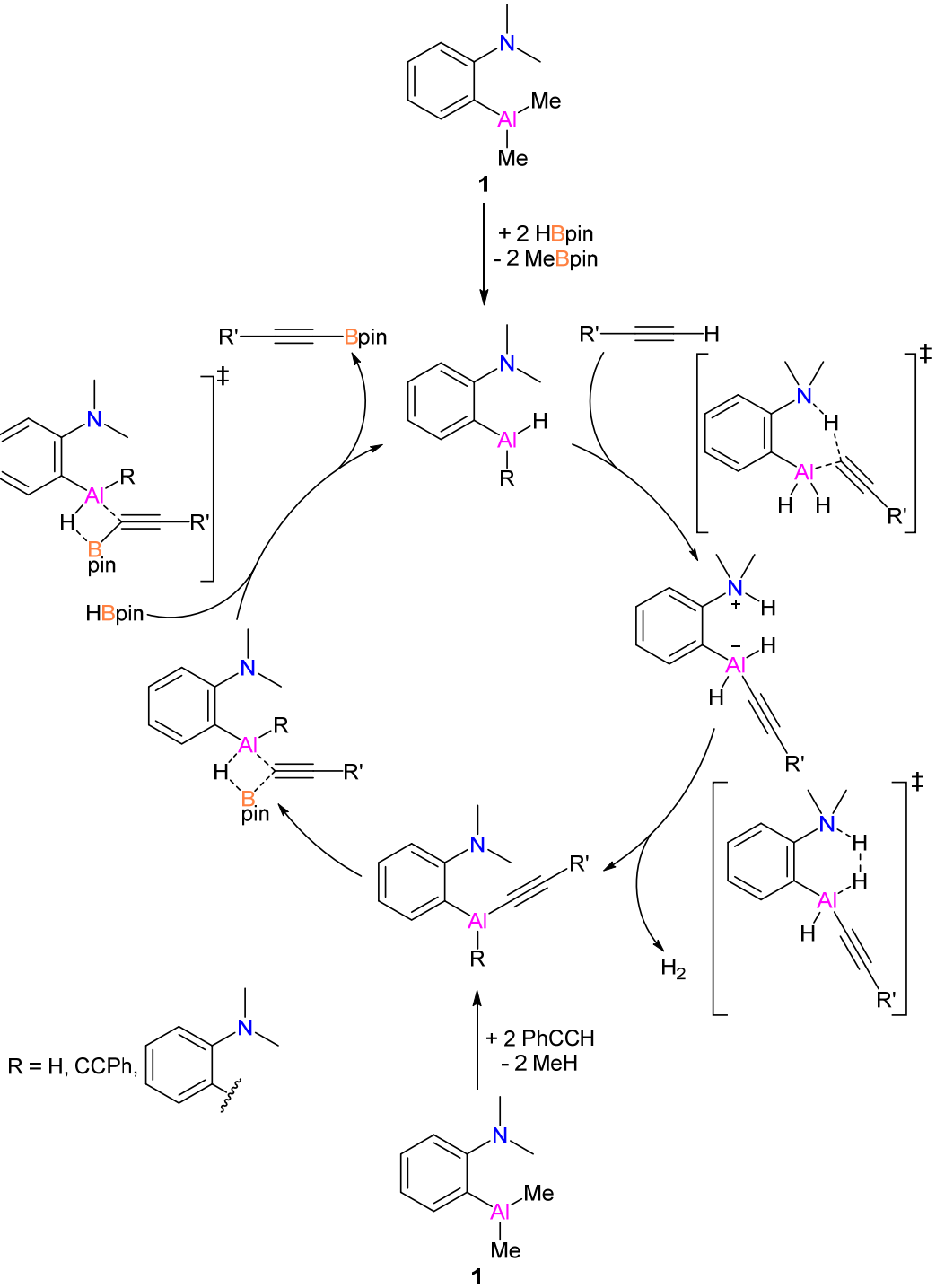

Scheme 60 – Improved model for the terminal C–H borylation of alkynes using 1 as a precatalyst.

This model is more complex than the initially proposed cycle (Scheme 55). The notable changes are the possibility of several different R groups attached to the on cycle catalyst species and the different entry points onto the catalytic cycle starting from the precatalyst **1**.

Experimentally, confirmation of precisely which of these is the major active catalytic species is difficult, as isolation of these species has proved elusive. It appears that the many of the species can react with multiple different components of the reaction mixture under catalytic conditions. Therefore when attempting to synthesise them under other conditions, they over react and form undesired products (*vide supra*), showing the great reactivity of the species.

4.8 Conclusions

Investigation of both the terminal C–H borylation and hydroboration of terminal alkynes by the dimethyl FLP precatalyst **1** has been carried out computationally. From this the origin of the catalyst selectivity has been determined, which is due to the ligand architecture with the pendant nitrogen donor arm greatly influencing the reactivity of the aluminium centre.

Additionally, analysis of the pathways to formation of the proposed catalytically active dihydride FLP **3** were analysed, explaining the presence of both MeBpin and methane in the reaction mixture, by reaction of **1** with HBpin and terminal alkyne respectively. Experimental investigation of on cycle species was also attempted, but no on cycle species could be isolated, showing how reactive these species must be. Combination of the above results led to a more detailed model of the catalytic system.

4.9 References

[1] George. Zweifel, R. B. Steele, *J. Am. Chem. Soc.* **1967**, *89*, 5085–5086.

[2] W. Uhl, *Coord. Chem. Rev.* **2008**, *252*, 1540–1563.

[3] J. C. Fettinger, P. A. Gray, C. E. Melton, P. P. Power, *Organometallics* **2014**, *33*, 6232–6240.

[4] A. Bismuto, S. P. Thomas, M. J. Cowley, *Angew. Chem. Int. Ed.* **2016**, *55*, 15356–15359.

[5] N. W. J. Ang, C. S. Buettner, S. Docherty, A. Bismuto, J. R. Carney, J. H. Docherty, M. J. Cowley, S. P. Thomas, *Synthesis* **2018**, *50*, 803–808.

[6] M.-A. Légaré, M.-A. Courtemanche, É. Rochette, F.-G. Fontaine, *Science* **2015**, *349*, 513–516.

[7] P. Atkins, J. de Paula, *Atkins' Physical Chemistry*, OUP Oxford, **2010**.

[8] Y. Chen, W. Jiang, B. Li, G. Fu, S. Chen, H. Zhu, *Dalton Trans.* **2019**, *48*, 9152–9160.

[9] R. L. Falconer, G. S. Nichol, M. J. Cowley, *Inorg. Chem.* **2019**, *58*, 11439–11448.

[10] C. Ganesamoorthy, S. Loerke, C. Gemel, P. Jerabek, M. Winter, G. Frenking, R. A. Fischer, *Chem. Commun.* **2013**, *49*, 2858–2860.

[11] "Advanced Inorganic Chemistry, 6th Edition | Wiley," can be found under https://www.wiley.com/en-gb/Advanced+Inorganic+Chemistry%2C+6th+Edition-p-9780471199571, **n.d.**

[12] N. N. Greenwood, A. Earnshaw, *Chemistry of the Elements*, Butterworth-Heinemann, Oxford ; Boston, **1997**.

[13] J. Légaré Lavergne, A. Jayaraman, L. C. Misal Castro, É. Rochette, F.-G. Fontaine, *J. Am. Chem. Soc.* **2017**, *139*, 14714–14723.

[14] W. Uhl, M. Willeke, F. Hengesbach, A. Hepp, M. Layh, *Organometallics* **2016**, *35*, 3701–3712.

5 Computational investigation of other group 13 based FLP compounds

Details of functionals and basis sets used can be found in chapter 6.4.6 (vide infra).

5.1 Introduction and aims

In the previous chapters the process of synthesis, trialling, and analysis of novel FLP species has been demonstrated, achieving the C–H borylation of heteroaromatics and terminal alkynes (Figure 38).

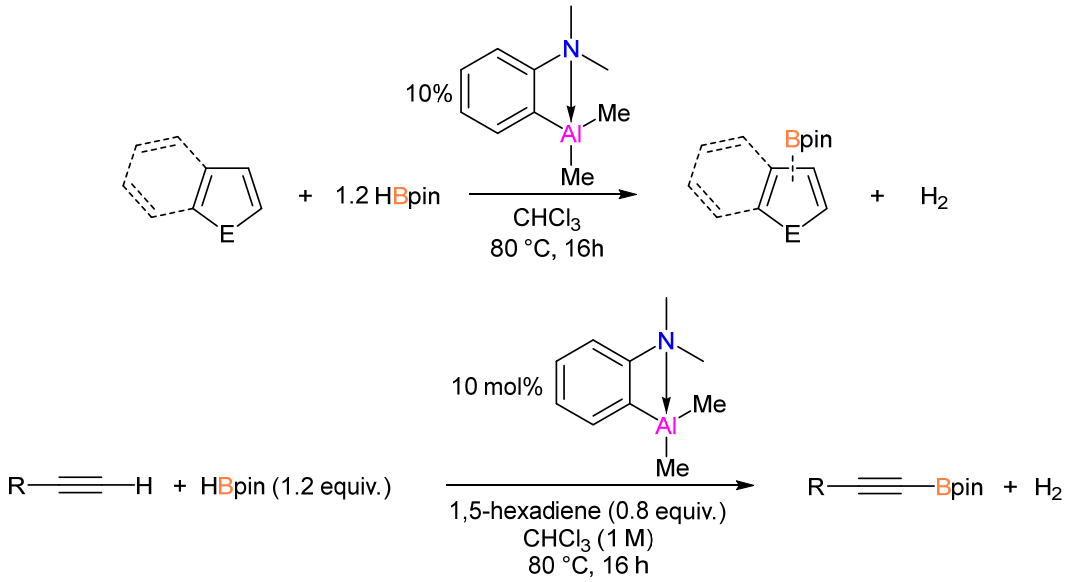

Figure 38 – C–H borylation of heteroaromatics and terminal alkynes using 2-dimethylaluminium-*N*,*N*-dimethylaniline a precatalyst.

Unfortunately, this system was unable to perform C–H borylation on pure carbon based arene substrates which was the initially targeted reactivity.

As we are still interested in achieving this arene C–H borylation with an FLP system, we wanted to gain more insight into how changing various aspects of the FLP would impact on the reactivity. When thinking about how to change the FLP, there are three main properties that can be influenced. The steric bulk surrounding the Lewis acidic and Lewis basic atoms can be changed by modification of the linker and R groups (Figure 39). The basicity of the Lewis basic half of the FLP can be changed by changing the atom itself or

the R groups attached to the Lewis basic atom (Figure 39). Finally, the acidity of the Lewis acidic half of the FLP can be changed by changing the atom itself or the R groups attached to the Lewis acidic atom (Figure 39).

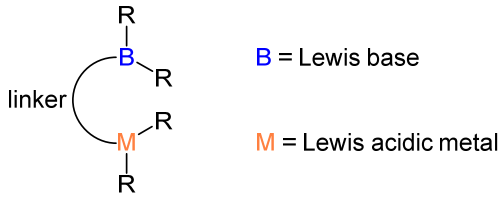

Figure 39 – Areas of an FLP that can be changed to modify the FLPs properties.

In order to gain information on how changing each of these three properties (steric bulk, basicity, acidity) affect the reactivity of the FLP in arene C–H borylation, we performed a computational survey of a range of selected potential FLP species to assess the trends in reactivity upon changing the various aspects of the FLP. We looked at the C–H activation steps of all these catalysts (Figure 40), as experimentally this appeared to be the limiting factor in achieving the desired reactivity with arenes as no reaction was seen between the catalyst and the arene. Both *N*-methylpyrrole and benzene were examined, to gain information on both heteroaromatic and arene substrates.

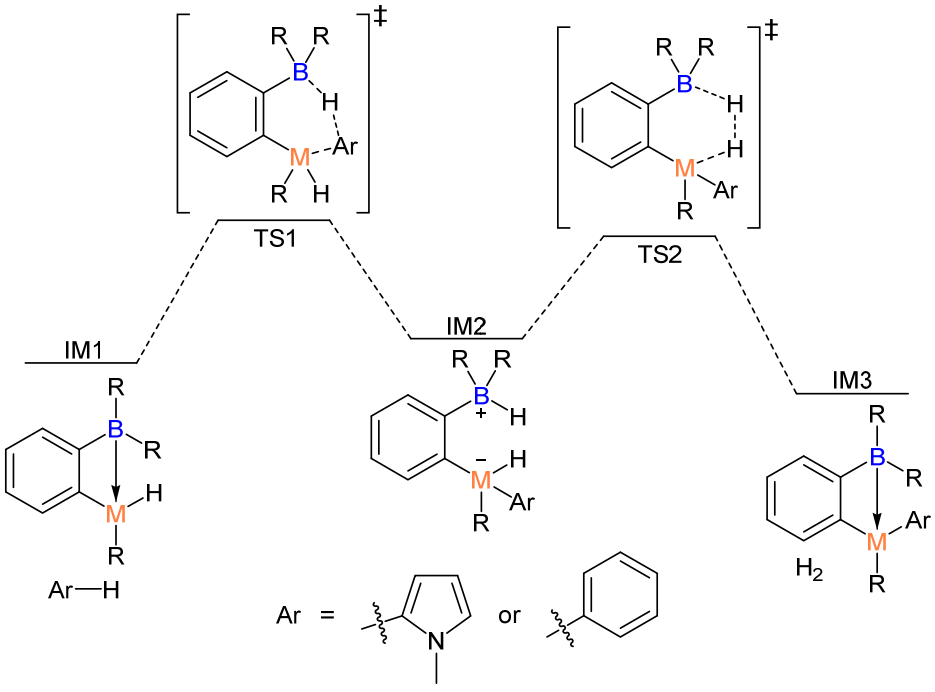

Figure 40 – Example profile of C–H activation steps calculated. B = base, M = metal.

As one of the initial goals of this research was to gain knowledge in the area of changing the Lewis acidic centre of the FLP, we decided to calculate three versions for each FLP ligand architecture, one each with boron, aluminium, and gallium as the Lewis acidic atom. Indium and lower elements of group 13 were not considered, due to the greatly increased computational cost of calculating these heavier elements given the limited amount of research time remaining. A small number of structures are missing from the profiles for the same reason, as they could not be optimised before the end of the research project.

5.2 Steric bulk

The first set of FLPs looked at were selected in order to gain information on how changing the sterics of the Lewis basic centre of the FLP affected the energy of the C–H activation steps. For this purpose FLPs with dimethylamino-, piperidyl-, and tetramethylpiperidyl-substitution were selected (Figure 41), as there are examples in the literature of using these groups for tuning FLP steric bulk on this ligand architecture for analogous C–H activation reactions.[1,2] In the work by Lavergne *et al*.,[2] it was shown that increased steric bulk caused destabilisation of the transition state for C–H activation step (TS1), and stabilisation of the transition state for hydrogen loss (TS2). For TS1 steric bulk will have two conflicting effects. Increased steric bulk will weaken the adduct bond in IM1 and so stabilise TS1. However, increased steric bulk will also be disfavoured in TS1 as TS1 involves inserting the C–H bond into the FLP and steric bulk will hinder this. In this case the steric bulk of the tetramethylpiperidyl-group is significant and the overall effect is destabilisation. TS2 on the other hand involves losing H_2 from the FLP and in this case steric bulk will favour this loss. While this provides excellent information on the trends that steric bulk imposes on the FLP reactivity, the data is only on boron based FLPs and so information on how this effect changes when the FLP atom changes can still be gained.

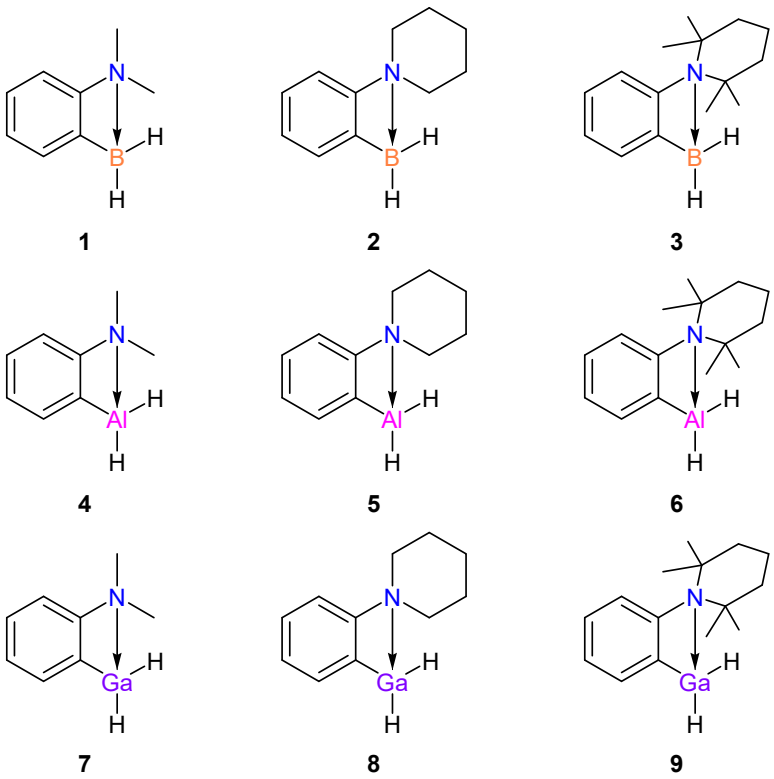

Figure 41 – Selected FLP frameworks for assessing steric bulk.

5.2.1 Boron

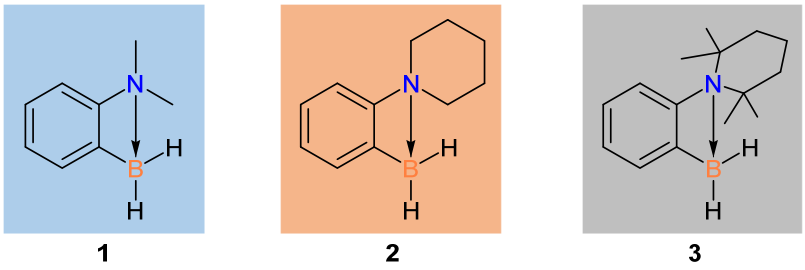

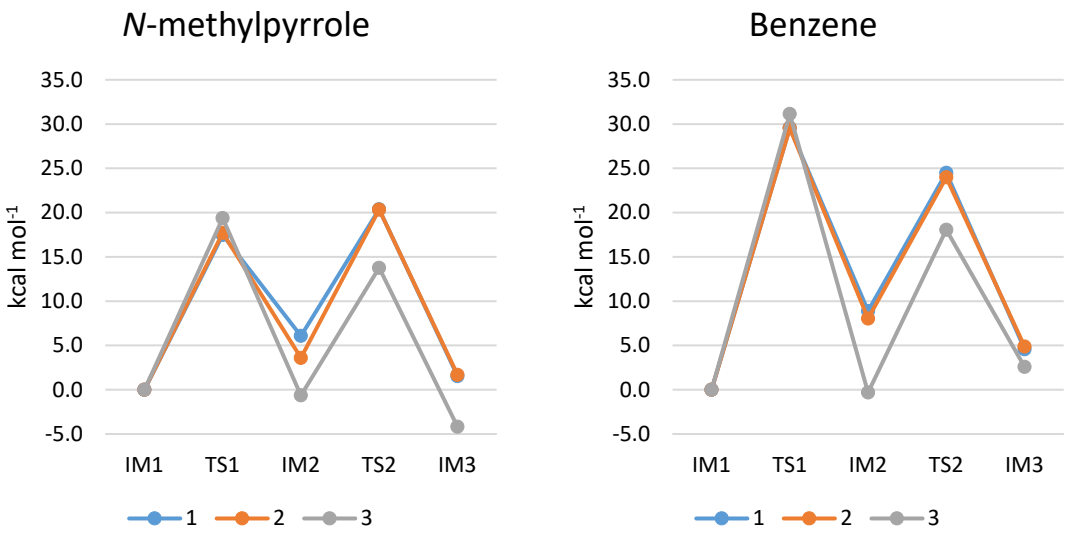

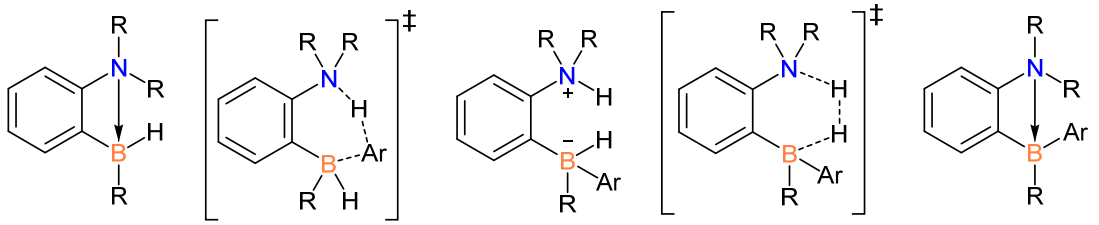

1	0.0	17.5	6.1	20.4	1.5	**1**	0.0	29.6	8.9	24.5	4.6
2	0.0	17.7	3.6	20.3	1.7	**2**	0.0	29.5	8.0	24.0	4.9
3	0.0	19.4	-0.6	13.8	-4.2	**3**	0.0	31.1	-0.3	18.1	2.6

Figure 42 – Energies of reaction steps for C-H activation of *N*-methylpyrrole and benzene for 1-3. All energies given in kcal mol^{-1} relative to the starting materials. Calculations carried out at the wb97xd/6-311++g(d,p) level of theory with SMD solvation (chloroform).

When looking at the results for the boron-based versions of the dimethylamino- (**1**), piperidyl- (**2**), and tetramethylpiperidyl-substituted (**3**) FLPs the results follow the same trends for both *N*-methylpyrrole and benzene. There is very little change in energy of the steps between FLPs **1** and **2**. Due to the extra bulk of the piperidyl ring pointing away

from the reactive area of the FLP between the Lewis acidic and basic atoms, it is unsurprising that this has little effect on the energies of the steps relative to **1**. However, when looking at the tetramethylpiperidyl-substituted (**3**) FLP, there is a substantial difference in the energies relative to **1** and **2**. There is a small increase in energy of the C–H activation step TS1 of around 1.5 kcal mol^{-1} for both *N*-methylpyrrole and benzene. In addition, the zwitterion IM2, hydrogen loss step TS2, and C–H activation product IM3 are all significantly stabilised. The increased steric bulk of the methyl groups of the tetramethylpiperidyl group pointing down towards the reactive area of the FLP between the Lewis acidic and basic atoms explains the increased energy of TS1, where the C–H bond is being inserted into FLP, and the decreased energy of TS2, where the H–H is being extruded from the FLP. In these cases the increased Pauli repulsion between the methyl groups of the tetramethylpiperidyl group and the aryl group/hydrogen increases/decreases the energy respectively in TS1 and TS2. Explaining the stabilisation of the zwitterion IM2 and C–H activation product IM3 requires more investigation of the computational data. NBO analysis of **1**-**3** reveals that the lone pair of **3** has more p character ($sp^{10.38}$) than **1** ($sp^{8.44}$) and **2** ($sp^{8.29}$). Looking at the sum of C-N-C angles around the three structures reveals that for 3 the sum is largest (344.1°), followed by **1** (338.6°) and then **2** (337.5°). The closer to 360° this total is the closer to a true p-orbital based lone pair the nitrogen is and so these angle sums map directly onto the sp character trend. This means that the basicity trend is likely due to the steric demand forcing the nitrogen centres towards a more planar geometry. The sp character analysis reveals that the lone pair of **3** is more basic than **1** and **2** and so the ammonium ion formed in the zwitterion IM2 will be more stable due to a stronger N–H bond. For the C–H activation product IM3, a closer look at the structures reveals that while IM3 for **1** and **2** possess an internal N–B dative bond, IM3 for **3** does not (Figure 43). One possible explanation for this is that the computational description is not accurate and that there is in fact a structure with an internal adduct for **3** that is more stable than this open form, or that open form versions of IM3 for **1** and **2** exist that are more stable. However, only the structures presented in Figure 43 were found during the computational analysis and so an explanation has been postulated based on the available data with the caveat that they may not be the true minima.

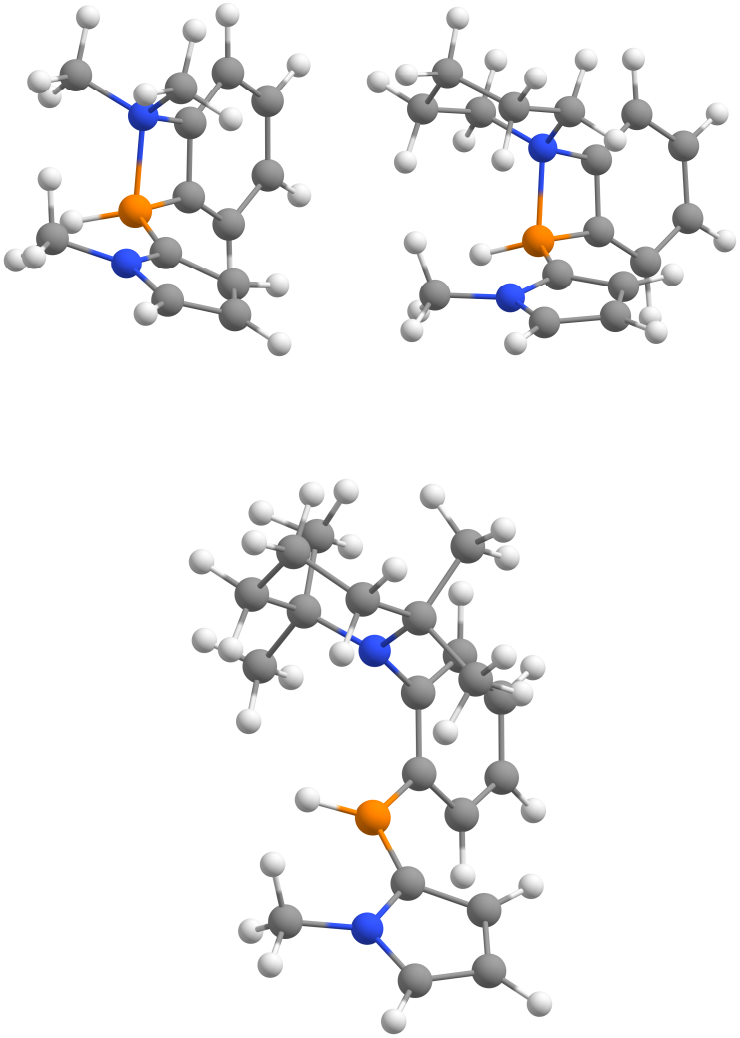

Figure 43 – Structures of IM3 for 1-3 when reacting with *N*-methylpyrrole. Structures when reacting with benzene are analogous.

If the open structure presented is the true form of IM3 for **3**, it is likely that the stabilisation of IM3 for **3** comes from delocalisation of the π-system of the *N*-methylpyrrole into the empty p-orbital on the boron, compensating for the loss of adduct interaction that is present for **1** and **2**. This is seen by a shortening of the B–C bond length between the boron and carbon of the *N*-methylpyrrole from 1.58 Å for both **1** and **2** to 1.52 Å for **3**. The size of the stabilisation seen is lower for benzene than for *N*-methylpyrrole. This is likely due to the decreased ability of the π-system of benzene to donate into the empty boron p-orbital. This is again backed up in the bond lengths, with a smaller shortening of the B–C bond length between the boron and carbon of the benzene from 1.60 Å for both **1** and **2** to 1.56 Å for **3**.

5.2.2 Aluminium

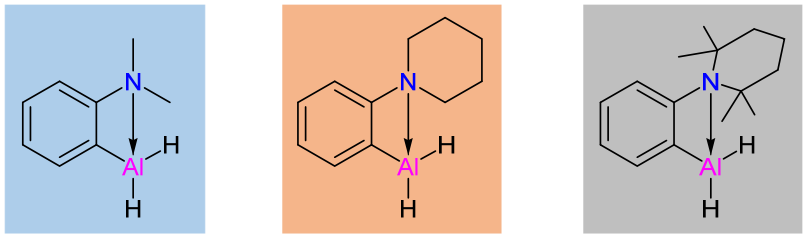

4 **5** **6**

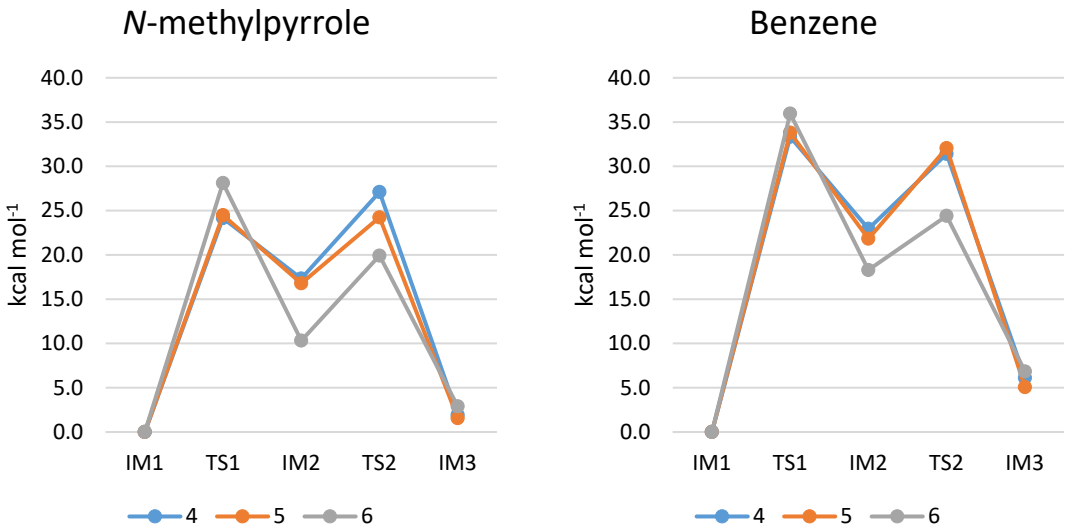

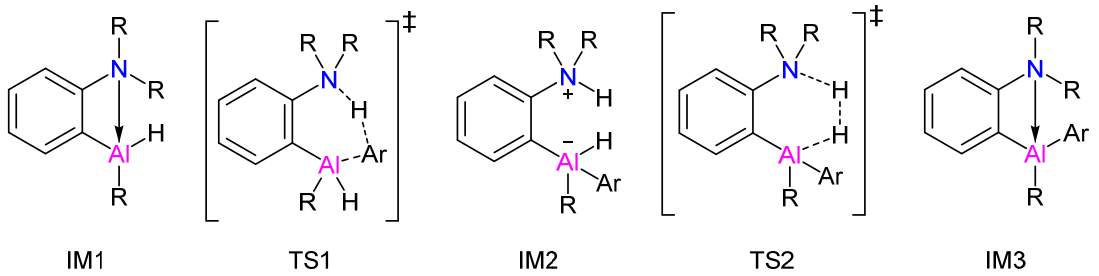

4	0.0	24.2	17.3	27.1	1.9	**4**	0.0	33.3	22.9	31.4	6.1
5	0.0	24.5	16.8	24.2	1.6	**5**	0.0	33.8	21.8	32.1	5.1
6	0.0	28.1	10.3	19.9	2.9	**6**	0.0	36.0	18.3	24.4	6.8

Figure 44 – Energies of reaction steps for C-H activation of *N*-methylpyrrole and benzene for 4-6. All energies given in kcal mol^{-1} relative to the starting materials. Calculations carried out at the wb97xd/6-311++g(d,p) level of theory with SMD solvation (chloroform).

The aluminium FLPs **4**-**6** follow the same trends in energy as for the nitrogen substituents are varied as for the boron FLPs. **4** and **5** again have very similar energy profiles to each other. **6** again shows a destabilisation of the C–H activation step TS1 and stabilisation of the zwitterion IM2 and hydrogen loss step TS2.

However, unlike for the boron FLP **3** where the C–H activation step IM3 was stabilised, IM3 for **6** is now slightly destabilised. Looking at the structures of IM3 for **4**-**6**, we now see that they now all have dative bonds between the nitrogen and aluminium (Figure 45), differing from the case for boron above where the tetramethylpiperidyl-substituted FLP did not have a dative bond present in IM3. Again with the caveat that these may not be the true minima, it can be proposed that the destabilisation seen in this case for IM3 for **6** is likely due to increased weakening of the adduct bond due to the steric bulk imposed by the tetramethylpiperidyl group. This is evident when looking at the N–Al bond lengths in the starting dihydrides and IM3 for **4**, **5**, and **6**. When looking at the difference in bond lengths between IM1 and IM3, in **4** and **5**, the N–Al bond length change is identical at 0.2 Å (2.08 Å to 2.10 Å), while in **6** it is greater at 0.3 Å (2.23 Å to 2.26 Å).

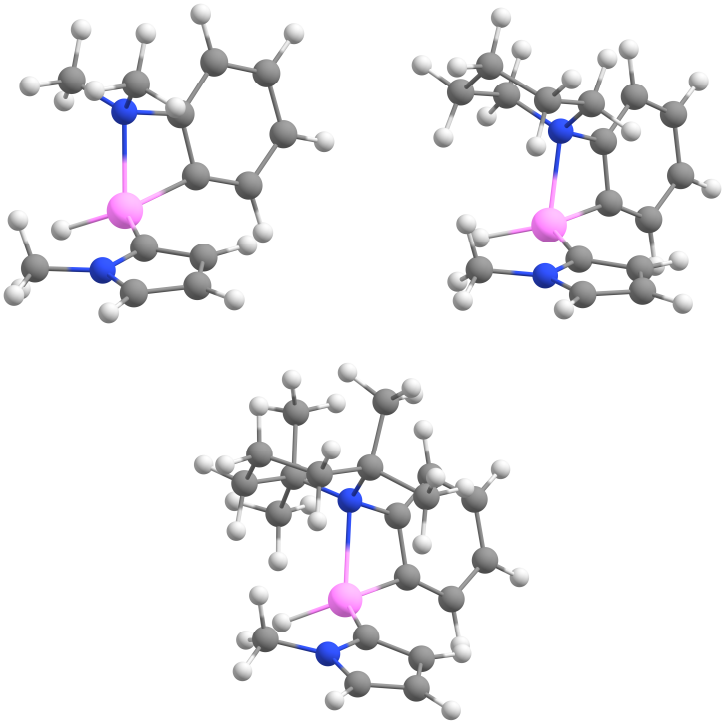

Figure 45 – Structures of IM3 for 4-6 when reacting with *N*-methylpyrrole. Structures when reacting with benzene are analogous.

Also notable is that the C–H activation step TS1 is significantly more destabilised for **6** versus **4** and **5** than it was for the analogous boron FLP **3** versus **2** and **1**. For reaction with *N*-methylpyrrole the destabilisation is 3.9 kcal mol^{-1} for the aluminium FLP **6**

compared to 1.9 kcal mol^{-1} for the boron FLP **3**. For reaction with benzene the difference is less pronounced with a destabilisation of 2.7 kcal mol^{-1} for the aluminium FLP **6** compared to 1.5 kcal mol^{-1} for the boron FLP **3**. A look at the structure of these transition states reveals that the longer Al–C bonds (2.00 Å and 2.08 Å for *N*-methylpyrrole and 1.99 Å and 2.14 Å for benzene) in the transition states of **6** force the substrate up towards the methyl groups of the tetramethypiperidyl group (Figure 46). For comparison the boron FLP 3 the bond lengths are 1.62 Å and 1.68 Å for *N*-methylpyrrole and 1.61 Å and 1.80 Å for benzene. This results in increased steric demand in the transition states. This can be seen by looking at the torsion angle indicated between the methyl groups on the tetramethylpiperidyl group.

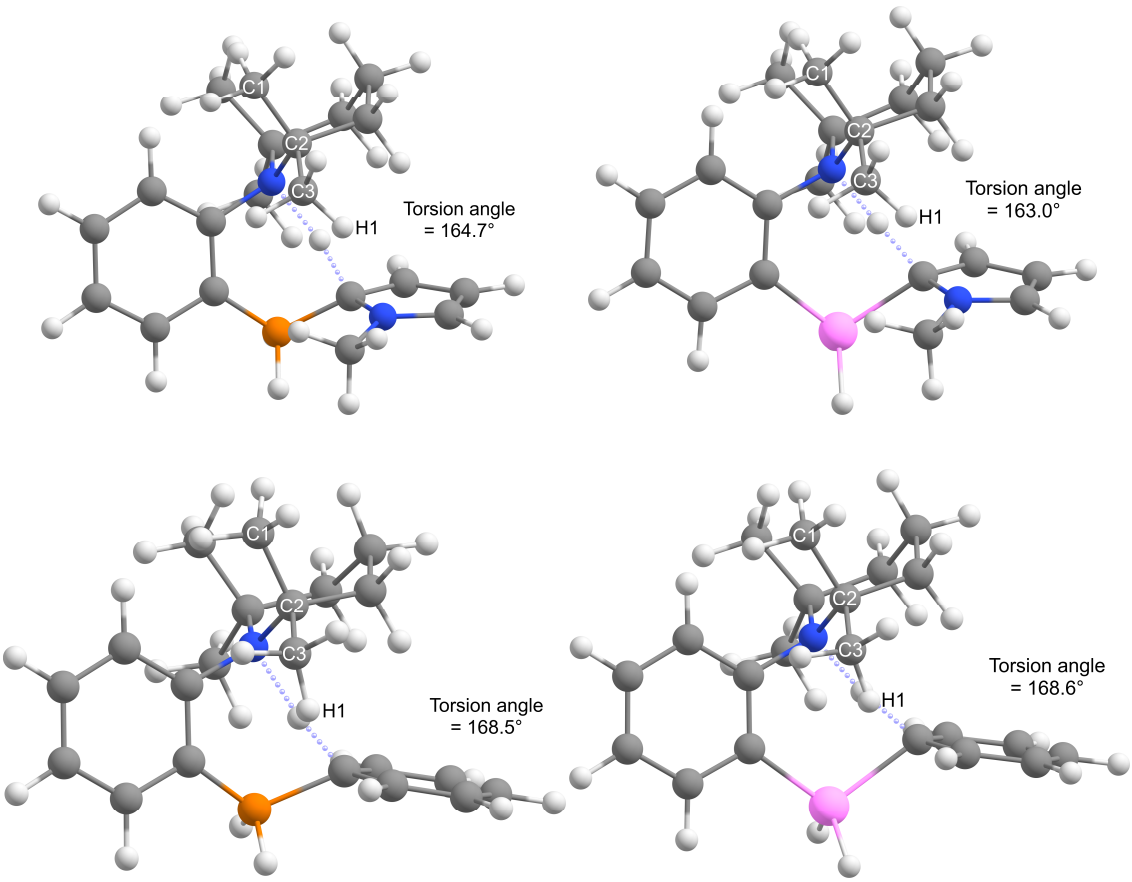

Figure 46 – Side on view of TS1 for 3 and 6 for reaction with *N*-methylpyrrole and benzene. Torsion angles (C1–C2–C3–H1) indicated.

For the transition states of **6** the torsion angles are further away from the ideal 180° than for the transition states of **3**, showing the increased steric demand. It can also be seen that the difference in torsion angles is greater for the transition states involving

N-methylpyrolle, as the methyl group on the *N*-methylpyrolle imposes greater steric demand than the flat benzene ring. This explains the increased destabilisation of the C–H activation step TS1 for the aluminium FLP **6** relative to the boron FLP **3**.

The last notable difference for the aluminium FLPs is that for all three FLPs the C–H activation step TS1, zwitterion IM2, and hydrogen loss step TS2 are all much higher in energy relative to IM1 than for the boron FLPs. Al–C bonds (58 kcal mol^{-1}) are significantly weaker than B–C bonds (107(7) kcal mol^{-1}).[3] Therefore the breaking of the C–H bond of the substrate is less compensated by formation of the Al–C bonds in TS1, IM2, and TS2 than by the B–C bonds. This raises the energy of these structures significantly relative to the boron FLPs.

5.2.3 Gallium

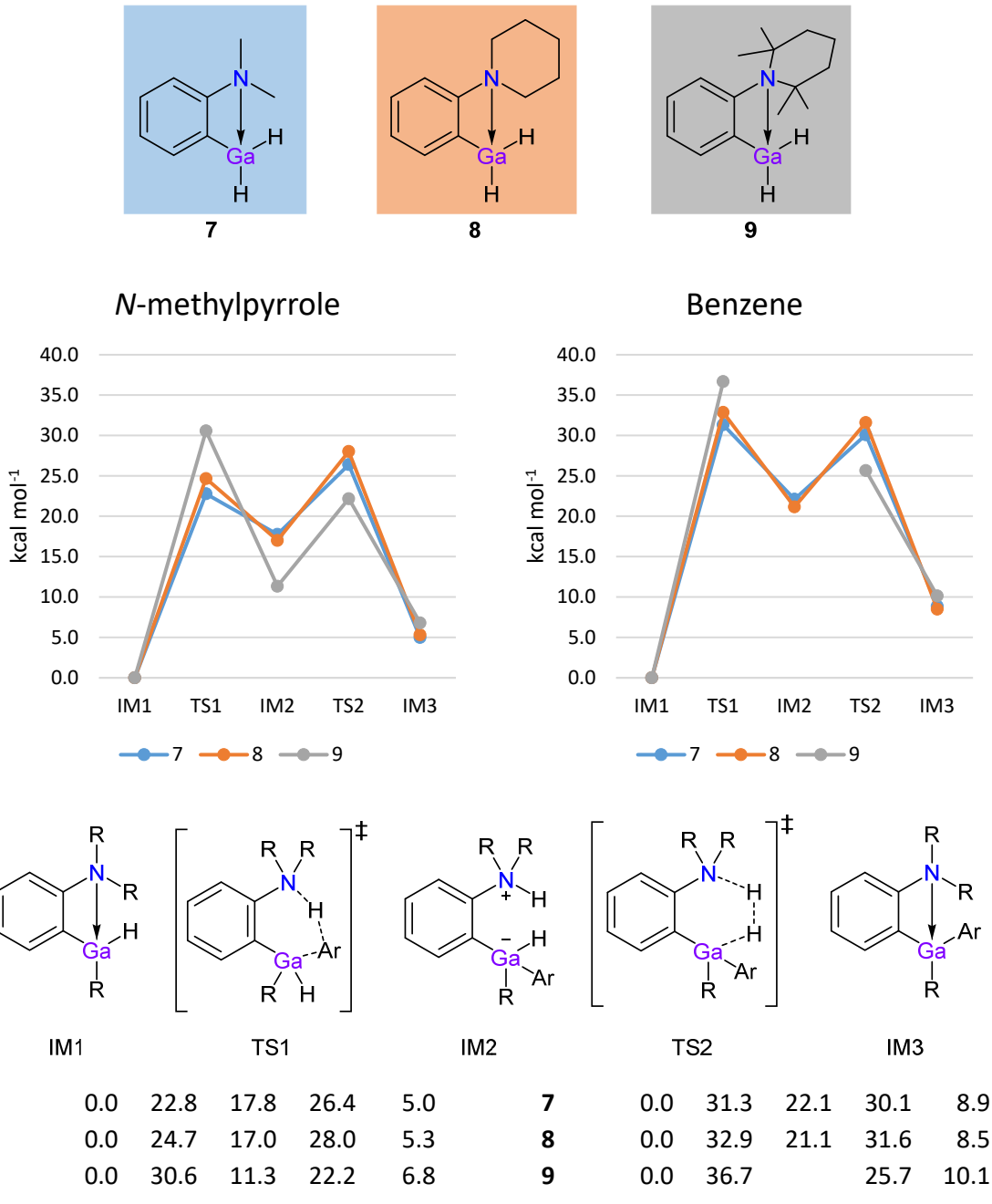

7	0.0	22.8	17.8	26.4	5.0	**7**	0.0	31.3	22.1	30.1	8.9
8	0.0	24.7	17.0	28.0	5.3	**8**	0.0	32.9	21.1	31.6	8.5
9	0.0	30.6	11.3	22.2	6.8	**9**	0.0	36.7		25.7	10.1

Figure 47 – Energies of reaction steps for C-H activation of *N*-methylpyrrole and benzene for 7-9. All energies given in kcal mol^{-1} relative to the starting materials. Calculations carried out at the wb97xd/6-311++g(d,p) level of theory with SMD solvation (chloroform).

The gallium-based FLPs **7**-**9** display trends in energies that are identical to that of aluminium FLPs. There is no marked increase in the energies of TS1, IM2, and TS2 relative to the aluminium FLPs like there was for the aluminium FLPs compared to the boron FLPs. Instead there is a slight decrease. As gallium is in the fourth period of the

periodic table it has an additional 10 protons and a fully occupied set of d orbitals, which boron and aluminium do not have in their frontier orbital configurations. The extra positive charge of the additional protons gives rise to gallium having anomalous properties. This effect is known as the d-block contraction. For example, gallium has a much smaller radius than would be expected for the trend down the group, and is in fact almost the same size as aluminium. It also possesses properties that are very similar to aluminium for the same reason. This similarity in properties can be seen in the bond energies where the Ga–C bond energy is 60 kcal mol^{-1} and the Al–C bond energy is 58 kcal mol^{-1},[3,4] relative to boron where the bond energy is 107(7) kcal mol^{-1}.[3] This explains the very minor change in energies of TS1, IM2, and TS2 when descending the group from aluminium to gallium.

The amount of destabilisation of the C–H activation step TS1 has once again increased for the gallium FLP **9** relative to the aluminium FLP **6**. This again shows in the torsion angles on the tetramethylpiperidyl group being smaller for **9**. For *N*-methylpyrrole the angle is 162.7° for **9** relative to 163.0° for **6**, and for benzene the angles are 166.6° for **9** and 168.6° for **6**.

5.2.4 Intramolecular N–H interactions in IM2

When looking more closely at the quantitative stabilisation of the zwitterion IM2 provided for boron, aluminium, and gallium when moving to the tetramethylpiperidyl-substituted FLPs **3**, **6**, and **9**, it can be seen that the amount of stabilisation is not consistent between *N*-methylpyrrole and benzene. For boron IM2 is more stabilised for the benzene reaction, while for aluminium and gallium IM2 is more stabilised for the *N*-methylpyrolle reaction. It was proposed that this is due to differing interactions between the N–H bond and atoms attached to the Lewis acidic half of the FLP.

Looking first at the aluminium and the gallium FLPs, in the case of reaction with both *N*-methylpyrrole and benzene the structures of the zwitterion IM2 are of the same general strucutre for both the dimethylamino- and tetramethylpiperidyl-substituted FLPs (Figure 48).

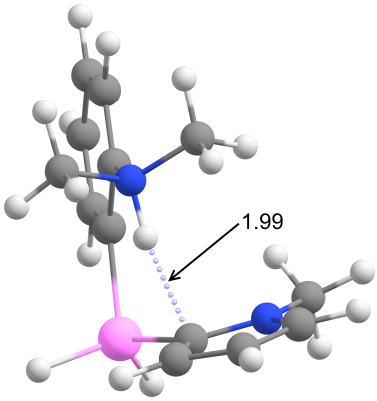

IM2 of **4** (*N*-methylpyrrole)

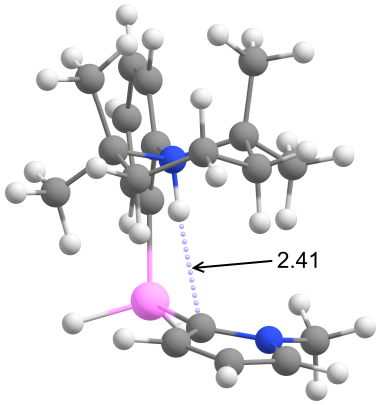

IM2 of **6** (*N*-methylpyrrole)

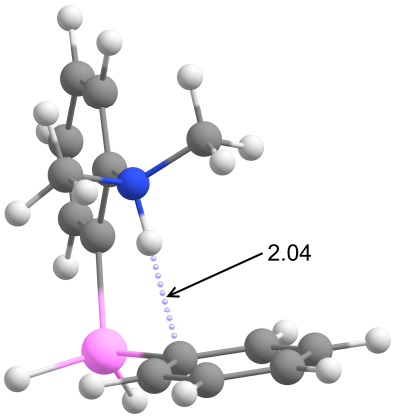

IM2 of **4** (benzene)

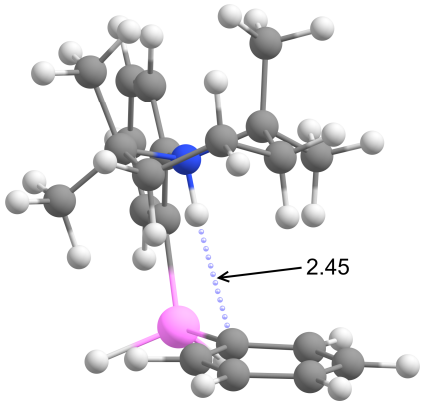

IM2 of **6** (benzene)

Figure 48 – Structures of IM2 for aluminium FLPs 4 and 6 with *N*-methylpyrrole and benzene. Select bond lengths are shown (Å). Structures are analogous for gallium FLPs 7 and 9.

The structures show an interaction between the N–H bond and the aromatic carbon atom α to the FLP metal centre. When moving from **4** to **6**, the greater basicity of the amine stabilises the interaction in **6** relative to **4**, despite the increased distance seen between the hydrogen and carbon atoms. This is likely one of the main contributing factors to the greater stabilisation in the *N*-methylpyrrole intermediate (6.5 kcal mol^{-1}) relative to the benzene intermediate (3.5 kcal mol^{-1}) due to the greater electron density

of the aromatic system in *N*-methylpyrrole making the interaction with the N–H even more stabilising.

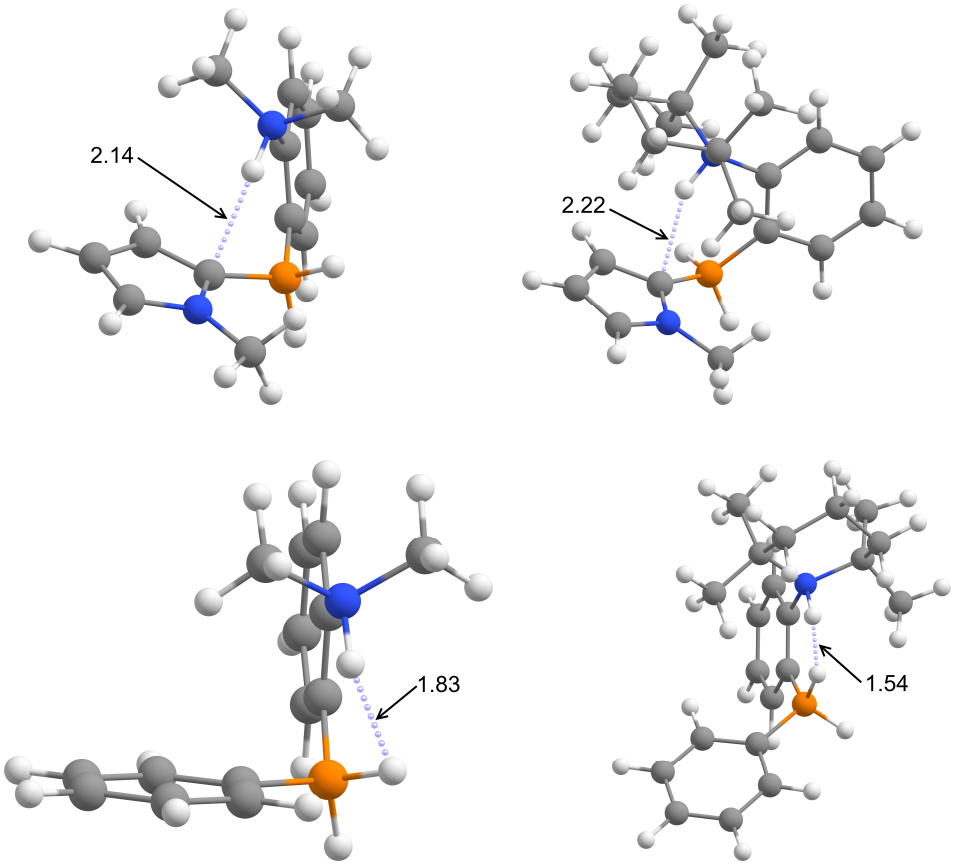

Figure 49 – Structures of IM2 for FLP 1 and 3 with *N*-methylpyrrole and benzene. Select bond lengths are shown (Å).

When now looking at the structures of the zwitterion IM2 for the boron FLPs, the structure is the same as previously for the reaction with *N*-methylpyrrole, displaying the interaction between the N–H bond and the aromatic carbon atom α to the boron centre (Figure 49). However, for the reaction with benzene, this interaction is no longer present and there is instead an interaction between the N–H bond and a hydride on the boron centre (Figure 49).

For the *N*-methylpyrrole intermediate the H–C distance increases on moving from **1** to **3**, in the same manner as was seen for the aluminium and gallium FLPs. In the benzene case however, the H–H distance decreases when moving from **1** to **3**. This means that the stabilisation trend is reversed for boron, with the *N*-methylpyrrole intermediate

being stabilised by 4.1 kcal mol^{-1} and the benzene intermediate being stabilised by 8.3 kcal mol^{-1}.

The reason for this differing interaction with boron is that the reduced B–C bond length (relative to the Al–C and Ga–C bond lengths) to the ligand and substrate twist the angle of the interaction between the N–H bond and the aromatic carbon atom α to the boron centre (Figure 50), greatly lowering the stabilisation due to decreased orbital overlap. For the reaction with *N*-methylpyrrole, this decreases the stabilisation in the case of boron to 4.1 kcal mol^{-1}, relative to the 6.5 kcal mol^{-1} stabilisation for aluminium and 5.7 kcal mol^{-1} stabilisation for gallium. For benzene, the destabilisation of this interaction is enough for the zwitterion IM2 to adopt the alternate configuration for the boron FLPs.

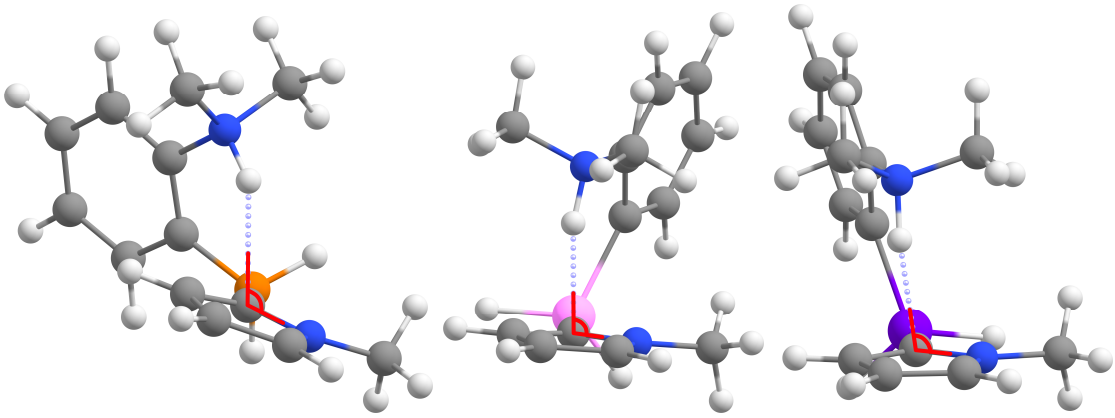

Figure 50 – View of torsion angle H–M–C–N (M = B, Al, Ga) for IM2 in reaction with *N*-methylpyrrole for 1, 4, and 7.

5.2.5 Effect of steric bulk on the reaction profile

To summarise the above analysis, the effect of increasing steric bulk on the reaction steps relative to the starting point IM1 is as follows (Table 2).

Step	Effect of increased steric bulk
TS1	Destabilising
IM2	Little effect
TS2	Stabilising
IM3	Destabilising

Table 2 – Summary of effect of increasing steric bulk on reaction steps.

In addition, it can be seen that increased steric bulk has a great effect on the boron FLPs, causing certain intermediates to have different structures when the steric bulk is increased, due to the short B–C bond lengths. Meanwhile in the aluminium and gallium FLPs the structures are the same regardless of the amount of steric bulk, but due to the Al–C and Ga–C bond lengths being longer than the B–C bonds, greater steric bulk at the nitrogen centre causes greatly increased destabilisation of the C–H activation step TS1, as the substrate is forced upwards towards the steric bulk at the nitrogen centre for the aluminium and gallium FLPs.

5.3 Lewis basicity

The second property examined was the Lewis basicity of the FLP. It was expected that increased Lewis basicity would decrease the energy of the C–H activation step TS1 and zwitterion IM2 due to stronger interaction with the H atom and increase the energy of the hydrogen loss step TS2 where the bond between the Lewis base and the hydrogen atom is broken.

In order to assess the effect of changing the Lewis basicity, the standard dimethylamino-substituted FLPs **1**, **4**, and **7** were used as the baseline for comparison. Pyrollidine and aziridine substituents were selected as a way of influencing the basicity of the nitrogen lone pair through constraining the C–N–C bond angle, increasing the s-character of the lone pair and so decreasing basicity as the angle tightens. The dimethylphosphino-substituent was chosen to see how descending group 15 affected the properties with the various group 13 elements as the Lewis acid. Finally the pyridine substituent was chosen due to the sp^2 hybridised lone pair in contrast to the sp^3 hybridisation of the other examples. This lead to the trial set of FLPs seen below (Figure 51).

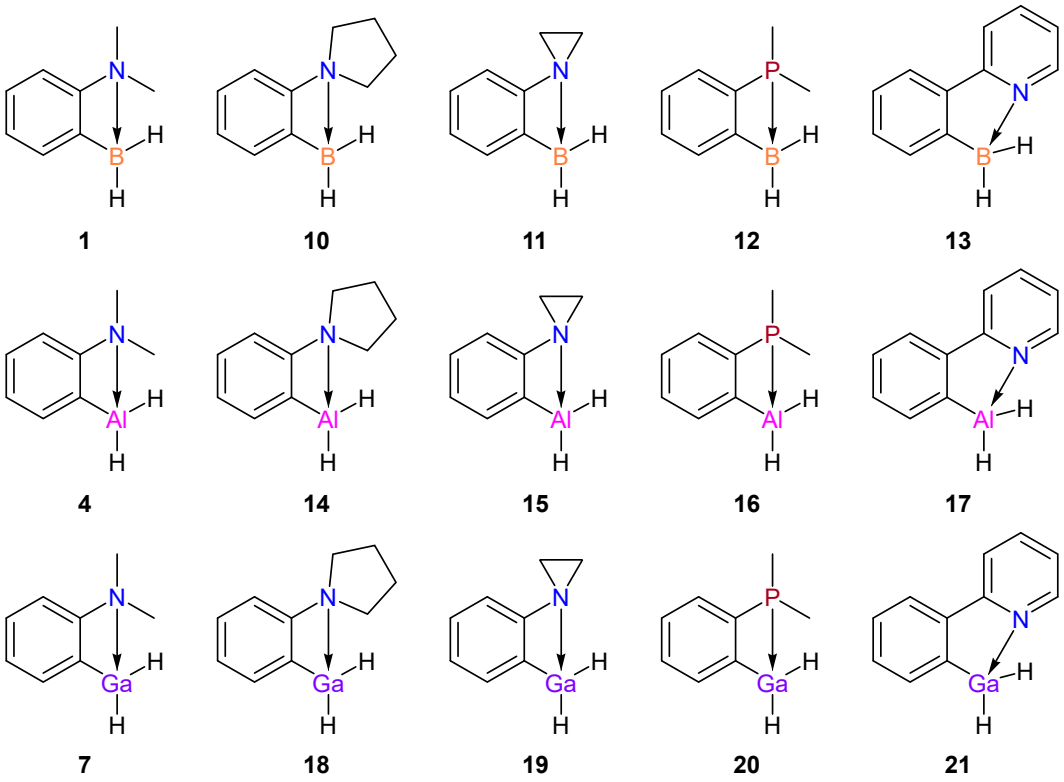

Figure 51 – Selected FLP frameworks for assessing Lewis basicity.

5.3.1 Boron

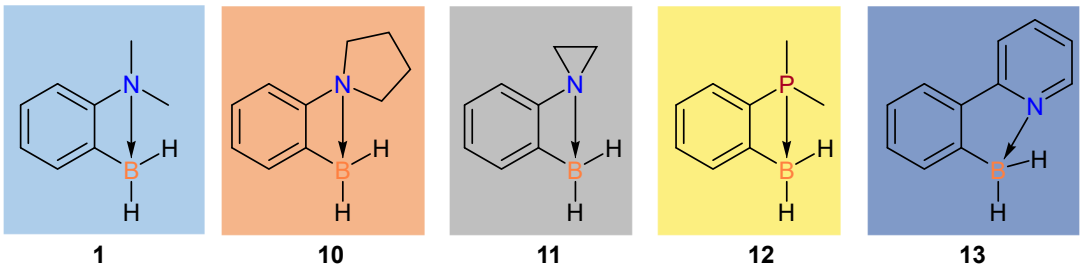

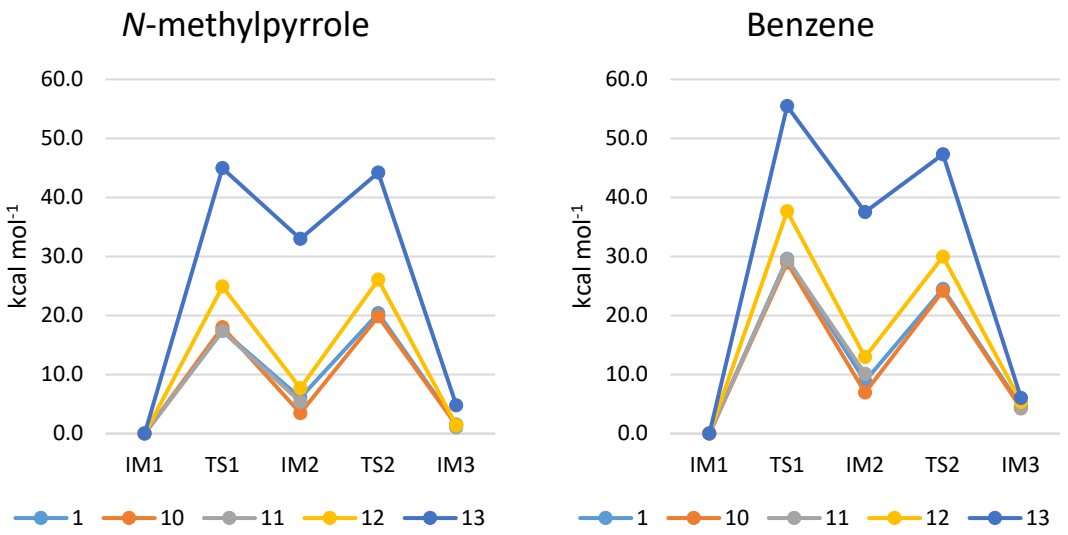

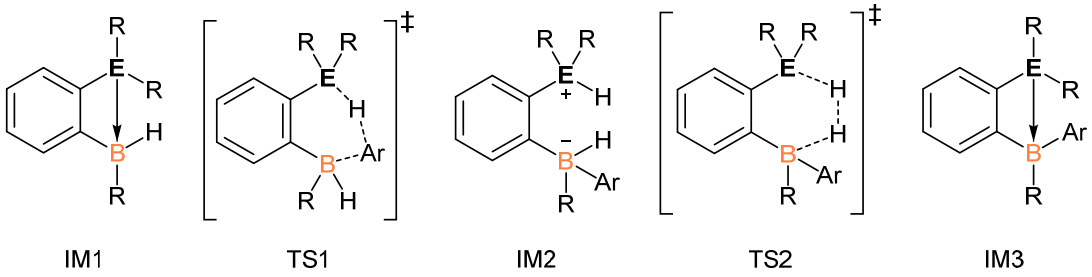

1	0.0	17.5	6.1	20.4	1.5	**1**	0.0	29.6	8.9	24.5	4.6
10	0.0	18.0	3.5	19.8	1.4	**10**	0.0	28.9	6.9	24.2	4.3
11	0.0	17.4	5.4		1.0	**11**	0.0	29.5	10.1		4.3
12	0.0	24.9	7.7	26.1	1.4	**12**	0.0	37.6	13.0	30.0	5.4
13	0.0	45.0	33.0	44.2	4.8	**13**	0.0	55.5	37.5	47.3	6.0

Figure 52 – Energies of reaction steps for C-H activation of *N*-methylpyrrole and benzene for 1 and 10-13. All energies given in kcal mol^{-1} relative to the starting materials. Calculations carried out at the wb97xd/6-311++g(d,p) level of theory with SMD solvation (chloroform).

In order to assess the basicity of each FLP, NBO analysis was carried out on **1** and **10**-**13** to look at the sp character of the lone pair based orbital in the N–B (or P–B) bond (Table 3).

FLP	sp hybridisation
1	$sp^{8.44}$
10	$sp^{8.55}$
11	$sp^{4.42}$
12	$sp^{2.08}$
13	$sp^{1.98}$

Table 3 – Results of NBO analysis for sp hybridisation of the lone pair based orbital in the N–B (or P–B) bond of FLPs 1, 10, and 11, 12, and 13.

Higher p character of the lone pair can be associated with higher basicity. Therefore, when looking at these results it can be suggested that the pyrrolidine-substituted FLP **10** has slightly increased basicity over **1**. The aziridine-substituted FLP **11** has highly reduced basicity due to the large ring strain greatly reducing the p character of the lone pair. **12** and **13** both appear to have have greatly reduced basicity relative to the amine based FLPs **1**, **10**, and **11**.

In order to check that this sp assessment of basicity is qualitatively accurate, pkaH values were found for the substituent groups to check the trends matched up (Table 4). These pkaH values map well onto the sp hybridisation trends seen from the computational NBO analysis (Table 3). The exception being that pyridine is experimentally more basic than suggested by the calculations.

Substituent	pkaH
Dimethylamine (**1**)	10.71
Pyrrolidine (**10**)	11.27
Aziridine (**11**)	8.04
Dimethylphosphine (**12**)	3.91
Pyridine (**13**)	5.17

Table 4 – pkaH values for the substituent groups of FLPs 1 and 10-13.[5]

When assessing how this change in basicity affects the energy of the reaction profile, it is important to note that changing of the ligand groups has also had an effect on the

steric bulk of the FLPs and so that must be taken into account. From the previous analysis of steric bulk, it was seen that increased steric bulk increased the energy of the C–H activation step TS1 and decreased the energy of the hydrogen loss step TS2. As the tertiary amine based FLPs **1**, **10** and **11** all possess the same type of nitrogen-based lone pair, it is easiest to tease apart these two combined effects when looking at the energies for these three FLPs.

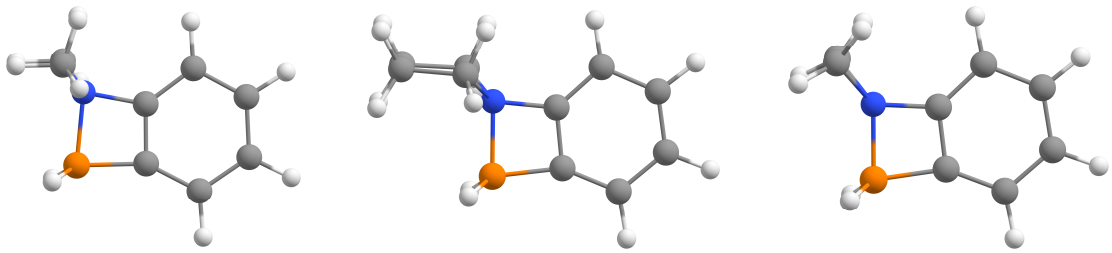

Figure 53 – Side on view of FLPs 1, 10, and 11.

By looking at a side on view of the **1**, **10** and **11** (Figure 53), it can be seen that for the pyrrolidine-substituted FLP **10**, the hydrogen atoms point on the carbon atoms alpha to the nitrogen point further downward towards the boron centre compared to the dimethylamino-substituted FLP **1**, meaning that **10** has slightly increased steric bulk at the reactive area of the FLP. In the aziridine-substituted FLP **11** however, the hydrogen atoms on the alpha carbon are much further away from the reactive area due to the highly constrained nature of the aziridine ring and so **11** has reduced steric bulk at the reactive area compared to **1**.

As the differences in energies for these calculations are small (within 1-2 kcal mol^{-1} of each other), the values are within error of each other, and so the discussion that follows is given with this caveat in mind.

For the C–H activation step TS1, the pyrrolidine-substituted FLP **10** has a 0.5 kcal mol^{-1} higher energy relative to the dimethylamino-substituted FLP **1** for *N*-methylpyrrole, and a 0.7 kcal mol^{-1} lower energy for benzene. As benzene has a C–H bond that is more difficult to activate that *N*-methylpyrrole, the effect of the basicity is more pronounced in this case. From this we can see that increased basicity lowers the energy of TS1, as expected. The increased energy of TS1 for *N*-methylpyrrole in this case is due to the

increased steric bulk of **10**. For the aziridine-substituted FLP **11** the energy of TS1 is almost identical to **1** for both substrates. This is due to the effect of decreased basicity and decreased steric bulk cancelling each other out.

For the zwitterion IM2, the same effect is seen as was discussed in section 5.2.4 (*vide supra*). Increased basicity stabilises this intermediate, which is seen for the pyrrolidine-substituted FLP **10** with stabilisations of 2.6 kcal mol^{-1} and 2.0 kcal mol^{-1} relative to **1** for *N*-methylpyrrole and benzene respectively. the aziridine-substituted FLP **11** is 1.2 kcal mol^{-1} less stable than the dimethylamino-substituted FLP **1** in the case of benzene as expected, but 0.7 kcal mol^{-1} more stable in the case of *N*-methylpyrrole. This is again due to the steric effect counteracting the effect of the basicity.

The effect on the hydrogen loss step TS2 is difficult to evaluate here due to the lack of data for **11** and will instead be discussed in detail for the aluminium FLPs.

For IM3, no significant difference in energies is seen for **1**, **10**, and **11**. This indicates that there is little effect of Lewis basicity on IM3. This can be explained by the fact that any effect of the Lewis basicity on IM3 will have also affected IM1, making their relative energies the same. For **12** and **13** the energy of IM3 is raised. This is likely due to the increased steric bulk provided by the now attached aryl group having more of an effect due to the weaker P–B bond and the different geometry of the pyridine FLP respectively.

The dimethylphosphino-substituted FLP **12** has slightly higher energies across the entire reaction profile. When moving down the group from phosphorus to nitrogen there are weaker P–H bonds (77 kcal mol^{-1}) vs N–H bonds (92 kcal mol^{-1}). The fact that these bonds are present in the C–H activation step TS1, zwitterion IM2, and hydrogen loss step TS2 explain the elevated energies.[4]

The pyridine-substituted FLP **13** has greatly increased energies for TS1, IM2, and TS2. The low basicity of the lone pair accounts for some of this but in addition, the change from a four membered FLP core to a five membered FLP core greatly stabilises the starting catalyst IM1 and the C–H activation product IM3, therefore raising the energy of TS1, IM2, and TS2 greatly.

5.3.2 Aluminium

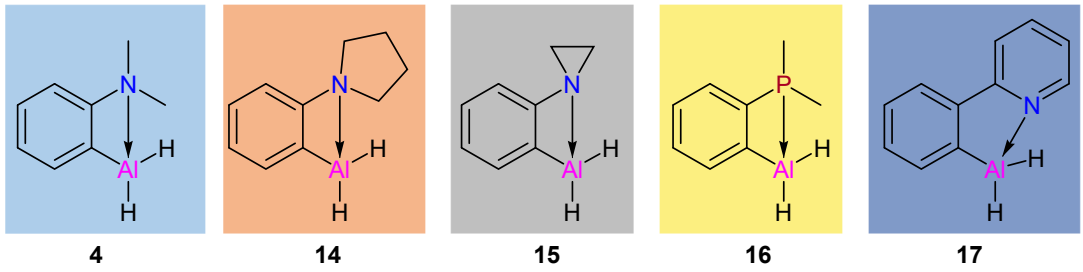

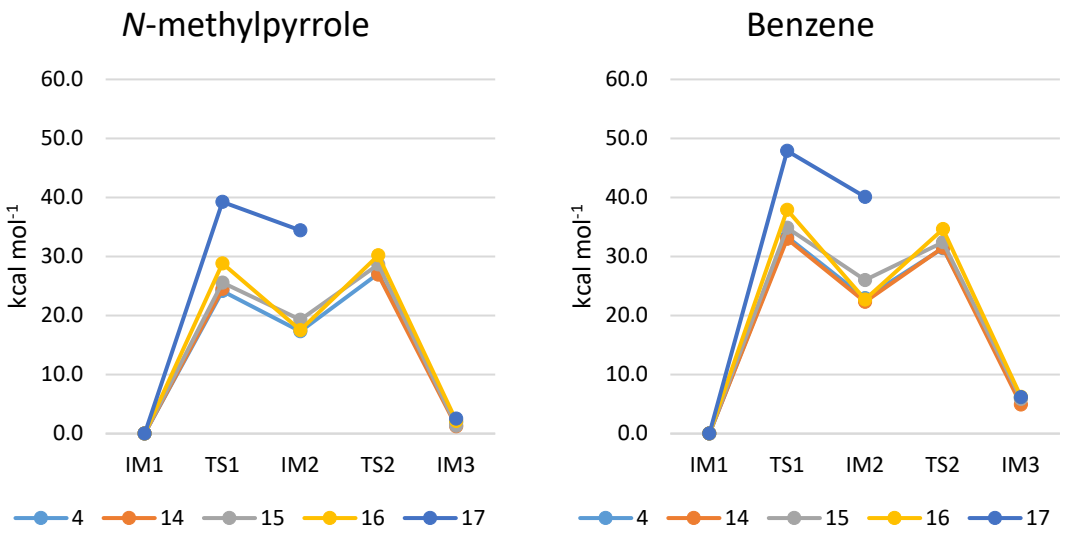

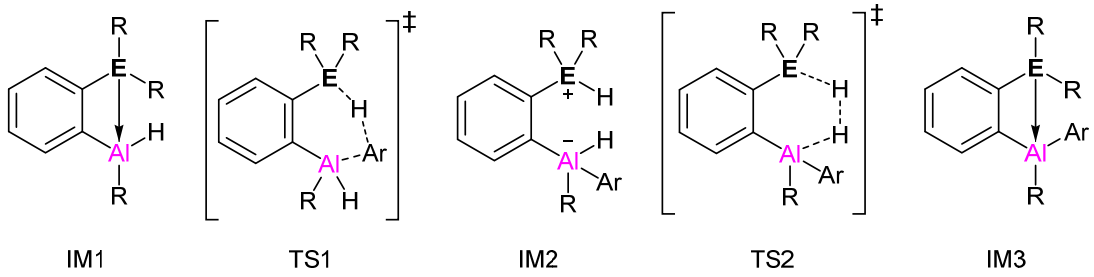

4	0.0	24.2	17.3	27.1	1.9	**4**	0.0	33.3	22.9	31.4	6.1
14	0.0	24.5		26.9	1.2	**14**	0.0	33.0	22.3	31.5	4.9
15	0.0	25.6	19.3	28.6	1.3	**15**	0.0	34.9	26.0	32.4	5.9
16	0.0	28.8	17.5	30.2	2.1	**16**	0.0	37.9	22.7	34.6	6.2
17	0.0	39.3	34.4		2.5	**17**	0.0	47.9	40.1		6.2

Figure 54 – Energies of reaction steps for C-H activation of *N*-methylpyrrole and benzene for 4 and 14-7. All energies given in kcal mol^{-1} relative to the starting materials. Calculations carried out at the wb97xd/6-311++g(d,p) level of theory with SMD solvation (chloroform).

When looking at the trends in energy for the aluminium FLPs **4** and **14**-**17**, the steric effect on the energy is slightly reduced due to the longer N–Al adduct bond and a more

accurate picture of the effect of the basicity can be seen. This is most evident for the aziridine-substituted FLP **15**, where the lower basicity is now the dominant factor in the energy difference, while for boron the steric factor was the most important. the C–H activation step TS1 and zwitterion IM2 are now higher in energy for both *N*-methylpyrrole and benzene as expected from the lower basicity of **15**.

Looking at hydrogen loss step TS2 in detail, it can be seen that for the pyrrolidine-substituted FLP **14**, a 0.2 kcal mol^{-1} destabilisation is seen for *N*-methylpyrrole and a 0.1 kcal mol^{-1} stabilisation is seen for benzene. Since increased steric bulk stabilised TS2, the fact that TS2 is destabilised for benzene indicates that the increased basicity destabilised TS2. This is a result of the more basic nitrogen having a stronger N–H bond to broken in TS2, raising the energy of this step. This means that for the aziridine-substituted FLP **15** the reduced basicity (and therefore weaker N–H bond) should stabilise TS2, but once again the greatly reduced sterics of the aziridine ring overrides this and a destabilisation of a 1.5 kcal mol^{-1} is seen for *N*-methylpyrrole and 1.0 kcal mol^{-1} for benzene.

The dimethylphosphino-substituted FLP **16** once again has higher energies across the board relative to the tertiary amine based FLPs due to the reduced basicity of the phosphorus lone pair. However, the size of the difference is not as large as for the boron FLP. B–N (90(2) kcal mol^{-1}) and B–P bonds (83(4) kcal mol^{-1}) are close in energy.[3] However, Al–P bonds (52(3) kcal mol^{-1}) are significantly weaker than Al–N bonds (88(4) kcal mol^{-1}).[3] This means that the energetic cost of breaking the Al–P bond is much lower relative to Al–N than the respective boron case. Consequently, this lowers the energy of the structures where this bond has been broken, namely the C–H activation step TS1, zwitterion IM2, and hydrogen loss step TS2, for **16** relative to the tertiary amine based FLPs **4**, **14**, and **15**.

The pyridine-substituted FLP **17** remains greatly destabilised, although the difference is not as great as for the boron FLPs, due to the decreased steric effect for the aluminium FLPs.

5.3.3 Gallium

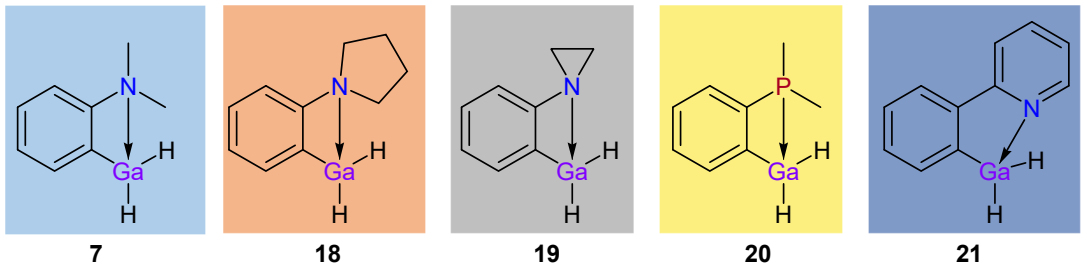

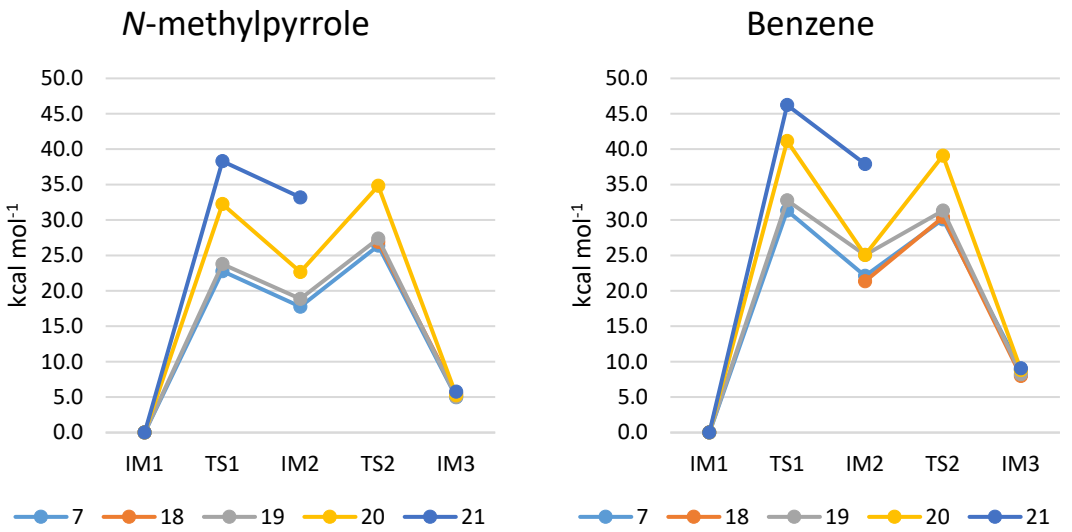

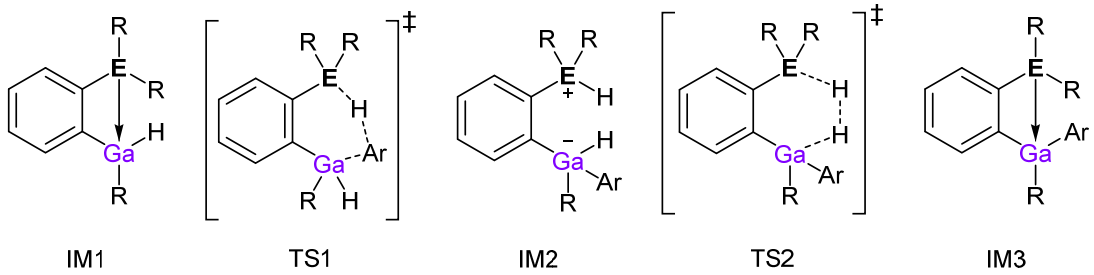

7	0.0	22.8	17.8	26.4	5.0	**7**	0.0	31.3	22.1	30.1	8.9
18	0.0			26.9	5.4	**18**	0.0		21.4	30.4	8.0
19	0.0	23.8	18.9	27.4	5.0	**19**	0.0	32.8	25.1	31.3	8.2
20	0.0	32.2	22.7	34.8	5.2	**20**	0.0	41.2	25.1	39.1	8.8
21	0.0	38.3	33.2		5.8	**21**	0.0	46.2	37.9		9.1

Figure 55 – Energies of reaction steps for C-H activation of *N*-methylpyrrole and benzene for 7 and 18-21. All energies given in kcal mol^{-1} relative to the starting materials. Calculations carried out at the wb97xd/6-311++g(d,p) level of theory with SMD solvation (chloroform).

For the gallium FLPs **7** and **18**-**21**, the differences in energies for the reaction profiles are similar to the aluminium FLPs, consistent with the similar nature of aluminium and gallium.

However, a notable difference is that the dimethylphosphino-substituted FLP **20** is greatly destabilised relative to the nitrogen based FLPs **7**, **18**, and **19**, in a manner more similar to that of the of the boron FLPs and unlike the case for the aluminium FLPs. Ga–P bonds (55(3) kcal mol^{-1}) are again weaker than Ga–N bonds (~72 kcal mol^{-1}).[3,6] However, The difference is not as great as for Al–P bonds (52(3) kcal mol^{-1}) versus Al–N bonds (88(4) kcal mol^{-1}).[3] This means that the trend in the energies of the C–H activation step TS1, zwitterion IM2, and hydrogen loss step TS2 returns to resembling the case for the boron FLPs.

5.3.4 Effect of Lewis basicity on the reaction profile

In summary of the above analysis, the effect of increasing Lewis basicity on the reaction steps relative to the starting point IM1 is as follows (Table 5).

Step	Effect of increased Lewis basicity
TS1	Stabilising
IM2	Stabilising
TS2	Destabilising
IM3	Little Effect

Table 5 – Summary of effect of increasing Lewis basicity on reaction steps.

5.4 Effect of changing Lewis acidity on C–H activation

The final property examined was the Lewis acidity of the FLP. It was expected that increased Lewis acidity would decrease the energy of the C–H activation step TS1 and zwitterion IM2 due to stronger interaction with the C atom of the aromatic molecule and increase the energy of the hydrogen loss step TS2 where the Lewis acid hydrogen atom bond is broken.

In order to investigate changes in the Lewis acidity of the FLPs, two differing methods were used. One was modification of the ligand backbone, and the other was direct substitution of the groups on the Lewis acidic atom. Addition of para-methoxy and para-CF_3 groups were chosen to assess the effect of electron donating and withdrawing groups on the aromatic backbone on the acidity. Pentafluorophenyl substitution directly on the Lewis acidic centre was chosen as C_6F_5 substitution is a common strategy for generating highly Lewis acidic species in the literature.[7–10] NHC substitution was chosen to assess the effect of using a cationic species. This lead to the trial set of FLPs seen below (Figure 56). For the reaction profile with *N*-methylpyrrole, optimisation of the structures for the NHC-substituted FLPs **25**, **29**, and **33** could not be achieved so they have been omitted from this analysis.

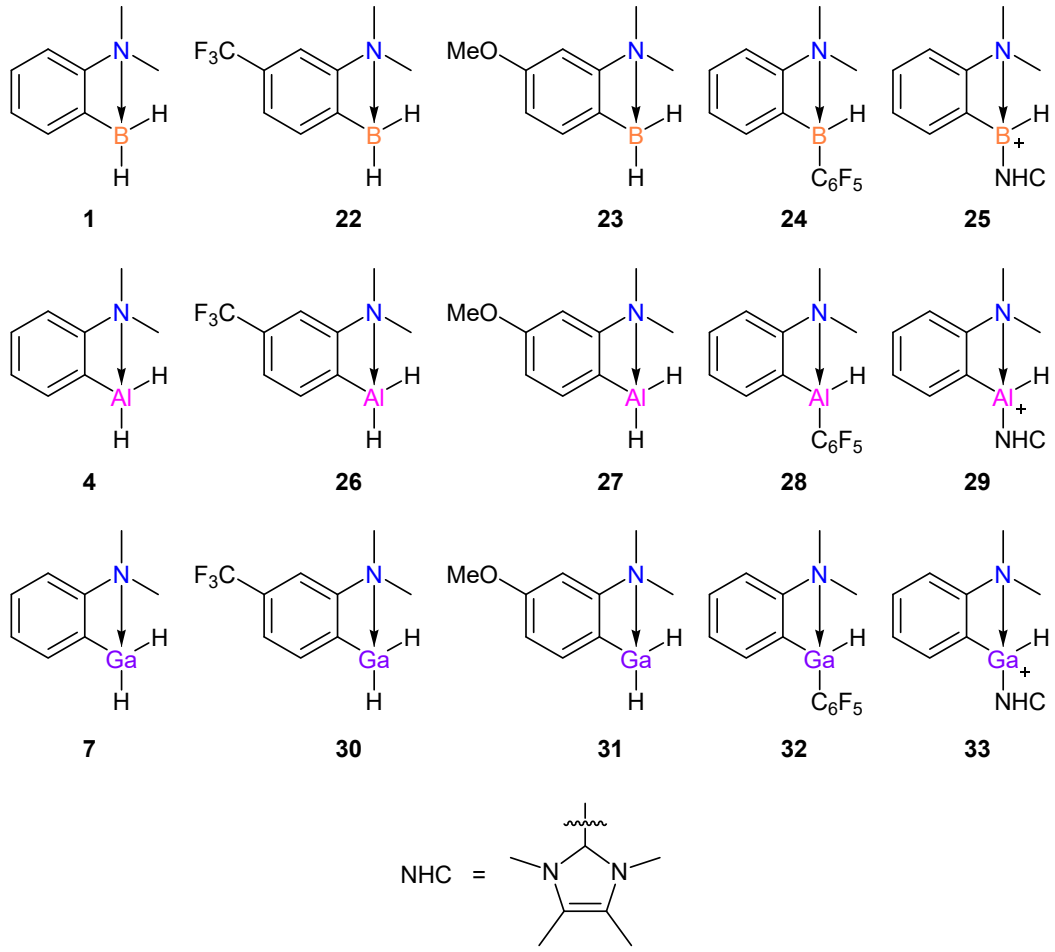

Figure 56 – Selected FLP frameworks for assessing Lewis acidity.

5.4.1 Boron

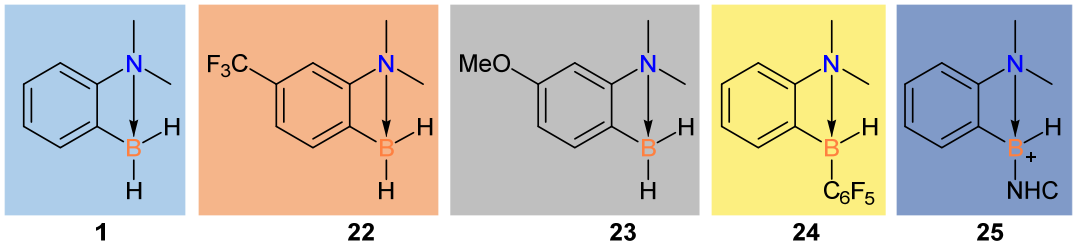

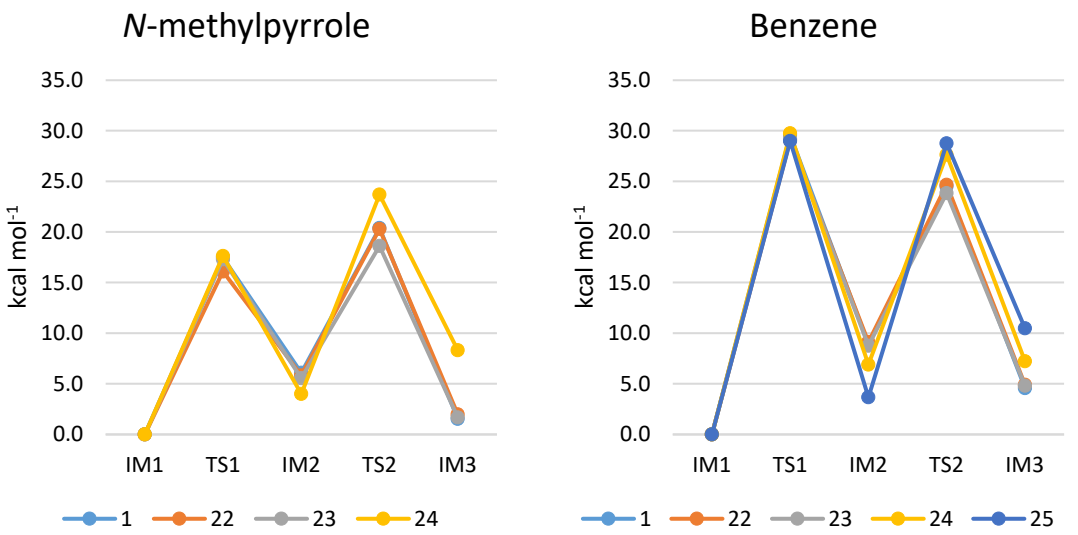

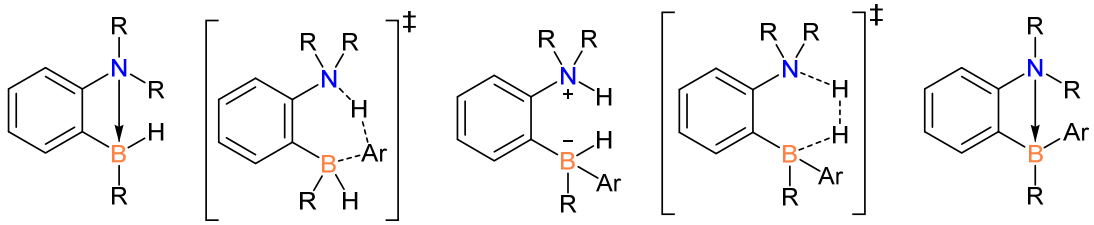

1	0.0	17.5	6.1	20.4	1.5
22	0.0	16.1	5.8	20.3	2.0
23	0.0	17.3	5.5	18.6	1.7
24	0.0	17.6	4.0	23.7	8.3

1	0.0	29.6	8.9	24.5	4.6
22	0.0	29.1	9.1	24.7	4.9
23	0.0	29.2	8.8	23.8	4.8
24	0.0	29.7	6.9	27.6	7.2
25	0.0	29.0	3.7	28.8	10.5

Figure 57 – Energies of reaction steps for C-H activation of *N*-methylpyrrole and benzene for 1 and 22-26. All energies given in kcal mol^{-1} relative to the starting materials. Calculations carried out at the wb97xd/6-311++g(d,p) level of theory with SMD solvation (chloroform).

In order to assess the acidity of each FLP, hydride ion affinity calculations were carried out. These were chosen over the also commonly used fluoride ion affinity calculations as the softer nature of the hydride ion better represents the carbon based aryl anions

that are present in the structures of the reaction mechanism. In order to do these calculations, open forms of the FLPs were first optimised to provide a vacant coordination site for the hydride to coordinate to. The affinities were then calculated by evaluation of the hydride migration reaction shown using BEt_3 as a reference molecule (Scheme 61), in order to avoid computational errors associated with naked hydride ions, using a method previously utilised in the literature.[11]

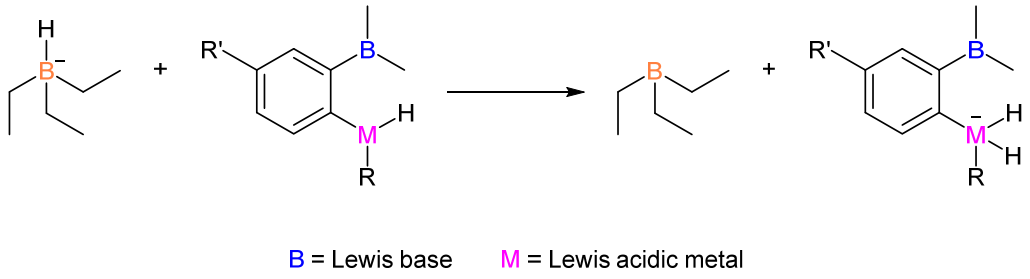

Scheme 61 – Reaction used to evaluate hydride ion affinities.

As well as the FLPs **1** and **22**-**25**, the hydride affinities of $B(C_6F_5)_3$ and of Fontaine's TMP-substituted boron based catalyst were also calculated, to give a reference point to one of the most commonly used Lewis acidic species and of the FLP catalyst used previously for these C–H borylations. This gave the following data on hydride affinities relative to BEt_3 (Table 6).

Species	Hydride affinity (kcal mol^{-1})
BEt_3	0.0
$B(C_6F_5)_3$	-41.7
Fontaine's catalyst	-18.6
1	-17.9
22	-22.2
23	-13.9
24	-25.0
25	-44.0

Table 6 – Hydride affinities of $B(C_6F_5)_3$, Fontaine's catalyst, and 1 and 22-25, relative to BEt_3. Calculations for structure optimisations were carried out at the wb97xd/6-311++g(d,p) level of theory with SMD solvation (chloroform).

As expected, the para-trifluoromethyl-substituted FLP **22** shows increased acidity relative to the dimethylamino-substituted FLP **1**, as shown by its increased hydride affinity. This is due to the electron withdrawing ability of the CF_3 group of **22** increasing

the Lewis acidity of the boron centre. Also notable is that the hydride affinity is close to that of Fontaine's catalyst, which is to be expected due to their similar structure.

The para-methoxy-substituted FLP **23** is conversely less Lewis acidic than **1**, shown by its lower hydride affinity. This is due to delocalisation of the oxygen lone pair through onto the boron as shown (Figure 58), increasing electron density at the boron centre.

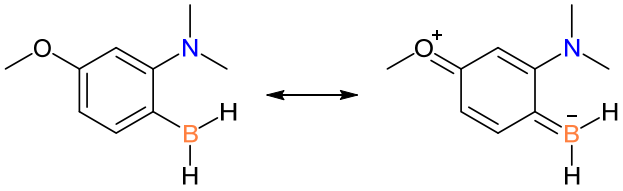

Figure 58 – Delocalisation of the oxygen lone pair onto the boron centre.

The pentafluorophenyl-substituted FLP **24** shows a much larger hydride affinity and therefore greatly increased Lewis acidity relative to **1**, as would be expected from the addition of the electron withdrawing group directly to the boron centre.

Finally, the NHC-substituted FLP **25** displays a much higher hydride affinity than the all of the other examples, even surpassing the hydride affinity of $B(C_6F_5)_3$. This is likely due to the highly electron deficient nature of **25**, given that it is cationic.

Now that the relative Lewis acidity of the FLPs has been established and explained, analysis of the effect it has on the energy of the reaction profile can be carried out. Again, the effects of both the changing Lewis acidity and steric bulk must be considered.

As before, the energies of the reaction profiles change little between the different FLPs, and so any conclusions drawn are given with the caveat that errors in the DFT calculation energies are significant relative to the differences in the energies.

Firstly considering TS1, it can be seen that the increased Lewis acidity of the para-trifluoromethyl-substituted FLP **22** causes a reduction in the energy of TS1 for the reactions with both N-methylpyrrole and benzene as would be expected as it is more able to activate the C–H bond for deprotonation. However, unexpectedly, the para-methoxy-substituted FLP **23** also causes a reduction in the energy of TS1 despite

its lower Lewis acidity. This can be rationalised by the fact that negative charge is building up on the boron centre in TS1 and the effect of inductive withdrawal by the para-methoxy group can stabilise this negative charge due to its para position. When considering the pentafluorophenyl-substituted FLP **24** and the NHC-substituted FLP **25**, it has been shown that the increased steric bulk of **24** and **25** will have destabilising effect on the C–H activation step TS1. Therefore, while their significantly greater Lewis acidity would be expected to lower the energy of TS1, but both **24** and **25** have very similar energies for TS1 compared to 1. This is due to the effect of the steric bulk.

The zwitterion IM2 is also stabilised by the increased Lewis acidity causing the B–C bond formed in IM2 to be stronger. This is seen my increasing stabilisation as the Lewis acidity of the FLPs increases from **22** to **25**. Again the para-methoxy-substituted FLP **23** goes against the trend with a lower energy of TS2 compared to **22**. This is again likely due to inductive withdrawal from the para-methoxy group stabilising the negative charge at the boron centre in the zwitterion.

For TS2, it is expected that increased Lewis acidity will raise the energy as the B–H bond being broken is stronger. This is indeed seen as **22**, **24**, and **25**, which all have higher Lewis acidity than **1** having increasing larger energies for TS2 versus **1**, even despite the stabilising influence of the steric bulk for **24** and **25**. As for **23**, which is the only FLP with lower Lewis acidity than **1**, it is seen to have a lower energy for TS2 than **1** as expected.

For IM3, no significant difference in energies is seen for **1**, **22**, and **23**. This indicates that there is little effect of Lewis acidity on IM3. In a similar manner to Lewis basicity, this can be explained by the fact that any effect of the Lewis acidity on IM3 will have also affected IM1, making their relative energies the same. For **24** and **25** the energy of IM3 is raised. This is due to the increased steric bulk as there are now two large aryl groups attached to the boron centre, which destabilised the N–B bond.

5.4.2 Aluminium

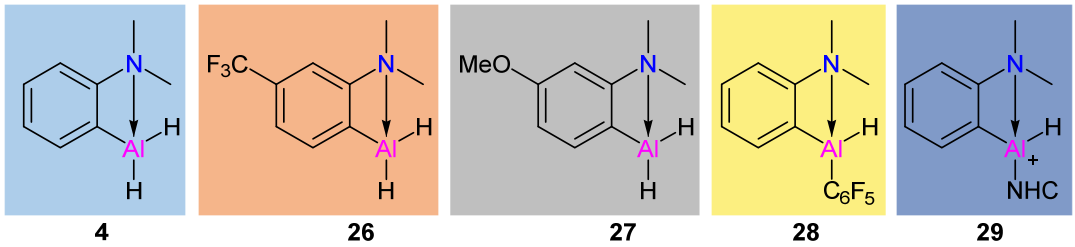

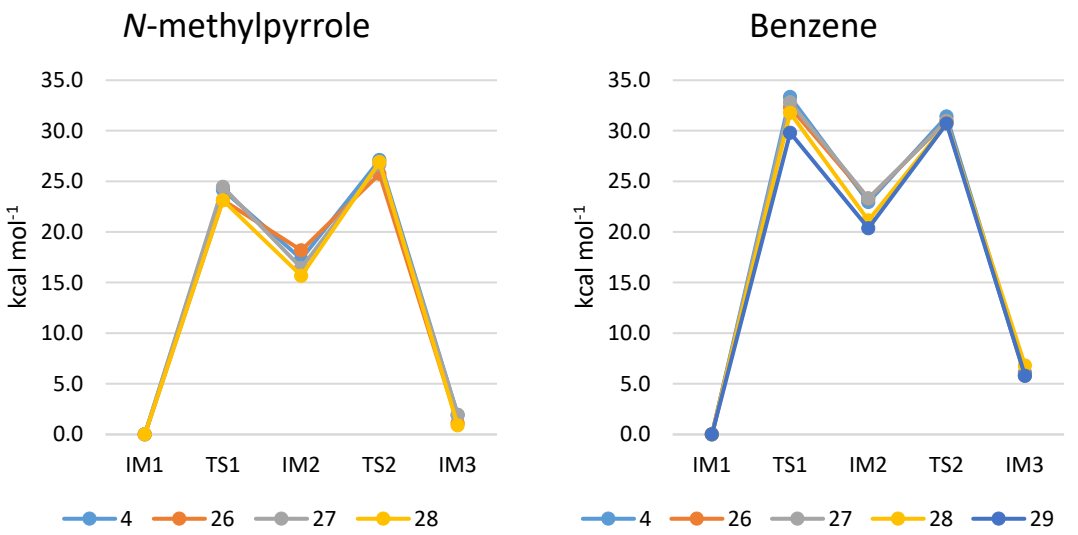

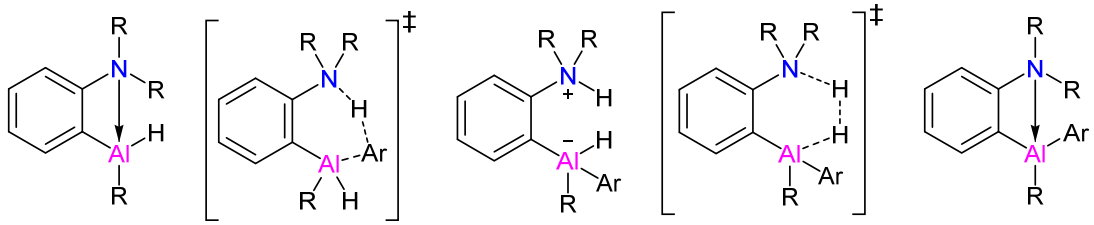

4	0.0	24.2	17.3	27.1	1.9
26	0.0	23.1	18.2	25.7	1.1
27	0.0	24.4	16.4	26.7	1.9
28	0.0	23.1	15.7	26.9	0.9

4	0.0	33.3	22.9	31.4	6.1
26	0.0	32.3	23.3	31.0	5.8
27	0.0	32.8	23.3	31.0	5.8
28	0.0	31.8	21.1	30.7	6.8
29	0.0	29.8	20.4	30.7	5.8

Figure 59 – Energies of reaction steps for C-H activation of *N*-methylpyrrole and benzene for 4 and 26-29. All energies given in kcal mol^{-1} relative to the starting materials. Calculations carried out at the wb97xd/6-311++g(d,p) level of theory with SMD solvation (chloroform).

In order to assess the acidity of each FLP, the hydride ion affinity calculations were again carried out giving the below results (Table 7). The hydride affinities for these aluminium FLPs are generally slightly lower than the boron FLPs, indicating slightly lower Lewis

acidity. The only exception is the para-methoxy substituted FLP **27**, which has a slightly higher hydride affinity than the analogous boron FLP **23**.

Species	Hydride affinity (kcal mol^{-1})
BEt_3	0.0
$B(C_6F_5)_3$	-41.7
Fontaine's catalyst	-18.6
4	-16.8
26	-20.1
27	-16.5
28	-23.1
29	-41.9

Table 7 – Hydride affinities of $B(C_6F_5)_3$, Fontaine's catalyst, and 4 and 26-29, relative to BEt_3. Calculations for structure optimisations were carried out at the wb97xd/6-311++g(d,p) level of theory with SMD solvation (chloroform).

The trends in energies for the aluminium FLPs **4** and **26**-**29** follow those observed for boron. In this case however, there is a reduced effect of steric bulk on the reaction profile, due to longer Al–C bonds to the bulky C_6F_5 and NHC groups. Therefore, **28** and **29** show greater stabilisations in the C–H activation step TS1 relative to **4** than were seen for the analogous boron FLPs. In addition, the hydrogen loss step TS2 is not as destabilised as for boron. This is reasoned to be a result of the increased Lewis acidity having less of an effect due to the much weaker Al–H bond (67(3) kcal mol^{-1}) being broken, relative to the B–H bond (83(1) kcal mol^{-1}) for the boron FLPs.[3]

5.4.3 Gallium

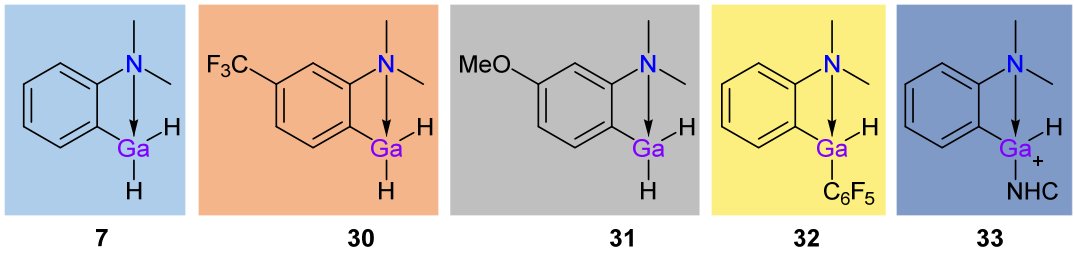

7 **30** **31** **32** **33**

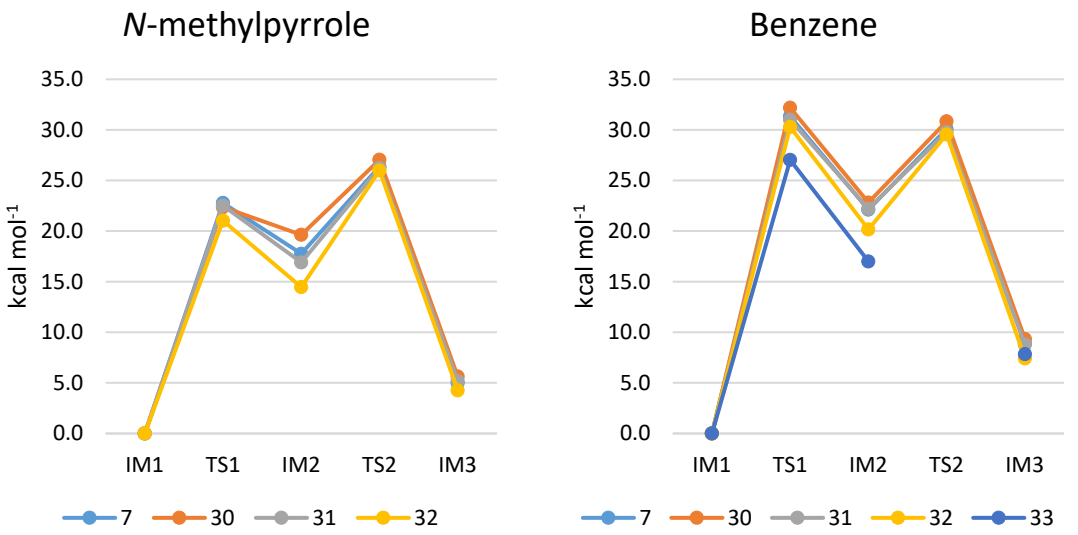

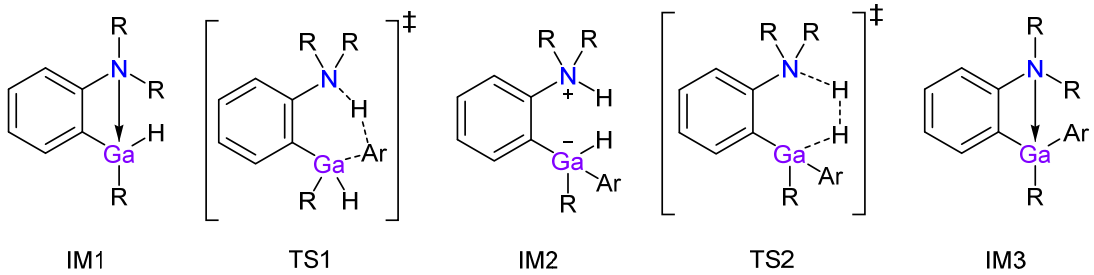

7	0.0	22.8	17.8	26.4	5.0
30	0.0	22.4	19.6	27.0	5.6
31	0.0	22.5	16.9	26.2	5.2
32	0.0	21.0	14.5	26.0	4.3

7	0.0	31.3	22.1	30.1	8.9
30	0.0	32.2	22.8	30.8	9.3
31	0.0	31.0	22.2	29.8	8.8
32	0.0	30.3	20.2	29.6	7.4
33	0.0	27.0	17.0		7.8

Figure 60 – Energies of reaction steps for C-H activation of *N*-methylpyrrole and benzene for 7 and 30-33. All energies given in kcal mol^{-1} relative to the starting materials. Calculations carried out at the wb97xd/6-311++g(d,p) level of theory with SMD solvation (chloroform).

In order to assess the acidity of each FLP, the hydride ion affinity calculations were again carried out giving the below results (Table 8). The hydride affinities for these aluminium

FLPs are slightly lower across the board again than the aluminium FLPs, indicating slightly lower Lewis acidity again.

Species	Hydride affinity (kcal mol^{-1})
BEt_3	0.0
$B(C_6F_5)_3$	-41.7
Fontaine's catalyst	-18.6
7	-13.1
30	-15.2
31	-12.8
32	-19.4
33	-39.4

Table 8 – Hydride affinities of $B(C_6F_5)_3$, Fontaine's catalyst, and 7 and 30-33, relative to BEt_3. Calculations for structure optimisations were carried out at the wb97xd/6-311++g(d,p) level of theory with SMD solvation (chloroform).

The gallium FLPs **7** and **30**-**33** follow the energy trends observed for the aluminium FLPs very closely, as expected due to their similar properties. As the steric effect is least for the gallium FLPs as the Ga–C bonds are longer than both the B–C and Al–C bonds. The main difference seen relative to the aluminium FLPs is further stabilisation of the C–H activation step TS1 and zwitterion IM2 for **32** and **33**.

5.4.4 Effect of Lewis acidity on the reaction profile

In summary of the above analysis, the effect of increasing Lewis acidity on the reaction steps relative to the starting point IM1 is as follows (Table 9).

Step	**Effect of increased Lewis acidity**
TS1	Stabilising
IM2	Stabilising
TS2	Destabilising
IM3	Little Effect

Table 9 – Summary of effect of increasing Lewis acidity on reaction steps.

5.5 Conclusions and future aims

The findings of the general trends on the reaction profile energies when increasing steric bulk, Lewis acidity, and Lewis basicity are summarised below (Table 10).

Step	Increased steric bulk	Increased Lewis basicity	Increased Lewis acidity
TS1	Destabilising	Stabilising	Stabilising
IM2	Little Effect	Stabilising	Stabilising
TS2	Stabilising	Destabilising	Destabilising
IM3	Destabilising	Little Effect	Little Effect

Table 10 – Summary of effect of increasing various parameters of the FLPs on reaction steps.

With this knowledge in hand, we can now design promising candidates for future experimental synthesis and trialling. In order to best improve the FLP as a catalyst, we must effect stabilisation of the highest energy point on the reaction profile for the substrate that is being C–H activated.

The main target of this research was the activation of arene substrates. In the model case analysed with benzene, the C–H activation step TS1 was the highest energy point and so the focus should be on designing an FLP to stabilise this transition state relative to IM1. An FLP with low steric encumbrance and highly Lewis basic and acidic centres should achieve this goal.

From the analysed FLPs the NHC-substituted gallium FLP **33** had the lowest energy for the C–H activation step TS1. The high Lewis acidity provided by the NHC group on the gallium caused this stabilisation and the negative effect of the steric bulk of the NHC is lessened for gallium relative to boron and aluminium.

In order to even further stabilise the C–H activation step TS1 addition of a para-methoxy group would be beneficial, as this was shown to stabilise both the C–H activation step TS1 and as an additional benefit it also stabilises the hydrogen loss step TS2. A final possible change is to increase the basicity of the nitrogen, without increasing the steric encumbrance. This is difficult as the chosen dimethyl amine is already highly basic and the main method of increasing the basicity would be to add additional steric bulk to decrease the pyramidalisation of the nitrogen centre.

Therefore, we arrive at the target FLP below (Figure 61). This target structure would be synthesised with an appropriate choice of weakly-coordinating anion such as tetrakis-pentafluorophenylborate.

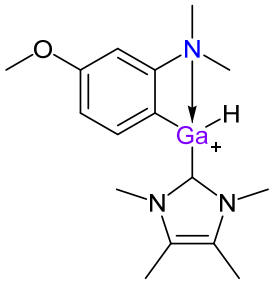

Figure 61 – Target FLP for C–H borylation of arene compounds.

5.6 References

[1] M.-A. Légaré, M.-A. Courtemanche, É. Rochette, F.-G. Fontaine, *Science* **2015**, *349*, 513–516.
[2] J. Légaré Lavergne, A. Jayaraman, L. C. Misal Castro, É. Rochette, F.-G. Fontaine, *J. Am. Chem. Soc.* **2017**, *139*, 14714–14723.
[3] Y.-R. Luo, *Comprehensive Handbook of Chemical Bond Energies*, CRC Press, **2007**.
[4] E. Lippert, *Angew. Chem.* **1960**, *72*, 602–602.
[5] "iBonD," can be found under http://ibond.nankai.edu.cn/, **n.d.**
[6] C. H. Hong, K. Wang, D. Pavlidis, *J. Electron. Mater.* **1995**, *24*, 213–218.
[7] K. Ishihara, N. Hanaki, M. Funahashi, M. Miyata, H. Yamamoto, *Bull. Chem. Soc. Jpn.* **1995**, *68*, 1721–1730.
[8] D. J. Parks, R. E. von H. Spence, W. E. Piers, *Angew. Chem. Int. Ed. Engl.* **1995**, *34*, 809–811.
[9] A. H. Cowley, G. S. Hair, B. G. McBurnett, R. A. Jones, *Chem. Commun.* **1999**, 437–438.
[10] K. Chernichenko, Á. Madarász, I. Pápai, M. Nieger, M. Leskelä, T. Repo, *Nat. Chem.* **2013**, *5*, 718–723.
[11] E. R. Clark, A. Del Grosso, M. J. Ingleson, *Chem. Eur. J.* **2013**, *19*, 2462–2466.

6 Experimental and computational methods

6.1 Chapter 2 experimental procedures

6.1.1 General considerations

All manipulations were carried out under an argon atmosphere using standard Schlenk or glovebox techniques. All glass apparatus was stored in a drying oven (12 h) prior to use. Solvents were dried over Na/benzophenone and distilled under argon. C_6D_6 was dried over potassium then distilled under argon.

NMR spectra were recorded on Bruker AVA 500 MHz (^{1}H 500.2 MHz, ^{13}C 125.8 MHz) or Bruker PRO 500 MHz (^{1}H 500.2 MHz, ^{13}C 125.8 MHz, ^{11}B 160.5 MHz, ^{27}Al 130.4 MHz) spectrometers at 298 K. ^{1}H and ^{13}C spectra were referenced to (residual) signals in the solvent.[1] Elemental analyses (CHN) were performed by Mr. Stephen Boyer at London Metropolitan University.

Single crystals for X-ray diffraction were mounted on a MITIGEN holder in Paratone oil on a Rigaku Oxford Diffraction SuperNova diffractometer. The crystals were kept at 120.0 K during data collection. Using Olex2,[2] the structure was solved with the ShelXT structure solution program using the Direct Methods solution method.[3] The model was refined with ShelXL using Least Squares minimisation. See appendix 7.2.1 for crystal specific details.

Trispentafluorophenyl borane was prepared using a literature procedure,[4] and then sublimed before use. $AlMe_2Cl$ (1.0M in hexanes) and *n*-BuLi (2.5M in hexanes) were transferred into airtight J. Young's tap ampoules and then used as supplied. All other reagents were used as supplied unless indicated otherwise.

6.1.2 Preparation of 2-lithio-*N*,*N*-dimethylaniline (4)

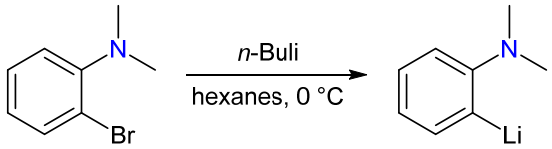

By the method of Chernichenko *et al.*,[5] 2-bromo-*N*,*N*-dimethylaniline (5.00 g, 3.62 cm^3, 25.0 mmol) was added to hexane (30 ml) and the resultant solution stirred and cooled to 0 °C in an ice bath. *n*-Butyllithium solution 2.5M in hexanes (10.0 cm^3, 25.0 mmol) was added dropwise via syringe and the solution stirred with ice bath cooling for another 3 hours. The solution was filtered leaving an off white solid which was washed with hexanes (3x5 ml). All solvent was removed *in vacuo* to give the product as an off-white amorphous solid (2.84 g, 89.4%).

^{1}H NMR: (500.12 MHz, C_6D_6)

2.08 (6H, s br, N–C$\underline{H}_3$), 7.01-7.05 (1H, m, Ar C–$\underline{H}$), 7.24-7.28 (2H, m, Ar C–$\underline{H}$), 8.27 (1H, s br, Ar C–$\underline{H}$).

^{13}C{^{1}H} NMR: (125.77 MHz, C_6D_6)

46.9 (s br, N–$\underline{C}H_3$), 119.0 (s, Ar $\underline{C}$–H), 126.2 (s, Ar $\underline{C}$–H), 128.0 (s, Ar $\underline{C}$–H), 140.3 (s, Ar $\underline{C}$–H), 166.2 (s, Ar $\underline{C}$–N), 168.9 (s br, Ar $\underline{C}$–Li).

All data were in accordance with those previously reported.[5]

6.1.3 Preparation of 2-dimethylaluminium-*N*,*N*-dimethylaniline (6)

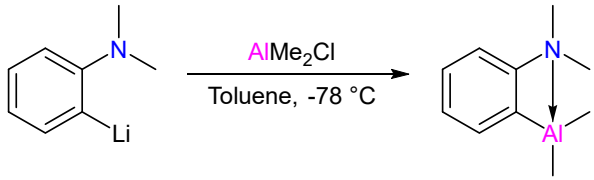

2-Lithio-N,N-dimethylaniline (1.00 g, 7.85 mmol) was added to toluene (50 ml) and the resultant suspension stirred and cooled to –78 °C in an acetone and dry ice bath. Dimethyl aluminium chloride solution 1.0M in hexanes (7.85 cm^3, 7.85 mmol) was added dropwise via syringe. The solution was then allowed to warm up to room temperature and stirred overnight. The solution was filtered to remove lithium chloride then all solvent removed *in vacuo* to leave the crude product as a yellow oil. Vacuum sublimation directly from this oil (1 mbar, 60-70 °C) gave the pure product as pure colourless plate-shaped crystals (620 mg, 44.5%).

^{1}H NMR: (500.12 MHz, C_6D_6)

–0.30 (6H, s, Al–C*H*$_3$), 2.10 (6H, s, N–C*H*$_3$), 6.61-6.64 (1H, m, Ar–*H*), 7.10-7.14 (1H, m, Ar–*H*), 7.17-7.20 (1H, m, Ar–*H*), 7.69-7.71 (1H, m, Ar–*H*).

^{13}C{^{1}H} NMR: (125.77 MHz, C_6D_6)

–9.1 (s br, Al–*C*H$_3$), 46.8 (s, N–*C*H$_3$), 116.3 (s, Ar *C*–H), 129.0 (s, Ar *C*–H), 136.9 (s, Ar *C*–H), 152.6 (s br, Ar *C*–Al), 159.0 (s, Ar *C*–N). One C–H carbon peak not observed due to being under the solvent peak.

^{27}Al NMR: (130.34 MHz, C_6D_6)

182 (s br).

HRMS: *m/z* (EI-MS) Found: 177.10995 ($C_{10}H_{16}AlN$, $[M]^+$ requires 177.10927)

CHN: Found: C, 62.6; H, 8.3; N 7.6. Calc. for $C_{10}H_{16}AlN$: C, 67.8; H 9.1; N 7.9%

Values found to be low in CHN are common for aluminium species due to incomplete combustion with formation of aluminium nitride and aluminium carbide.

MP: 63-65 °C

See appendix 7.2.1 for crystal data.

6.1.4 Reaction of 2-Lithio-*N*,*N*-dimethylaniline with dimethyl aluminium chloride to form 2-dimethyl aluminium-*N*,*N*-dimethylaniline dimethyl aluminium chloride adduct (8)

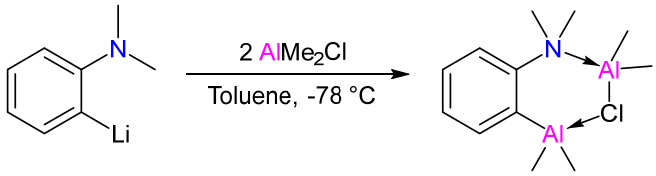

2-Lithio-*N*,*N*-dimethylaniline (0.50 g, 3.93 mmol) was added to toluene (10 ml) and the resultant solution stirred and cooled to –90 °C in an ethanol and liquid nitrogen bath. In a separate schlenk flask dimethyl aluminium chloride solution 1.0M in hexanes (7.85 cm^3, 7.85 mmol) was cooled to –90 °C and added to the first solution in one portion via cannula. The solution was then allowed to warm up naturally to room temperature and stirred overnight. The solution was filtered to remove lithium chloride then all solvent removed *in vacuo* to leave the crude product as a pale red oil from which a precipitate deposited over time. The crude product was dissolved in hexane and placed in a freezer at –20 °C and colourless block-shaped crystals of the product were obtained.

See appendix 7.2.1 for crystal data.

6.1.5 Reaction of 2-dimethylaluminium-*N*,*N*-dimethylaniline with trispentafluorophenyl borane to form 2-bispentafluorophenylaluminium-*N*,*N*-dimethylaniline (10)

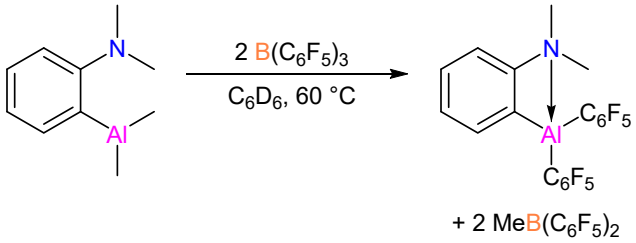

In an NMR tube, 2-dimethylaluminium-*N*,*N*-dimethylaniline (4.2 mg, 23.7 µmol) and trispentafluorophenyl borane (24.5 mg, 47.9 µmol) were dissolved in C_6D_6 (0.6 ml) and heated overnight at 60 °C. This effected full conversion to the desired products. The products were not isolated.

^{1}H NMR: (500.23 MHz, C_6D_6)

1.35* (3H, p, B–C<u>*H*</u>$_3$), 2.15 (6H, s, N–C<u>*H*</u>$_3$), 6.49 (1H, dt, Ar C–<u>*H*</u>, *J* = 8.03, 0.74 Hz), 7.06-7.10 (1H, m, Ar C–<u>*H*</u>), 7.14-7.18 (1H, m, Ar C–<u>*H*</u>), 7.79 (1H, dq, Ar C–<u>*H*</u>, *J* = 7.14, 0.63 Hz). * Arises from $MeB(C_6F_5)_2$ and is not part of the product.

^{11}B NMR: (160.49 MHz, C_6D_6)

–16.0 (s, $[Me\underline{B}(C_6F_5)_3]^-$), 59.9 (s br, $\underline{B}(C_6F_5)_3$), 71.9 (s br, $Me\underline{B}(C_6F_5)_2$), 80.8 (s br, $Me_2\underline{B}(C_6F_5)$).

6.1.6 Preparation of *N*-(2-iodophenyl)-2,2,6,6-tetramethylpiperidine (3)

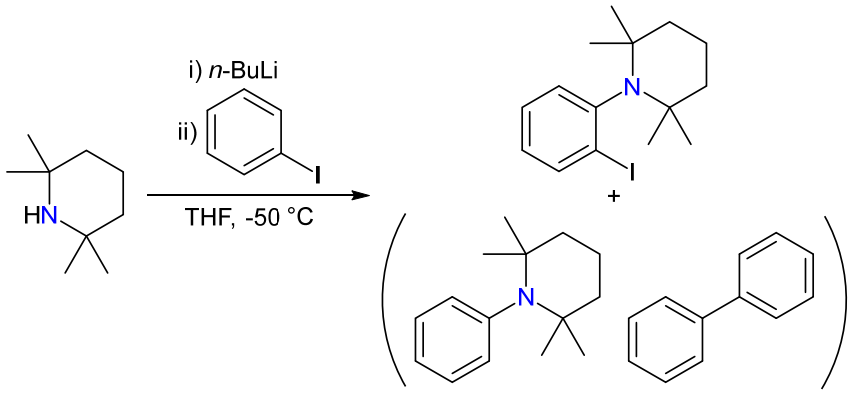

By the method of Chernichenko *et al*,[5] 2,2,6,6-tetramethylpiperidine (10.0 g, 70.8 mmol) was added to tetrahydrofuran (150 ml) and cooled to –40 °C in an acetone and dry ice bath. *n*-Butyllithium solution 2.5M in hexanes (28.4 ml, 70.8 mmol) was added dropwise over 5 mins giving a yellow solution which was stirred at –20 °C for 20 mins. The resultant solution was cooled to -50 °C and iodobenzene (28.88 g, 15.84 cm^3, 142 mmol) was added dropwise over 5 mins, giving an orange solution with precipitate. The resultant solution was stirred at –40 °C for 1 h giving a dark orange solution with no precipitate. The solution was allowed to warm up overnight, giving a dark brown purple solution. Hexane (50 ml) and saturated ammonium chloride solution (10 ml) as well as water (200 ml) were added and the organic layer separated. The aqueous layer was additionally washed with hexane (50 ml). The organic layers were combined, dried over sodium sulphate and all solvent removed *in vacuo* to give the impure product as a brown oil. Vacuum distillation (1 mbar) gave recovered iodobenzene (40 °C), then N-phenyl-2,2,6,6-tetramethylpiperidine and biphenyl (70-100 °C), and finally the product in 87% purity as a yellow oil (7.21 g, 29.7%).

^{1}H NMR: (500.12 MHz, $CDCl_3$)

0.92 (6H, s, R–C$\underline{H}_3$), 1.30 (6H, s, R–C$\underline{H}_3$), 1.58 (2H, dt, R–C$\underline{H}_2$, *J* = 12.54, 3.30 Hz), 1.64 (1H, m, R–C$\underline{H}_2$), 1.17-1.85 (2H, m, R–C$\underline{H}_2$), 1.91 (1H, tt, *J* = 13.13, 2.96 Hz), 6.87-6.91 (1H, m, Ar–$\underline{H}$), 7.28-7.32 (1H, m, Ar–$\underline{H}$), 7.42-7.44 (1H, m, Ar–$\underline{H}$), 7.94 (1H, dd, Ar–H, *J* = 7.93, 1.61 Hz).

All data were in accordance with those previously reported.[5]

6.1.7 Preparation of *N*-(2-lithiophenyl)-2,2,6,6-tetramethylpiperidine (5)

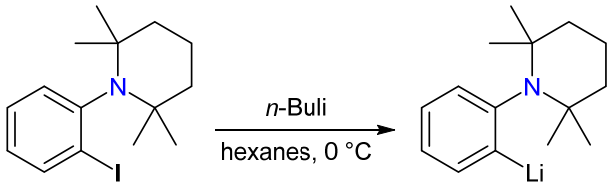

By the method of Chernichenko *et al*,[5] *N*-(2-iodophenyl)-2,2,6,6-tetramethylpiperidine (6.91 g, 20.13 mmol) was added to hexane (100 ml) and the resultant solution stirred and cooled to 0 °C in an ice bath. *n*-Butyllithium solution 2.5M in hexanes (8.06 cm^3, 20.13 mmol) was added dropwise and the solution stirred with ice bath cooling for another 4 h. The solution was filtered leaving an off white solid which was washed with cold hexane (3x15 ml). All solvent was removed *in vacuo* to give the product as an off-white amorphous solid (3.15 g, 70.1%).

^{1}H NMR: (500.12 MHz, C_6D_6)
0.94 (6H, s br, R–C$\underline{H}_3$), 1.28 (6H, s br, R–C$\underline{H}_3$), 1.37-1.75 (6H, m br, R–C$\underline{H}_2$), 7.23-7.37 (2H, m br, Ar–$\underline{H}$), 7.42 (1H, m, Ar–$\underline{H}$), 8.34 (1H, d br, Ar–$\underline{H}$, J = 4.96 Hz).

All data were in accordance with those previously reported.[5]

6.1.8 Preparation of *N*-(2-dimethyl aluminium phenyl)-2,2,6,6-tetramethylpiperidine (7)

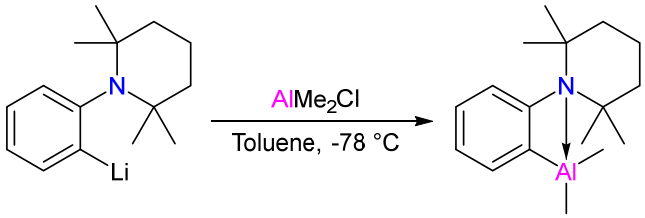

N-(2-Lithiobenzyl)-2,2,6,6-tetramethylpiperidine (1.00 g, 4.50 mmol) was added to toluene (50 ml) and the resultant solution stirred and cooled to –78 °C in an acetone and dry ice bath. Dimethyl aluminium chloride solution 1.0M in hexanes (4.50 cm^3, 4.50 mmol) was added dropwise by syringe. The solution was then allowed to warm up to room temperature and stirred overnight. The solution was filtered to remove lithium chloride then all solvent removed *in vacuo* to leave the crude product as a yellow oil. Vacuum sublimation directly from this oil (1 mbar, 120-130 °C) gave the pure product as colourless block-shaped crystals (615 mg, 50.2%).

^{1}H NMR: (500.23 MHz, C_6D_6)

0.03 (6H, s, Al–C*H*$_3$), 0.91 (6H, s, R–C*H*$_3$), 0.95-1.03 (2H, m, R–C*H*$_2$), 1.23-1.30 (1H, m, R–C*H*$_2$), 1.38 (6H, s, R–C*H*$_3$), 1.52-1.63 (3H, m, R–C*H*$_2$), 7.02-7.08 (2H, m, Ar C–*H*), 7.17-7.20 (1H, m, Ar C–*H*), 7.68-7.71 (1H, m, Ar C–*H*).

^{13}C{^{1}H} NMR: (125.77 MHz, C_6D_6)

–0.9 (s br, Al–*C*H$_3$), 16.8 (s, R–*C*H$_2$), 29.6 (s, R–*C*H$_3$), 33.2 (s, R–*C*H$_3$), 35.6 (s, R–*C*H$_2$), 59.6 (s, *C*–CH$_3$), 122.7 (s, Ar *C*–H), 127.3 (s, Ar *C*–H), 127.6 (s, Ar *C*–H), 135.8 (s, Ar *C*–H), 155.8 (s, Ar *C*–N). One carbon signal arising from Ar *C*–Al is not observed.

^{27}Al NMR: (130.36 MHz, C_6D_6)

185 (s br).

HRMS: *m/z* (EI-MS) Found: 272.19673 ($C_{17}H_{28}AlN$, $[M]^+$ requires 272.19534)

CHN: Found: C, 70.9; H, 9.9; N 5.2. Calc. for $C_{17}H_{28}AlN$: C, 74.7; H 10.3; N 5.1%

Values found to be low in CHN are common for aluminium species due to incomplete combustion with formation of aluminium nitride and

aluminium carbide.

MP: 113-115 °C

See appendix 7.2.1 for crystal data.

6.1.9 Reaction of *N*-(2-Lithiobenzyl)-2,2,6,6-tetramethylpiperidine with dimethyl aluminium chloride to form *N*-(2-methyl chloro aluminium phenyl)-2,2,6,6-tetramethylpiperidine (9)

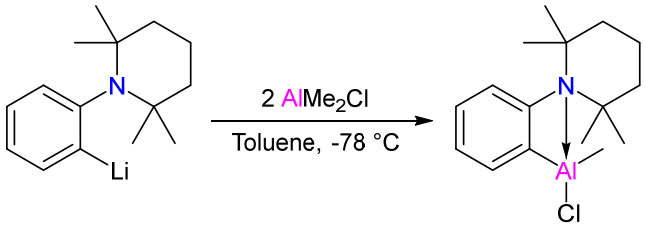

N-(2-Lithiobenzyl)-2,2,6,6-tetramethylpiperidine (1.00 g, 4.50 mmol) was added to toluene (50 ml) and the resultant solution stirred and cooled to –78 °C in an acetone and dry ice bath. Dimethyl aluminium chloride solution 1.0M in hexanes (4.50 cm^3, 4.50 mmol) was added dropwise via syringe. The solution was then allowed to warm up to room temperature and stirred overnight. The solution was filtered to remove lithium chloride then all solvent removed *in vacuo* to leave the crude product as a yellow oil. Colourless block-shaped crystals suitable for crystallography grew spontaneously from this oil.

See appendix 7.2.1 for crystal data.

6.1.10 Reaction of *N*-(2-dimethyl aluminium phenyl)-2,2,6,6-tetramethylpiperidine with trispentafluorophenyl borane to form *N*-(2-bispentafluorophenyl aluminium phenyl)-2,2,6,6-tetramethylpiperidine (11)

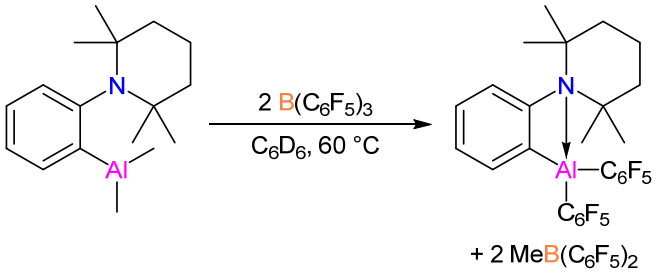

In an NMR tube, *N*-(2-dimethyl aluminium phenyl)-2,2,6,6-tetramethylpiperidine (5.3 mg, 19.4 µmol) and trispentafluorophenyl borane (19.8 mg, 38.7 µmol) were dissolved in C_6D_6 (0.6 ml) and heated overnight at 60 °C. This effected full conversion of to the desired products. The products were not isolated.

^{1}H NMR: (500.23 MHz, C_6D_6)

0.70 (6H, s, R–C$\underline{H}_3$), 0.87-0.94 (2H, m, R–C$\underline{H}_2$), 1.18-1.24 (1H, s, R–C$\underline{H}_2$), 1.35* (3H, qu, B–C$\underline{H}_3$), 1.42 (6H, s, R–C$\underline{H}_3$), 1.46-1.54 (3H, s, R–C$\underline{H}_2$), 6.96-7.00 (1H, m, Ar C–$\underline{H}$), 7.02-7.06 (1H, m, Ar C–$\underline{H}$), 7.23 (1H, td, Ar C–$\underline{H}$, J = 7.13, 0.69 Hz), 7.97 (1H, d, Ar C–$\underline{H}$, J = 7.10 Hz). * Arises from $MeB(C_6F_5)_2$ and is not part of the product.

^{11}B NMR: (160.49 MHz, C_6D_6)

–16.0 (s, $[Me\underline{B}(C_6F_5)_3]^-$), 60.0 (s br, $\underline{B}(C_6F_5)_3$), 71.9 (s br, $Me\underline{B}(C_6F_5)_2$), 80.8 (s br, $Me_2\underline{B}(C_6F_5)$).

6.2 Chapter 3 experimental procedures

6.2.1 General considerations

All manipulations were carried out under an argon atmosphere using standard Schlenk or glovebox techniques. All glass apparatus was stored in a drying oven prior to use. Solvents were dried over Na/benzophenone and distilled under argon. C_6D_6 was dried over potassium then distilled under argon.

NMR spectra were recorded on Bruker AVA 500 MHz (^{1}H 500.2 MHz, ^{13}C 125.8 MHz) or Bruker PRO 500 MHz (^{1}H 500.2 MHz, ^{13}C 125.8 MHz, ^{11}B 160.5 MHz) spectrometers at 298 K. ^{1}H and ^{13}C spectra were referenced to (residual) signals in the solvent.[1]

All reagents were purchased from Sigma Aldrich, Alfa Aesar, Acros organics, Tokyo Chemical Industries UK, Fluorochem and Apollo Scientific or synthesised within the laboratory. $AlMe_2Cl$ (1.0 M in hexanes) was transferred into an airtight J. Young's tap ampoule and then used as supplied. All other reagents were used as supplied unless indicated otherwise.

6.2.2 Reaction of 2-dimethylaluminium-*N*,*N*-dimethylaniline (3) with HBpin to form 2-dihydroaluminium-*N*,*N*-dimethylaniline (5)

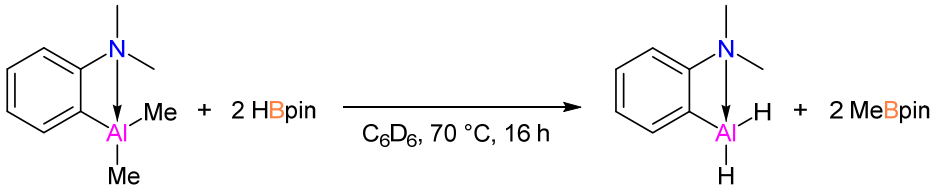

Under an inert atmosphere, 2-dimethylaluminium-*N*,*N*-dimethylaniline (18 mg, 0.10 mmol) was added to an NMR tube containing C_6D_6 (0.6 mL). HBpin (29 µL, 0.20 mmol) was added to the NMR tube and the mixture was then heated in an oil bath at 70 °C for 16 h. ^{1}H NMR spectroscopy of this sample showed complete consumption of the aluminium methyl peaks and a mixture of products. The identity of the formed aluminium species could not be clearly seen from the NMR data. This was not unanticipated, as previous work in the group has shown similarly unselective reactivity for this type of exchange for both $AlMe_3$ and $AlEt_3$ reacting with HBpin.[6]

6.2.3 C–H borylation of heteroaromatics scope

General procedure for the C-H borylation of heteroaromatics

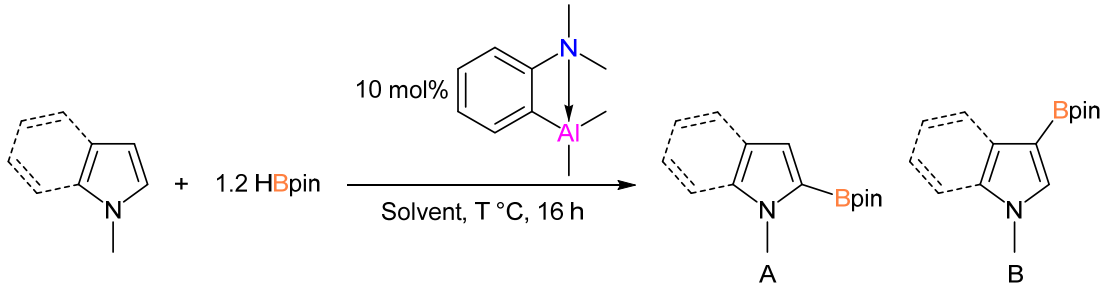

Under an inert atmosphere, 2-dimethylaluminium-*N,N*-dimethylaniline (18 mg, 0.10 mmol) and HBpin (1.20 mmol, 174 µL) were dissolved in chloroform (1 mL). The heteroarene (1.00 mmol) was added, and the mixture heated at 80 °C overnight. All volatiles were removed *in vacuo*, with heating (up to 80 °C). NMR yields were calculated by ^{1}H NMR of the crude reaction mixture relative to the remaining starting material.

Major: 1-methyl-2-(4,4,5,5-tetramethyl-1,3,2-dioxaborolan-2-yl)pyrrole

Minor: 1-methyl-3-(4,4,5,5-tetramethyl-1,3,2-dioxaborolan-2-yl)pyrrole

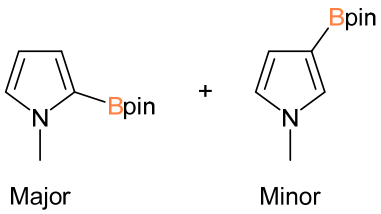

Synthesised using the standard procedure: Under an inert atmosphere, 2-dimethylaluminium-*N,N*-dimethylaniline (18 mg, 0.10 mmol) and HBpin (1.20 mmol, 174 µL) were dissolved in chloroform (1 mL). 1-methylpyrrole (89 µL, 1.00 mmol) was added and the mixture heated at 80 °C overnight.

^{1}H NMR: (500 MHz, $CDCl_3$)

7.05* (1H, m, Ar–*H*), 6.82 (2H, m, Ar–*H*), 6.63* (1H, m, Ar–*H*), 6.47* (1H, m, Ar–*H*), 6.15 (1H, m, Ar–*H*), 3.84 (3H, s, N–C*H*$_3$), 3.66* (3H, s, N–C*H*$_3$), 1.31 (12H, s, C–C*H*$_3$) 1.26* (12H, s, C–C*H*$_3$)

^{11}B NMR: (128 MHz, $CDCl_3$)

28.1 (s br), 31.5* (s br)

*arises from minor product

All data were in accordance with those previously reported.[7]

1-methyl-3-(4,4,5,5-tetramethyl-1,3,2-dioxaborolan-2-yl)indole

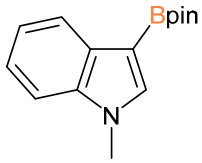

Synthesised using the standard procedure: Under an inert atmosphere, 2-dimethylaluminium-*N,N*-dimethylaniline (18 mg, 0.10 mmol) and HBpin (1.20 mmol, 174 µL) were dissolved in chloroform (1 mL). 1-methylindole (125 µL, 1.00 mmol) was added and the mixture heated at 80 °C overnight.

^{1}H NMR: (500 MHz, $CDCl_3$)

8.06 (1H, m, Ar–*H*), 7.52 (1H, s, Ar–*H*), 7.33–7.29 (1H, m, Ar–*H*), 7.26–7.18 (2H, m, Ar–*H*), 3.75 (3H, s, N–C*H*$_3$), 1.37 (12H, s, C–C*H*$_3$)

^{11}B NMR: (128 MHz, $CDCl_3$)

30.2(s br)

All data were in accordance with those previously reported.[7]

6.2.7 C–H borylation of alkynes scope

General procedure for the C-H borylation of terminal alkynes

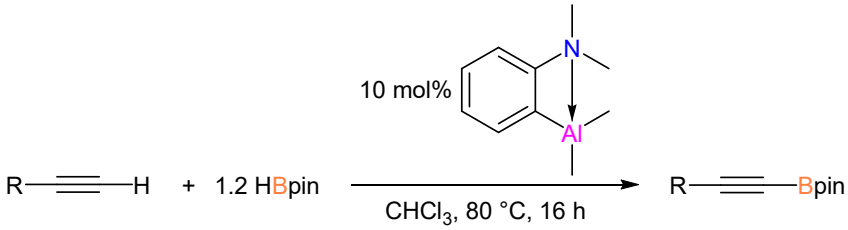

Under an inert atmosphere, 2-dimethylaluminium-*N,N*-dimethylaniline (18 mg, 0.10 mmol) and HBpin (1.20 mmol, 174 µL) were dissolved in chloroform (1 mL). The terminal alkyne (1.00 mmol) was added, and the mixture heated at 80 °C overnight. All volatiles were removed *in vacuo*, with heating (up to 80 °C). NMR yields were calculated by ^{1}H NMR of the crude reaction mixture relative to the remaining starting material.

4,4,5,5-Tetramethyl-2-(phenylethynyl)-1,3,2-dioxaborolane

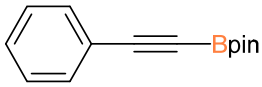

Synthesised using the standard procedure: Under an inert atmosphere, 2-dimethylaluminium-*N,N*-dimethylaniline (18 mg, 0.10 mmol) and HBpin (1.20 mmol, 174 µL) were dissolved in chloroform (1 mL). Phenylacetylene (1.00 mmol, 110 µL) was added and the mixture heated at 80 °C overnight.

^{1}H NMR: (500.12 MHz, C_6D_6)

1.03 (12H, s, C*H*$_3$), 6.82-6.92 (3H, m, Ar C–*H*), 7.37-7.41 (2H, m, Ar C–*H*)

^{11}B NMR: (128.34 MHz, C_6D_6)

24.9 (s br)

^{13}C{^{1}H} NMR: (125.77 MHz, C_6D_6)

24.7, 84.1, 101.9, 122.7, 128.5, 129.3, 132.7

All data were in accordance with those previously reported.[8,9]

4,4,5,5-Tetramethyl-2-(*p*-*N,N*-dimethylaniline)-1,3,2-dioxaborolane

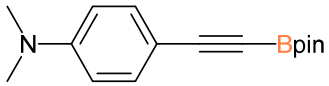

Synthesised using the standard procedure: Under an inert atmosphere, 2-dimethylaluminium-*N,N*-dimethylaniline (18 mg, 0.10 mmol) and HBpin (1.20 mmol, 174 µL) were dissolved in chloroform (1 mL). 4-ethynyl-*N,N*-dimethylaniline (1.00 mmol, 145 mg) was added and the mixture heated at 80 °C overnight.

^{1}H NMR: (500 MHz, C_6D_6)

1.06 (12H, s, C*H*$_3$), 2.28 (6H, s, N-C*H*$_3$), 6.19 (2H, d, *J* = 8.9 Hz, Ar C–*H*), 7.48 (2H, d, *J* = 8.9 Hz, Ar C–*H*)

^{11}B NMR: (128 MHz, C_6D_6)

25.3 (s br)

^{13}C{^{1}H} NMR: (126 MHz, C_6D_6)

24.8, 39.5, 83.7, 109.6, 112.0, 134.3, 150.9

All data were in accordance with those previously reported.[10]

4,4,5,5-Tetramethyl-2-(1-cyclohex-1-enyl)-1,3,2-dioxaborolane

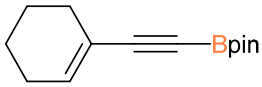

Synthesised using the standard procedure: Under an inert atmosphere, 2-dimethylaluminium-*N,N*-dimethylaniline (18 mg, 0.10 mmol) and HBpin (1.20 mmol, 174 µL) were dissolved in chloroform (1 mL). 1-ethynylcyclohex-2-ene (1.00 mmol, 118 µL) was added and the mixture heated at 80 °C overnight.

^{1}H NMR: (500.12 MHz, C_6D_6)

1.01 (12H, s, C$\underline{H}_3$), 1.18 (2H, m, C$\underline{H}_2$), 1.25 (2H, m, C$\underline{H}_2$), 1.67 (2H, m, C$\underline{H}_2$), 2.05 (2H, m, C$\underline{H}_2$), 6.18 (1H, sept, C=C–$\underline{H}$)

^{11}B NMR: (128.34 MHz, C_6D_6)

24.9 (s br)

^{13}C{^{1}H} NMR: (125.77 MHz, C_6D_6)

21.5, 22.2, 24.7, 25.8, 28.9, 83.8, 120.9, 138.1

All data were in accordance with those previously reported.[11]

4,4,5,5-Tetramethyl-2-(1-dodec-1-yn-1-yl)-1,3,2-dioxaborolane

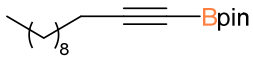

Synthesised using the standard procedure: Under an inert atmosphere, 2-dimethylaluminium-*N,N*-dimethylaniline (18 mg, 0.10 mmol) and HBpin (1.20 mmol, 174 µL) were dissolved in chloroform (1 mL). 1-dodecyne (1.00 mmol, 214 µL) was added and the mixture heated at 80 °C overnight.

^{1}H NMR: (500.12 MHz, C_6D_6)

0.90 (3H, t, *J* = 7.2 Hz, C$\underline{H}_3$), 1.01 (12H, s, C$\underline{H}_3$), 1.06-1.39 (16H, m, C$\underline{H}_2$), 2.01 (2H, t, *J* = 7.1, C$\underline{H}_2$)

^{11}B NMR: (128.34 MHz, C_6D_6)

24.1(s br)

^{13}C{^{1}H} NMR: (125.77 MHz, C_6D_6)

14.4, 19.8, 23.1, 24.7, 28.5, 29.1, 29.5, 29.7, 29.8, 30.0, 32.3, 83.6

All data were in accordance with those previously reported.[9]

4,4,5,5-Tetramethyl-2-(trimethylsilylethynyl)-1,3,2-dioxaborolane (8s)

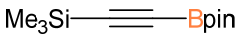

Synthesised using the standard procedure: Under an inert atmosphere, 2-dimethylaluminium-*N,N*-dimethylaniline (18 mg, 0.10 mmol) and HBpin (1.20 mmol, 174 µL) were dissolved in chloroform (1 mL). 2-trimethylsilylethyne (1.00 mmol, 139 µL)was added and the mixture heated at 80 °C overnight.

^{1}H NMR: (500.12 MHz, C_6D_6)

0.07 (9H, s, C*H*$_3$), 0.96 (12H, s, C*H*$_3$)

^{11}B NMR: (128.34 MHz, C_6D_6)

23.6 (s br)

^{13}C{^{1}H} NMR: (125.77 MHz, C_6D_6)

-0.5, 24.6, 84.0, 110.7 (br s)

All data were in accordance with those previously reported.[9]

6.3 Chapter 4 experimental procedures

6.3.1 General considerations

All manipulations were carried out under an argon atmosphere using standard Schlenk or glovebox techniques. All glass apparatus was stored in a drying oven prior to use. Solvents were dried over Na/benzophenone and distilled under argon. C_6D_6 was dried over potassium then distilled under argon.

NMR spectra were recorded on Bruker AVA 500 MHz (^{1}H 500.2 MHz) or Bruker PRO 500 MHz (^{1}H 500.2 MHz) spectrometers at 298 K. ^{1}H spectra were referenced to (residual) signals in the solvent.[1]

Single crystals for X-ray diffraction were mounted on a MITIGEN holder in Paratone oil on a Rigaku Oxford Diffraction SuperNova diffractometer. The crystals were kept at 120.0 K during data collection. Using Olex2,[2] the structure was solved with the ShelXT structure solution program using the Direct Methods solution method.[3] The model was refined with ShelXL using Least Squares minimisation. See appendix 7.2.2 for crystal specific details.

All reagents were used as supplied unless indicated otherwise.

6.3.2 Preparation of 2-dihydroaluminium-*N*,*N*-dimethylaniline (3) by $AlCl_3$ then $LiAlH_4$

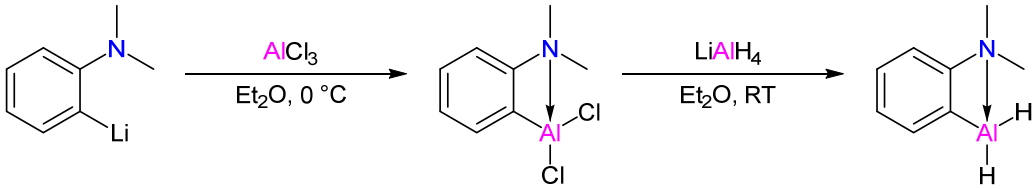

2-lithio-*N*,*N*-dimethylaniline (500 mg, 3.934 mmol) was dissolved in Et_2O (20 ml) and cooled to 0 °C. $AlCl_3$ (520mg, 3.901 mmol) was dissolved in Et_2O (20 ml), cooled to 0 °C, and added to the 2-lithio-*N*,*N*-dimethylaniline solution in one portion. The mixture was allowed to slowly warm up to room temperature and stirred for 16 h. The mixture was filtered *via* cannula onto $LiAlH_4$ (374 mg, 10.1218 mmol) and stirred for a further 16 h. The solution was filtered, concentrated and cooled in a freezer at –20 °C, affording colourless crystals of 2-dihydridoaluminium-*N*,*N*-dimethylaniline suitable for crystallography.

^{1}H NMR: (500.12 MHz, C_6D_6)

2.07 (s (broad), 6H, N(C*H*$_3$)$_2$), 7.00-7.04 (m, 1H, Ar-*H*), 7.22-7.27 (m, 2H, Ar-*H*), 8.26 (s, 1H, Ar-*H*). Hydride resonance not observable.

See appendix 7.2.2 for crystal data. Structure is for isomeric tetramer **40**.

6.3.3 Preparation of 2-dihydroaluminium-*N*,*N*-dimethylaniline (3) by $AlH_3.NEtMe_2$

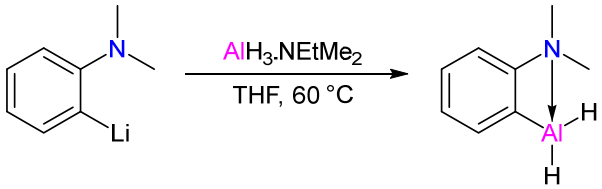

2-lithio-*N*,*N*-dimethylaniline (98 mg, 0.771 mmol) was dissolved in THF (20 ml) and heated to 60 °C. Ethyldimethylamine adduct of aluminium trihydride solution (0.5 M in toluene, 3.3 ml, 1.65 mmol) was added dropwise to the pale-yellow solution and stirred for 3 hours. The colourless product solution was cooled to room temperature and solvent removed *in vacuo*, yielding a colourless oil. To this toluene (25 ml) was added. The solution was filtered, concentrated and cooled in a freezer at –20 °C, which afforded 2-dihydridoaluminium-*N*,*N*-dimethylaniline as a yellow crystalline solid (11.9 mg, 10.3%).

^{1}H NMR: See 6.4.1.

6.3.4 Preparation of AlH_2Cl

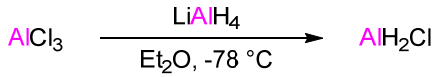

By the method of Ganesamoorthy et al.,[12] ether (30 ml) was added dropwise to $AlCl_3$ (233 mg, 1.75 mmol) at –78°C, followed by dropwise addition of a solution of $LiAlH_4$ (61.4 mg, 1.54 mmol) in ether (25 ml). The solution was stirred for 2 h and then allowed to warm to room temperature. The solvent was removed *in vacuo* to yield AlH_2Cl as a white solid, which was used without further purification.

6.3.5 Preparation of 2-dihydroaluminium-*N*,*N*-dimethylaniline (3) by AlH_2Cl

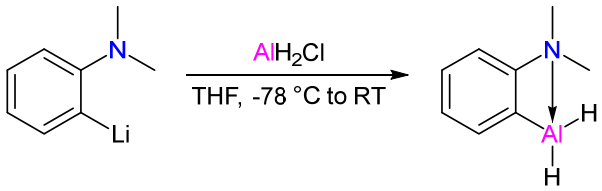

2-lithio-*N*,*N*-dimethylaniline (1.00 g, 7.87 mmol) was dissolved in THF (30 ml) and cooled to -78°C, to which a solution of AlH_2Cl (15 mmol) in THF (30 ml) was added dropwise. The yellow solution was stirred for 3 hours, warmed to room temperature and stirred for 20 h. The solution turns pale yellow over the course of the reaction. THF was removed *in vacuo* to yield a yellow oil. To this toluene (25 ml) was added and filtered. The filtrate was concentrated and hexane added, such that the solution was approximately a 1:1 volume ratio of toluene and hexane. The solution was cooled in a freezer to –20 °C, affording the white crystalline 2-dihydridoaluminium-*N*,*N*-dimethylaniline.

^{1}H NMR: See 6.4.1.

6.3.6 Preparation of tris(phenylethynyl)aluminium *N*,*N*-dimethylaniline adduct (47)

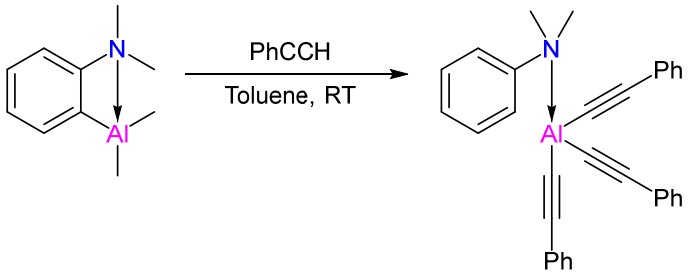

2-Dimethylaluminium-*N*,*N*-dimethylaniline (0.204 g, 1.15 mmol) was dissolved in toluene (20 ml), to which phenylacetylene (0.38 ml, 0.353 g, 3.46 mmol) was added dropwise and stirred for 1 h. The solution was then concentrated *in vacuo* to remove residual phenyacetylene, precipitating upon cooling the acetylide product as a white powder (0.268 g, 66%). The alkynylaluminium product was recrystallized from minimum toluene at 2 °C to afford colourless block-shaped crystals for XRD structure determination.

^{1}H NMR: (500.12 MHz, C_6D_6)

2.84 (s, 6H, N(C<u>*H*</u>$_3$)$_2$), 6.90-6.98 (m, Ar-<u>*H*</u>), 7.05 (m, Ar-<u>*H*</u>), 7.45 (m, Ar-<u>*H*</u>), 7.5 (m, Ar-<u>*H*</u>).

^{13}C{^{1}H} NMR: (125.77 MHz, C_6D_6)

43.2, 77.8, 83.9, 108.4, 117.3, 121.7, 122.9, 125.4, 129.2, 132.4, 149.2

MP: 100 °C – partially melts (presumably due to dissociation of the adduct) then slowly decomposes into a brown solid upon heating.

See appendix 7.2.2 for crystal data.

6.4 Computational chemistry

6.4.1 Computational modelling

Computational chemistry is a growing field, finding application in both the rationalisation of experimental phenomena and the exploration and prediction of unknown behaviour.

Computational calculations or simulations can be broadly divided into two categories, based on the underlying mathematics involved: classical and quantum mechanical (QM). As the names suggest, classical calculations make use of classical mechanics and experimentally or QM derived parameters to describe atoms and molecules, while QM calculations use quantum mechanics and attempt to solve the multi-electron Schrödinger Equation.

Both methods have their individual merits and drawbacks: classical calculations are far less computationally demanding and hence can be used to describe larger systems; however, QM calculations are more accurate and are able to obtain information about a system which classical calculations cannot.

QM calculations are used extensively in the elucidation of reaction mechanisms in the literature for systems containing small-molecule substrates and catalysts and is the computational method utilised in this work. This section presents the techniques used along with their background theory.

6.4.2 Quantum Mechanical Theory

The core concept of QM computational chemistry is the Schrödinger equation, which for its time-independent form can be expressed in shorthand form as seen below (Equation 1). This is an eigenvalue problem: the Hamiltonian operator, $\hat{H}$, acts on the wavefunction, Ψ (the eigenfunction), to give the permitted energy levels, E (the eigenvalues), of the atom or molecule.

$$\hat{H}\Psi = E\Psi$$

Equation 1 – The time-independent Schrödinger equation.

The Hamiltonian operator describes the total energy of the system, which comprises potential and kinetic energy terms, as shown (Equation 2), where T_e represents the kinetic energy of electrons, T_n the kinetic energy of nuclei, V_{nn} the potential energy of the nucleus-nucleus repulsions, V_{ee} the potential energy of the electron-electron repulsions, and V_{ne} the potential energy of nucleus-electron attraction.[13,14]

$$\hat{H} = Te + Tn + Vnn + Vee + Vne$$

Equation 2 – Breakdown of the Hamiltonian operater $\hat{H}$.

By solving the Schrödinger equation and determining the eigenvalues many different chemical properties can be calculated for the system in question. However, the Schrödinger equation can only be solved exactly for a one-electron system. The electron-electron potential energy term is impossible to solve for a multi-electron system. This is because electron motion is correlated; the electrostatic field of one electron will influence others and be influenced by the others. Therefore, in order to "solve" the Schrödinger equation of systems with more than one electron, approximations must be made. The accuracy of the calculations for multi-electron systems therefore depend on the validity of the approximations made.

The Born-Oppenheimer approximation

The primary approximation employed is the Born-Oppenheimer approximation. It states that, because electrons move so much faster than the comparatively much heavier nuclei, electron and nuclear motion can be separated and treated independently, as from the point of view of an electron, the nucleus can be considered stationary. Therefore, in the Hamiltonian operator, the kinetic energy term for the nuclei is set to zero and the nucleus-nucleus repulsion term is a constant (which is calculated classically and so not included in the QM equations). This simplifies the problem and gives the electronic Hamiltonian, $\hat{H}_{\text{elec}}$ (Equation 3).[15]

$$\hat{H}_{elec} = T_e + V_{ee} + V_{ne}$$

Equation 3 – The electronic Hamiltonian operator.

This equation could be solved for one electron at a time. However, the Born-Oppenheimer approximation has not removed the issues with multi-electron systems, as all the electron-related terms still remain in the electronic Hamiltonian. There is still the problem of electron correlation and also of electron exchange (each orbital will accommodate a pair electrons, but the electrons must be of opposite spin), which affects each of the remaining three terms in Equation 3. The combination of two theories, Hartree theory and Fock theory, allow a first approximation to handling these issues.

Hartree Fock theory

Hartree Fock (HF) theory employs both Hartree theory and Fock theory. Hartree theory approximates the multi-electron correlation problem (each electrons movement influencing and being influenced by the others' movement) to a single electron moving in a uniform field generated by the other electrons, therefore setting the correlation energy to zero.[16] Fock theory allows electron exchange to be accounted for by the use of an anti-symmetric wavefunction. The wavefunction must be antisymmetric "with respect to the interchange of the coordinate x (both space and spin) of any two electrons".[16] For example, in the two electron system (Equation 4), where both electrons are of spin up, if x_1 (the position of the electron) is set equal to x_2 the wavefunction is zero. As the square of the wavefunction defines the electron probability function, in effect this renders impossible the positioning of two electrons with the same spin in the same place. This antisymmetry principle equates to the Pauli Exclusion Principle.[16]

$$\Psi_a \uparrow (x_1) \uparrow (x_2) - \Psi_a \uparrow (x_2) \uparrow (x_1)$$

Equation 4 – Example two-electron system.

While the approximations introduced through HF theory work well for many systems, for some they do not, particularly in systems with areas of high electron density. However, there are higher levels of theory which improve upon HF theory, by using additional terms to better account for the missing energy attributed to electron

correlation. Improved representation of the wavefunction and Hamiltonian operator is easy to verify because of the variation principle, which states that the energy obtained through approximations will always be higher than the true energy.[13] Therefore, a decrease in energy on changing the level of theory or wavefunction description indicates that the model chemistry is improved. HF theory and the higher levels of theory are termed *ab initio* methods. Although *ab initio* methods can prove very successful and accurate (especially the higher level of theory methods), the computational demand they impose quickly becomes extremely high as system size increases. However, there exists an alternative theory which is somewhat less computationally demanding, that being density functional theory.

Density Functional Theory

Rather than using electron positions, Density functional theory (DFT) uses electron density to calculate the energy and properties of a ground state system. Hohenberg and Kohn showed that there is a one-to-one correspondence of electron density and the ground-state energy of a system,[15,17] which indicates there is a functional (a function of a function) connecting these two properties. This functional (in this case a function of the electron density) is used to calculate the energy and in theory, this should yield an exact answer, which fully considers electron correlation and exchange. In practice however, this is not the case, because the identity of the correct functional is unknown. Thus, a wide variety of approximate functionals are employed instead, with each better suited to different chemical systems.

Using these functionals, the N one-electron Schrödinger equations, introduced in the previous section, are replaced with N equations of the form given in Equation 5, which are based on the electron density. The electron-electron repulsion term is split into a Coulomb part, $J[\rho]$, and an Exchange part (incorporated into the exchange-correlation term).[15] An exchange-correlation term, $E_{XC}[\rho]$, is formed to encompass the electron correlation and exchange effects, which are impossible to solve exactly for almost all systems. This term is customarily separated into pure exchange, $E_X[\rho]$, and correlation, $E_C[\rho]$.[15]

$$E[\rho] = T_e[\rho] + E_{ne}[\rho] + J[\rho] + E_X[\rho] + E_C[\rho]$$

Equation 5 – The DFT equations based on electron density.

DFT methods differ in how they treat the exchange-correlation energy, i.e. in how they approximate the functional for $E_{XC}[\rho]$. For example, this can be done by making use of the Local Density Approximation (LDA), which assumes that the density varies slowly and so the local density can be treated as a uniform electron gas.[15] This method therefore fails when the electron density has sharp variations, such as for a molecular system. For these, the Generalised Gradient Approximation (GGA) can be utilised, where the gradient of the electron density is incorporated into the functionals.[15] All pure DFT methods use an approximate functional for $E_{XC}[\rho]$ and are thus approximating both the electron exchange and correlation. However, the exact treatment of electron exchange from HF can be incorporated into DFT, providing a combination method known as hybrid DFT.[13,15] Hybrid functionals incorporate varying amounts of HF treatment of the exchange energy, as demonstrated in Equation 6, where E_{XC} is the exchange and correlation energy, E_{XC}^{DFT} is the DFT treatment of exchange and correlation energy, E_X^{HF} is the HF treatment of the exchange energy, and a is the weighting factor.

$$E_{XC} = (1-a) + aE_X^{HF}$$

Equation 6 – Weighting of hybrid DFT functionals.

Some functionals and hybrid functionals are lacking in their treatment of dispersion interactions between atoms.[18–20] As the work in this thesis focuses on FLP type molecules where dispersion interactions between the Lewis acidic and Lewis basic centres may contribute significantly, it is important that these are accounted for in this work. Therefore, the hybrid functional ωB97X-D was used.[21] This functional includes 100% long-range and a small fraction (about 22%) of short-range HF exact exchange and is parameterised (incorporating 18 empirically optimised parameters into the exchange-correlation functional) to better account for dispersion interactions.

Basis sets

The wavefunction, the mathematical description of a molecular orbital, is constructed from basis sets, which are linear combinations of functions to describe atomic orbitals, which in turn are used to construct molecular orbitals. Two common ways of describing the orbitals are Slater-Type orbitals,[22] or Gaussian-Type orbitals.[23] The former mirror the orbitals for the hydrogen atom and are more accurate but more demanding to solve. The latter are less demanding to calculate and can mimic the atomic radial functions if a linear combination of them is employed. This means the wavefunction is expressed as a sum of i weighted (by coefficients, c_i, in order to best mimic the size and shape of the orbital), "primitive" Gaussian functions, ϕ_i as expressed in Equation 7, where ϕ_i captures both the radial (i.e. size) and angular momentum (i.e. shape) components for describing the orbital.

$$\Psi = \Sigma_i \, c_i \phi_i$$

Equation 7 – The wavefunction expressed as a linear combination of Gaussian functions.

For example, consider the 6-311++G** basis set,[24,25] which is one of those used in this work. It consists of a function built from six primitive Gaussian functions, which are used to describe the core orbitals, and three functions built from three, one, and one primitive Gaussian functions, respectively, which describe the valence orbitals. More flexibility is introduced to describe the valence orbitals as they are the orbitals involved in chemical bonding. This basis set is of the split-valence, Triple Zeta (TZ) type, as it treats the core orbitals separately from the valence and it uses three times as many functions as the minimum basis set (which is e.g. two s functions, one each for the 1s and 2s orbitals, and one set of p functions, for the 2p orbitals) to describe the (valence) orbitals.[15] Using more functions increases the accuracy of the basis set, so a TZ basis set will be better than, e.g. a Double Zeta basis set (one which uses two times the number of functions as the minimum basis set), such as 6-31+G**, which is also used in this work.

The 6-311++G** basis set also contains additional functions which increase its accuracy: polarisation and diffuse functions, denoted by the * and + symbols, respectively. Polarisation functions add a function with a higher angular momentum than that required for the ground state description for each atom, allowing the orbitals to change shape. For example, a hydrogen atom only requires an s-type orbital to be described, but a p-type can be added. This allows for a more accurate description of the molecular orbitals formed in atomic orbital overlap. A single * means that polarisation is only applied to heavy atoms (i.e. only d-type functions have been added); the double ** means that polarisation is applied to heavy atoms and hydrogen (i.e. d-type functions are added to heavy atoms and p-type functions are added to hydrogen atoms). Polarisation functions on hydrogen atoms are important to include in this work as many interactions present in the explored structures arise from the interaction of hydrogen atoms with other atoms.

Diffuse functions allow orbitals to take up more space and extend further from the nuclei. They are larger versions of the functions and are important when loosely bound electrons are present.[15] As with the notation for polarisation functions, the single + denotes that a diffuse function has been added to heavy atoms and a ++ that they have been added to heavy atoms and hydrogen atoms. In this work, diffuse functions are included due to the longer distance interactions between the Lewis acidic and Lewis basic atoms in the FLP structures due to the imposed geometric constraint of the ligand.

Although increasing the size of the basis set (the number of functions used) will improve the accuracy of the calculation, in practice this is only possible to a certain extent, depending on how much compute time is available. Therefore, there will always be some error in the calculations, and this error can be quite large.[15] However, provided the same basis set(s) are used between systems, the relative energies can be calculated and used as a means of comparison and understanding as the errors will usually be similar.

Implicit solvent modelling

In this work, implicit solvent modelling is used, where the solvent is treated as a continuous medium. The Self-Consistent Reaction Field (SCRF) model is employed. In this model the solvent is considered to be a uniform polarisable medium with a specific dielectric constant and the solute is in a suitably shaped hole within the solvent medium.[15,26] The energy of solvation is determined from the (destabilisation) energy of creating the hole for the solute, the (stabilisation) energy for the dispersion interactions of the solute with the solvent, and the (stabilisation) energy of the electrostatic interaction of the solute with the solvent due to the charge distribution on the solute. Different reaction field methods treat the aspects of the model (e.g. how the size and shape of the solute hole is defined, how the dispersion contributions are calculated, etc.) in different ways. In this work the SMD continuum solvation model[27] is used. The model separates the observable solvation free energy into two main components.

The first component is the bulk electrostatic contribution in the same manner as the polarizable continuum model (IEF-PCM). It uses "a van der Waals surface type cavity, a detailed description of the electrostatic potential, and parameterizes the cavity/dispersion contributions based on the surface area" of the cavity.[15]

The second component is called the cavity-dispersion solvent-structure term and is the contribution arising from short-range interactions between the solute and solvent molecules in the first solvation shell. For this component the SMD model has been parametrized with a large training set (2821 various solvation data).

6.4.3 Quantum Mechanical Calculations

Geometry optimisation

Geometry optimisation calculations allow the minimum energy structure of a molecule or assembly to be found. From this, other calculations can be conducted (e.g. vibrational frequency calculations) to gain extremely valuable information, such as the Gibbs free formation energies and simulated spectra.

Set up as a series of iterative calculations (as illustrated in Figure 2.1), geometry optimisation begins with the specification of a starting geometry. This can be taken from many sources, e.g. from a crystal structure or drawn in a model builder, however, geometry optimisation will only target the local minimum close to the starting structure, so it is important to choose a starting structure close to the target minimum. The first step in the actual geometry optimisation cycle is the determination (or estimation) of the wavefunction for the starting configuration of atoms. This is a self-consistent field (SCF) cycle where the weighting coefficients of the basis set are varied until the wavefunction converges to one that most accurately approximates the electronic ground state of the system. The energy of the input structure is calculated from this wavefunction, along with the forces acting on the atoms and estimates of the force constants. From this a set of new atomic coordinates is predicted, and the atoms are moved to this position. The SCF cycle is repeated for this new geometry and the energy obtained is compared to the energy of the previous geometry. This iterative process continues until the convergence criteria are met: usually that the forces on the atoms are close to zero, determined by the gradient of the potential energy surface (PES) being close to zero, and the atomic displacements have become very small. At this point, the geometry is considered optimised (within the convergence criteria specified).

However, this process does not guarantee that the optimised geometry is a minimum. For example, the gradient of the PES is also zero at a transition state. To confirm the nature of the stationary point obtained, a vibrational frequency calculation should be employed, wherein the force constants are calculated (and consequently the vibrational frequencies of the optimised geometry are determined). If negative force constants are found, giving rise to imaginary frequencies, then a transition state structure has been obtained instead of a minimum. If a minimum is desired, the geometry optimisation process can be repeated with a slightly modified structure or with tighter convergence criteria.

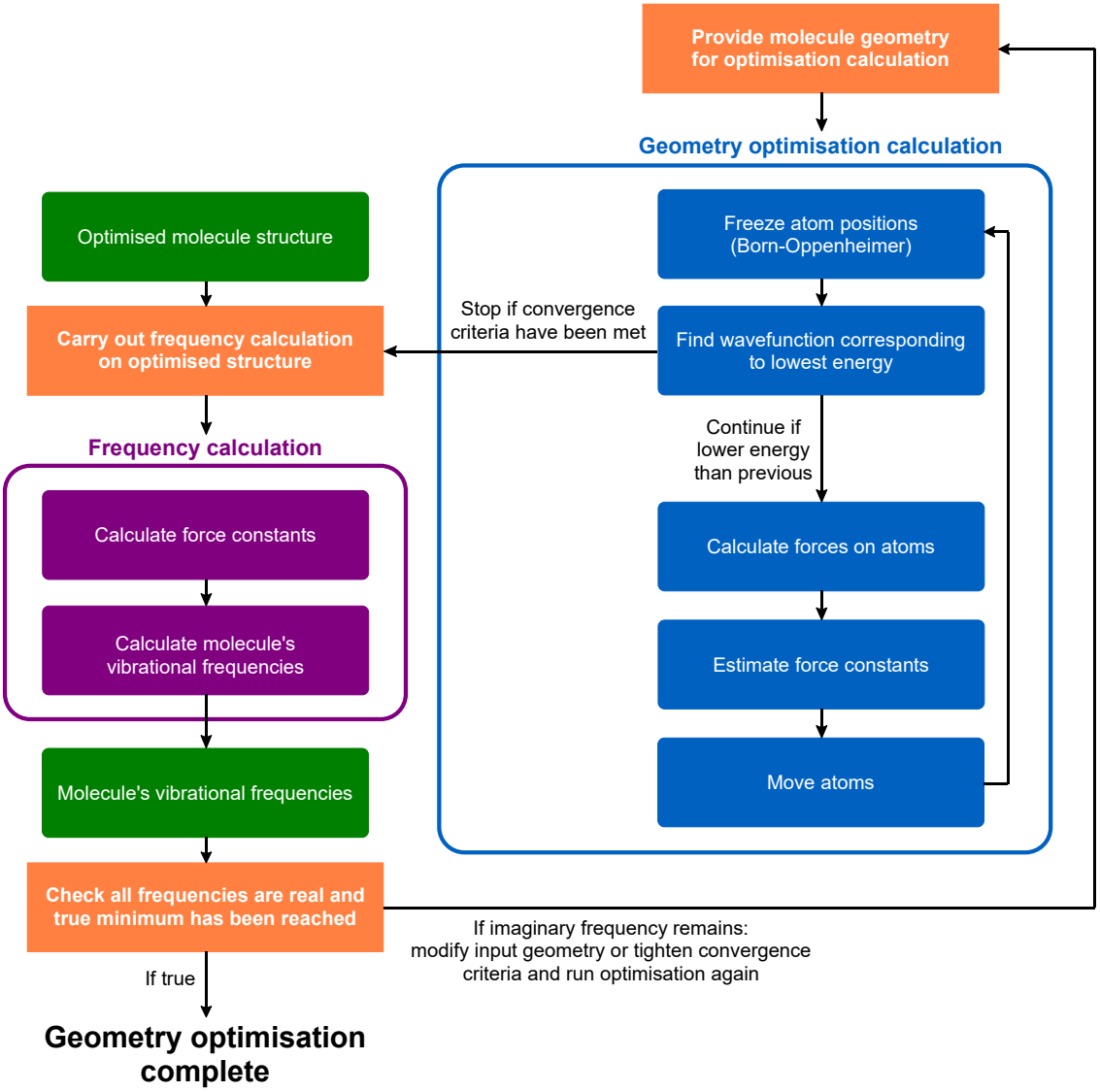

Figure 62 – Procedure of a QM geometry optimisation and frequency calculation to determine the minimum energy structure, including most likely user steps (in orange). Convergence criteria are based on how close the forces and atomic displacements are to zero.

The energies reported in geometry optimisation calculations are SCF energies but corrections, such as the zero-point energy correction and those for enthalpy and entropy to convert SCF energies to Gibbs free energies, can be determined from the vibrational data given by the frequency calculations. The energies discussed in this work are all Gibbs free energies, unless otherwise specified.

Transition-state optimisation

A transition-state optimisation calculation follows the same steps as for a geometry optimisation calculation. However, in this case instead of searching for a structure at the bottom of a potential energy well, the search is performed for a structure at a first order saddle point on the potential energy surface. As such, when moving the atoms in the optimisation step, the calculation moves the atoms in such a way as to minimise the energy in all directions except the one in which the curvature of the Hessian eigenvalue is negative. This results in moving the structure towards the saddle point of the potential energy surface.

To confirm that a transition state has been obtained, in a similar manner to a geometry optimisation calculation, a vibrational frequency calculation is employed. In this case, an imaginary frequency indicates that a first order transition state has been found, linking two potential energy wells.

In order to confirm that the transition state found links the correct energy minima, a number of methods can be used. One method used is to perform an Intrinsic Reaction Coordinate (IRC) calculation on the transition state, which follows the minimum energy reaction pathway (MEP), by taking small steps along the potential energy surface by following the path of steepest descent in small steps in both directions from the transition state.[15] This requires optimisation of a large number of structures to reach the energy minima and as such is relatively computationally expensive.

Another possible method involves displacing the found transition state structure a small amount along the imaginary frequency in either direction and performing geometry optimisation calculations until they converge on the minima either side of the saddle point. This is computationally much simpler and is the method employed in this work.

6.4.4 Method choice

When undertaking calculations on a system, it is important to choose a functional that will correctly model your system and a basis set that is sufficiently detailed so as to obtain meaningful data. In the reactions that are being performed here, dispersion interactions are vitally important due to the separated nature of the Lewis acidic and basic centres and their interactions with the substrates.

In order to choose a functional that was suitable for calculations on FLP type systems, a search of the literature was conducted. From this a series of functionals were chosen for testing. The functionals M06 and M06-2X have found widespread and standard usage in the field of main group chemistry.[28] The ωB97X-D functional,[29] has been previously used for the calculation of the mechanism of the FLP C–H borylation by Fontaine and co-workers,[30] and was chosen by them due to recommendation by Grimme.[19]

Initial testing of all three of these functionals was carried out using the 6-31+G(d,p) basis set on an initially proposed catalytic cycle modelled on that reported and calculated by Fontaine and co-workers.[30] All functionals gave very similar energies for the structures they were able to converge geometry optimisations for, showing that the basis set was a good description of the system. Ultimately, ωB97X-D was selected as the functional of choice for the calculations that will be discussed within this thesis, as that meant that the calculations were consistent with and comparable to the previously performed computational work.

6.4.5 Computational details for chapter 2

All calculations in this work were carried out on the Edinburgh Compute and Data Facility's Eddie Mark 3 cluster. Geometry optimizations and harmonic frequency calculations were performed using the Gaussian16 program package[31] employing the ωB97X-D density functional[21] in combination with the 6-31+G(d,p) basis set[32] using standard convergence criteria. The SMD continuum solvation model[27] was employed to account for solvent effects (Toluene or Benzene). Stationary points were characterized as minima or 1st order transition states by analysis of the frequency calculations with zero or one imaginary frequency respectively. Transition state structures were confirmed by displacing the transition state structure a small amount along the imaginary frequency in either direction and optimizing downhill to the connected minima. Unscaled zero-point vibrational, thermal and entropic corrections were obtained from the frequency calculations at the ωB97X-D/6-31+G(d,p) level using standard procedures to obtain free-energy corrections at standard conditions (T = 298.15 K, p = 1 atm) and combined with internal energy to give Gibbs free-energy values at greater accuracy with lower computational cost of geometry optimisation. Free-energy reaction schemes are presented relative to the free energies of the starting materials. Natural bond orbital (NBO) analysis was carried out with the NBO 7.0 program.[33] Pictures of molecular structures were generated with the ChemCraft[34] program.

6.4.6 Computational details for chapter 4 and chapter 5.

All calculations in this work were carried out on the Edinburgh Compute and Data Facility's Eddie Mark 3 cluster. Geometry optimizations and harmonic frequency calculations were performed using the Gaussian16 program package[31] employing the ωB97X-D density functional[21] in combination with the 6-31+G(d,p) basis set[32] using standard convergence criteria. The SMD continuum solvation model[27] was employed to account for solvent effects (Chloroform). Stationary points were characterized as minima or 1st order transition states by analysis of the frequency calculations with zero or one imaginary frequency. Transition state structures were confirmed by displacing the transition state structure a small amount along the imaginary frequency in either direction and optimizing downhill to the connected minima. Single-point calculations were conducted on the optimized geometries using the ωB97X-D functional in combination with the higher level 6-311++G(d,p) basis set.[24] Unscaled zero-point vibrational, thermal and entropic corrections were obtained from the frequency calculations at the ωB97X-D/6-31+G(d,p) level using standard procedures to obtain free-energy corrections at standard conditions (T = 298.15 K, p = 1 atm) and combined with internal energy from the 6-311++G(d,p) higher level calculation to give Gibbs free-energy values at greater accuracy with lower computational cost of geometry optimisation. Free energy reaction schemes are presented relative to the free-energies of the starting materials. Natural bond orbital (NBO) analysis was carried out with the NBO 7.0 program.[33] Pictures of molecular structures were generated with the ChemCraft[34] program.

6.5 References

[1] G. R. Fulmer, A. J. M. Miller, N. H. Sherden, H. E. Gottlieb, A. Nudelman, B. M. Stoltz, J. E. Bercaw, K. I. Goldberg, *Organometallics* **2010**, *29*, 2176–2179.

[2] O. V. Dolomanov, L. J. Bourhis, R. J. Gildea, J. a. K. Howard, H. Puschmann, *J. Appl. Crystallogr.* **2009**, *42*, 339–341.

[3] G. M. Sheldrick, *Acta Crystallogr. Sect. C Struct. Chem.* **2015**, *71*, 3–8.

[4] D. S. Lancaster, "Alkylation of boron trifluoride with pentafluorophenyl Grignard reagent; Tris(pentafluorophenyl)boron," DOI 10.1039/SP215can be found under http://cssp.chemspider.com/215, **2003**.

[5] K. Chernichenko, M. Nieger, M. Leskelä, T. Repo, *Dalton Trans.* **2012**, *41*, 9029–9032.

[6] A. Bismuto, S. P. Thomas, M. J. Cowley, *Angew. Chem. Int. Ed.* **2016**, *55*, 15356–15359.

[7] M.-A. Légaré, É. Rochette, J. L. Lavergne, N. Bouchard, F.-G. Fontaine, *Chem. Commun.* **2016**, *52*, 5387–5390.

[8] C. I. Lee, J. Zhou, O. V. Ozerov, *J. Am. Chem. Soc.* **2013**, *135*, 3560–3566.

[9] D. Wei, B. Carboni, J. B. Sortais, C. Darcel, *Adv. Synth. Catal.* **2018**, *360*, 3649–3654.

[10] T. León, E. Fernández, *Chem. Commun.* **2016**, *52*, 9363–9366.

[11] H. E. Ho, N. Asao, Y. Yamamoto, T. Jin, *Org. Lett.* **2014**, *16*, 4670–4673.

[12] C. Ganesamoorthy, S. Loerke, C. Gemel, P. Jerabek, M. Winter, G. Frenking, R. A. Fischer, *Chem. Commun.* **2013**, *49*, 2858–2860.

[13] A. R. Leach, L. AR, *Molecular Modelling: Principles and Applications*, Pearson Education, **2001**.

[14] P. W. Atkins, R. S. Friedman, *Molecular Quantum Mechanics 4th Edition*, Oxford University Press, **2005**.

[15] F. Jensen, *Introduction to Computational Chemistry*, Wiley-Blackwell, Chichester, UK ; Hoboken, NJ, **2017**.

[16] A. Szabo, N. S. Ostlund, *Modern Quantum Chemistry : Introduction to Advanced Electronic Structure Theory*, Mineola, N.Y. : Dover Publications, **1996**.

[17] P. Hohenberg, W. Kohn, *Phys. Rev.* **1964**, *136*, B864–B871.

[18] S. Kristyán, P. Pulay, *Chem. Phys. Lett.* **1994**, *229*, 175–180.

[19] L. Goerigk, S. Grimme, *Phys. Chem. Chem. Phys.* **2011**, *13*, 6670–6688.

[20] S. Grimme, J. Antony, S. Ehrlich, H. Krieg, *J. Chem. Phys.* **2010**, *132*, 154104.

[21] J. Da Chai, M. Head-Gordon, *Phys. Chem. Chem. Phys.* **2008**, *10*, 6615–6620.

[22] J. C. Slater, *Phys. Rev.* **1930**, *36*, 57–64.

[23] S. F. Boys, A. C. Egerton, *Proc. R. Soc. Lond. Ser. Math. Phys. Sci.* **1950**, *200*, 542–554.

[24] R. Krishnan, J. S. Binkley, R. Seeger, J. A. Pople, *J. Chem. Phys.* **1980**, *72*, 650–654.

[25] K. Raghavachari, G. W. Trucks, *J. Chem. Phys.* **1989**, *91*, 1062–1065.

[26] J. Tomasi, M. Persico, *Chem. Rev.* **1994**, *94*, 2027–2094.

[27] A. V. Marenich, C. J. Cramer, D. G. Truhlar, *J. Phys. Chem. B* **2009**, *113*, 6378–6396.

[28] Y. Zhao, D. G. Truhlar, *Theor. Chem. Acc.* **2008**, *120*, 215–241.

[29] J.-D. Chai, M. Head-Gordon, *Phys. Chem. Chem. Phys.* **2008**, *10*, 6615–6620.

[30] M.-A. Légaré, M.-A. Courtemanche, É. Rochette, F.-G. Fontaine, *Science* **2015**, *349*, 513–516.
[31] M. J. Frisch, G. W. Trucks, H. B. Schlegel, G. E. Scuseria, M. A. Robb, J. R. Cheeseman, G. Scalmani, V. Barone, G. A. Petersson, H. Nakatsuji, et al., **2016**.
[32] R. Ditchfield, W. J. Hehre, J. A. Pople, *J. Chem. Phys.* **1971**, *54*, 724–728.
[33] E. D. Glendening, C. R. Landis, F. Weinhold, *J. Comput. Chem.* **2019**, jcc.25873.
[34] "Chemcraft - graphical software for visualization of quantum chemistry computations.," can be found under https://www.chemcraftprog.com, **n.d.**

7 Appendix

See electronic attachment for appendix data.